CONJUGATE HEAT TRANSFER IN MINICHANNEL WITH EMBEDDED PIN FINS OR POROUS MEDIUM: APPLICATION TO BATTERY COOLING SYSTEM

by

Samson Olusegun Fatukasi
FTKSAM002

Submitted in partial fulfilment of the requirements for the degree

Doctor of Philosophy in Mechanical Engineering

in the

Faculty of Engineering and the Built Environment

University of Cape Town South Africa.

Under the Supervision of
Prof. Tunde Bello-Ochende

May, 2025

Abstract

Title: Conjugate heat transfer in minichannel with embedded pin fins or porous medium: application to battery cooling system

Supervision: Prof. Tunde Bello-Ochende

Department: Mechanical Engineering

Degree: Doctor of Philosophy (Mechanical Engineering)

University: University of Cape Town South Africa

Electric vehicle technology is gaining global attention as a sustainable alternative to fossil fuels, rapidly replacing internal combustion engine vehicles. However, managing the thermal performance of lithium-ion batteries - the optimal energy storage system for electric vehicles remains a significant challenge. This study focuses on developing an effective cooling system to manage the thermal challenges of a cylindrical lithium-ion battery pack operating under a high discharge rate of 6 C, generating volumetric heat transfer of $3340135\,\mathrm{W/m^3}$ of $20\mathrm{Ahm^{-2}}$ arranged in parallel and operating at a temperature of 298 K. The thermal performance of the cooling system was analyzed under varying Reynolds numbers by evaluating different configurations of channels mounted on a rectangular frame. The study explored the potential of heat transfer enhancement using circular, elliptical, and rectangular solid pin fins, as well as aluminum foam inserts with varying porosities. The effects of insert location, spacing, and three insert arrangements within the fluid domain were also investigated. Numerical simulations were conducted using ANSYS® Fluent 20R1 to solve the governing equations of heat transfer and fluid dynamics under different flow orientations. Results show that the cooling system achieved the highest heat transfer rate density when three channels were mounted on the rectangular frame, irrespective of the insert configuration. The insert placed closest to the inlet yielded the best thermal performance. Although low- and medium-porosity aluminum foam inserts enhanced heat transfer, their use was discouraged due to the high pumping power requirements. Among the three-insert arrangements, a spacing of 2.0 mm provided optimal thermal performance. Counterflow configurations consistently outperformed parallel flow arrangements. Notably, a single insert positioned at one-eighth of the channel length from the inlet *(L/8)* outperformed systems with three inserts, regardless of spacing arrangements. At the peak performance of the system with a circular, elliptical, and rectangular aluminum foam of 0.9 porosity insert, 46.1%, 36.2%, and 39.40% of improved enhancement

factors were achieved respectively, by the cooling system compared with solid pin fin counterparts. Overall, a cooling system with a circular solid pin fin insert positioned at L/8 demonstrated superior performance, exceeding elliptical and rectangular inserts by 10.6% and 4.2%, respectively. The optimization of this system using constructal theory, achieved a thermal performance enhancement of over 390% at a Bejan number of 7×10^8 compared to its unoptimized counterpart. Generally, the findings from this study show that for a battery cooling system, the number of mounted channels, flow orientation, insert's (solid pin fin or aluminum foam) location, and its number in the fluid domain have a significant effect on the dissipation of the heat from the battery pack. The influence of types, shapes, and porosities of the aluminum foam insert on the overall thermal performance enhancement of the cooling system was demonstrated. Overall, this study provides useful knowledge for enhanced design and effective electric vehicle battery pack heat dissipation of the cooling system.

Keywords: Electric vehicle batteries, heat transfer rate density, heat transfer enhancement, solid pin fin, aluminum foam, porosity.

Dedication

This thesis is dedicated to: The Almighty God (the Alpha and Omega), and my dear loving wife, as well as my son.

Acknowledgment

First and foremost, I would like to give my deep and sincere gratitude to my God almighty for who He is in my life. His Kindness, mercy, provision, protection, and guidance over my life before and during this research work are not taken for granted.

I am extremely grateful to my esteemed supervisor, Prof. Tunde Bello-Ochende, for his patience, unwavering support, and priceless counsel throughout my PhD studies. Your vast expertise and wealth of experience have inspired me throughout this research program.

To all the staff of the Mechanical Engineering Department, University of Cape Town South Africa, I say thank you for your kind support.

My gratitude extends to the Tertiary Education Trust Fund (TETFund), Nigeria, and the UCT postgraduate funding office for the provision of funding opportunities to undertake and finish this program successfully.

I want to express my profound gratitude to my Mentor, Prof. Miracle Olayiwola, who facilitated my coming to the University of Cape Town to study. Your sincerity and continuous support for my career progression will remain fresh in my mind forever.

My appreciation also goes to my friends, colleagues, lab mates, and research team for their continuous encouragement as well as effective emotional and social support. Raymond Ikeleji, Dr.Tanimu Jatau, Dr.Ariyo David, Sunday Judge, and Qudus Jimoh-Taiwo, you are all appreciated.

Dr. Lovemore, my esteemed writing workshop facilitator, indeed you came to boost my confidence for the successful completion of my study. Just as I always tell you, I can't thank you enough.

To my spiritual family in South Africa, Pastor Muyiwa Oloniyo, Bro. Makinde Isreal, Bro. Tope and his wonderful family as well as the entire church of all nations, I sincerely thank you all for your support.

My gratitude specifically goes to my father Late Snr. Apostle Moses Kokumon Fatukasi for the demonstration of fatherly love in terms of financial and moral support. Although you are no longer here, your work continues to speak well of you. What will I say about my mother Mrs Florence Idowu Fatukasi, you are a mother indeed. It is very emotional to remember those

days of hunger and pain you went through deliberately for me to succeed in life. Odunayo, Sade, Bose, and Bukola, I appreciate your prayers and encouragement during this research program.

It is very difficult to describe your personality Mr Adegboyega Adesiyan, you always show up at very critical times to provide strong support for me throughout my PhD program. You will never be stranded in the journey of life in the name of Jesus Christ. Mr and Mrs Adedayo Adesiyan as well as Mr and Mrs Gbenga Adedeji, the story of my PhD program will not be completed without showing you my sincere appreciation for your financial support.

To my ever-supportive and loving wife Dr. Mrs Bolade Adetutu Fatukasi, you provided a shoulder to lean on, when times were tough. Your continuous encouragement and prayer were very significant to the successful completion of this study. Special thanks to my lovely and handsome son, Testimony Oreoluwa Fatukasi for your understanding and tolerance for the period of undertaking my PhD research work.

Finally, I would like to thank all my colleagues at Osun State Polytechnic Iree, Nigeria, particularly members of staff of the Mechanical Engineering department for your support and consistent encouragement.

Declaration

I SAMSON OLUSEGUN FATUKASI, hereby declare that the work on which this thesis is based is my original work (except where acknowledgment indicates otherwise) and that neither the whole work nor any part of it has been, is being, or is to be submitted for another degree in this or any other university. I authorize the university to reproduce for the purpose of research either the whole or any portion of the contents in any manner whatsoever.

Signature: Signed by candidate Date: 19/05/2025

Table of Content

List of Figures

List of Tables

Publication in journals and conferences

During this research work, the following conference papers and articles were produced:

1) S. O. Fatukasi and T. Bello-Ochende, "Numerical development of effective cooling system for battery pack of electric vehicles," Materials Today: Proceedings, no. 65 (2020) 2192-2200, 2022, doi: 10.1016/j.matpr.2022.06.070.

2) S. O. Fatukasi and T. Bello-Ochende, "Numerical investigation of porosity and locations effects of rectangular aluminum foam in the flow channel on thermal performance of electric vehicles battery cooling system", 6th international conference on Engineering for a sustainable world, Ota, Nigeria, 28th-30th November, 2022. (Presented).

3) S. O. Fatukasi and T. Bello-Ochende, "The combined effect of the integrated channel and circular solid pin fin on thermal performance enhancement of electric vehicle battery at a high discharge rate." Scientific African Journal. (Under review).

4) S. O. Fatukasi and T. Bello-Ochende "Thermal combined analysis of electric vehicle battery cooling system performance enhancement with elliptical aluminum foam of varying porosities and locations in the flow channel" Submitted.

Nomenclature

A Surface area of a flow channel (m^2)

a Volumetric area (m^2m^{-3})

C Specific heat capacity ($J.kg^{-1}.K^{-1}$)

c Concentration of Li ($molm^{-3}$)

C_F Inertial coefficient

D Thermal diffusivity m^2/s

D_f Circular solid pin fin diameter.

D_h Hydraulic diameter (m)

E Potential (V)

F Faraday constant ($96485\ Qmol^{-1}$)

$f_{\pm}$ Mean molar salt activity coefficient.

F_h Frame height (mm)

F_t Frame thickness (mm)

G (NC, NE, or NR)

$G1.5M$ Cooling system of three channels with multiple inserts and spacing of 1.5mm.

$G2.0M$ Cooling system of three channels with multiple inserts and spacing of 2.0mm.

$G2.5M$ Cooling system of three channels with multiple inserts and spacing of 2.5mm

H Minichannel height (mm)

h Convective heat transfer coefficient (W/m^2K)

H_c Height of channel (mm)

H_f Circular solid pin fin height.

i Current density (Am^{-2})

K Thermal conductivity ($W.m^{-1}.K^{-1}$)

L Minichnannel length (mm)

L_{fr} Area of the rectangular frame (m)

$L/2$ Centre of the channel.

$L/4$ Quarter of the length of the channel towards the inlet.

$L/8$ Half of a quarter of the length of the channel towards the inlet.

N Cooling system without insert

NC Cooling system with circular insert.

NE Cooling system with elliptical insert.

NR Cooling system with rectangular insert.

P Pressure (pa)

q Heat transfer rate (W)

q''_d	Dimensionless heat transfer rate density
q'''	Volumetric heat transfer (W)
R	Radius (m)
r	Radial coordinate (m)
Re	Reynolds number
R_g	Universal gas constant $(8.3145 \mathrm{Jmol^{-1}k^{-1}})$
R_{th}	Dimensionless thermal resistance
S_a	Specified frame flat surface area with multiple flow channels.
T	Temperature (K)
t	Time (s)
t_+^0	Transference number of the electrolyte.
V	Volume (m^3)
$\dot{V}$	Volumetric flow rate $(\mathrm{m}^3/\mathrm{s})$
W	Minichannel width (mm)
W_c	Width of channel (mm)
x	Through plane coordinate (m)

Greek symbols

α	Transfer coefficient m^2/s
ε	Porosity
k	Ionic conductivity $(\mathrm{Sm^{-1}})$
ρ	Density $(\mathrm{kg.\,m^{-3}})$
σ	electronic conductivity $(\mathrm{Sm^{-1}})$
$\emptyset$	Potential (V)
∇	Differential operator
ν	Kinematic viscosity m^2/s

Subscripts

1,2,.5	Number of channels (with or without centrally located insert)
a	Anode
c	Cathode
CF	Counterflow orientation
e	Electrolyte phase
eff	effective
eq	Equilibrium

exp	Experimental
i	Particle interface
J	Insert located at L/4 in the channel
in	Inlet
Irr	Irreversible
n	Intercalation
P	Constant pressure
PF	Parallel flow orientation
p	Particle
f	Fluid
M	Insert located at L/8 in the channels
max	Maximum, Peak
$Ohms$	Ohmic heat generation
o	Initial condition
Rev	Reversible
s	Solid
tot	Total

CHAPTER ONE

INTRODUCTION

1.1 BACKGROUND INFORMATION

The concern about greenhouse gas emissions and the depletion of natural resources has propelled automotive researchers and engineers to develop electric vehicles to replace the gasoline type. Anthropogenic greenhouse gas emissions are thought to affect the climate and marine environment [1] strongly. Meanwhile, the global energy crisis and rising greenhouse gas emissions are largely caused by internal combustion engines. For instance, 60.5% and 62% of the world's petroleum was reportedly consumed by gasoline vehicles in 2006 and 2020 which resulted in a significant amount of CO_2 emissions [2]. According to the World Health Organization (WHO), 4.2 million people die each year from conditions directly related to air pollution, and at least 91% of the world's population is exposed to poor air quality [3].

An improvement in air quality recorded during the COVID-19 pandemic was linked to a sharp decline in fossil fuel demands due to the drop in transportation using gasoline vehicles, especially in highly populated cities [4]. As a result of this development, using internal combustion engine cars might likely be outlawed locally and internationally within the next decades, as proposed by many nations [5]. For instance, Denmark introduces tax rates of 180% on vehicles with internal combustion [6].

Also, the Norwegian government waived electric vehicle registration and value-added tax, while China formulated a policy that encourages scientific research and production of electric vehicles [2]. A motion prohibiting the sale of internal combustion engine vehicles by 2025 was recently passed by the lower house of the Dutch parliament [7]. These efforts by the governments of nations are directed towards the gradual replacement of internal combustion engines with electric vehicles, as it is generally accepted that these steps significantly minimize air pollution. Hence, the development of electric vehicles with the hope of little or no damage to the ecosystem. However, the effective operation of the electric vehicle largely depends on the batteries as its power source.

Among various batteries, lithium-ion battery (Figure 1.1) is considered the most preferred for electric vehicle operation due to certain advantages such as high energy density, high voltage, low self-discharge, and ease of maintenance [8]. However, the wide acceptance and large production of lithium-ion batteries are restricted due to excessive heat generated during

charging or discharging working conditions [9]. Accelerated power degradation, capacity reduction, and thermal runaway are major consequences of heat generated in the lithium-ion battery [10-12]. Therefore, developing the cooling system for thermal management of lithium-ion batteries becomes inevitable.

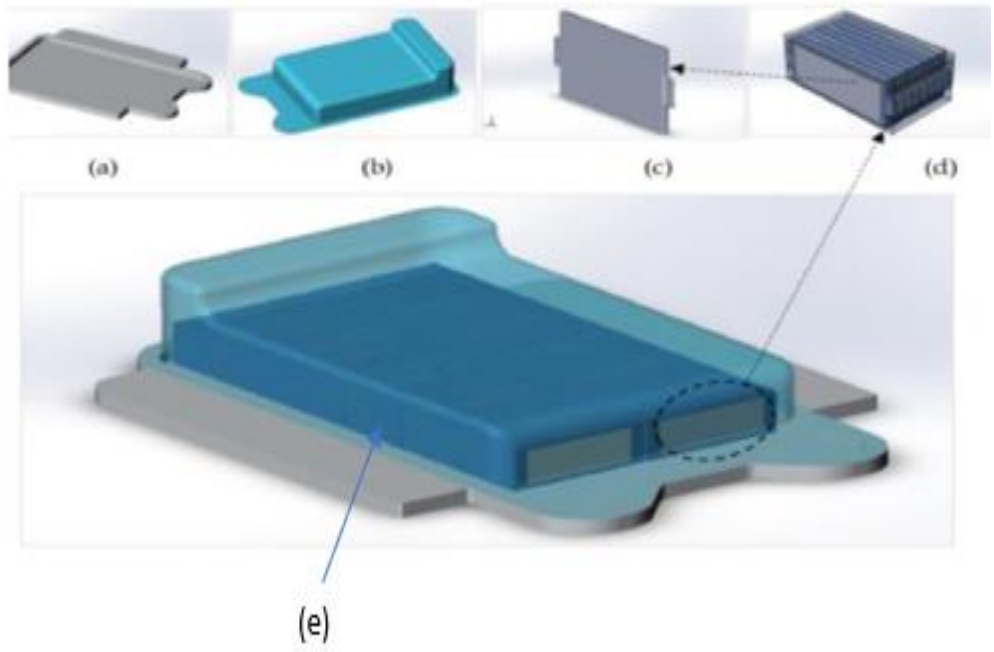

Figure 0.1. Lithium-ion battery, Chassis (a) cover (b) Cellule (c) Module (d) Battery pack (e). [13]

Rao, et al., [14] reported heat pipe [15-17], phase change material (PCM) [18-20], air [21-23], and liquid [24-26] cooling as the four major techniques for managing the temperature challenges of the lithium-ion batteries, and that two or more techniques could be integrated for the enhancement of the heat transfer process [10]. Among all, liquid cooling was reported by [27] to be more effective for temperature control of lithium-ion batteries, particularly when dealing with larger battery packs operating at a very high discharge rate. According to [28, 29], the cooling system principle of operation is based on transferring heat without transferring fluid that carries the heat. In most cases, the cooling system's effectiveness is related to its hydraulic diameter because the heat transfer coefficient increases with the reduction of hydraulic diameter, as reported by [30]. A developed system with a smaller hydraulic diameter, known as micro/mini-channel was proved by [31] to have a better thermal performance in removing heat than a conventional heat exchanger with a larger hydraulic diameter ($D_h > 3$ mm).

Proposing micro/mini-channel as the best alternative cooling system in replacement of traditional heat exchangers, their work demonstrated the removal of 790 W/cm^2 heat flux experimentally by a micro/mini-channel heat sink. Thakre et al.[32] claimed 50% heat transfer coefficient improvement of micro/mini-channel over the conventional heat exchanger. According to [33], Manufacturing and operating costs reduction with ease of pressure control, and high energy efficiency have given micro/mini-channel special consideration as suitable cooling technologies. Therefore, the application of minichannel for thermal control of electric vehicle batteries will be an interesting adventure. A number of studies dedicated to the thermal management of lithium-ion batteries with minichannel have been reported both numerically [33-35] and experimentally [36].

The heat transfer enhancement between the minichannel internal structure and the working fluid can potentially to improve the cooling system's thermal performance. An improved heat transfer due to better fluid mixing in the flow channel equipped with an insert has been observed to yield better thermal performance enhancement of the cooling device [37-41]. The thermal analysis of the different shapes of solid pin fin or aluminum foam insert on thermal performance enhancement of the minichannel cooling system specifically designed for battery thermal runaway prevention, was documented by several studies [42-44]. In addition, researchers investigated the influence of increased numbers, and arrangements of pin fins or aluminum foam in the fluid domain on the thermal performance of cooling systems [41, 45, 46]. The friction factor effect on the enhanced heat transfer in the flow channel remains significant in evaluating the overall thermal performance of a minichannel cooling system equipped with an insert. Guo et al. [45] employed the thermal performance enhancement factor to present a battery thermal management system with a tolerable working fluid friction factor.

To achieve the optimal performance of the battery thermal management system, significant research [41, 47-52] has been carried out on cooling system optimization through the application of the constructal law and design. The laws hold a better flow architecture, resulting in minimum global flow resistance and the best equilibrium of all the internal flow resistance of the cooling configuration. Therefore, cooling system optimization should be considered to realize optimal performance.

Computational fluid dynamics (CFD) is an entrenched design tool used in engineering. It has become the standard technique for configuration development and analysis in many fields. The tool provides the possibility of multiparameter optimization within a short time and is

recognized as a cost-effective method that can supplement the shortcomings of field and laboratory investigations.

1.2 Motivation for the study

Higher energy efficiency and zero emission benefits have attracted the invention of electric vehicles, thereby replacing conventional gasoline vehicles. However, the increasing reports of fire and explosion of electric vehicles due to poor thermal management of lithium-ion batteries [53-55] as optimum power storage for this electrifying vehicle calls for more research attention. Hence, the motivation for this present research work. This work involves the development of a lithium-ion battery pack coupled with a minichannel cooling system equipped with the solid pin fins or aluminum foam insert(s). With the application of constructal theory and design, the optimized cooling system for maintaining the battery pack in an allowable temperature range of $25℃ - 42℃$ and temperature variation of less than $5℃$ inside the pack will be presented.

1.3 Aim of the research

This research aims to develop a compact and effective minichannel cooling system for the thermal management of a lithium-ion battery pack in an electric vehicle operating at a very high discharge rate. Different types of cooling systems will be modeled to enhance the performance of the developed system. The optimized system will be obtained with the application of constructal theory and design.

1.4 Objectives of the study

The objectives of this study are to:

i) Develop and validate a model for predicting the thermal performance of a cooling system coupled with an electric vehicle battery pack operating under a steady state condition.

ii) Investigate the effect of the number of channels (with or without insert) mounted on a rectangular frame on the cooling system's thermal performance.

iii) Investigate the heat transfer enhancement potential of varying the location of a single circular, elliptical, and rectangular solid pin fin or aluminium foam of varying porosities inserted in the channels on the thermal performance of the developed cooling system.

iv) Compare the enhancement potential of a single with multiple (three) insert(s) of varying spacing arrangement from the best point of insert (circular, elliptical, and rectangular solid pin fin or aluminium foam) location in the channels towards the inlet on cooling system performance.

v) Compare the enhancement potential of different configurations (circular, elliptical, and rectangular) of solid pin fins with aluminum foam on the cooling system performance.

vi) Optimize the cooling system for best performance using constructal theory and design approach.

1.5 Scope of the research

In this study, the thermal performance of the cooling system for thermal management of electric vehicle battery pack is developed using CFD code with forced convective heat transfer, steady, laminar, and incompressible fluid flow. The battery pack of five similar 26650 cylindrical lithium-ion batteries with each of $20Ahm^{-2}$ capacity operating at a high discharged rate of 6C (Columbus) is coupled with a cooling system of a rectangular frame mounted with minichannel(s). With volumetric heat transfer of $3340135\ \mathrm{W/m^3}$ equivalent to the total heat generated by the battery pack, various velocity boundary conditions are employed for the simulation process. The enhancement of the cooling system performance was numerically analyzed based on the number of channels (with or without insert) mounted on the rectangular frame, varying location of single, and spacing arrangements of multiple (three) insert(s) in the fluid domain. The solid pin fin and aluminum foam of low (0.1), medium (0.5), and high (0.9) porosities of the same base and height were employed as inserts in this study. The thermal performance of the developed cooling systems is evaluated with the maximum rectangular frame wall temperature, dimensionless thermal resistance, dimensionless heat transfer rate density, and thermal performance enhancement factor. Throughout this study, water with constant and temperature-dependent properties assumptions is considered as the working fluid to present all simulation results in steady-state working conditions of the battery pack model.

With the application of fixed channel length and volume, the optimization of the cooling system with the highest value of thermal performance enhancement factor indicating superior performance in dissipating heat from the battery pack, is presented for the optimization process using the constructal theory and design approach.

1.6 Research Methodology

The aims and objectives of this research work were actualized with the adoption of numerical analysis. Using commercial computational fluid dynamics (Ansys® 2020) Fluent comprises goal-driven optimization algorithms, the numerical approach which entails modeling and discretization of the computational domain, conjugate heat transfer problem solving by employing appropriate governing equations, and result processing as well as searching for optimal design variables with global objective in view were effectively accomplished.

1.7 Material selection

With a view to the development of an engineering system characterized by a high level of durability, optimal performance, and effective cost implication, careful selection of materials becomes inevitable. For this study, aluminum is considered a suitable material because of its excellent corrosion resistance, easy manufacturing, low density, high thermal conductivity, and specific heat transfer in reference to other materials such as diamond, copper, silicon e.t.c. However, according to manufacturer specifications, the cathode and anode of the 26650 cylindrical lithium-ion battery considered for this work are designed with Lithium-ion phosphate and graphite, respectively.

1.8 The novelty of the study

According to [56, 57], the placement of an insert in the flow channel reduces the thermal boundary layer leading to an improved heat transfer coefficient. However, the thermal boundary layer thickness increases with the length of flow channels [45] indicating that the thermal boundary layer grows with the location. This suggests that the re-initialization of the thermal boundary layer for enhanced heat transfer in the channel is sensitive to the location of an insert in the channel. Available open literature shows no research attention to the search for the finest location of an insert in the channel for improved system performance. The novelty of this work is in simulating the flow and heat transfer characteristics of several insert locations in order to identify the point that gives the appropriate best performance for significant improvement in battery cooling system performance.

1.9 Thesis Organization

This thesis is organized into ten chapters each with different sections and subsections for ease of reading and referencing. Each chapter provides a detailed description of the analysis carried out in this study.

- Chapter 1 provides the background information and motivation for the study, the research objectives, and the methodology employed to carry out the study.

- Chapter 2 provides a detailed review of relevant publications on electric vehicle batteries, heat generation, and cooling techniques of lithium-ion batteries. It also presents a relevant discussion based on the open literature on the liquid cooling system performance enhancement, constructal theory and design approach, and cooling system optimization techniques.

- Chapter 3 briefly reviews the fundamental principle governing heat generation in cylindrical lithium-ion batteries. It also presents the numerical modeling used in this study. The discussion on mass, momentum, and energy conservation equations governing the transport of mass and heat as well as porous media mathematical formulations, is well-detailed in this chapter. The chapter also explained the equations governing the optimization algorithm.

- Chapter 4 presents the numerical model for the cylindrical lithium-ion battery pack cooling system with mounted channels on a rectangular frame. The chapter demonstrates the behavior of the system design with the number of channels without an insert mounted on the rectangular frame, under the influence of different flow orientations.

- Chapters 5, 6, and 7 respectively, provide the enhancement potential of a circular, elliptical, and rectangular sold pin fin and aluminum foam of varying porosities inserted into the performance of the cooling system designed in Chapter 4. Different locations of the insert effects on the system performance were detailed and compared with the varying spacing arrangements of three inserts. Finally, the enhancement potential of the aluminum foam inserts was compared with that of the solid pin fin

- Chapter 8 presents the comparative analysis of the different shapes of the solid pin fin insert on the system performance enhancement.
- Chapter 9 presents the optimization of the cooling system with the highest thermal performance from Chapter 8.
- Chapter 10 presents the general findings from this study and gives recommendations for future work.

CHAPTER TWO

LITERATURE REVIEW

2.1 Electric vehicle batteries

The importance of crude oil in driving the economy of any nation is so significant [58]. However, its harmful effects on the environment and humanity paved the way for the innovation of electric vehicles as an alternative to gasoline and diesel (a constituent of crude oil) vehicles. Improved energy efficiency, performance, and environmental friendliness are some of the notable advantages of electric vehicles listed by Tamaldin et al.[59]. Tesla Model S, BMW i3, Smart Electric Vehicle Drive, Nisan Leaf. BYD and Kia Soul EV are a few among other commercial electric vehicles present in the market today [55]. These zero-emission vehicles depend mainly on stored electricity in a battery pack to power an electric motor that turns the wheels. The operational characteristics of power batteries to meet vehicle necessities are a concern to both battery manufacturers and users. Lithium-ion batteries, which were first introduced to the market in 1991 by Sony Corporation and are composed of electrolyte, carbon-based anode, lithium compound-based cathode, and separator as their major components (Figure 2.1) have received general applications in developing zero-emission transportation and are the leading candidates for hybrid and electric vehicles [60].

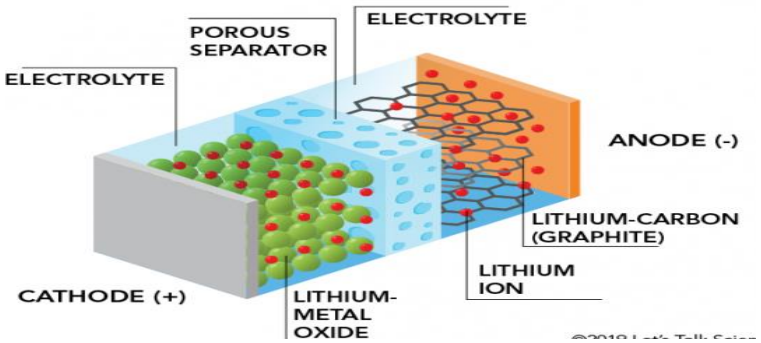

Figure 0.1. Lithium-ion battery composition [61]

As shown in Figures 2.2. the lithium-ion battery is manufactured in three shapes: prismatic, pouch, and cylindrical.

- Lithium-ion prismatic cells are comprise of large sheets of anodes, cathodes, and separators that are sandwiched, rolled up, and compressed into a cubic shape to fit within a metallic or hard-plastic housing.
- Pouch cells employed a sealed piece of flexible foil rather than a solid enclosure as their cell container. This is a more simplistic method of packaging that results in flexible cells that may easily fit the available area for a particular product.
- A cylindrical cell comprises cathodes, separators, and anodes in the form of sheets that are sandwiched, wound up, and crammed into a container with a cylinder shape. Due to this battery's rounded design, the internal pressure from side reactions is distributed practically evenly across the cell's perimeter. This enables the cell to sustain greater internal pressure without deforming.

The anode and cathode materials are usually coated with copper foil and aluminium foil, respectively. Serving as the current collectors, aluminum and copper can complement the extension of the life span of lithium-ion batteries [60, 62]. High energy density, lightweight, low self-discharge rate, high cycle life span, and ability to store higher electrical energy in a bit of space are specific lithium-ion battery advantages itemized by [53] for its popularity as a preferred primary energy source for electric vehicles. Categorized as a rechargeable type of battery, the lithium-ion battery works on the principle of intercalation or deintercalation of lithium ions into the structure of the electrode materials**.** The oxidation state of lithium changes from 0 to +1 as it oxidizes from Li to Li+ in the lithium graphite anode during the discharge operation as reflected in the Equation. (2.1)**.** Following Equation (2.2), the lithium ion is integrated into lithium cobalt oxide as it migrates to the cathode through the electrolyte medium in which the cobalt oxidation state reduces from +4 to +3. The battery cell is recharged when the lithium-ion migrates back to the cathode [63]

$$C_6Li \rightarrow 6C(graphite) + Li^+e^- \quad (2.1)$$

$$Li_{1-x}CoO_2(s) + xLi^+ + xe^- \rightarrow Li\ CoO_2(s) \quad (2.2)$$

The migration of the lithium ions from one electrode to another during battery operation generates extensive heat in the battery cell. The hotter the cell, the shorter the life span of the

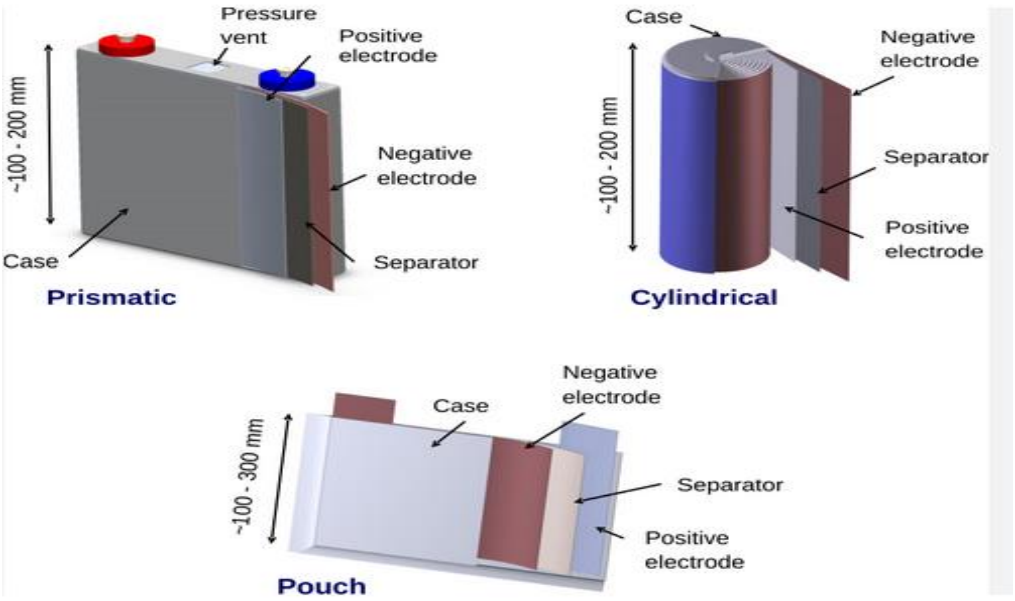

Figures 0.2. Different configurations of Lithium-ion cells [64]

battery module [10]**.** The depletion of running lithium ions and active materials in conjunction with an increase in the internal resistance of lithium-ion batteries was traced by [65] to elevate the operating temperature. Meanwhile, [66] documented significant differences in kinetic and thermodynamic properties impact the rate of heat generated by different lithium-ion battery components. The internal capacity of the battery cell was said to deteriorate by 30% and 70% when operating at 25℃ and 55℃ respectively after 800 cycles of operation [67]. According to [68], the state of charge (SOC) and state of health (SOH) of lithium-ion battery cells will be greatly retarded with overheating and non-uniform temperature differences resulting in premature cell failure and thermal runaway. At a discharge rate of 1-C, an increase of 5℃ – 20℃ of temperature was recorded by [69] for a single lithium-ion polymer cell with a temperature increment higher at low SOC. In a battery operating temperature range of 30℃ – 40℃ [70] reported approximately 2 months deterioration of lithium-ion battery life span for every degree of temperature increment, and suggested the maintenance of temperature gradient in both battery level and module level below 5℃

However, battery working conditions below the temperature of −10℃ will hasten the rate of cell capability and aging deterioration [71, 72]. Liu et al. [10] fixed the optimum working temperature of lithium-ion cells within the range of 20℃ and 40℃ for effective performance, durability, and longevity of the battery of electric vehicles.

2.1.1 Heat generation process in a lithium-ion battery

Itemising the three factors influencing heat generation in lithium-ion batteries, [73] reported the larger impact of the C rate to increase the generation of heat than other factors such as temperature and state of charge (SOH). According to [74] thermal runaway and premature cell failure are direct consequences of uncontrolled exothermic reactions in the battery cell. The safety enhancement of this energy storage facility can be better achieved when there is an adequate understanding of internal thermal behavior as well as the source of heat generation in the battery. Different electrochemical methods, such as voltage temperature coefficient, galvanostatic intermittent titration technique (GITT), and hybrid pulse power characteristics, have been employed by various researchers [74-76] to calculate the contribution of different heat sources to the total heat generated by lithium-ion batteries.

According to Basu et al. [62], The following have been identified as the three primary sources of the total heat generated by the lithium-ion battery during working operation: (i) reversible heat generation, (ii) Irreversible heat generation, and (iii) ohmic heat generation.

(i) *Reversible heat generation*.: This type of heat generation is susceptible to cell entropy changes. Charge transfer in the electrolyte and electrode reactions is the main cause of the entropy change in an electrochemical cell. More than 50% of the total heat generated by a lithium-ion battery at a discharge rate of 1.0 C was reported to have contributed by reversible heat generation as thermodynamically analyzed by [77] which depicts the significant effect of reversible heat generation on total heat dissipated by a cell of lithium-ion battery at a low discharge rate and high temperature [73, 78]. However, this generated amount of reversible heat was of the same proportion at the cathode and anode [62]. The influence of the local heat effects inherent in electrodes on reversible heat generated by the battery cell of a lithium-ion battery was reported by [79]. Using an electrochemical thermodynamic measurement system, [75] documented a higher value of reversible heat generation for $LiCoO_2$ base electrode when compare to $LiNixCoyMnzO_2$ and $LiFePO_4$,base electrodes, while lithium titanate was observed with the lower change of entropy in comparison with graphite base anodes using this same electrochemical method.

(ii) *Irreversible heat generation*.: Characterized as an exothermic reaction, irreversible heat generation is connected to the overpotential needed to drive the reaction at a finite rate. This type of heat generation rises with discharge rate and temperature. For instance, with an increase

in discharge rate from 0.25A to 5A, an increase of irreversible potential from 0.034V to 0.369V was reported by [80] and significant value of irreversible heat generation was documented with the temperature varied between $15℃ \; and \; 55℃$. During the intercalation of Lithium in the graphite anode, a spike of exothermic heat effect was experimentally observed by [81] which suggests the contribution of irreversible heat generation to total heat generation is more significant during the intercalation process [82].

(iii) *Ohmic heat generation*.; Ohmic heat generation is a function of resistance offered to the electronic and ionic transport in the solid and liquid phases, respectively. This was further simplified by [83] as the authors analyzed the three main components of ohmic heat generation as (i); heat due to the transformation of lithium-ion in the electrolyte, (ii); heat due to intercalation or deintercalation chemical process of lithium-ion into solid particles, and (iii); heat originated from aluminum and copper current collectors. In the presence of high current, this type of heat generation strongly influence on the discharge capacity of the lithium-ion battery as a consequence of voltage drop [73]. Ohmic heat generation at the cathode was experimentally observed with significant contribution to total heat generated by lithium-ion battery at a high discharge rate but at a lower discharge rate an isothermal operation with other sources of heat generation was reported [62]

Proper understanding of the heat generation mechanism in a lithium-ion battery is essential for developing its cooling system. Hence, the focus of this research.

2.1.2 Thermophysical properties of cylindrical Lithium-ion battery

According to [84], Commercial lithium-ion batteries often have electrodes that are made of a combination of electrochemically active materials, carbon black conductive agents, and polymer adhesives, which are coated on metal foil collectors. While the anode-active material is composed of carbonaceous materials in which intercalation and deintercalation of Lithium-ion take place, the cathode-active material was reported [85] to be classified into four major categories: lithium manganese oxide ($LiMn_2O_4$), lithium nickel manganese cobalt oxide ($LiNiMnCoO_2$ or NMC), lithium cobalt oxide ($LiCoO_2$), and lithium iron phosphate ($LiFePO_4$ or LFP). The thermal properties and stability of the active materials are among the most important factors that affect battery performance, as they limit the operating temperature range of the battery in response to heat generation [86]. Additionally, the lithium-ion batteries' ability to perform effectively during charge and discharge operations depends on the ionic and electronic conductivity of this active material, which is temperature-dependent. Low thermal

conductivity of the separator has been indicated as one of the major hindrances to effective heat transfer in the lithium-ion battery [87]. Yang et al. [88] achieved a five times enhancement of lithium-ion battery separator when the authors developed a nano/micro-Al_2O_3 PVdF-HFP-based composite separator of high thermal conductivity. Their study expressed the influence of nano Al_2O_3 on the improvement of composite thermal conductivity.

However, the physical construction of a cylindrical lithium-ion battery (Figure 2.3) necessitates the need for adequate knowledge of its anisotropic thermal energy transport in the battery cell electrodes. It is expedient to note that improving limiting components of a lithium-ion battery can easily be achieved with effective knowledge of the battery cell thermal conductivity. In their combined experimental and CFD simulation analysis, [89] respectively documented $4.32\ \mathrm{W/mK}$ and $11.5\ \mathrm{W/m/K}$ as a measured radial and axial thermal conductivity for cylindrical Tesla NCA ternary lithium battery Using a calorimeter, [90] experimentally measured and documented heat capacity of certain batteries including lithium-ion battery. Their work reported the influence of the battery pack design model on cell temperature distribution. Meanwhile, 18odelling the battery cell using effective thermal conductivity and heat capacity is more appropriate due to the distributed nature of heat generation within a Li-ion cell [85]. This was experimentally demonstrated by [91] where the authors employed xenon flash technology (XFT) and steady-state measurements to analyze the Sony US- 18650 lithium-ion battery and its componens' thermal properties with and without electrolyte. Their study reported the rise of specific heat capacity and thermal conductivity with an increase in open circuit voltage. Identifying certain flaws such as; inadequate presentation of whole cells' thermal conductivity, cumbersomeness, and high cost of analysis related to the use of the XFT method, [85] employed cell axial thermal response in an adiabatic geometry as a new method to determine rapid measurement of axial and radial thermal conductivity as well as heat capacity of cylindrical lithium-ion battery cells. The authors documented the simplicity and effectiveness of this method as an advantage over the XFT method for the accurate measurement of heat capacity and anisotropic thermal conductivity of 26650 and 18650 cylindrical lithium-ion battery cells simultaneously in a single experiment. The pipe method in conjunction with nichrome and type K thermocouples was adopted by [92] to measure lithium-ion battery radial thermal conductivity effectively. Investigating the accuracy of this method, 25% of the uncertainties resulted in the study by [93], and a more precise value of radial thermal conductivity of cylindrical lithium-ion battery was documented when the authors combined differential scanning calorimetry (DSC) and laser flash method (LFA) in addition to

the pipe method. The need for an automated process of sensor positioning and heating wire for accurate temperature measurement was stressed by their study as a means of averting possible uncertainties related to the pipe method.

Either at cell or module level, the basic thermal properties information related to the heat capacity and thermal conductivity of lithium-ion batteries is critical to the development of a reliable and effective battery cooling system.

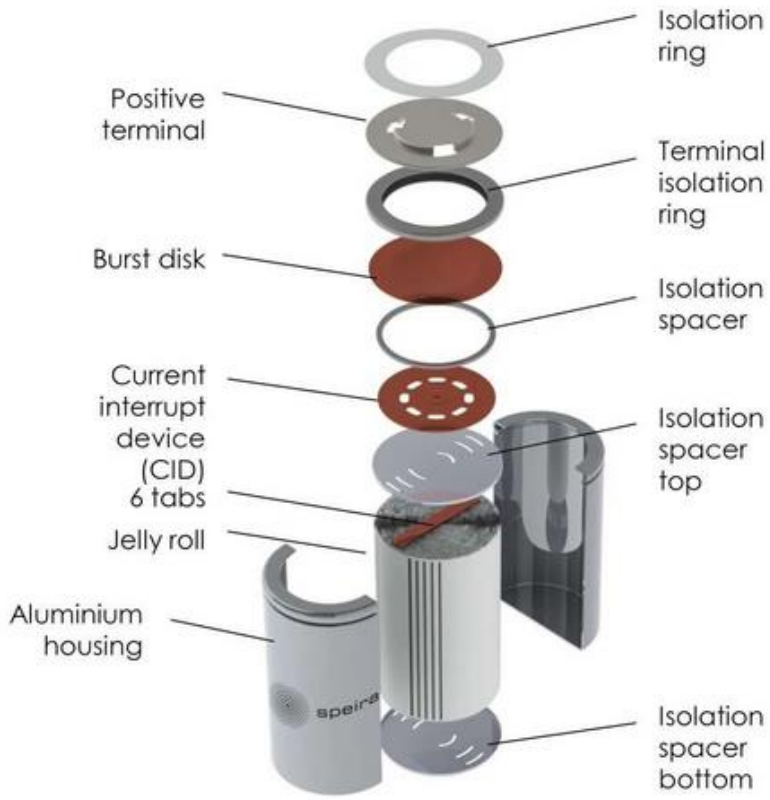

Figure 0.3. Cylindrical Lithium-ion battery components. [94]

2.2 Battery Cooling Techniques

For the safety, durability, and efficient operation of batteries of electric vehicles, the development of a battery cooling system to mitigate the excessive heat generated by this energy storage device becomes very crucial. Researchers have conducted several studies in pursuit of the best cooling technology to address the rising temperature challenges in the battery during working operation. Generally, numbers of cells are combined to give a large battery pack/module in either parallel or series arrangement [10]. The cell's thermal and electrical conditions in the module should be excellently guided to ensure adequate battery safety and desirable operation [55]. Thus, the decay of hotter cells corresponds to the malfunctioning of

the pack or module [10]. Charge acceptance, round-trip efficiency, system electrochemical operation, life and lifecycle cost, power and energy capability reliability are certain battery aspects capable of being affected by unchecked temperature rise in lithium-ion battery [69].

In 2019 and 2018 respectively, a fire accident in Tesla Model S in Pittsburgh and flames bursting out from the Porsche Panamera E-Hybrid while connected to a household charging plug-in in Thailand were blamed on poor thermal management of lithium-ion batteries [55]. Hence, an effective cooling system for the electric vehicle batteries is needed. Benabdelaziz et al. [13] numerically studied the impact of different external cooling solutions on the internal temperature of the battery pack.

However, with the knowledge of heat transfer media, thermal management for Lithium-ion batteries can be categorized into (i) Heat pipe cooling system, (ii) Phase change material (PCM) cooling system, (iii) Air cooling system and (iv) water cooling system [14]. However, two or more techniques could be integrated for the enhancement of the heat transfer process [10].

i) Heat pipe cooling system for lithium-ion batteries of electric vehicles: Heat pipe as one of the favorite devices for transferring heat between two solid interfaces is characterized by very high effective thermal conductivity which makes it popular for the thermal management of battery of electric vehicles [17] Made up of a closed tube, the heat pipe comprises of an adiabatic, evaporator, and condenser section, section as a major component is shown in Figure 2.4. At constant temperature, the capacity of the heat pipe to homogeneously maintain the surface of an evaporator was reported by [95].

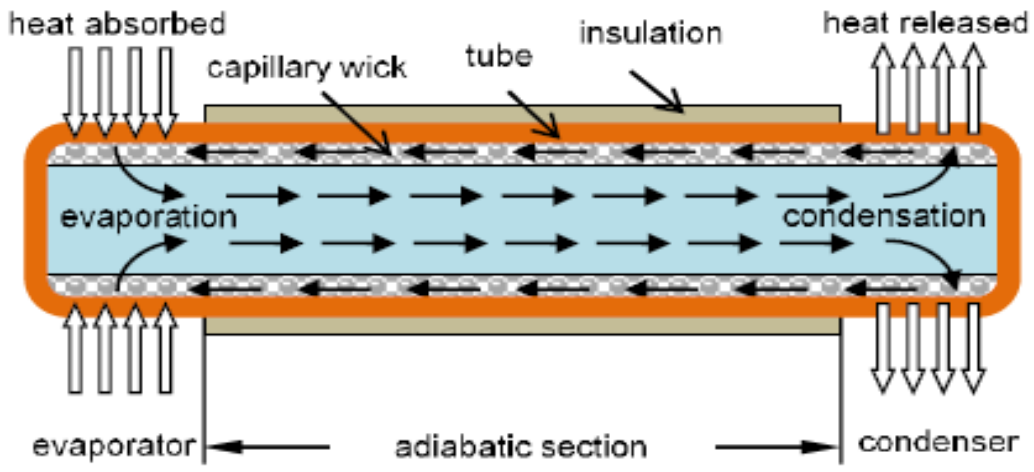

Figure 0.4. Heat pipe designed [96]

Based on the cooling strategies adopted in the cooling ends, heat pipes can be combined with an air-cooled and water-cooled system [17]. Flexible configuration, compact structure, easy maintenance, bidirectional characteristics, and long life time are expected advantages associated with heat pipes[10, 17]. The capacity of a heat pipe inserted into the cooling system to adequately manage the thermal behavior of lithium-ion batteries of electric vehicles was numerically and experimentally demonstrated by **[15]** when the cooling effectiveness of forced and natural convection with and without a heat pipe in the battery module was investigated. Rao et al. [16] achieved less than $50℃$ peak temperature of a lithium-ion battery operating with a heat generation rate below $50W$ and successfully lowered the maximum temperature gradient to $5℃$ with a $30W$ reduction of heat generation rate when using a thermostat water bath as a water-cooled heat pipes battery thermal management system. Meanwhile, an experimental investigation of the cooling and heating capacity of ultra-thin micro heat pipe for thermal management of a lithium-ion battery pack in the electric vehicle was conducted by [10].

The optimal working temperature of the lithium-ion battery was fixed between $20℃$ and $40℃$. While authenticating the superiority of wet cooling integrated heat pipe as a cooling system, the effect of the internal structure of the heat pipe on the thermal performance of the battery thermal management system was experimentally reported by [17] to be more significant than the angular impact of ultra-thin heat pipes. However, [97] documented the angular effect of oscillating heat pipe (OHP) on its operation as a cooling system for the battery of electric vehicles. The best angle for the excellent operation of the OHP was fixed between $1° - 5°$ by the authors when they experimentally investigated the effectiveness of the OHP battery thermal management system. Although, the heat pipe was found by [98] to be 90 times better than copper bars of the same size in terms of thermal conductivity, and the possibility of attaining a uniform temperature profile along the evaporator section of the heat pipe was also reported by [99] which suggests its capacity to secure uniform battery temperature when it is applied as a battery cooling system, yet its application for commercial electric vehicle battery thermal management system comes with challenges of cost and gravity [55]

ii) *Phase change material cooling system for Lithium-ion battery:* Working on the principle of heat absorption during phase change, phase change materials (PCMs) can retain and release thermal energy in large amounts at a certain temperature. The latent heat stored during the solid-phase transition stage by phase change material is utilized to passively control the

extensive heat generated in the batteries. According to [18], reduction in thermal inertia, effective heat transfer coefficient over a small temperature gradient, and thermal energy are notable advantages of using latent heat instead of sensible heat by PCMs

Meanwhile, the capacity of (PCMs) to excellently dissipate generated heat from the batteries is somehow limited because of their low thermal conductivity [100] as larger thermal conductivity yields faster dissipation of heat generated by the battery [101]. Mills et al. [18] reported 20-30 times, that the composite matrix's thermal conductivity was higher than that of pure PCM. While suggesting the adoption of PCM composite for thermal management of lithium-ion batteries, the authors showed that thermal conductivity augmentation for PCM is best obtained when a graphite matrix is saturated with paraffin. The possibility of improving PCM thermal conductivity was also demonstrated, when [19] integrated graphene into the paraffin wax. Their work documented critical improvement of lithium-ion battery module performance when latent heat storage, sensible heat, and enhanced thermal conductivity of a PCM were employed to manage the thermal behavior of a battery pack. It is worth noting that, the latent heat contribution to the total heat storage in a PCM is a majorly larger contribution when compared with the sensible heat content [20]. The fin structure intercalation approach was the focus of [102] to improve the thermal conductivity of PCM and 2℃ as well 6.4℃ of battery temperature reduction was numerically achieved at 2C and 3C, respectively. Earlier, the influence of varied fin inclination angles from $0° - 180°$ on the duration of the melting process in PCM was researched by [20] and a direct relationship of melting time with fin inclination angle was established. The authors demonstrated the increase in the natural convection flows and the number of vortices in the liquid PCM as the reason for this effect.

However, [103] noted that the suitability of phase change materials to manage the thermal effect of lithium-ion batteries was hinged on the constant transition temperature. Their experimental investigation shows the PCMs' effectiveness in sustaining battery temperature below the allowable maximum temperature. The effect of latent heat on PCM with natural convection was observed with insignificant temperature reduction as well as low-temperature uniformity of the battery when the numerical investigation of the latent heat effect was conducted by [101] on the cooling effect of PCM as a battery thermal management system. Naturally, the PCM cooling system is known for temperature homogeneity during phase change transition and this effect can be enhanced with an increase in air convenction [102]. The capacity of combined PCM and liquid cooling to avert thermal runaway of a lithium-ion battery was studied by [104], and the authors documented effective performance with a high

level of safety for the battery pack. A large surface area for much airflow was actualized when the commonly blocked–shaped module of a phase change material was replaced with serpentine plates for battery thermal management [105], and their work reported the attainment of a much lower peak temperature of the battery module. Thus, an outperformance of combined phase change with fluid cooling against sole phase change materials for thermal management of the battery was established [104, 105]. Despite the number of developments documented above, weak structural strength, leakages, acting as an insulator after the melting process, overweight, high cost of maintenance, and lower thermal conductivity are known challenges limiting the application of PCM as a thermal management system for the lithium-ion battery of electric vehicles [20, 55, 102, 104].

iii) *Air-cooled system for Lithium-ion batteries of electric vehicles:* As another attractive battery cooling technology, the air cooling system is characterized by certain advantages such as simple structure, ease of integration, lightweight, low cost of maintenance, and no leakage threat [22]. The abundant availability of air as a medium of heat transfer projected this type of cooling system the cheapest, which consequently translates to lower prices for electric vehicles [10, 22, 27, 44]. According to [55], commercial electric vehicles such as the Toyota Prius Prime and Nissan eNV-200 employed this cooling technology to effectively control the temperature rise in their battery pack. Adopting air as a cooling medium [106] minimized the peak temperature in the battery pack to 1.1℃ with tapper flow ducts of air-cooled battery thermal management, and a very low-pressure drop was documented with this developed cooling technology. Their work demonstrated improvement in the heat conduction of air-cooled battery thermal management with the replacement of an aluminum cooling plate by a copper cooling plate. The effectiveness of a designed air-cooling system on the thermal performance of aligned and staggered array battery packs was investigated by [107] based on the transverse and longitudinal spacing of lithium-ion battery cells. While reporting the direct impact of transverse interval on the temperature rise of the battery and increase of inlet duct for cooling air on improvement of battery temperature uniformity, the direct and indirect relationship between peak temperature rise, and the longitudinal interval were respectively reported by the authors for staggered and aligned battery arrays. According to [108], an effective cooling process for a 5×5 cubic structure is best attained with an air flow of $1\mathrm{m/s}$ when the battery cell inter-spacing is fixed at $1\mathrm{mm}$. The influence of air jet cooling was demonstrated when [21] developed a two-dimensional air flow thermal management technology to augment the dissipation of heat accumulated in the middle cell of a battery pack. Meanwhile, the essence of

battery pack structure and flow configuration adjustment for actualization of highly effective battery air cooling system with low temperature difference between battery cells has once been pointed out by [22].This was demonstrated when [23] developed air-cooled battery thermal management with a U-tube type flow duct to successfully enhance its thermal performance when the battery module was changed from longitudinal to horizontally array. 6.5℃ of battery pack maximum temperature rise with 1.96℃ peak temperature difference of the battery pack was affirmed when the authors numerically employed forced air-cooling technology. The widths and convergence/divergence ducts of developed U, Z and I type of air parallel cooling battery thermal systems were optimized to effectively minimize battery packs' temperature difference, and excellent results of improved thermal performance of air-cooling technology were reported [109]. Numerical optimization was considered by [22] using the LMB model to propose effective air-cooled battery thermal management with the number of inlets and inlet air temperature of 25℃ yielded 33.1℃ and 14.9℃ respectively as average temperature and maximum temperature difference; a cooling configuration was suggested as a standard for a battery packing cooling system. Moreover, [46, 110], seeks to enhance the performance of an air-cooled battery thermal management by designing and optimizing an embedded flow channel with pin fin and aluminum foam. Significant improvement of heat dissipation obtained with this development over a straight channel depicts the influence of inserts in the fluid domain on the heat transfer coefficient.

However, low heat dissipation from battery packs by air-cooled battery thermal technology because of the low thermal conductivity and heat capacity of air as a working fluid is an unavoidable concern to researchers and engineers despite the number of research studies dedicated to the thermal performance improvement of this type of cooling technology [21, 22, 105, 109]..

iv) *Water-cooled system for Lithium-ion battery of electric vehicles*: The choice of water-cooled technology for Electric vehicle battery thermal management is likely traceable to certain advantages such as structure flexibility and compactness as well as higher heat transfer capacity than air. The liquid-cooled system, which has been used in vehicles like the Tesla and Chevrolet Volt, can specifically satisfy the requirement for better heat dissipation and reduced temperature difference of LIB cells [111]. In agreement with the National Renewable Energy Laboratory (NREL) of the United States, the excellent performance of liquid-cooled technology over other cooling systems was testified to by [112] and its capacity for maximum safety for lithium-ion battery is better than PCM and air-cooled systems, as documented by [8].

Direct and indirect cooling techniques are generally used in liquid-based cooling systems. However, the practicality and improved efficiency of indirect liquid-based cooling systems over direct liquid-based cooling systems have been documented [55, 113]. This form of cooling technique involves removing the heat produced by an electric vehicle's battery using a fluid (deionized water, water: ethylene glycol, nanofluids, and refrigerant) that is running through a metal plate with a certain hydraulic diameter.

The capacity of double inlet and flow direction on thermal management of lithium-ion batteries was reported by[111]. Their work recorded lower energy consumption of the designed indirect liquid cooling technology with an increase in the channel's width, although little or no cell temperature reduction was documented. Reporting the impact of contact resistance on the thermal performance of the battery module [27] successfully maintained the developed liquid cooling system at a 7K peak temperature rise of the Lithium-ion battery operating at a high discharge rate with low flow velocity. Meanwhile, [14] numerically played down the influence of flow direction on battery thermal management system effectiveness with the continuous increase of mass flow rate. Affirming better performance of the cooling system with an increase in channel number, their work documented $13.77℃$ as the highest value of battery local temperature difference at $2 \times 10^{-5}\,\mathrm{Kgs}^{-1}$ of flow rate. Although, [114] earlier documented the superiority of the thermal performance of indirect liquid cooling systems over all the developed cooling systems, the authors discouraged the usage of lower flow rates with indirect liquid cooling systems to actualise effective temperature control of Evs batteries. Considering the uniform and non-uniform heat generation model of a cylindrical lithium-ion battery, the significant effect of axial convective heat transfer and thermal conductivity of the developed indirect liquid cooling system on temperature minimization of the battery cell was analytically documented [115]. Zhao et al. [24], numerically lowered the maximum temperature of Lithium-ion batteries below $40℃$ employing a liquid cooling approach. For their innovative indirect liquid cooling system, an actual number of (eight) flow channels with a liquid flow rate of $1 \times 10^{-3}\,\mathrm{Kg/s}$ was taken into consideration. Operating at a discharge rate of 1C, a single prismatic lithium-ion battery maximum cell temperature and across the cell temperature were numerically maintained by [25] below $27.8℃$ and $0.8℃$ respectively with the designed aluminum tubes liquid cooling system subjected to 0.20L/min of flow rate. Combining a liquid cooling configuration with copper material as battery housing [26] attained a reduction of battery maximum temperature from $53℃$ to $28℃$ when water with a temperature of $20℃$ was adopted as a coolant. The authors claimed the effectiveness of the proposed cooling structure

in managing the battery temperature operating up to a discharge rate of 5C. A transient numerical study was conducted by [113] to investigate lithium-ion batteries' external and internal cooling. Running a refrigerant through a rectangular microchannel for battery external cooling and an electrolyte as a coolant in a rectangular microchannel with negative and positive electrodes for internal battery cooling, the authors attached a considerable influence of internal cooling on lowering peak temperature in the battery and enhancement of battery cells temperature uniformity to increase the cost of pumping power. External cooling was observed on the battery with little or no effect on the maximum temperature and standard deviation of the internal temperature field of the battery.

Wiriyasart et al. [116] sought to improve heat dissipation of heat from the battery surface by running nanofluids as a coolant instead of water through a corrugated minichannel. 28.65% enhancement of performance over the conventional cooling system was documented. Declaring its viability in managing the thermal challenge of electric vehicle batteries, [117] adopted liquid metal to demonstrate its capacity to improve the transfer of heat from the battery rather than water as a coolant. However, the enhanced thermal conductivity recorded by [116, 117] was not a without pressure drop surge.

2.3 Heat transfer in a liquid cooling system

The compactness of liquid cooling systems for effective and efficient thermal management of electric vehicle batteries is a practical concern for researchers. Indirect liquid cooling identified as the best cooling technique, involves the transfer of generated heat from the battery to the coolant flowing through a component (flow channel) attached to the battery surface [118, 119]. The popularity of indirect liquid cooling systems with micro/minichannel flow passages is gaining momentum because of their high surface-area and volume ratio advantages. Without any wall surface effects, such as electrokinetic or electroosmotic forces, the flow in minichannels and microchannels is not anticipated to differ significantly from the continuum approximation used in microfluidic applications [120]. Sobhan & Garimella [121] however, conclude that channels with the smaller hydraulic diameter perform better thermally than conventional heat exchangers. This was first experimentally demonstrated by Tuckerman and Pease [31] when their developed microchannel heat sink dissipated a high heat flux of 790 W/cm^2. The authors proposed microchannel as the best alternative cooling system in place of traditional heat exchangers like shell and tube heat exchangers. The heat transfer coefficient of a specific fluid h_f is conventionally known as a function of the hydraulic diameter of the heat

pipe (D_h) [30]. In line with this theory, [122] experimentally reported the significant effects of geometrical parameters on the convective heat transfer in a single phase forced convention mini/microchannel of different diameters ranging from $0.133\text{mm} - 0.367\text{mm}$. Meanwhile, [123] reported increased heat transfer coefficient with a decrease in aspect ratio and concluded that the combined effect of thermal conductivity and aspect ratio of heat sink results in better thermal performance of microchannel. The capacity of mini/microchannels to lower the thermal resistance of heat generated device was experimentally and theoretically reported by [124]. To minimize thermal resistance, [125] proposed an analytical model solution that lowers the maximum heat surface temperature and temperature gradient. This was achieved by optimizing the rectangular conduit of the mini/micro heat exchangers' cross-sectional dimension in terms of uniform and non-uniform width as a function of the conduit's axial coordinate. Compared to a model with a uniform cross-section of the conduits, the analytical model for a non-uniform conduit was shown to be more successful in lowering the maximum surface temperature.

According to [126], a flow passage with the hydraulic diameter between $3\text{mm to } 200\mu\text{m}$ is referred to as minichannel. An ultra-thin minichannel liquid cooling plate (LCP) was adopted by [127] to manage the thermal problem of electric vehicle batteries. An optimized U-turn type microchannel cold plate was reported to keep the $50V$ battery pack's maximum temperature and temperature non-uniformity below $40℃ \; and \; 4℃$, respectively [128]. Their study reported the best performance of the developed cooling configuration with 1.54mm of hydraulic diameter and the indirect relationship between β and Re was established. The minichannel stacked on a rectangular frame of developed indirect cooling configuration was designed by [44] to numerically control the temperature challenges of cylindrical lithium-ion batteries of electric vehicles. The reduction of frame wall temperature of the designed cooling structure with an increase in flow rate was documented in their work. Reporting the significant effect of coolant temperature on the peak temperature of the designed cold plates with a serpentine-channel cooling system to check the temperature rise of the rectangular lithium-ion battery, [129] established the inconsequential effect of coolant inlet temperature on pressure and temperature standard deviation. The authors gradually attained the decline of standard deviation and peak wall temperature of their novel system when they raised the number of cooling channels to five. Qian et al. [130] also suggested 5 cooling channels as adequate for the effective performance of their novel minichannel cold plate cooling configuration. The impact of channel width and flow rate on heat transfer coefficient was documented by their

study. Improvement of design1 with another cold plate (design 2) was observed to improve temperature uniformity of the battery module, hence proposed by the authors as efficient cooling structures for temperature control of the battery of electric vehicles.

Furthermore, the effectiveness of minichannel in dissipating huge amounts of heat generated by electric vehicle batteries was also demonstrated by [14, 25, 27, 110, 131] and a drastic reduction of battery temperature was documented (Figures 2.5). Nevertheless, efforts must be geared towards enhancement of heat transfer coefficient of an indirect liquid cooling system designed with minichannel

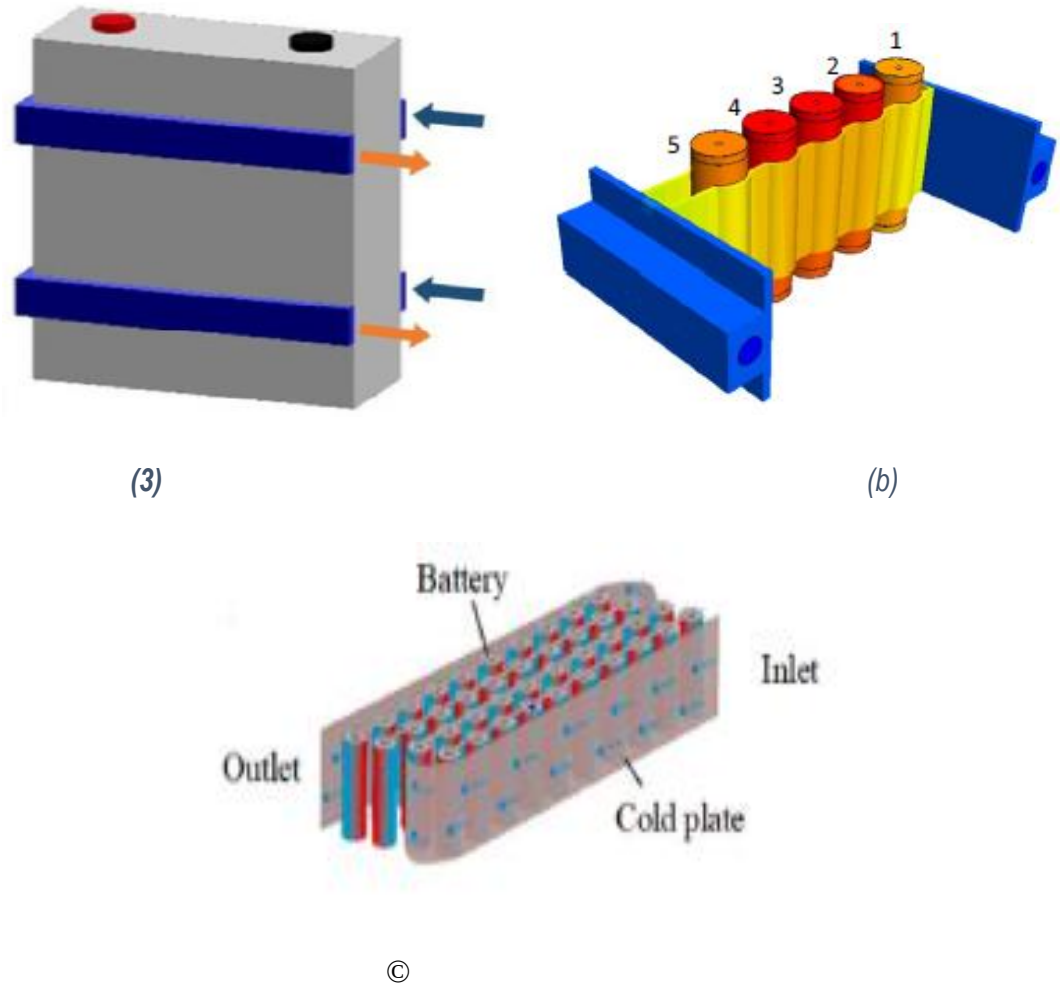

Figures 0.5. Examples of minichannel application as an indirect liquid system for dissipation of heat generated by battery of electric vehicle: [25] (a), [27] (b), and [43] (c).

2.4 Heat transfer enhancement in a liquid cooling system

The ability of micro/mini channels to effectively dissipate heat from the electronic device/ battery of electric vehicles has been established by many researchers, as narrated in section 2.2. The enhancement of the cooling process in micro/mini channels will be an added advantage to its applications both industrially and domestically. Experimental, analytical, and numerical analysis of minichannel heat transfer enhancement methods such as; the introduction of working fluid with different thermal conductivity, dimple and grooved structure, surface roughness structure, ribs cavities porous media, and pin fin of different geometry inserted in the flow channel have been documented by several authors [112]. Disruption of fluid flow in the channel for the ultimate transfer of heat from the heat-generating device to the fluid is the fundamental goal of the researchers.

The chaotic mixing theory was applied by [132] to invoke chaotic convection aiming to improve the thermal performance of mini/microchannel heat sinks using nanofluids as a coolant. Their work concluded that the overall better thermal performance of DRC (double-sided rib channel) than SRC (single-sided rib channel). However, Nohooji et al.[133], numerically reported less or insignificant effect of nanofluid (water/Al2O3) on heat transfer enhancement in mini/microchannel when compared with the porosity effect for the same purposes. This method was adopted by [117] when the authors introduced liquid metal as a coolant instead of water to effectively manage the thermal challenges of the battery of electric vehicles. Numerical and mathematical results show that battery stressful operating conditions of cell defects, high power drawn as well as higher ambient temperature, can be excellently controlled with the application of their novel cooling system. Adding 2% volume of alumina nanofluid to deionized water as a coolant, $1.2℃$ and $0.4℃$, improvement of maximum temperature and temperature difference of lithium-ion battery pack over deionized water was actualized [134]. Their study reported $0.19℃$ reduction of battery cells' temperature non-uniformity with stair-type of channel during battery discharge operation. The designed honeycomb-shaped channel cooling system was employed by [135] to investigate the effectiveness of CuO, Al_2O_3 and TiO_2 thermal conductivity properties for management of thermal challenge of the cylindrical and square battery pack. Their study proposed CuO and Al_2O_3 as the best nanofluids respectively for cylindrical and squared battery modules. Meanwhile, the influence of nanofluid as the coolant in the channel with the combination effect of phase change material on temperature control of lithium-ion battery was investigated by

[136, 137]. Significant improvement in cooling system performance with nanofluid about traditional liquid coolant was documented.

Studies on different modifications of mini/microchannel geometry for cooling of battery pack of electric vehicles have been conducted by researchers: stair channel [134], U-turn type microchannel cold plate [128], Ultra-thin minichannel liquid cold plate [127], serpentine-channel liquid cooling plate [111] corrugated minichannel [116]. Their respective studies documents the enhancement of the thermal performance of these modified flow minichannels against conventional straight channels. The development of the thermal boundary layer with improved fluid mixing results from free stream separation at the leading edge of integrated micro/minichannel in the presence of insert(s) to provoke flow disruption is said to enhance the heat transfer coefficient [138]. With the attachment of the block to the lower plane of a flow channel, 60% of heat transfer enhancement was reported [139] using nanofluid as a coolant. Recording the growth of Nusselt number with the flow Reynolds number, their work exhibited a decline in thermal performance when the number of attached blocks is more than 3. Thermal characteristics of different heights of dimples on microchannel walls with or without fillets were numerically investigated by [140]. Obtaining 20% of improved Nusselt number over plain channel with dimples of $1mm$ height, the authors reported fillet's influence to augment microchannel's thermal behaviour with insignificant rise of pressure drop. In reference to plain microchannel, the combined effect of fillet profile and dimple with 1mm height was found by their work to yield 60% higher value of Nusselt number. Tesla valve used by [141] to enhance stability of supercritical CO_2 based natural circulation loop and considered as a mini/micro heat exchanger by [142, 143] for controlling flow and heat transfer was employed by [38] to develop a minichannel cold plate for mitigating the thermal challenges of pouch-type batteries. Adequate flow mixing with their novel cooling system was found to facilitate improved cooling effectiveness of the electric vehicle battery. Although, the enhancement results from mixing mechanism and flow bifurcation were not without pressure drop challenges. Guo et al [144] employed the staggered arrangement of pin in the fluid domain of minichannel to improve the thermal performance of Lithium-ion battery pack. Using their developed model, the multi-physics behaviours in various working cycles of the BTMS with the X and Y direction mini-channel cold plate were simulated. A drastic drop of peak temperature and maximum temperature gradient in 1000 Cycles of battery thermal management was actualised with an embedded circular pin fin in the Y direction of minichanel. Also, considering the influence of varying diameter of pin fin arranged in both X and Y

directions in the computational domain of a battery cooling system of electric vehicles, [145] obtained a battery peak temperature reduction of 1.04℃ to about parallel minichannel when the authors optimized the designed cooling structure with non-uniform pin fin. Their study earlier reported, lowered the value of temperature, weight and pressure drop when the pin fins' diameter was increased along the Y direction. An opposite effect was observed with pin fin in the X direction. Meanwhile, a staggered arrangement of number of pin fins with different heights increasing linearly along the width of a flow channel was also designed by [110] to control the temperature challenges of Lithium-ion battery. In reference to case 1(cooling configuration without insert) all integrated cooling configurations with pin fin were documented with better performance, greater than case 1. According to the authors, the arrangements of pin fins in case 3, were found to be the most suitable among all the cases considered for thermal management of the battery of electric vehicles.

The31icrochanntal study conducted by [146] showed the capacity of porous stainless steel inserted in a minichannel to remove $6\,\mathrm{MW/m^2}$ of heat flux from a mini-device. Considering the effectiveness of porous stainless steel over aluminium foam as a porous medium with no limitation of pressure drop, the authors reported $55K$ of the temperature difference between the wall and the bulk water. The above claim was further numerically substantiated when [147] reported improvement of convective heat transfer coefficient of a porous media microchannel with a decrease in porosity and pumping power. On the other hand, the effect of fins thickness as a porous medium on the thermal performance of parallel plate channels was numerically investigated by [148] and the thermal conductivity ratio and inertial coefficient influence on Nusselt number in the porous domain was reported. Marafie & Vafai, [149] also adopted an analytical method to provide a solution to the problem of full porous media in a heat tube. They reported enhanced heat transfer but with a high cost of pressure drop. This challenge was also considered by Hung et al. [147], when they numerically investigated the thermal performance of different configuration designs of porous medium inserted into a microchannel. In their study, porous media with fewer obstacle and a lower friction factor were observed with improved convective and conductive heat transfer. However, high Reynolds number gives rise to Nusselt number with a large obstacle in a porous media configuration. Improvement in wall temperature effectiveness control, and convective heat transfer was reported with a lesser obstacle porous configuration.

To address the basic temperature gradient and thermal inconsistencies linked to a plain channel for cooling pouch-type Li-ion batteries, [55] designed and incorporated a multi-stage Tesla

valve cold plate with forward and reverse flow arrangement. The authors numerically enhanced the integrated flow configuration's thermal performance significantly, better than the plain flow channel to serve as a lithium-ion battery cooling system. The influence of both pin fin and aluminium foam inserted in the fluid domain of minichannel for the improvement of heat transfer coefficient was investigated by [44]. An increase in porosity level was reported to depreciate the performance of their novel cooling system when the aluminium foam was inserted in the cooling channel. The combined effect of aluminium foam and solid pin fin in an airflow channel for enhancement of cooling performance was also reported by [42] Affirming their capacity (pin fin and aluminium foam) to reduce battery temperature when used individually, their combination was found to drastically improve battery cells' temperature uniformity. However, this battery cell temperature uniformity was tied to the pore density of aluminium foam [150]. Investigating the aluminium foam porosity and pores density effects on the thermal performance of cooling system designed for temperature control of electric vehicle batteries, [7] suggested the replacement of cold plate with an aluminium foam heat sink as the authors reported the best thermal performance as well as lowest flow resistance of their novel cooling configuration with 10 Pores Per Inch (PPI) aluminium foam at 0.918 of porosity. It is an unchallenging fact, that the insertion of another configuration in the fluid domain of the flow channel for enhancement of the heat transfer coefficient always comes with a penalty of higher cost of pumping power [7, 44, 55, 110]. The development of integrated cooling structures with either pin fin or aluminium foam as a porous medium for a lithium-ion battery of electric vehicles with a higher capacity of heat transfer coefficient and a lower value of pumping power still needs to be researched.

2.5 Constructal design and cooling systems

The search for more innovative and fundamentally new approaches to heat transfer engineering and science has been propelled by the need to cool heat-generating devices more effectively. Constructal Law, used to explain the universal phenomenon of the generation and evolution of technology design (configuration, shape, structure, pattern, rhythm), can be rightfully included among the energy efficiency-inspired actions [151]. This law was inspired by the development of flows in nature and more generally, by the "invisible hand" of natural phenomena design. Constructal law as stated by [152] every flow system grows through time into the flow architecture that maximizes flow access given the flow's restrictions. This law provides a ground-breaking technique for comprehending and anticipating the designs that appear in all living things as well as inanimate objects and constructed systems [153]. Efficient use of this

law guarantees geometry with better flow developments which result in minimum global flow resistance and best equilibrium of the entire internal flow resistance. For a finite-size system to persist in time (to live), according to Adrian Bejan [154], it must evolve in a way that makes it easier to access the imposed (global) currents that pass through it. The theory connects engineering and nature. It also draws attention to geometry as an unknown in any shape design, with our minds guided in the direction of discovering it. This law can achieve the optimal spacing between two solid components for better thermal performance.

This approach recently applied by many researchers to provide a solution to the problem of conjugate heat transfer challenges for maximum performance is known as the optimization technique, which involves specification constraints. The optimization of square and circular configurations with a volumetric heat source was analytically and numerically presented by [155] using the constructal theory approach.

With fixed global volume constraints, the influence of pressure difference on optimized hydraulic diameter and channel spacing at fixed porosity was reported by the authors. Their study documented optimized square geometry with better performance over the circular configuration. Subjected to the restriction of a fixed global solid material volume, the influence of flow orientation was further considered on circular geometric cooling structures by [156] to present a configuration with minimized maximum temperature. Their numerical analysis reported the impact of porosities, heat generation rate, and applied pressure difference, on the optimal developed cooling system hydraulic diameter and channel-to-channel spacing.

Meanwhile, Yilmaz et al. [157] investigated parallel plate, circular, square, and equilateral triangle geometries of ducts to determine the optimal shape and dimensions for convective heat transfer of laminar flow at constant wall temperatures. The Prandtl number (Pr) and the duct shape factors were employed to approximate equations for maximum dimensionless heat flux and optimal dimensionless hydraulic diameter. Based on constructal theory, scale analysis and the intersection of the asymptotes approach, were also considered by [48] to undertake a three-dimensional study of heat sinks and cooling channels with heat flux. Their work demonstrates that the degrees of freedom significantly impact on the maximum thermal conductivity and the peak temperature. Utilizing a multiscale design approach, [158] also applied this technique to microtube heat sinks and heat exchangers to achieve the highest possible heat transfer density. This author was able to demonstrate that, interstitial microtubes increased the maximum heat transfer rate density for a collection of circular tubes.

Similarly, scale analysis and the intersection of the asymptotes method, based on constructal theory, were used by [159] to study a three-dimensional optimization of the heat sink and cooling channels with heat flux to investigate and predict the design and optimization of the geometric configurations of the cooling channels. Using constructal design, [160] optimized the placement of discrete heat sources on a wall with a specified forced convection heat generation rate to reduce the temperature of the hot spot on the wall. The author reported the influence of vast numbers of optimally placed heat sources on extremely complex configurations.

To comprehend the morphology of particle agglomeration and the design of air cleaning devices, [161], designed the interior configurations of parallel plate and cylindrical channels utilizing constructal theory. Under the imposed global constraints, their work demonstrates how constructal theory results in the design of air-cleaning systems that reach the maximum performance per unit volume. For different solid configurations [41] the maximum temperature of the optimized cooling system of integrated microchannel embedded with pin fins was minimized using constructal design and theory. The influence of the Bejan number on parameters such as hydraulic diameter and channel aspect ratio, solid volume fraction, pin fin aspect ratio, and minimized maximum temperature was numerically investigated. An inverse relationship between the Bejan number and minimized peak temperature was reported.

The effect of Bejan number and porosity on the minimization of thermal resistance of a designed cylindrical cooling system was numerically conducted by [52]. The authors employed constructal design and theory to present an optimal inlet and outlet diameter at a specified porosity and Bejan number with a minimized friction factor and global thermal resistance. Recently, [50] furthered the study of [48] using constructal techniques to predict the optimal performance of microchannel heat sink fin geometry. Using open foam software to provide solutions to model equations, the significance of an accurate number of solid material additions to microchannel for improved thermal performance was highlighted in their study. Using the mathematical optimization [162] a lower dimensionless peak temperature was reported for the liquid cooling channel of the triangular section over the square section of the integrated heating body embedded with triangle and square geometry cooling channels. The influence of the increased number of cooling channels on the performance of their developed cooling structures was substantiated using constructal theory.

The impact of flow orientation on the thermal behavior of two-stacked microchannel heat sink was considered by [47]. To attain the best configuration with the lowest thermal resistance, pressure drop, and flow velocity, the authors employed constructal theory to present a configuration with counterflow orientation as the most suitable for cooling electronic devices with high heat generation capacity. The superiority of two-phase flow over one-phase flow regime in a rectangular microchannel for dissipation of higher heat-generated electronic devices was presented by [163]. Allowing the morphing of flow parameters with geometry, their study demonstrated the indirect relationship between Reynolds number and thermal resistance.

Meanwhile, [164] focused on the entropy generation minimization of their developed solar collector with a flat plate for raising the water temperature. Fixing the riser tube volume and the surface of the plate, their optimization results documented the impact of fluid volume on the flat plate optimal length, diameter, and spacing of the riser tube. The capacity of their configuration to reduce entropy generation with an increase of fluid volume in the riser tubes was also reported. The design of a boiler with optimum overall thermal performance coefficient using constructal law was considered by [165], and a boiler designed with 24 tubes was presented as the best configuration. With a variation of geometrical parameters of the developed boiler configuration, the authors attained a significant reduction of pressure drop with optimized configuration. In another development, constructal theory determined an optimal diameter for the effective performance of a biomass boiler under a thermal load of 46 KW by [51].

Reis and Bejan [166] applied this law to study the diurnal scale of atmospheric circulation and a 7K average temperature gradient between day and night was documented. Constructal Law was applied by [167] to the blast furnace's hot metal yield maximization, and the findings suggest that less hot metal enhance the original process by 2.6%. The authors proposed a methodology that yields the performance and cost-effectiveness of iron manufacturing in a blast furnace process. The performance of balanced two-stream parallel flow heat exchangers was also examined in [168] which used constructal law to analyze the configuration and implementation of the stream flows as a tree network. The influence of flow orientation on heat exchangers designed in a treelike manner was reported. A CFD analysis of different tube configurations to dissipate heat from high heat-generating devices was presented by [169]. A greater influence of Reynolds number than the type of cooling flow structure on the plate

average temperature was reported. The tubes with a tree-shaped flow were found to have better performance using the technology of constructal theory.

In advance of the cooling of electric vehicle batteries, recently [170] adopted a constructal approach to propose a canopy-to-canopy cooling structure for thermal control of lithium-ion batteries. Their designed cooling structures demonstrated, excellent thermal performance with a minimum flow rate. Substantiating the excellent performance of their geometric configuration to sustain cell temperature below its critical temperature, configuration with 5 branches in parallel was documented with the lowest cost of pumping power and the highest value of thermal efficiency. The design of a cooling plate with a double-layer tree-like channel for temperature control of lithium-ion batteries with the innovation of construal technology was presented by [171]. In reference to the serpentine net channel, under the same flow rate and surface area, a tree-like channel's overperformance for the cooling process. The optimized cold plate was found with the capacity to reduce surface temperature standard deviation, peak temperature, and pressure drop by 69.25%, 1.79%, and 79.13% respectively.

Fan et al [172] enhanced the temperature consistency of a rectangular lithium-ion battery at a very low cost of pumping power with an indirect liquid-cooling plate using the constructal theory approach. Their designed dendritic flow channel was documented to have a 28% pressure drop lower than the serpentine flow channel. An optimized cooling configuration of their study demonstrates the capacity to reduce plate surface temperature standard deviation from 5.31℃ to 1.96℃ and plate peak temperature from 52.59℃ to 39.3℃. With this same technology, the influence of contact thermal resistance on the thermal performance of a novel cooling structure of an electric vehicle battery was pointed out when [173] showed the relationship between the cold plate and the contact thermal resistance. Their study reported an integrated configuration with the cold plate and vascular flow channels as the best-performing cooling system. Although documented with a quality strategy for the dissipation of heat generated by lithium-ion batteries, the application of constructal theory to thermal control of electric vehicle batteries is less researched.

2.6 Response surface optimization and cooling system

First introduced by Georgy and Wilsson in 1951, for optimal response with a sequence of their experimental design, Response surface methodology (RSM) is defined as a set of statistical and mathematical methods employed for the design, enhancement, and optimization process [174]. The most frequent applications of RSM are in specific circumstances when several input

factors may impact a given performance measure or process quality characteristic. The evolution and development of RSM at different stages since its introduction in the early 1950s which was categorized into three parts was surveyed and presented by [175]. Describing the principle and different designs of RSM, [176] applied this technique to document various food process optimizations. During the optimization process of cutting conditions in the milling of the cutting mold, a 10% mold surface roughness improvement was actualized [177] with the application of this method. Quanhong and Caili [178] reported the influence of the liquid-solid ratio on the extraction of protein from germinated pumpkin seeds when they employed RSM optimization techniques.

The developed sinusoidal wavy structure of the 37icrochannell was optimized with the combination of finite volume method (FVM) and response surface methodology (RSM) [179]. An optimum heat transfer coefficient of their novel heat sink was observed when the wavelength and amplitude values were fixed at 100 and 40. Similarly, the integration of non-dominated sorting genetic algorithm-II with response surface methodology to present excellent performance of the cooling structure about the accurate concentration of selected nanofluid was considered [180]. Channel width and diameter of the cylinder influence on their developed heat sink was observed to yield 21% and 18% of enhancement when the nanofluid concentration was raised from 0% to 8%. According to [181] the reduction of expensive cost analysis techniques formed the basis of employing RSM for the optimization processes of a developed heat sink to search for different nanoparticle thermal influences on the performance of the microchannel cooling structure. Their study documented the presence of Ag-water as a nanoparticle with the highest value of Nusselt number, the capacity of increased volume fraction of nanoparticle to suppress the coolant and heat sink wall temperature. Based on copper oxide mass concentration and varying temperature, [182] relied on RSM to experimentally predict the thermal conductivity of $CuO(II)$/water. The suitability of their designed model to forecast the thermal conductivity of a specified nanofluid at a specified temperature and mass concentration range was reported. Azizi et al. [181] adopted RSM to experimentally show the superior effect of Reynolds number over nanoparticle fraction on the heat transfer coefficient of the optimized microchannel heat sink. The application of this technique was also considered by [41, 47, 155, 183] for the optimizing their developed cooling models using water as the working fluid, and excellent cooling results were reported in their respective studies.

Recently, several studies have been dedicated to the optimization of electric vehicle lithium-ion battery cooling systems with the application of response surface methodology. Weight

reduction of the battery thermal management system was the focus of [184] where the authors employed the RSM for the optimization process. Their optimized geometry was characterized by a reduction of 94.1% and 55.6% of PCM mass and volume, respectively. In the same vein, [185] documented 3.05mm and 1.0 mm as the best PCM thickness and gap with DHPD (sodium hydrogen phosphate dodecahydrate) as the best PCM material for their optimized thermal management system of electric vehicle battery. The purpose of their study was hinged on the mass reduction of supercooling phase change material for maximum performance of their developed model using RSM. Meanwhile, the thermal capacity of different coolants to control temperature challenges of electric vehicle batteries was numerically examined by [185] using RSM. Reporting the influence of various coolants to generate different maximum temperature performances of the battery pack, their study discouraged the usage of oil as a working fluid for the thermal management of the battery of electric vehicles. Using air as a working fluid [186] numerically lowered the maximum temperature of the battery pack by 2.7K when the authors optimized their cooling system with RSM. The combination of RSM and NSGA-II algorithm for optimizing the process of the designed thermal system for temperature control of electric vehicle Lithium-ion battery was found to yield 93.7% and 9.3 % reduction of pressure drop and maximum temperature difference, respectively [187]. With the available literature, RSM can effectively aid the attainment of optimum response and optimum conditions brought about by various responses of the developed battery cooling system.

2.7 Conclusions

Relevant publications related to the need for the development and efficient running of electric vehicles in our world today were presented in this chapter. The composition, mode of heat generation, thermophysical properties and different cooling techniques of lithium-ion batteries as the optimal power source of electric vehicles were substantially discussed. Various experimental, analytical, and numerical studies dedicated to the designs and performance enhancements of the cooling systems for the thermal management of the batteries of electric vehicles were outlined. Among various performance enhancement techniques adopted by researchers for battery cooling systems, the insertion of solid pin fins or aluminum foam in the fluid domain is paramount. The consideration of thickness, diameter, height, shapes, number, and varying arrangement (inline, staggered) effect of the solid pin fin or aluminum foam inserted in the channels on the enhancement of cooling devices has been significantly explored by researchers. However, available literature shows that the search for the best insert location in the flow channel for the realization of maximum performance of the cooling system has not

received any research attention. Hence, the novelty of this study. The effect of different shapes of the solid pin or aluminum foam inserted at varying locations in the channels on the thermal performance enhancement of the cooling system for thermal management of lithium-ion batteries is numerically investigated using the computational fluid dynamics code. The potential of single and multiple solid pin fins or aluminum foam enhancements in the developed cooling system is further compared. In addition, the constructal theory and design approach will be applied to present an optimized cooling system of superior thermal performance in dissipating heat from the battery pack of electric vehicles.

CHAPTER THREE

MATERIALS AND METHODS

3.1 Preview

Computational fluid dynamics (CFD) is a group of numerical modeling methods based on fundamental principles that can simulate and forecast the behavior of single-phase and multiphase fluid flows related to heat and mass transfer processes[188]. Ansys® 2020R1, which uses a finite volume approach, was employed as commercial CFD software for numerical analysis in this research work. The theoretical framework of the current conceptual design with the heat generation mechanism is detailed in this chapter. Furthermore, the steps taken in using CFD software to define the cooling system geometry, discretization of the computational domain, solution to heat and mass transport governing equations, and optimization technique of the cooling system geometry will be adequately detailed in the succeeding sections.

3.2 Fundamental governing equations for the electrochemical description of the (dis-) charging operation in a cylindrical lithium-ion battery

According to [27] specific electrochemical characteristics, such as open circuit potential, diffusivity in electrolyte, and electrodes are fundamentally temperature functions. Consequently, the heat generation in the Lithium-ion battery largely depends on the ions and electron transportation in the electrolytes and the electrochemical process reaction in the battery cells. Therefore, to avoid the deterioration of battery cells, a necessary understanding of the dynamics of ionic concentrations and electrolyte as well as electrode potentials during battery operation conditions becomes inevitable. Equations (3.1-3.8) describe the mathematical principles governing the internal operation of the lithium-ion battery cells [27].

Lithium-ion concentration in the electrodes (solid phase): Employing Fick's law of diffusion, with the assumption of spherical electrode particles and isotropic diffusion, the ionic concentration in a single spherical particle of active material is estimated by:

$$\frac{\partial(C_s)}{\partial t} = \frac{1}{r^2}\frac{\partial}{\partial r}\left(D_s r^2 \frac{\partial C_s}{\partial r}\right) \tag{3.1}$$

With boundary conditions

$$-D_s \frac{\partial C_s}{\partial r}\Big|_{r=R_p} = \frac{i_n}{F} \tag{3.2}$$

Utilizing the electrode open circuit potential (OCP) curves, the initial concentration is determined by applying a zero-flux condition at the particle's center (Equation (3.2))

Lithium-ion concentration in the electrolyte (liquid phase): Adopting the concentrated solution theory, the lithium-ion salt mass conservation in the electrolyte is determined as:

$$\frac{\partial(\varepsilon_e C_e)}{\partial t} - \nabla.\left(D_e^{eff} \nabla C_e\right) - \frac{1-t_+^0}{F} a_s i_n = 0 \tag{3.3}$$

The solid phase potential in the electrode region: Current conservation in connection with improved Ohm's law for the solid electrode (cathode and anode) phase is given as:

$$\nabla.\left(\sigma_s^{eff} \nabla \emptyset_s\right) - a_s i_n = 0 \tag{3.4}$$

Having the porous media composition fitted on the electrodes, the effect of porosity is calculated via effective electronic conductivity σ_s^{eff}.

However, the boundary conditions for the electrode region were set to zero at the end of the anode current collector, and a defined discharge current was fixed at the end of the cathode current collector.

The potential in the liquid (electrolyte) phase: Considering the effect of electronic transference, the estimate of lithium-ion salt mass conservation in the electrolyte phase (electrode and separator phases) is estimated as:

$$\nabla.\left(k_e^{eff} \nabla \emptyset_e + \frac{2R_g T k_e^{eff}}{F}(t_t^0 - 1)\left(1 + \frac{dlnf_{\pm}}{dlnC_e}\right)\nabla lnC_e\right) + a_s i_n = 0 \tag{3.5}$$

The above-analyzed governing equations in connection with the volume-specific rate of reaction that satisfied the Butler-Volmer electrochemical kinetic expression were then employed to explain the reaction current density of the electrolyte and electrode potentials.

$$i_n = i_0\left(exp\left(\frac{\alpha_a F}{R_g T}\left(\emptyset_s - \emptyset_e - E_{eq}\right)\right) - exp\left(-\frac{\alpha_c F}{R_g T}\left(\emptyset_s - \emptyset_e - E_{eq}\right)\right)\right) \tag{3.6}$$

Equation (3.7) indicatates the electrode overpotential, which is defined in terms of liquid and solid phases as well as the equilibrium potential. At a discharge rate, this quantity was used to calculate the voltage lost to discharge the battery cell. Interestingly, an increase in discharge rate leads to an increase in the overpotential quantity.

$$\emptyset_s - \emptyset_e - E_{eq} \tag{3.7}$$

Meanwhile, the exchange current density from Butler-Volmer electrochemical kinetic expression is determined by:

$$i_0 = F(K_c)^{\alpha_c}(K_a)^{\alpha_a}\left(\frac{C_e}{C_e^{ref}}\right)^{\alpha_a}(C_s^{max} - C_S)^{\alpha_a}C_s^{\alpha_c} \tag{3.8}$$

3.2.1 Mechanism of heat generation in a cylindrical lithium-ion battery

The energy equation for the Lithium-ion batteries is represented by the thermal conduction equation, with the conductivity as the mass-weighted average of all the parts. However, the heat-generated mechanism in the lithium-ion battery is categorized into three major sources expressed below:

***Reversible heat generation**:* This is the heat generated through the temperature-dependent changes in open-circuit voltage. It is determined as follows:

$$Q_{rev} = a_s i_n T \frac{\partial E_{eq}}{\partial T} \tag{3.9}$$

***Irreversible heat generation**:* This type of heat is generated through over-potential or voltage loss because of a finite current output rate. It is determined as follows:

$$Q_{irr} = a_s\, i_n \left(\emptyset_s - \emptyset_e - E_{eq}\right) \tag{3.10}$$

***Ohmic heat generation**:* This type of heat is generated through the electronic transport resistance in the solid phase and ionic transport resistance in the liquid (electrolyte) phase. It is also calculated as:

$$Q_{ohms} = -i_e\left(\frac{\partial \emptyset_e}{\partial x}\right) - i_s\left(\frac{\partial \emptyset_s}{\partial x}\right) \tag{3.11}$$

Where,

$$i_n = i_o\left(\exp\left(\frac{F\,\alpha_a}{TR_g}\right)\left(\emptyset_s - \emptyset_e - E_{eq}\right) - \exp\left(\frac{F\alpha_c}{TR_g}\right)\left(\emptyset_s - \emptyset_e - E_{eq}\right)\right) \tag{3.12}$$

and

$$i_o = F(K_c)^{\alpha_c} (K_a)^{\alpha_a} \left(\frac{C_e}{C_e{}^{reff}}\right)^{\alpha_a} (C_s{}^{max} - C_s)^{\alpha_a} C_s{}^{\alpha_c} \quad (3.13)$$

The summation of three sources of heat gives the total heat generated by the lithium-ion battery cells (Equation. (3.14))

$$Q_{total} = Q_{rev} + Q_{irr} + Q_{ohms} \quad (3.14)$$

Equations (3.9-3.14) are well-detailed in the published work of [27, 62]

Equation (3.14) is adopted for the calculation of volumetric heat transfer in the battery pack of the electric vehicle being considered in this work, which is estimated to be $340135\ \mathrm{W/m^3}$.

3.2.2 26650 Cylindrical lithium-ion battery thermophysical property

The 26650 Cylindrical lithium-ion battery cells characterized with (lithium iron phosphate) $LiFePO_4$ active material as a cathode and carbon, (mesocarbon microbead, MCMB) based anode, were selected for this study. The selection was based on the attainable higher heat capacity of a 26650 cylindrical lithium-ion battery cell [85] and the lowest thermal diffusivity of $LiFePO_4$ as an active material [189].

Notably, the heat dissipation rate from the cylindrical lithium-ion battery cell to the external environment depends mainly on the heat exchange surface area per unit volume of the cell [193]. Because of many interfaces between the electrode and electrolyte layers in the radial conduction path that are lacking in the axial direction, the spiral assembly of the cylindrical lithium-ion battery is expected to generate a significant anisotropy in thermal conductance between the radial and axial directions. Hence, the radial and axial thermal conductivities as detailed by [85] as well as other thermophysical properties of the considered battery cell for this research work, are displayed in Table 3.1.

Table 0.1 26650 Cylindrical lithium-ion battery thermophysical property specification

S/N	Description	Value
1)	Diameter of the battery	26 mm
2)	Height of the battery cell	65 mm
3)	Battery cell mass density	2285 $Kgm{-}3$
4)	Battery cell specific heat capacity	1605 $JKg{-}1K{-}1$
5)	Battery cell discharge rate	6 C
6)	Battery cell operating temperature	298 K
7)	Battery cell capacity	20 Ahm^{-2}
8)	Radial thermal conductivity	0.14 $\mathrm{W.m^{-1}.K^{-1}}$
9)	Tangential thermal conductivity	0.14 $\mathrm{W.m^{-1}.K^{-1}}$
10)	Axial thermal conductivity	30.4 $\mathrm{W.m^{-1}.K^{-1}}$
11	Battery cathode active material	$\mathrm{LiFePO_4}$ (Lithium iron phosphate)

3.3 Numerical modeling procedure

The approach of using CFD codes for numerical analysis and data structure to examine and provide solutions to fluid flow problems involves three critical steps as stated below:

- Pre-processing: This is the first step before the simulation process, and it involves geometry definition, fluid flow description represented with a written set of partial differential equations, discretization of the fluid domain into small grids or elements, and specifying the initial and boundary conditions to solve the mathematical equations.

- Solver- execution: This second step involves the prediction of fluid flow behavior by developing a mathematical model with the aid of a computer; a process called

simulation, which may involve the adoption of finite difference method (FDM), finite element method (FEM), finite volume method (FVM) or spectral element method (SEM).

- Post-processing: At this stage, the obtained simulation results are analyzed. The CFD software tools are equipped with versatile data visualization tools for comprehensive analysis of the numerical results.

3.4 Geometry and grid generation

After the definition of geometry known as the computational domain, a grid generation that involves the division of complex geometry into simple elements on which governing equations can be solved is conducted. However, for the accuracy of CFD simulation procedures, the discretization of the computational domain is actualized by employing Ansys 2020® fluent software [190]. The CFD software package also provided solutions to non-linear partial differential equations such as mass, momentum, and energy equations for fluid flow and heat transfer numerical analysis.

3.5 Continuity Equations

Due to its efficient computational advantages, the Eulerian frame of reference is generally considered for 45odelling fluid transportation in a control volume [191]. According to [192], the general form of the fluid continuity equations representation in the Eulerian frame of reference is as stated in Equation (3.15):

$$\frac{D\rho}{Dt} + \rho divV \tag{3.15}$$

Where ρ, V and t respectively, signified fluid density, fluid velocity vector, and time.

For emphasis on fluid flow with constant density (incompressible flow), Equation (3.15) is reduced to:

$$divV = 0 \tag{3.16}$$

3.6 Conservation of Momentum Equations

The analysis of fluid motion in a control volume is carried out by employing Newton's second law of motion. Derived from Newton's second law, the conservation of momentum equations described the relationship between applied force and acceleration of a particle with mass.

Employing the indicial symbol, Navier and Stokes derived the following equations for Newtonian viscous fluid:

$$\rho \frac{Dv}{Dt} = \rho g - \nabla P + \frac{\partial}{\partial x_j}\left[\mu\left(\frac{\partial v_i}{\partial x_j} + \frac{\partial v_j}{\partial x_i}\right)\right] + \partial_{ij}\lambda div V \quad (3.17)$$

Where, g, P, x, μ, V, dij and λ represents vector acceleration, pressure, special coordinate, coefficient of viscosity, velocity component, Kronecker delta, and vexing coefficient associated with volume expansion, respectively [192].

Adopting Stokes' hypothesis ($\lambda = -\frac{2}{3}\mu$) with emphasis on incompressible flow, the vexing coefficient λ as well as $div\ V$ vanish (because of the continuity equation) and Equation (3.17) then becomes:

$$\rho \frac{DV}{Dt} = \rho g - \nabla P + \mu \nabla^2 V \quad (3.18)$$

3.7 Conservation of Energy Equations

According to the first law of thermodynamics through which the conservation of energy equation is derived, a change in the energy of the thermodynamic system is brought about by the addition of heat and work to the system.

Neglecting the radiation influence, the energy equation can then be written as:

$$\rho \frac{Dh}{Dt} = \frac{DP}{Dt} + div(K\nabla T) + \phi \quad (3.19)$$

Where h, K, T, and ϕ respectively, the signified enthalpy of the fluid, thermal conductivity, temperature of the fluid, and dissipation function. Note that ϕ is defined as:

$$\phi = \mu\left[2\left(\frac{\partial u}{\partial x}\right)^2 + 2\left(\frac{\partial v}{\partial y}\right)^2 + 2\left(\frac{\partial w}{\partial Z}\right)^2 + \left(\frac{\partial v}{\partial x} + \frac{\partial u}{\partial y}\right)^2 + \left(\frac{\partial w}{\partial y} + \frac{\partial v}{\partial z}\right)^2 + \left(\frac{\partial u}{\partial z} + \frac{\partial w}{\partial x}\right)^2\right]$$

$$+\lambda\left(\frac{\delta u}{\delta x} + \frac{\partial v}{\partial y} + \frac{\partial w}{\partial z}\right)^2 \quad (3.20)$$

Also, it should be noted that viscous dissipation becomes insignificant when dealing with incompressible fluid flowing at low velocities with constant thermal conductivity. Hence Equation (3.19) is simplified to:

$$\rho_f C_{Pf}(\overline{u}.\nabla T) = K_f \nabla^2 T \quad (3.21)$$

And energy equation for a solid with a volumetric heat source is given as:

$$\nabla.(k_s \nabla T_s) = -q''' \tag{3.22}$$

Where K_s is the solid thermal conductivity and K_f is the fluid thermal conductivity.

The simplified equations are documented in a steady state.

3.8 Porous media: Mathematical formulations

3.8.1 Porous media characterization

A solid structure with channels for fluid flow is the most basic way to describe the concept of a porous medium. Due to the increase in surface area to volume ratio and improved flow mixing caused by highly complex flow pathways, porous media made up of the solid and liquid phases, tend to yield significantly improved heat transfer. In this research work aluminum foam is considered a porous media because of its large surface area, lightweight configuration, and nature-like morphology of its solid matrix.

Meanwhile, the following assumptions were considered for the porous region simulation process:

- Heat transfer by natural convection is neglected.
- Heat transfer by radiation is neglected.
- Constant thermal conductivities of porous matrix and fluids
- Solid matrix is isotropic and homogeneous.

3.8.2 Mass and momentum equations for a porous medium

The continuity equation for porous media is derived through the application of mass balance across a macroscopic control volume as well as the replacement of certain variables with the most appropriate qualities to porous media [42, 188]. This is as expressed in Equations (3.23 – 3.38).

$$\frac{\partial \rho_f}{\partial t} + \nabla.\left(\rho_f \vec{v}\right) = 0 \tag{3.23}$$

Where ρ_f and $\vec{v}$ represents fluid density and velocity vector.

A momentum source term is incorporated into the conventional fluid flow equations for modeling a porous medium, and the source term is composed of Darcy and inertial loss terms as stated in Equations (3.24-3.25)

$$\frac{\partial}{\partial t}\left(\rho_f \vec{v}\right) + \nabla.\left(\rho_f \vec{v}\vec{v}\right) = -\nabla P + \nabla.(\bar{\tau}) + \rho\vec{g} + \vec{S} \tag{3.24}$$

$$\vec{S} = -\left(\sum D\mu\vec{v} + \sum C\frac{1}{2}\rho|v|\vec{v}\right) \tag{3.25}$$

Where,

$$C = \frac{2C_F\varepsilon^3}{\sqrt{K}} \tag{3.26}$$

$$D = \frac{\varepsilon^2}{K} \tag{3.27}$$

$$\varepsilon = \frac{V_v}{V_t} \tag{3.28}$$

Where $P, \vec{S}\, D, C, |v|, K, \varepsilon, V_v$, and V_t signified Pressure, source term, viscous resistance, inertial resistance, velocity magnitude, permeability, porosity, the volume of void in the porous medium, and total volume of the solid matrix, respectively.

3.8.3 Energy Equations for a Porous Medium

In this study, the viability of the multi-fluid model for the volume-averaged energy equation is considered for both the solid matrix and the liquid phase [193] and for incompressible fluid with insignificant viscous dissipation, the energy equations for the fluid phase are given as:

$$(\rho c_p)f\ (V.\nabla {T_f}^f) = \nabla.(k_{fe}\nabla {T_f}^f) + h_{sf}\alpha_{sf}({T_s}^s - {T_f}^f) \tag{3.29}$$

Where h_{sf}, α_{sf}, ${T_s}^s$, and ${T_f}^f$ represents interfacial heat transfer coefficient, interfacial specific area, solid phase temperature, and liquid phase temperature, respectively.

While solid matrix is given by:

$$\nabla.(k_{se}\nabla {T_s}^s) - h_{sf}\alpha_{sf}\left({T_s}^s - {T_f}^f\right) = -q''' \tag{3.30}$$

And thermal conductivity of the solid matrix and fluid is also given as:

$$-k_s\frac{\partial T_s}{\partial y} = \left(-k_{fe}\frac{\partial {T_f}^f}{\partial y} - K_{se}\frac{\partial {T_s}^s}{\partial y}\right) \tag{3.31}$$

$$T_s = T_f{}^f = T_s{}^s \tag{3.32}$$

3.9 Boundary conditions

After the importation of meshed geometry with the generated grid into the FLUENT [193]; then boundary conditions for geometry surfaces and parameters are specified for the commencement of the simulation process. Setting boundary conditions is a function of the engineering problem at hand.

3.10 Numerical Method

Employing the Ansys® 2020 Fluent software package incorporated with the finite volume method, the conservation equations (mass, momentum, and energy) and boundary conditions were numerically solved. The details of this technique can be found in [190]. The discretization of the computational domain into a finite number of discrete elements and control volumes was achieved with tetrahedra and pyramid elements. The simulation process was conducted with a pressure-based second-order model, and the SIMPLE algorithm was employed for the solution of coupled pressure-velocity field equations. When the scaled residual falls below 10^{-6}, it was discovered that it corresponds with the predicted convergence of the flow and thermal energy equations' solution.

3.11 Thermal performance indicator measurement of the designed cooling system

The measurement of the thermal behavior of the considered cooling systems for the removal of heat generated by a cylindrical lithium-ion battery pack in this work is actualized through certain parameters such as:

1) Dimensionless thermal resistance: This is the measure of the resistance to the free flow of heat from the battery pack imposed on the rectangular frame as volumetric heat transfer through the conduction element into the working fluid in the channel. It is determined in this work as:

$$\mathrm{R_{th}} = \frac{(\mathrm{T_{max}} - \mathrm{T_{in}})\,\mathrm{K_f}}{\mathrm{q'''}\,\mathrm{L_{fr}}\mathrm{D_h}} \tag{3.33}$$

2) Convective heat transfer coefficient: This is characterized by the transfer of generated heat from the battery between the working fluid and the stacked wall of the flow minichannel. The idea is that the higher the convective heat transfer coefficient, the better the thermal performance of the designed cooling system. It is determined in this work as:

$$h = \frac{q'''D_h}{(T_{max} - T_{in})} \quad (3.34)$$

3) Cost of Pumping power: This is required to force the working fluid through the stacked flow channel(s). In this work, the cost of pumping power is calculated as:

$$Pp = N\dot{V}(P_{in} - P_{out}) \quad (3.35)$$

4) Dimensionless heat transfer rate density: This parameter was employed to determine the total heat transfer rate per channel's unit volume to actualize the effective interaction of the working fluid and cooling structure elements. In this study, heat transfer rate density is determined as:

$$q''_d = \frac{q}{NV_c} \quad (3.36)$$

Where:

$$q = \frac{q'''L_{fr}D_h}{K(T_{max} - T_{in})} \quad (3.37)$$

And

$$V_c = H_c W_c L \quad (3.38)$$

5) Thermal performance enhancement factor: In consideration of total heat transfer and coolant flow resistance in the channel, the overall assessment of the designed cooling system performance will be calculated as*:*

$$TPF = \frac{Nu/Nu_o}{(f/f_o)^{1/3}} \quad (3.39)$$

Where:

$$Nu = \frac{hL}{K_f} \quad (3.40)$$

And

$$f = \frac{\Delta P}{(\rho\mu^2/2)(L/D_h)} \quad (3.41)$$

3.12 Optimization techniques

Ansys DesignXplorer is a design optimization program that runs in the Ansys Workbench environment. For the realization of the system performance and designed variable relationships, this application uses a goal-driven methodology to combine both conventional

and unconventional optimization [194]. Goal-driven optimization employed response surface methodology to determine the optimal design candidate. Employed a set of mathematical and statistical tools to provide variation of a given performance about the input parameters. Myers et al [174] and Khuri et al. [175] narrated this expression with equations in their respective published studies.

Representing y as the response variable of interest and $x_1, x_2, x_3, \ldots\ldots\ldots x_k$ as input variables, their operational relationship could be written using two models. Based on the underlying principle, an already known operational relationship between the response variable of interest and input variables could be represented with a mechanistic model as stated below:

$$y = g(x_1, x_2, x_3 \ldots\ldots\ldots x_k) + \varepsilon \tag{3.42}$$

Where ε signified the error of the system.

However, if the fundamental concept is not fully understood, the unknown function g must be approximately estimated using the appropriate empirical model and the relationship can be represented as.

$$y = f(x_1, x_2, x_3 \ldots\ldots\ldots x_k) + \varepsilon \tag{3.43}$$

While the functional f is often a first- or second-order polynomial, the empirical model is called a response surface model.

3.12.1 Response surface methodology and computer experiments

Computer and simulation models are the foundation on which engineers and scientists develop products and processes. As a very effective experimental technique for product or process optimization, response surface methodology is integrated into computer simulation experiments to evaluate the influence of certain significant factors on the developed system to generate a model called a metamodel. The goal of metamodel optimization is to minimize the number of samples in computer experiment design and analysis while maintaining a high degree of approximation accuracy and enhancing the optimal outcome with each optimization iteration. The optimization outcome will be a suitable representation of the real system's optimal conditions if the meta-model accurately captures the characteristics of the real system [195]. When there is randomness or uncertainty, stochastic as one of the types of model simulation is utilized to estimate possible outcomes. Various outcomes' probability is estimated using stochastic model simulation, which permits random fluctuation in the inputs.

Deterministic as another type of model simulation, is the exact opposite of stochastic model simulation in that it does not incorporate any uncertainty or unpredictability. Any uncertainty in deterministic model simulation is external to the model and does not affect its output.

After developing the model and defining parameters, a response surface is generated through the response surface optimization tool integrated with Ansys 20.0 design explorer. Depending on the number of input parameters, a specified number of solutions (design points) are needed to create this response surface. The design space is established by providing the lowest and highest values to be taken into account for each input variable once the response surface has been inserted. For each parameter, a response surface is generated when the design of experiments (DOE) space sampling is developed through the design of experiments (DOE) response surface system.

The Goal-Driven Optimization (GDO) approach is employed to identify the design candidates from the response surfaces. After setting the objectives in the GDO, the solution to the optimization problem is provided. However, the response surface accuracy for each design candidate is verified by changing it to a design point. A complete simulation is then run for this point to affirm that the output parameters are valid [194]. Compared to the ad hoc trial-and-error technique, the design of the experiment approach is preferred for the design of engineering products

For simplicity purposes, the deterministic simulation model (optimal space filling) is adopted to design the experiment in this study. The non-parametric regression 52odelling algorithm, known for its high non-linear performance prediction of outputs in reference to inputs, is then employed to generate the response surface. For instance, if X represents the generated input sample from the DOE, where X is defined as

$$X = \{x_1, x_2, x_3, \dots\dots\dots\dots\dots\dots x_M\} \tag{3.44}$$

x_1 is an N-dimensional vector, that defines the input variables, the focus is to estimate an equation of the form,

$$Y = \sum_{i=1}^{N}(A_i - A_i^*)K\left(\overrightarrow{X_i}\, X\right) + b \tag{3.45}$$

Where, $K\left(\overrightarrow{X_i}\, X\right)$ represents Kernel map and the quantities A_i and A_i^* are Lagrange multipliers.

The screening method, a non-iterative direct sampling technique, is utilized for the design optimization after the response surface is developed. Characterized by a low discrepancy sequence, the screening method employs a quasi-Monte Carlo generator based on the Hammersley algorithm. Meanwhile, the Hammersley algorithm applies the radix-R notation of an integer to create a set of N Hammersley points. An integer n, for instance, can be expressed as a sequence of digits.

$$n = n_1, n_{m-1}, \dots\dots\dots\dots\dots\dots\dots n_2, n_1, n_0 \tag{3.46}$$

The integer n can be expressed in radix R- R notation as follows:

$$n = n_0 + n_1 R + n_2 R^2 + \dots\dots\dots\dots\dots\dots n_m R^m \tag{3.47}$$

$$\text{Thus, } m = [\log_R n] = \left[\frac{\ln n}{\ln R}\right] \tag{3.48}$$

The square brackets indicate the integer of the number in the brackets.

Equation (3.49) which represents an inverse radix number function, is derived from Equation (3.48). This function reverses the order of n's digits around the decimal point to create a unique number on the interval $[0, 1]$.

$$\phi_R(n) = .n_0 n_1 n_2 \dots\dots\dots n_m = n_0 R^{-1} + n_1 R^{-2} + \dots\dots\dots + n_m R^{-m-1} \tag{3.49}$$

The Hammersley sequence for K-dimensional points can finally be determined by:

$$H_K(i) = \left[\frac{i}{N}, \varphi_{R_1}(i), \varphi_{R_2}(i), \dots\dots\dots\dots\dots \varphi_{R_{k-1}}(i)\right] \tag{3.50}$$

Note: $i = 0, \dots\dots\dots, N$ represents the same points and $R_1, R_2, \dots . . R_{K-1}$ indicates the first

$K - 1$ prime numbers.

3.13 Conclusions

This chapter presents procedures for solving fluid and heat transfer problems using the Ansys® 2020 R1 computational fluid dynamics software. It also documents the governing equations for the heat generation and thermophysical properties of the 26650 cylindrical lithium-ion battery cells were also documented. Meanwhile, the mathematical formulation of porous media and optimization techniques for the battery cooling system are detailed.

CHAPTER FOUR

DEVELOPMENT OF CYLINDRICAL LITHIUM-ION BATTERY PACK COOLING SYSTEM

4.1 Preview

In this chapter, the capacity of the cooling system, comprised of the channel(s) without insert mounted on the rectangular frame, to manage the thermal challenges of the cylindrical lithium-ion battery pack is analyzed and reported. The goal is to actualize a compact cylindrical lithium-ion battery pack cooling system with the highest thermal performance. The influence of the number of channels mounted on the rectangular frame under different flow orientations on cooling system thermal performance for Reynolds number ranges from 128.38 to 2054.08 is numerically investigated. Meanwhile, the cooling system performance was evaluated with maximum rectangular frame wall temperature, dimensionless thermal resistance, pumping power, and heat transfer rate density.

4.2 Physical and Computational Model

The study by Basul et al. [27] employed the physical model shown in Figure 4.1a to illustrate the application of a minichannel for the dissipation of heat generated by the pack of cylindrical lithium-ion batteries of electric vehicles, is considered a reference model for this study. The designed liquid cooling system is based on the generated heat by the battery cells into the liquid in the channels via the aluminum conducting element. However, the thermal analysis of the system performance under a very high discharge rate of 6 C (coulombs) was investigated in this study with the application of symmetry conditions to a single battery pack from the fundamentally designed unit. Symmetry condition implementation is assumed to minimize the cost and simplify the simulation process.

The computational model of the battery pack comprises five 26650 $LiFePO_4$ cylindrical lithium-ion battery cells of similar thermophysical properties operating under a temperature of 298K coupled with a cooling system of minichannel(s) with dimensions $59.4\ \text{mm} \times 1.7\ \text{mm} \times 1.9\text{mm}$ and hydraulic diameter $1.29\ \text{mm}$ mounted on a rectangular frame is depicted in Figure 4.1b. Designed with a distance of 28 mm from one battery center to another in a parallel array, the $3340135\ \text{W/m}^3$ of volumetric heat transfer, equivalent to the total heat generated by the cylindrical lithium-ion battery pack is imposed through the conducting element on the rectangular frame of dimensions $59.4\ \text{mm} \times 60\ \text{mm} \times 3\ \text{mm}$. The density, axial, and radial

thermal conductivities adopted for the considered battery cells in this work are as documented by [85] (Table 3.1). In contrast, the mechanism of global heat generated in the cylindrical lithium-ion battery cell is determined using Eqns. (3.9-3.14) as expressed in [62] and adequately discussed in Chapter 3 of this report. The simulation process of dissipating heat generated by the battery under a steady-state battery operation was commenced by forcing a working fluid through the minichannel(s) under a varying Reynolds number. The transfer of heat in the channel(s) is considered a conjugate heat transfer problem, and the solution to conduction in the solid phase through the conduction element, as well as convection in the liquid phase, is analyzed to present an effective compact cooling system for temperature control of the battery pack. Water, a homogenous, single-phase, incompressible, and constant thermophysical property, was employed as the working fluid for this study. The front, top, and bottom surfaces of the minichannel(s) are assumed to be adiabatic (Figure 4.1b). At the same time, the thermal radiant and natural convection effects are also considered to be negligible. Meanwhile, the components of the cylindrical lithium-ion battery pack coupled with the cooling system are represented in Figure 4.1c.

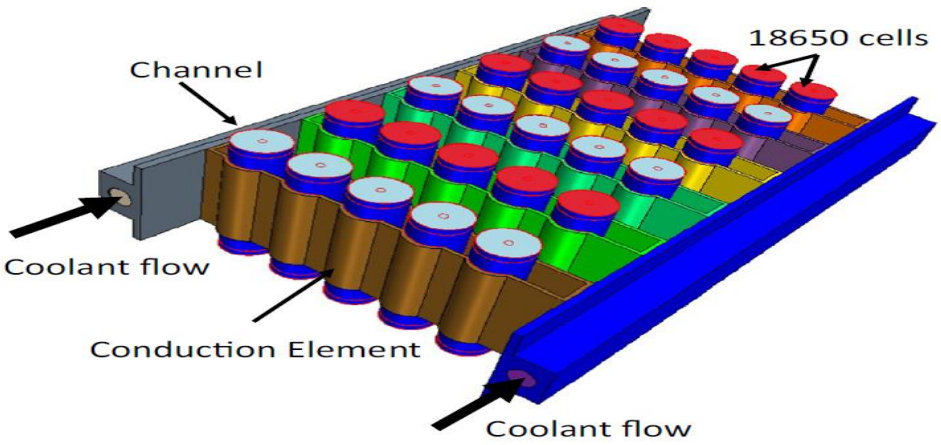

(a)

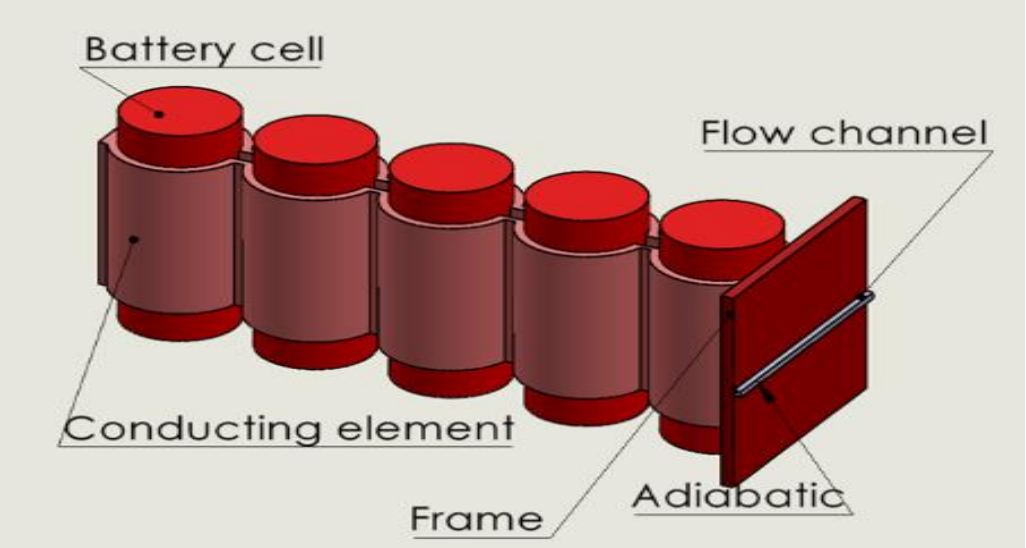

(b)

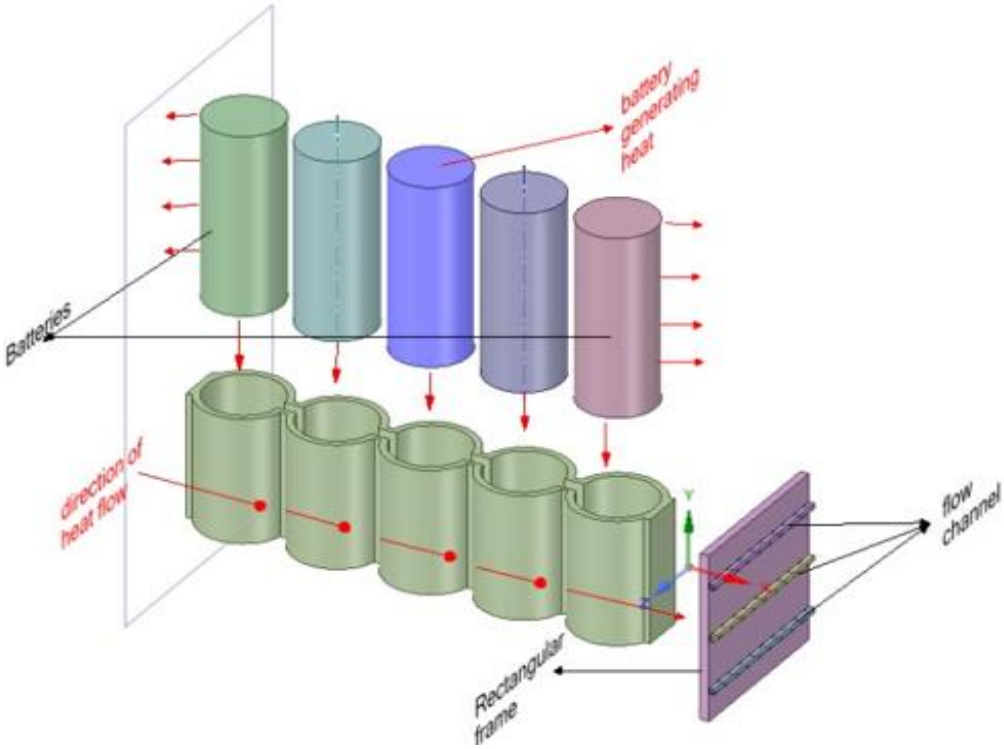

(c)

Figures 0.1. Physical model of the cooling system coupled with a lithium-ion battery pack [27] (a), Computational domain of the developed cooling system (b), and Components of the developed cooling system (c)

4.3 Ansys code validation and grid refinement test analysis

4.3.1 Ansys code validation

The employed geometric configurations for validation purposes (numerical and experimental) were reproduced and subjected to grid and mesh generation. The numerical study of [117] and the experimental work of [196] were employed for the validation of the Ansys® 2020 code adopted for this work. The comparison results of the present study's simulation data with the available numerical and experimental work are presented below:

4.3.1.1. Comparison of the present study with the past work of [117]

The reproduced cooling system and mesh grid generation are shown in Figure 4.2(a and b). Four half battery cells of similar shape and thermophysical properties were attached to a wall frame of a plain channel aluminum jacket. A steady state simulation was conducted with the adoption of the Finite volume method by the commercial software Fluent. Using water as a coolant, the total rate of heat generated by the battery $(\dot{q})$ is determined with Equation (4.1)

$$\dot{q} = 0.493I^2 + 0.2312IT \quad (4.1)$$

Where; I *and* T represents the discharge current and operating temperature of the cell.

(Note: The battery operating temperature is taken as $50℃$. For each of the cells, the discharge current is calculated as the ratio of the discharge rate to the period of battery operation).

If a single battery cell generates 790.5 W (calculated with Equation (4.1)), then half of the battery cell will generate 395.25 W. The total rate of heat generated by 4 half battery cells is 1581 W. The volumetric heat transfer is determined with Equation (4.2).

$$\text{Volumetric heat transfer} = \frac{\text{Total rate of heat genetated by the batteries}}{\text{Volume of the flow channel}} \quad (4.2)$$

The cooling channel dimensions are taken as $141\ \text{mm} \times 109\ \text{mm} \times 25\ \text{mm}$

The cooling channel is imposed with calculated volumetric heat transfer as a constant heat source. Aside from the channel's wall attached with four half batteries all other sides of the

wall is considered adiabatic. The computation model and mesh grid generation of [117] are

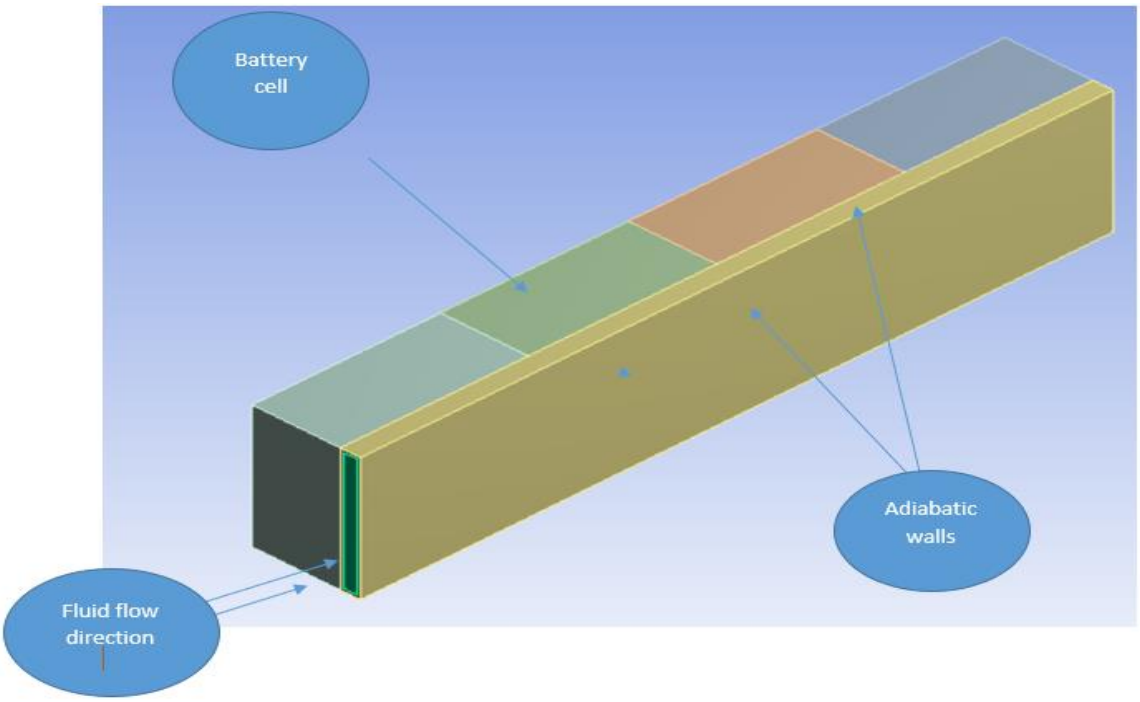

(a)

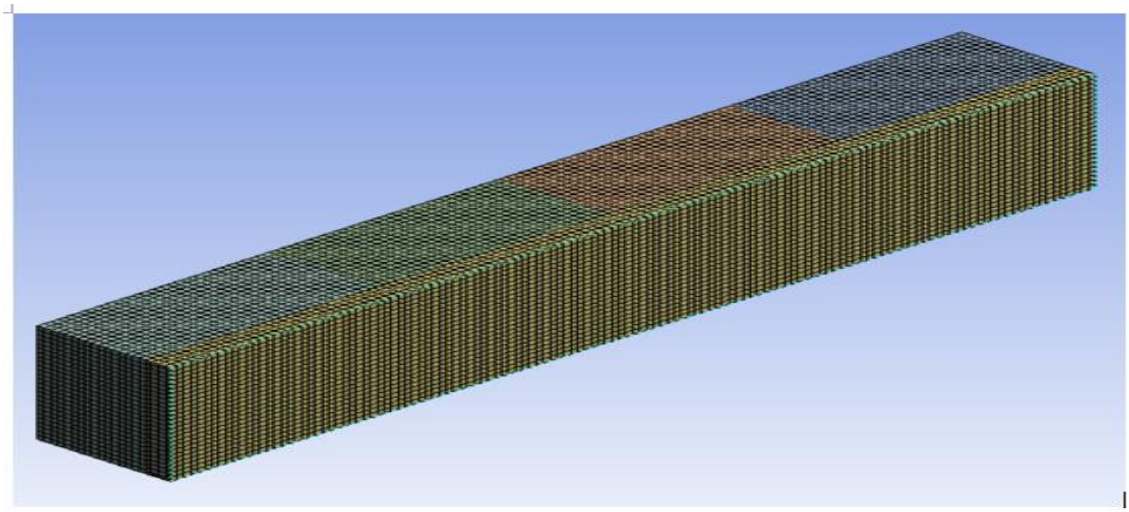

(b)

Figure 0.2. Computational fluid domain coupled with battery cells (a), and Mesh grid generation (b).

Table. 4.1 and Figure 4.3, respectively, displayed the test refinement results and graph of the current work in comparison to the numerical work of [117]. The attainment of less than 5% disparities, as shown in Figure 4.3, affirmed the accuracy of the adopted Ansys® 2020 Fluent code to predict the thermal performance of the proposed cooling system.

Table 0.1. Grid refinement test for the numerical study of [117].

Number of cells	ΔT (K)	*Deviation* $\left\lvert\frac{(\Delta T)_i - (\Delta T)_{i-1}}{(\Delta T)_i}\right\rvert$
90450	239.0812	----------
78519	239.0935	0.000051
73376	239.2123	0.000050
93606	238.9201	0.001222

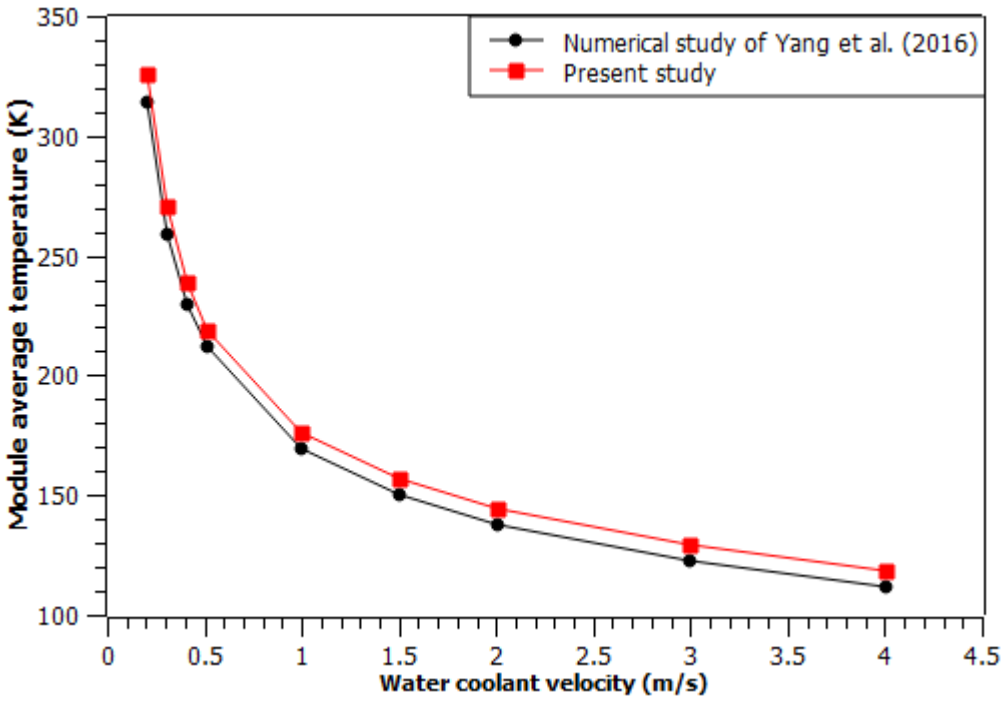

Figure 0.3. Module average temperature as a function of water coolant velocity for battery thermal management system.

4.3.1.2 Present study comparison with the Experimental past work of [196]

The reproduced geometric configuration and mesh grid generation of the experimental work of [196] are displayed in Figures 4.4(a and b). Under a steady state of operation, 106 cylindrical lithium-ion batteries with an orthogonal arrangement on a cold plate of $227\text{mm} \times 206\ \text{mm} \times 10\ \text{mm}$ dimensions populated with minichannels of dimensions $3\ \text{mm} \times 8\ \text{mm}$ (Figure 4.4c) are subjected to the cooling process to dissipate the imposed heat from the battery cells on the cold plate using water as a working fluid. With 2W of the generated heat rate by a single battery cell, the total rate of heat generated by 106 cylindrical lithium batteries, is calculated to be 212W. Using Equation (4.2), the different rates of heat generated by the total number of cylindrical lithium-ion battery cells are employed to determine the imposed volumetric heat transfer on the cold plate.

$$\text{Volumetric heat transfer}(\dot{q}\ ) = \frac{\text{Total rate of heat generated by the battery cells}}{\text{Volume of flow cold plate.}} \qquad (4.3)$$

For example, $(\dot{q}\ )$ with 4 W of heat generated $= \frac{4\times106}{0.000468755} = 904{,}523.685\ \text{Wm}^{-3}$

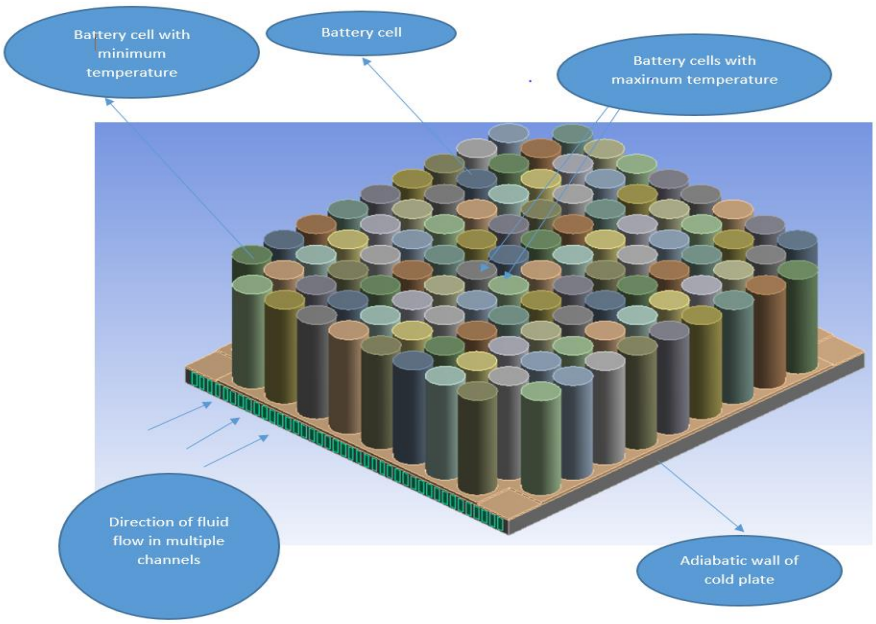

(a)

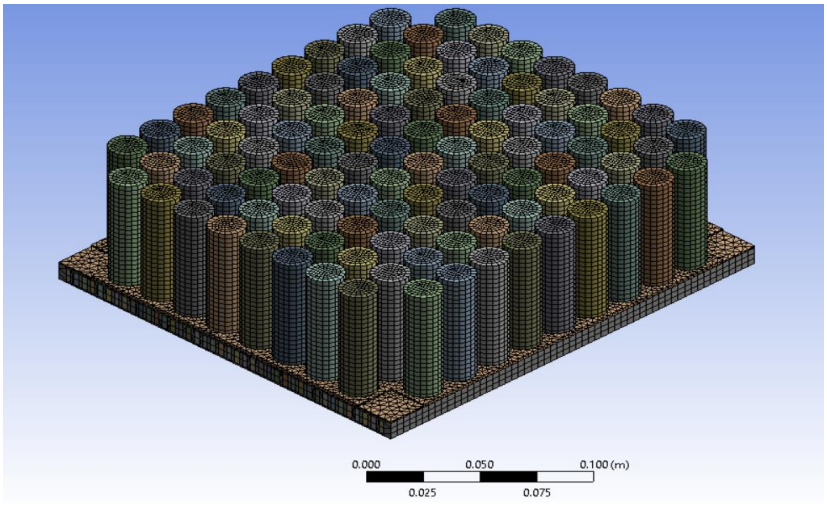

(b)

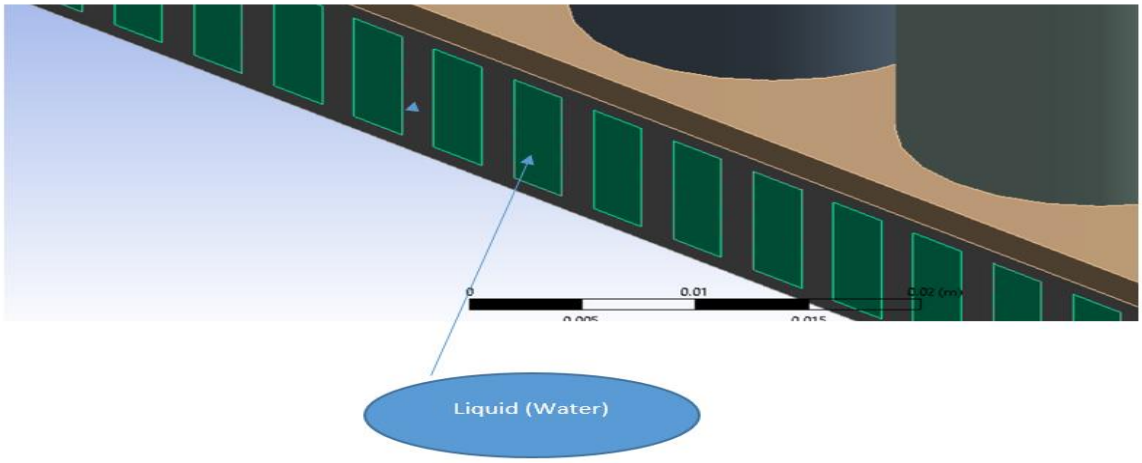

(c)

Figure 0.4. Computational fluid domain coupled with a numbers of cylindrical lithium-ion battery cells (a) Mesh grid generation (b), and Cold plate populated with minichannels of water as a coolant (c)

At a flow rate of 10L/min, the Tbmax is calculated as the average temperature of battery cells with maximum surface temperature while ΔTb is determined by the difference of Tbmax and Tbmin (Figure 4.5a). Aside from the top surface of the cold plate, all other walls are considered adiabatic (Figure 4.5a).

Table 4.2 displays the grid refinement test analysis for the experimental work of [196]. The comparison of the experimental with the obtained simulation results for Tbmax(℃) was represented in Figure 4.5a. A similar comparison for ΔTb(℃) was displayed in Figure 4.5b.

The actualization of less than 5% disparities as shown in Figure 4.5(a and b), substantiates the viability of the adopted Ansys® 2020 fluent code to predict the thermal performance of the proposed cooling system for cylindrical lithium-ion battery in electric vehicles.

Table 0.2. Grid refinement test for experimental study of [196]

Number of cells	*Number of elements*	*ΔT (^{O}C)*	*Deviation* $\left\lvert\frac{(\Delta T)_i - (\Delta T)_{i-1}}{(\Delta T)_i}\right\rvert$
257896	245620	43.4402	----------
270007	255969	43.4645	0.0005593
251593	263486	43.5300	0.0015069
255011	243670	44.0152	0.0111463

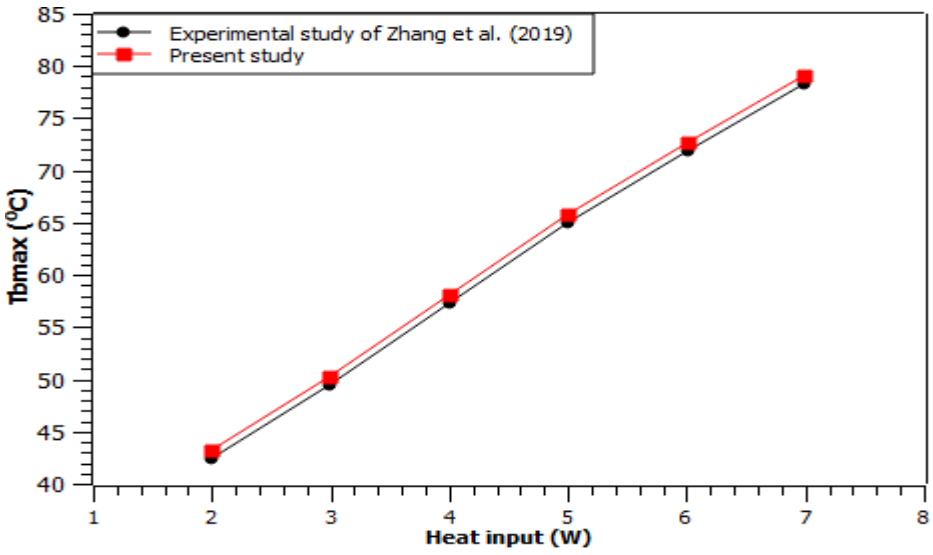

(a)

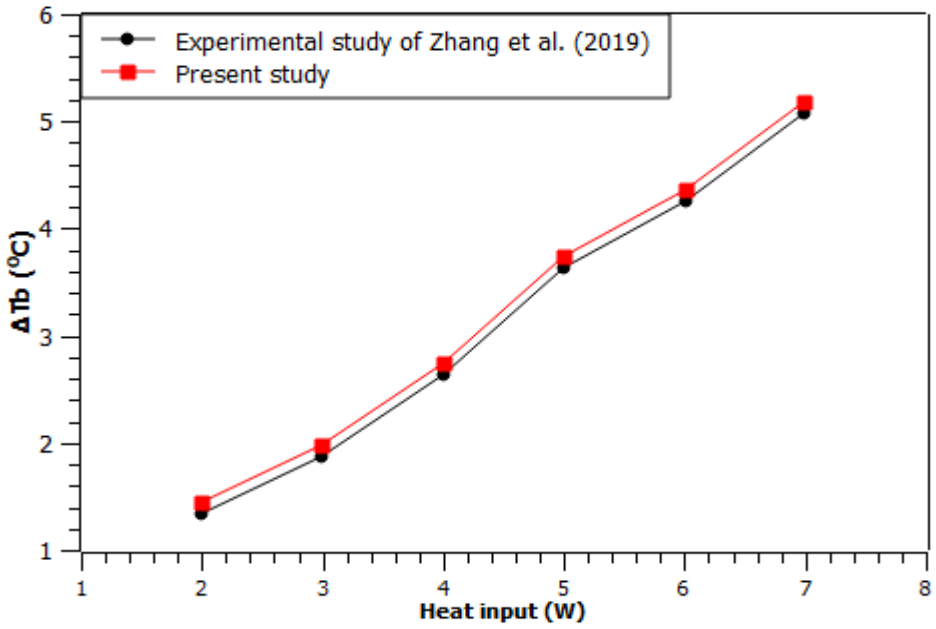

Figures 0.5. Maximum battery temperature ($Tbmax$) as a function of heat input for a liquid cooling system (a) and the Maximum battery temperature difference (ΔTb) as a function of heat input for a liquid cooling system (b).

4.3.2 Grid refinement test analysis

The attainment of an accurate simulation result in this study was based on several grid refinement tests conducted for each of the designed cooling systems. However, the same node and element sizes were considered for the cooling systems of the same setup subjected to different flow orientations. At an inlet velocity of $0.2\ \mathrm{m/s}$ (Reynolds number 256.76) and volumetric heat transfer of $3340135\ \mathrm{W/m^3}$. The grid independence density and maximum rectangular frame wall temperature are determined for the cooling systems. Employing the scaled residual for tracking purposes of solution convergence, the continuity and momentum equations as well as the energy equation, are assumed to converge when it drops below 10^{-6}. Table 4.3 displays the geometric dimensions adopted for the cooling systems. In contrast, Table 4.4 depicts the conducted grid refinement test for N_{3PF} as an example for all grid refinement analyses carried out in this section. However, Figure 4.6 shows the mesh grid generation of the developed cooling systems mounted with different numbers of channels on the rectangular frame.

Note that the single channel is centrally mounted on the rectangular frame, while 35.9mm, 20.3 mm, 10.7 mm and 7.375 mm spacing between the channels was respectively, considered for two, three, four, and five channels.

Table 0.3. Geometric dimensions for grid refinement test

F_h (mm)	F_t (mm)	W (mm)	H (mm)	L (mm)	Hc (mm)	Wc
60	3	1.7	1.9	59.4	1.4	1.2

Table 0.4. Grid refinement test for N_{3PF}

Number of cells	Peak frame wall temperature (K)	Deviation $\left\|\frac{(\Delta T)_i - (\Delta T)_{i-1}}{(\Delta T)_i}\right\|$
98020	346.8860	----------
310782	346.8953	0.00002681
90539	345.6459	0.00360166

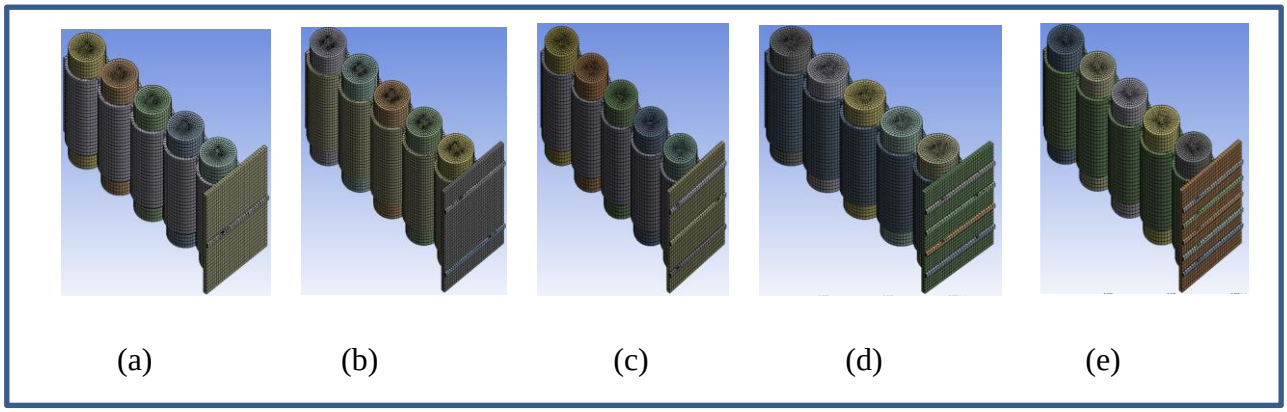

(a) (b) (c) (d) (e)

Figures 0.6. Mesh grid generation for the cooling system of one (a) two (b) three (c) four (d) and five (e) channels mounted on the rectangular frame**.**

4.4 Results and Discussions

With fixed 1.29 mm of the hydraulic diameter of the flow channel regardless of the design and $3340135\ \mathrm{W/m^3}$ of volumetric heat transfer imposed on the rectangular frame of the cooling system through the conducting element as total heat generated by the battery pack of an electric vehicle, the influence of the number of flow channel on the thermal performance of developed cooling structures under different flow orientations were investigated and reported in this section.

4.4.1 Reynolds number effect on cooling system characterization under different flow orientations

4.4.1.1 Maximum rectangular frame wall temperature

From Figure 4.7, the rectangular frame's maximum wall temperature *(T_{max})* decreased as the Reynolds number *(Re)* increased. A gradual reduction in T_{max} occurred as the *Re* increased from 128.38 to 1027.04, beyond which further increases in the *Re* had an insignificant effect on the T_{max}. Additionally, a more pronounced T_{max} reduction was observed with an increase in the number of channels mounted on the rectangular frame. For instance, at the highest *Re* (2054.08) N_{5CF} reduced T_{max} by 1.9%, 5.3%, 12.6%, and 33.6% compared to N_{4CF}, N_{3CF} N_{2CF}, and N_1 respectively. A similar T_{max} reduction behavior was noted with parallel flow cooling systems. However, counterflow cooling systems provide slightly lower T_{max} values than parallel flow cooling systems.

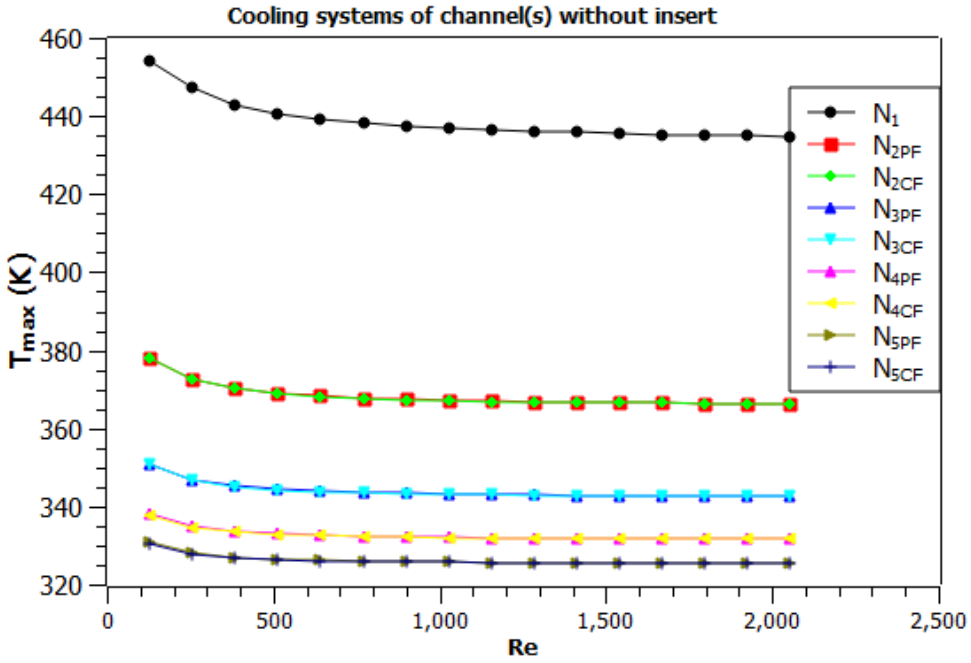

Figure 0.7. Maximum rectangular frame wall temperature (T_{max}) vs Reynolds number (*Re*) of the cooling system without an insert in the channel(s). The color markers represent the cooling system of different numbers of channel(s) mounted on the rectangular frame.

4.4.1.2 Dimensionless thermal resistance

Figure 4.8 shows the variation of dimensionless thermal resistance *(R_{th})* with an increase in Reynolds number *(Re)* regardless of the number of channels mounted on the rectangular frame

of the cooling system. From the result, the dimensionless R_{th} decreases with an increase in the *Re.* A gradual drop in the dimensionless R_{th} was noticed when the *Re* increased from 123.83 to 1027.04. However, when the *Re* exceeded 1027.04, an insignificant dimensionless R_{th} was recorded. An improved dimensionless R_{th} reduction was realized with increased channels mounted on the rectangular frame. However, counterflow cooling systems achieved a slightly lower dimensionless R_{th} than cooling systems with parallel flow cooling systems.

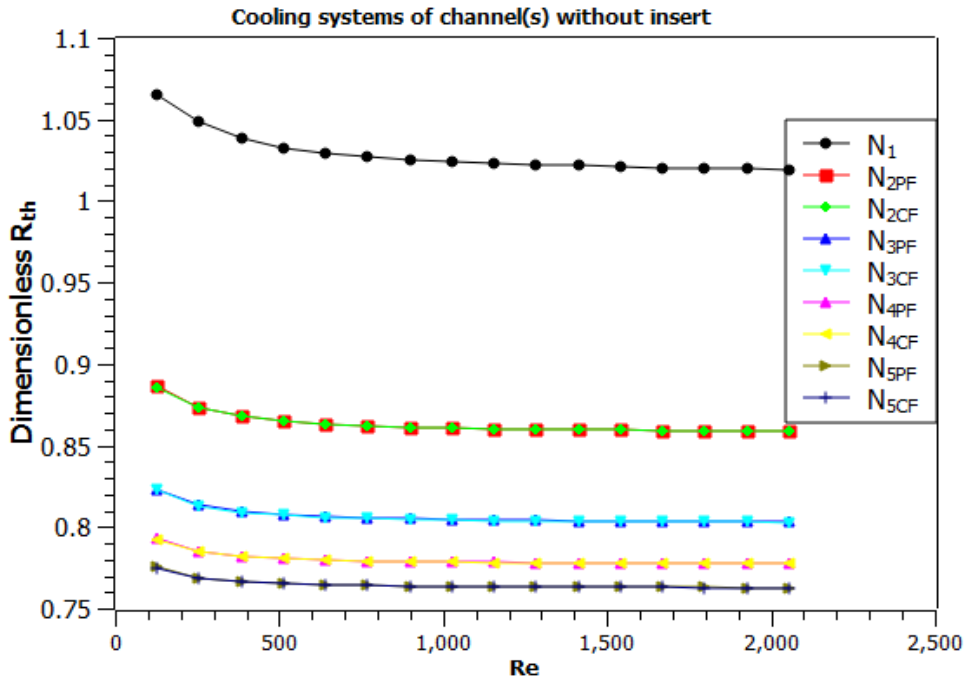

Figure 0.8. Dimensionless thermal resistance (R_{th}) vs Reynolds number (*Re*) of the cooling system without an insert in the channel(s). The color markers represent the cooling system of different numbers of channels mounted on the rectangular frame.

4.4.1.3 Cost of pumping power

Figure 4.9 shows an increase in the cost of pumping power *(Pp)* with an increase in Reynolds number *(Re)* regardless of the number of channels mounted on the rectangular frame. At a lower *Re* below 641.9, a gradual increase of *Pp* was realized and above this point, a further increase in *Re* yields a substantial upward trend of *Pp*. However, an increased *Pp* was observed with the increase in the number of channels mounted on the rectangular frame [197]. For instance, 80%, 60%, 40%, and 21% of increased *PP* were respectively realized with N_{5CF} compared to N_1, N_{2CF}, N_{3CF}, and N_{4CF} at *Re* 641.9. Thus, the lesser the channel number, the

lesser the *Pp*, and vice versa. Furthermore, counterflow cooling systems were recorded with slightly higher values of *Pp* than parallel flow cooling systems. This result is consistent with the published work of Ariyo and Bello-Ochende [47].

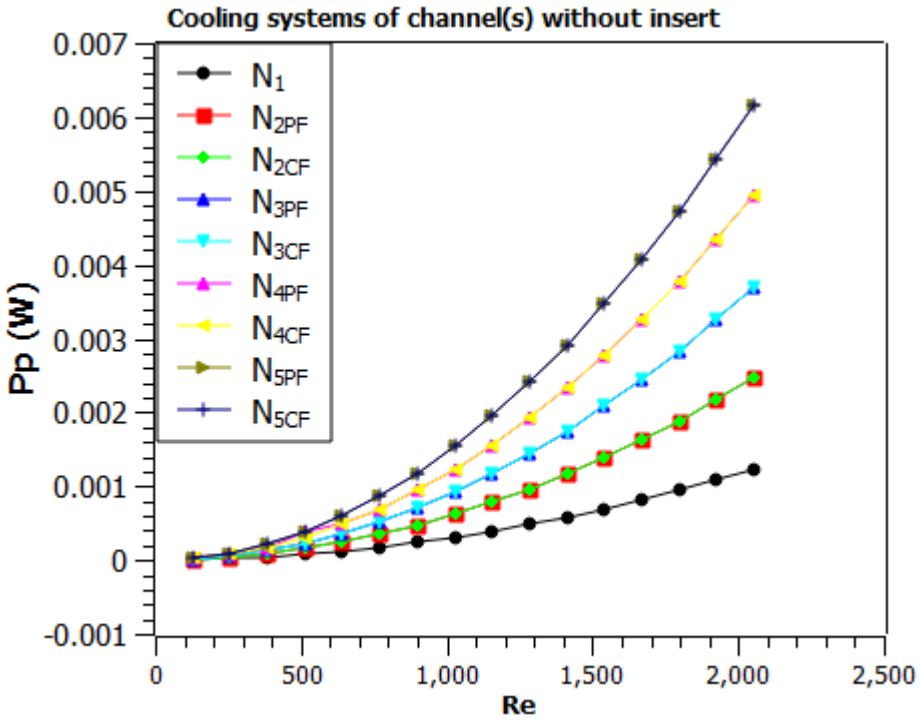

Figure 0.9. Cost of pumping power (*Pp*) vs Reynolds number (*Re*) of the cooling system without an insert in the channel(s). The color markers represent the cooling system of different numbers of channels mounted on the rectangular frame.

4.4.2 Effect of channel number on dimensionless heat transfer rate density for the cooling systems with no insert in the channel

Figure 4.10 illustrates the behavior of the cooling system to the dimensionless heat transfer rate density influenced by the varying number of channels mounted on the rectangular frame. A higher dimensionless heat transfer rate density value implies an improved thermal performance of the cooling system (Equations (3.36-3.38)). Regardless of the flow orientation or the number of channels, an increase in Reynolds number (*Re*) leads to an increase in the dimensionless heat transfer rate density. Parallel flow cooling systems (Figure 4.10a), demonstrated a slightly lower dimensionless heat transfer rate density compared to the counterflow cooling systems (Figure 4.10b). Notably, the highest dimensionless heat transfer rate density was achieved when the three (3) channels were mounted on the rectangular frame of the cooling system. For the counterflow cooling system as an example, 2.5%, 2.3%, 0.67%, and 2.4% of increased dimensionless heat transfer rate density at *Re* 2054.08 were realized when 3 channels were

mounted on the rectangular frame compared to 1,2.4, and 5 channels, respectively (Figure 4.10b). A similar pattern was demonstrated by parallel flow cooling systems (Figure 4.10a). Thus, adequate interaction of the working fluid and solid elements of the cooling systems is suspected to be more pronounced when three channels are mounted on the rectangular frame [198, 199].

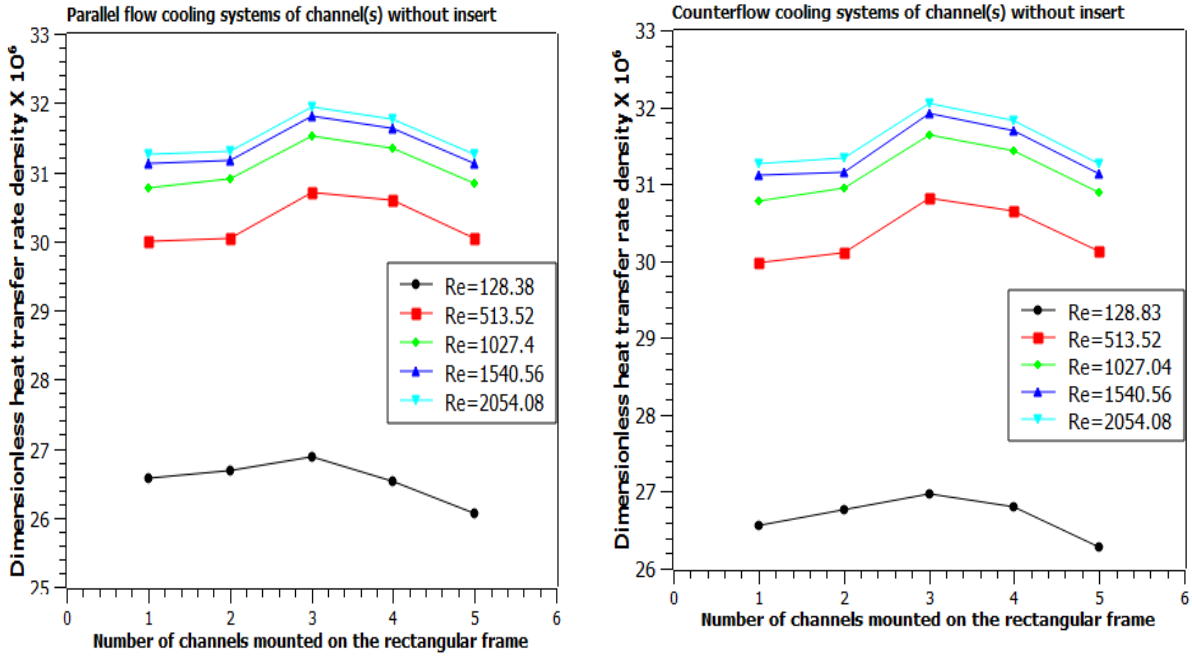

Figure 0.10. Dimensionless heat transfer rate density vs. Number of channels mounted on the rectangular frame in parallel (a) and counterflow (b) cooling systems without an insert. Colored markers represent different Reynolds numbers (Re): Re = 256.76 (black), Re = 641.9 (red), Re = 770.28 (green), Re = 1155.42 (blue), and Re = 1925.7 (cyan)

4.4.3 Temperature uniformity of the battery cells in the pack

According to [5, 13], maintaining good temperature uniformity among battery cells in a pack extends the lifespan of lithium-ion battery packs. Therefore, it is essential to study the impact of the cooling system on the temperature uniformity of cylindrical lithium-ion cells within the battery pack. Lower temperature uniformity values indicate better cooling system performance. As an example of different cooling system designs, Figure 4.11(a-c) illustrate the effect of the Reynolds number on the temperature uniformity of battery cells in a pack. Within the range of Reynolds numbers used in this study, the designed cooling systems achieved a temperature variation of less than 2℃ between battery cells, indicating their ability to maintain uniform

temperatures [13]. In particular, the N_{3CF} design (Figure 4.11b) showed slightly better temperature uniformity than the N_{3PF} design (Figure 4.11a), demonstrating the influence of different flow orientations on heat dissipation. In contrast, the N_I design (Figure 4.11a) exhibited higher temperature uniformity values than N_{3PF} and N_{3CF} (Figures 4.11a and b), highlighting the improved cooling performance of the additional channels mounted on the rectangular frame.

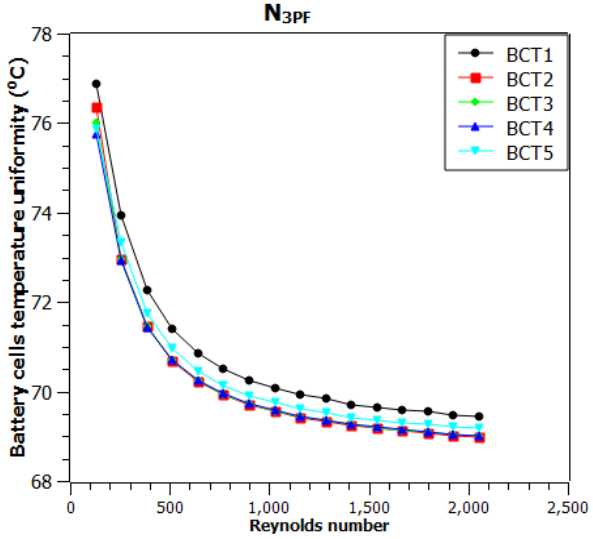

(a)

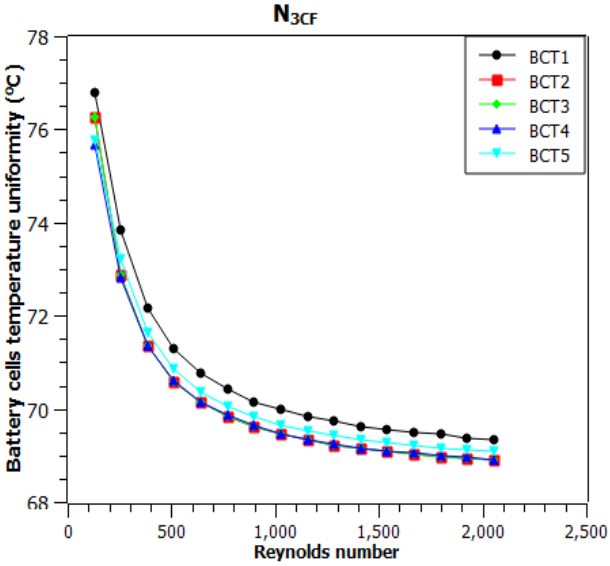

(b)

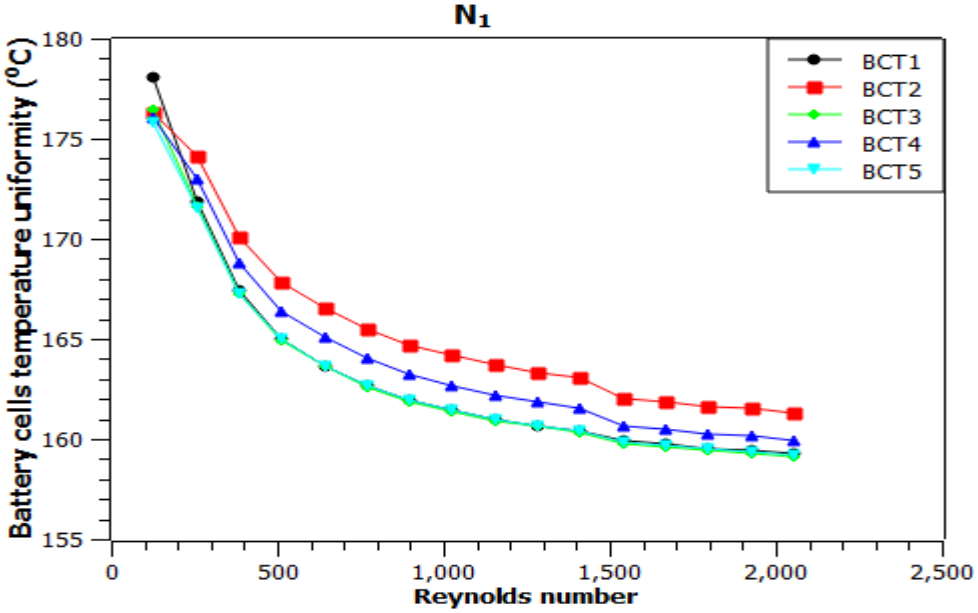

(c)

Figure 0.11. Battery cells temperature uniformity vs Reynolds number for cooling systems of three channels with the parallel flow (a) and counterflow (b) arrangement as well as a single channel (c). The color makers represent the temperatures of each battery cell in a pack

4.4.4 Temperature contours

Figures 4.12 (a-c) displays temperature contours with an illustration of the temperature distributions of the cooling systems designed for the thermal management of cylindrical lithium-ion batteries of an electric vehicle imposed with a volumetric heat source of $3340135\,W/m^3$ Reynolds number 1412.18. Compared to Figure 4.12b, the highest temperature profile is observed in Figures 4.12 (a) shows the improved cooling 70ddition70ce by the70ddition70nal channels mounted on the rectangular frame. However, a slight drop in temperature profile was observed in Figure 4.12c (counterflow cooling system) compared to Figure 4.12b (Parallel flow cooling system), reflecting the influence of flow orientation on the dissipation of heat from the battery pack.

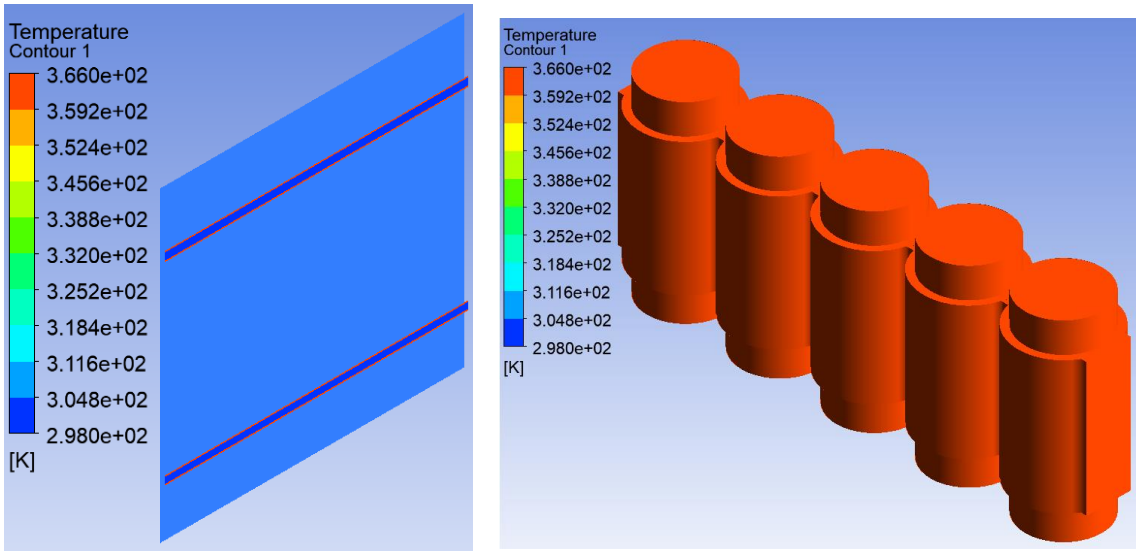

(a)

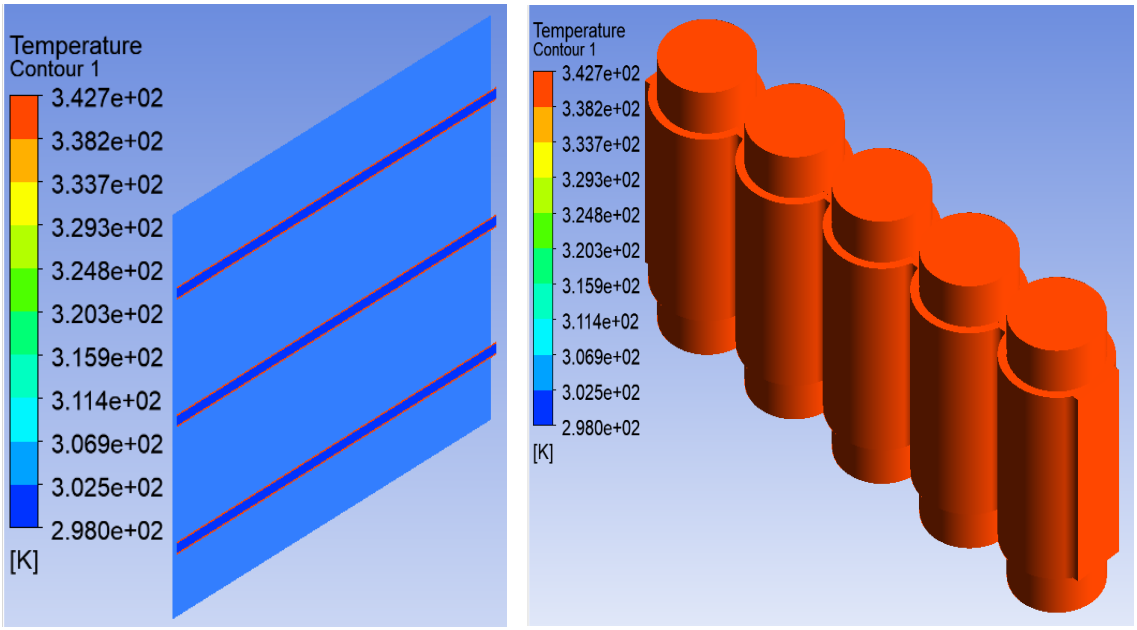

(b)

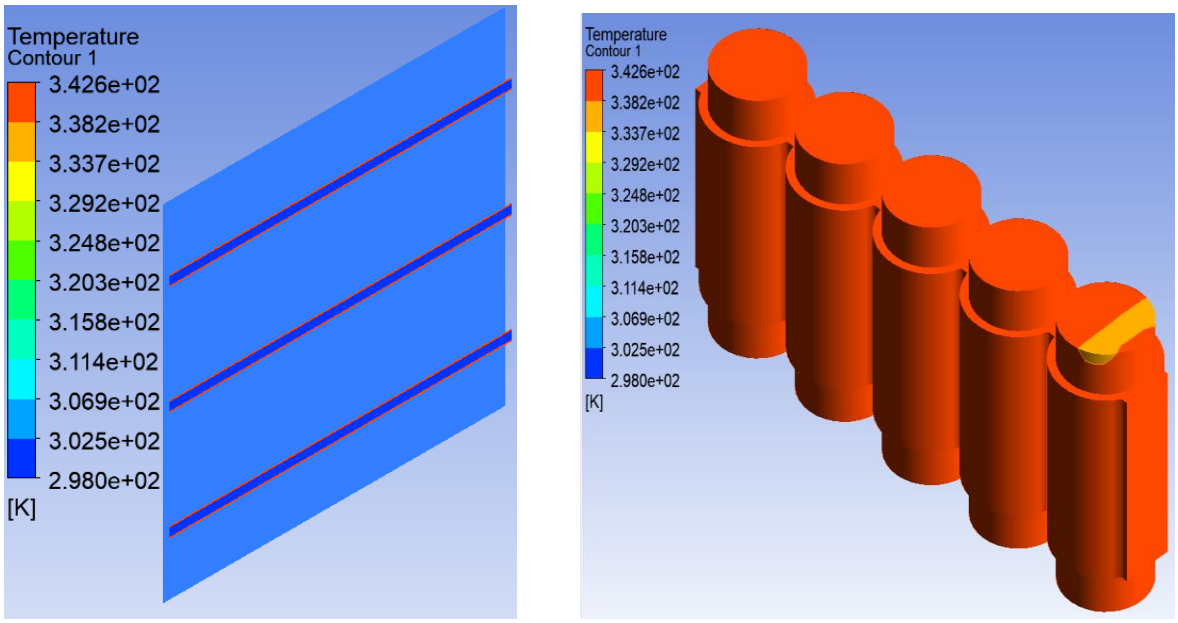

©

Figure 0.12. Temperature contour for the cooling system of two channels with parallel flow arrangement (a), three channels with parallel flow (b), and counterflow (c) arrangements at Reynolds number 1412.18 in plain X=25 mm.

4.5 Conclusions

In this chapter, the designs of the cooling systems coupled with a pack of five cylindrical lithium-ion batteries were considered. The details of the grid refinement test and code

validation were adequately reported. The effects of the number of channels and the flow orientation on the thermal performance of the designed cooling system for effective dissipation of heat from the battery pack were numerically evaluated for *Re* values between 128.38 and 2054.08. Key findings include:

Counterflow versus. Parallel Flow Systems: Counterflow cooling systems demonstrated a slight advantage in reducing maximum wall temperature and thermal resistance compared to parallel flow systems.

Number of mounted channels: (a) An additional number of channels mounted on the rectangular frame yields a better improvement in the system performance (b) Pumping power increases with additional channels mounted on the rectangular frame (c) Highest thermal performance of the cooling system is achieved with three channels mounted on the rectangular frame.

Hence, the counterflow cooling system of the three channels mounted on the rectangular frame is recommended as the best for controlling the temperature of an electric vehicle’s battery pack.

CHAPTER FIVE

ENHANCEMENT OF CYLINDRICAL LITHIUM-ION BATTERY PACK OF ELECTRIC VEHICLE COOLING SYSTEM WITH CIRCULAR SOLID PIN FIN / ALUMINIUM FOAM OF VARYING POROSITIES INSERT(S)

5.1 Preview

This chapter presents the enhancement potential analyses of the circular solid pin fin or aluminum foam of various porosities inserted in the channels of the designed cooling system from Chapter 4. The cooling system's performance with the centrally located insert in the channels will be compared with the results previously obtained in Chapter 4. The varying locations' effect of a single insert on the system performance was later considered and compared with varying spacing arrangements of three inserts in the channels. However, the system performance will be evaluated with maximum rectangular frame wall temperature, thermal resistance, heat transfer rate density, and performance enhancement factor parameters. The discr'tization, mesh grid generation, and simulation process of the cooling systems were conducted with the Ansys® 2020 Fluent software package.

5.2 Physical and Computational Model

Figures 5.1(a-d), shows the cross-section of the computational domain for the cooling system inserted with single or three circular solid pin fins/aluminum foam. With fixed dimensions of the cooling system as stated in Chapter 4, varying locations of a single circular solid pin fin/aluminum foam insert in the fluid domain are first considered. The 1.5 mm, 2.0 mm, and 2.5 mm spacing arrangements of three circular solid pin fin/aluminum foam inserts in the fluid domain of the cooling system were later considered. The circular solid pin fin/aluminum foam used in this work is of dimension $1.1\ \mathrm{m} \times 0.6\ \mathrm{mm}$ while the considered porosities for the aluminum foam are low (0.1), medium 0.5, and high (0.9)

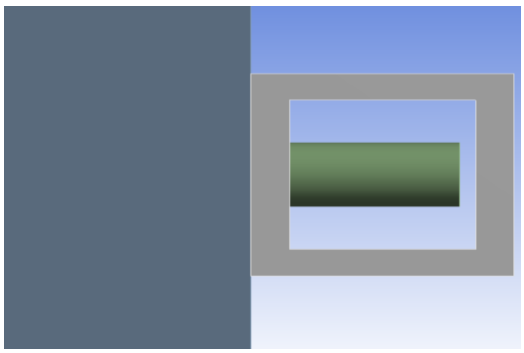

(a). Cooling system cross-section with a circular solid pin fin or aluminum foam insert in the channel

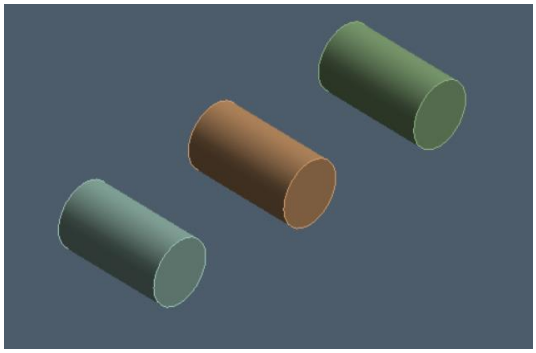

(b). Same size of circular solid pin fins or aluminum foam with a spacing of 1.5 mm in the channel

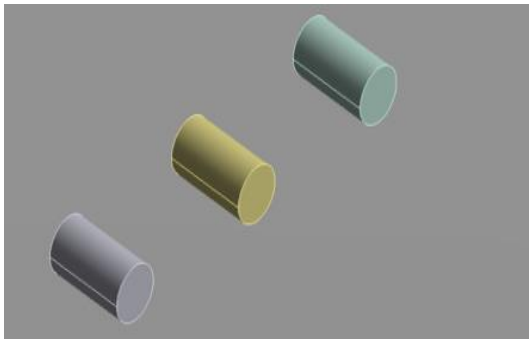

(c). Same size of circular solid pin fins or aluminum foam with a spacing of 2 mm in the channel

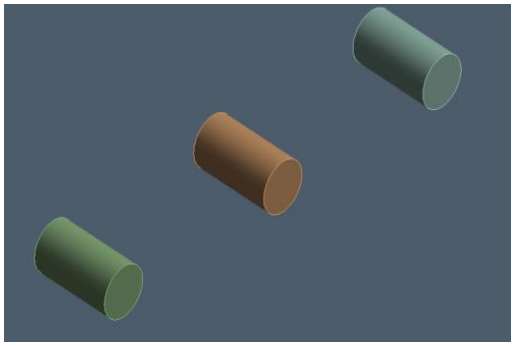

(d). Same size of circular solid pin fins or aluminum foam with a spacing of 2.5 mm in the channel

Figures 0.1. Cooling system cross-section with single (a), 1.5 mm (b), 2.0 mm (c), and 2.5 mm (d) spacing arrangements of three circular solid pin fins insert(s) in the channel.

5.2.1 Grid refinement test analysis

The exact number of nodes and element sizes was considered for the cooling system with solid pin fin/aluminum foam (irrespective of porosity) inserted at the same point in the flow channel(s) for accurate comparative analysis. A similar consideration was given to the cooling system of three inserts with the same spacing arrangements in the channels. Tables 5.1 and 5.2 respectively depicts the conducted grid refinement test for counterflow cooling systems of three channels inserted with a single circular solid pin fin centrally located in the channels *(NC_{3CF})* and counterflow cooling system with three inserts of circular aluminum foam arranged with

2.0 mm spacing ($NC2.0M_{CF}$) as an example for all grid refinement analyses carried out in this chapter.

Table 0.1. Grid refinement test for NC_{3CF}

Number of cells	Peak frame wall temperature (K)	Deviation $\left\|\frac{(\Delta T)_i - (\Delta T)_{i-1}}{(\Delta T)_i}\right\|$
223784	307.9172	----------
335968	307.9120	0.000163
414523	309.7204	0.000473

Table 0.2. Grid refinement test for $NC2.0M_{CF}$

Number of cells	Peak frame wall temperature (K)	Deviation $\left\|\frac{(\Delta T)_i - (\Delta T)_{i-1}}{(\Delta T)_i}\right\|$
224809	307.6347	----------
337025	307.6359	0.0000039
415581	306.7261	0.0029574

5.3 Results and Discussion

5.3.1 Case 1: Enhancement of the cooling system's thermal performance with the insertion of circular solid pin fin(s) in the channel(s) under different flow orientations

5.3.1.1 Reynolds number effect on the cooling system characterization with centrally located (L/2) circular solid pin fin (CSPF) under different flow orientations

5.3.1.1.1 Maximum rectangular frame wall temperature

Figure 5.2 shows the decrease in the maximum wall temperature (T_{max}) of the rectangular frame with an increase in Reynolds number *(Re*) for the cooling systems equipped with the circular

solid pin fin (CSPF) insert. A substantial reduction in the T_{max} was observed when the *Re* increased from 123.83 to 1238.3. However, beyond this point, the effect of increases in *Re* on T_{max} becomes insignificant. At the highest *Re* (2054.08) considered in this study, NC_{5CF} reduces the T_{max} by 0.054%, 0.20%, 0.86%, and 2.9% compared to the NC_{4CF}, NC_{3CF}, NC_{2CF}, and N_1, respectively. Thus, an improved T_{max} reduction is obtained with additional channels of centrally located CSPF inserts mounted on the rectangular frame of the cooling systems. Within the range of *Re* values in this study, cooling systems with a counterflow arrangement exhibited slightly lower T_{max} values than those with a parallel flow configuration. Moreover, a significant reduction in T_{max} was achieved in cooling systems with CSPF insert (Figure 5.2) compared to those without insert (Figure 4.7), demonstrating the enhanced thermal performance provided by the use of an insert.

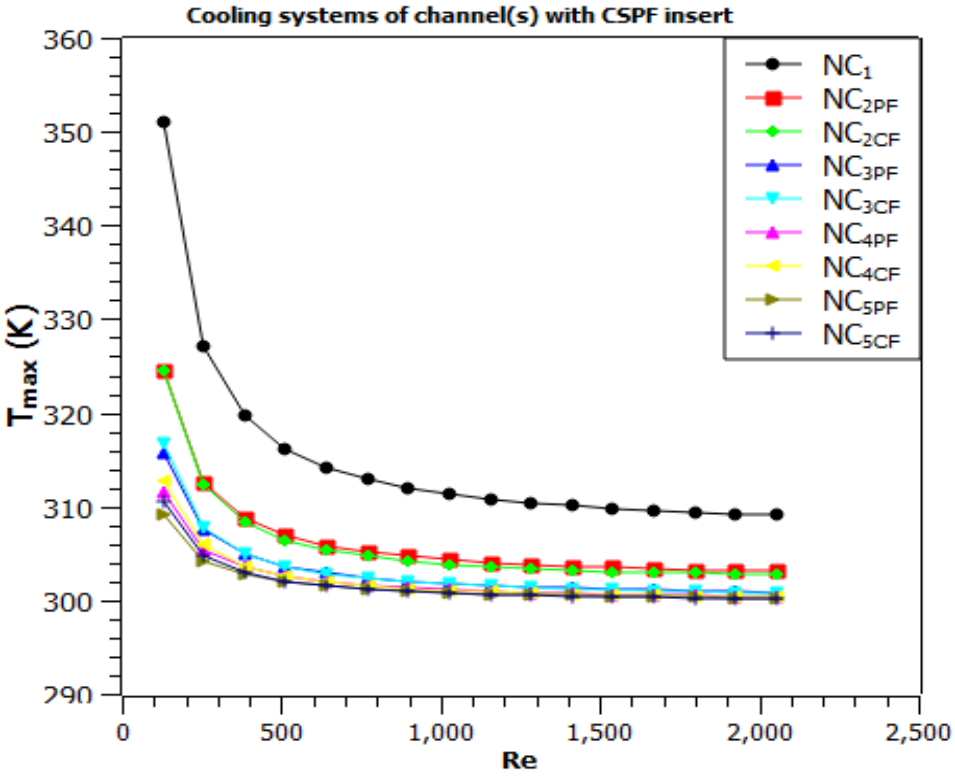

Figure 0.2. Maximum rectangular frame wall temperature (T_{max}) vs Reynolds number (*Re*) of the cooling system with a centrally located circular solid pin fin (CSPF) in the channel(s). The color markers represent the cooling system of different numbers of channel(s) with a CSPF insert mounted on the rectangular frame.

5.3.1.1.2 Dimensionless thermal resistance

From Figure 5.3, an increase in Reynolds number *(Re)* reduces the dimensionless thermal resistance *(R_{th})*. A drastic reduction of the dimensionless R_{th} was observed when the *Re* increased from 128.38 to 1283.8. At *Re* higher than 1283.8, an insignificant decrease of the dimensionless R_{th} was noticed. The figure shows that the rate of dimensionless R_{th} reduction grows with an additional channel mounted on the rectangular frame. However, counterflow cooling systems achieved a slightly dimensionless R_{th} lower than parallel flow cooling systems. The dimensionless R_{th} decreases significantly when CSPF is inserted into the cooling systems' channels, as seen by a comparison of Figures 4.8 and 5.3 indicate how the inclusion of an insert in the fluid domain augments the thermal performance of the cooling system.

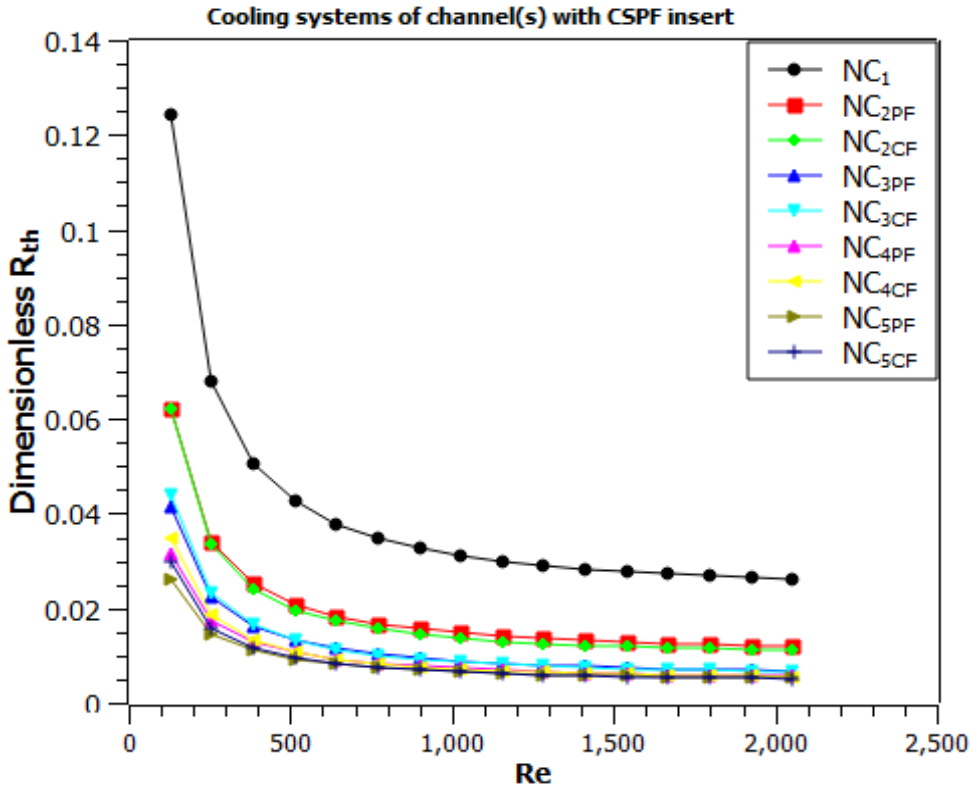

Figure 0.3. Dimensionless thermal resistance (R_{th}) vs Reynolds number (*Re*) of the cooling system with a centrally located circular solid pin fin (CSPF) in the channel(s). The color markers represent the cooling system of different numbers of channel(s) with a CSPF insert mounted on the rectangular frame.

5.3.1.1.3 Cost of pumping power

Figure 5.4 illustrates the cost of pumping power *(Pp)* versus Reynolds number *(Re)*. When the Re increased from 128.38 to 641.9, a gradual increase in the *Pp* was recorded with all cooling systems, and above this point, a further increase in *Re* yields a significant hike in the *Pp* value.

A direct relationship between the number of channels mounted on the rectangular frame of the cooling systems and *Pp* was realized. In addition, counterflow cooling systems achieve a slightly higher value of *Pp* than those with Parallel flow design. However, the effect of the CSPF in the channel(s) to outrageously raise the cost of the pumping power is recorded in this work as the cooling systems of channel(s) with CSPF insert (Figure 5.4) give a higher *Pp* value compared to those without an insert (Figure 4.9).

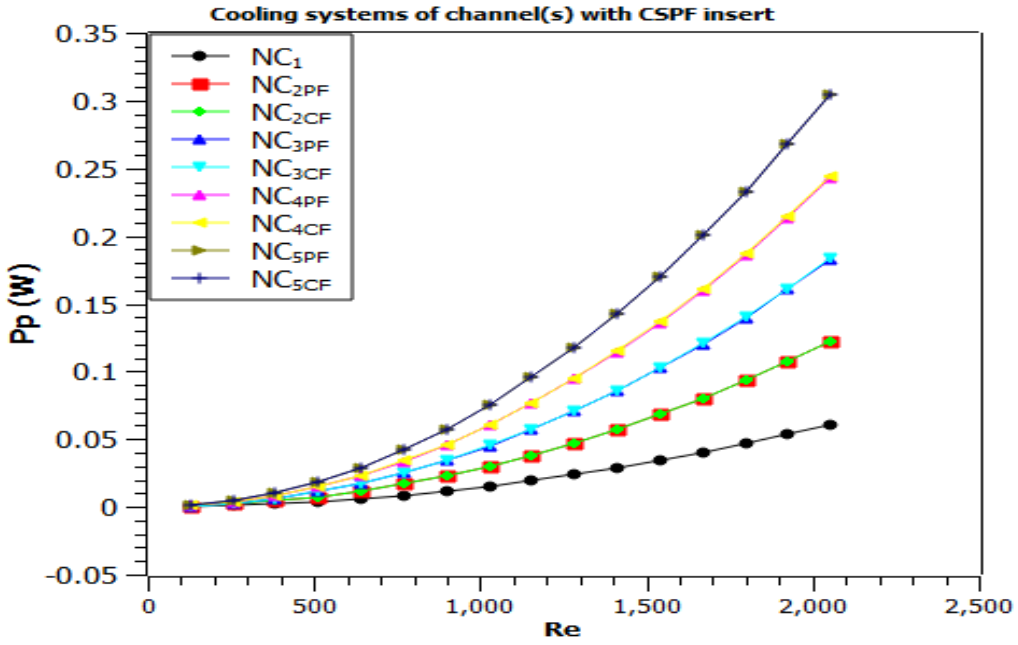

Figure 0.4. Cost of pumping power (*Pp*) vs Reynolds number (*Re*) of the cooling system with a centrally located circular solid pin fin (CSPF) in the channel(s). The color markers represent the cooling system of different numbers of channel(s) with a CSPF insert mounted on the rectangular frame.

5.3.1.2 Effect of channel number on the dimensionless heat transfer rate density for the cooling system with centrally located (L/2) circular solid pin fin (CSPF)

Figures 5.5 represent the relationship between the dimensionless heat transfer rate density and the number of channels with a centrally located circular solid pin fin (CSPF) insert, mounted on the rectangular frame of the cooling systems. An increase in the dimensionless heat transfer rate density indicates an improved system thermal performance (Equations (3,36-3.38)). The graph shows that the dimensionless heat transfer rate density increases with the Reynolds number *(Re)* regardless of the flow orientation and number of channels. Parralel flow cooling systems (Figure 5.5a) exhibit slightly lower dimensionless heat transfer rate density than

counterflow cooling systems. (Figure 5.5b). The highest dimensionless heat transfer rate density was achieved with three channels containing CSPF insert. In the parallel flow system, with three (3) channels at Re 2054.08, dimensionless heat transfer rate density increased by 19.7%, 13.3%, 10.0%, and 21.1% compared to 1, 2, 4, and 5 channels, respectively at *Re* 2054.08 (Figure 4.10a). This suggests that the best interaction between the working fluid and heat transfer surfaces occurs with three channels [198, 199]. At *Re* 2054.08 the parallel flow system with three channels and CSPF insert (Figure 5.5a) demonstrated a 93.51% increase in heat transfer rate density compared to systems without insert (Figure 4.10a). A similar enhancement of 93.82% was observed in counterflow systems, highlighting the significant role of CSPF inserts in improving the thermal performance of the cooling systems.

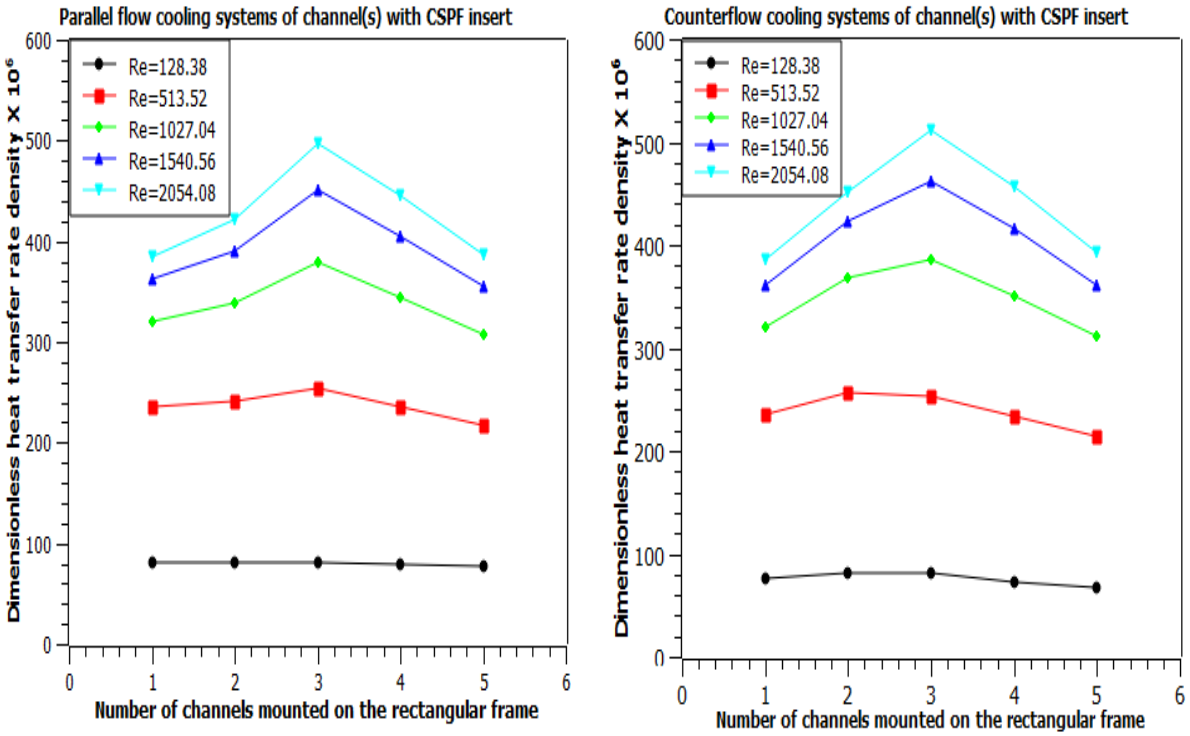

Figure 0.5. Dimensionless heat transfer rate density vs. number of channels mounted on the rectangular frame in Parallel (a) and Counterflow (b) Cooling systems with circular solid pin fin (CSPF) Inserts. Colored markers represent different Reynolds numbers (Re): Re = 128.38 (black), Re = 513.52 (red), Re = 1027.04 (green), Re = 1540.56 (blue), and Re = 2054.08**.**

5.3.1.3 Effect of varying locations of a single circular solid pin fin (CSPF) insert in the channel(s) on the cooling system's performance

The previous section demonstrates that the cooling system with three channels and a centrally located CSPF *(L/2)* yields the highest dimensionless heat transfer rate density, indicating superior thermal performance for dissipating heat from the battery pack. This section further analyzes the effect of varying the location of the CSPF inserts within the channels of this cooling system to assess how different placements may influence thermal performance and heat dissipation efficiency. This analysis explores whether alternative CSPF placements can further enhance cooling system performance beyond the best configuration identified earlier.

Figure 5.6 reflects the relationship between the dimensionless thermal resistance (R_{th}) and the Reynolds number (*Re)* of cooling systems with varying locations (*L/2*, *L/4*, and *L/8*) of a single CSPF in the channel. Regardless of the CSPF location within the channels, the dimensionless R_{th} consistently decreased with an increasing (*Re*). A notable reduction in dimensionless R_{th} was observed as *Re* increased from 128.38 to 1283.8; beyond this point, further increases in *Re* had an insignificant effect on dimensionless R_{th} reduction. Across the range of *Re* values used in this study, cooling systems with a counterflow arrangement exhibited slightly lower dimensionless R_{th} values than those with a parallel flow configuration. Specifically, at *Re* 898.66, the system with CSPF located at *L/8* (NC_{MPF}) reduced dimensionless R_{th} by 10.2% and 24.8% compared to when it was located at *L/4* (NC_{JPF}) and *L/2* (NC_{3PF}), respectively. A similar trend was observed in counterflow cooling systems, suggesting that the closer the CSPF is to the inlet, the better the cooling system's thermal performance.

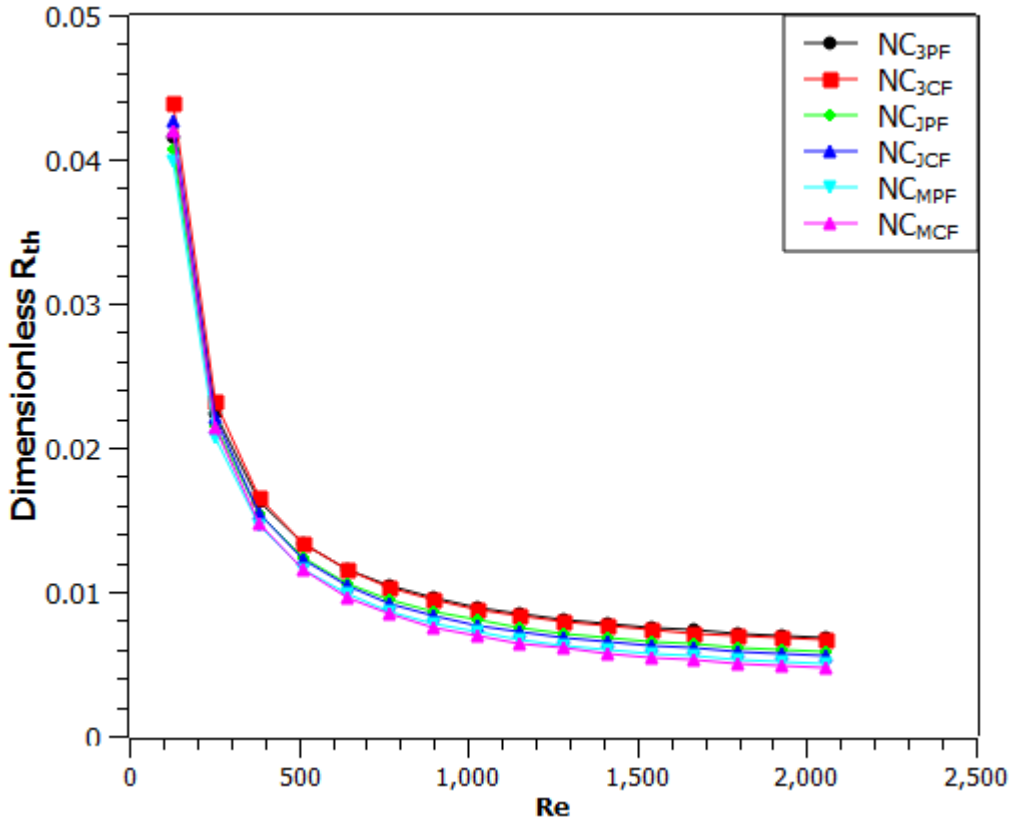

Figure 0.6. Dimensionless thermal resistance (R_{th}) vs Reynolds number (Re) of the cooling system with a single circular solid pin fin (CSPF) insert. The colored markers illustrate counterflow (CF) and parallel flow (PF) cooling systems equipped with a single CSPF located at *L/2 (NC_{3CF} and NC_{3PF}), L/4 (NC_{JCF} and NC_{JPF}),* and *L/8 (NC_{MCF} and NC_{MPF}),* in the channels

5.3.1.4 Comparison of a single and varying spacing arrangement of three circular solid pin fin (CSPF) insert(s) in the channel(s) on the cooling system's performance

The realization of the optimum thermal performance of a designed cooling system with at most 3-pin fins in the channel was earlier reported by [208] with no emphasis on the search for the best insert location in the channels. Therefore, in this study, CSPF was increased to three in the channels of NC_{MPF} and NC_{MCF} to compare the influence of multiple (three) inserts with a single insert located at the best point *(L/8)* in the channels. With the varying spacing (1.5mm, 2.0mm, and 2.5mm) of in-line arrangements, the multiple CSPFs of the exact dimensions are arranged in the channels from L/8 towards the inlet.

The dimensionless *(R_{th})* reduction with the growth in the Reynolds number *(Re)* is presented in Figure 5.7 regardless of the number and spacing arrangements of CSPF in the cooling system's channels. A substantial dimensionless R_{th} reduction was noticed when the *Re* increased from

128.38 to 1283.8, and beyond this, an insignificant effect of *Re* on dimensionless R_{th} reduction was realized. At a *Re*, 770.28, NC1.5M_{PF} reduced the dimensionless R_{th} by 1.3% and 1.8% compared to $NC2.0M_{PF}$ and $NC2.5M_{PF,}$ respectively, which implies that the minimization of space between CSPF benefits the dissipation of heat from the battery pack. Counterflow cooling systems were also observed to exhibit a similar reduction of dimensionless R_{th}. However, cooling systems with a single CSPF in the channels consistently exhibited the lowest dimensionless R_{th} values compared to those with channels of multiple multiple (three) CSPF inserts, regardless of the spacing arrangements and flow orientations. Thus, NC_{MCF} reduced dimensionless R_{th} by 16.9%, 16.1%, and 14.8% compared to $NC2.5M_{CF}$, $NC2.0M_{CF,}$ and $NC1.5M_{CF,}$ respectively, at *Re* 770.28. Meanwhile, the counterflow cooling systems achieve slightly lower dimensionless R_{th} values than those with the parallel flow cooling system, regardless of the number and spacing arrangements of the CSPF in the channel.

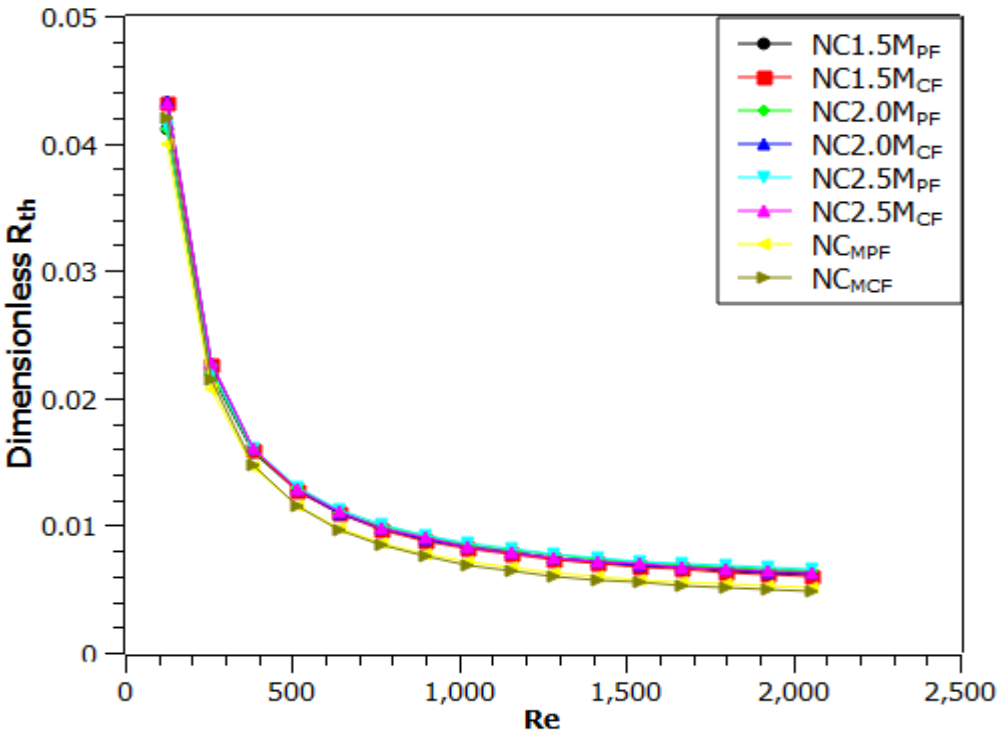

Figure 0.7. Dimensionless thermal resistance (R_{th}) vs. Reynolds number (*Re*) of cooling system with circular solid pin fin (CSPF) insert(s). The color markers illustrate counterflow (CF) and parallel flow (PF) cooling systems equipped with a single CSPF *(NC_{MCF} and NC_{MPF})*, and 1.5mm *($NC1.5M_{CF}$ and $NC1.5_{PF}$)*, 2.0mm *($NC2.0M_{CF}$ and $NC2.0M_{PF}$)*, as well as 2.5mm *($NC2.5M_{CF}$ and $NC2.5M_{PF}$)* spacing arrangements of three CSPFs in the channels.

5.3.1.5 Normalized friction factor effect between the varying location of a single and spacing arrangement of three circular solid pin fin (CSPF)

Figure 5.8a shows the normalized friction factor *(NFF)* of the cooling systems with varying locations of a single CSPF. At the same time, the same analysis was indicated in Figure 5.8b for the cooling systems with three CSPF inserts of varying spacing arrangements in the channels. With single or multiple CSPF insert(s), an increase in *NFF* was recorded with an increase in Reynolds number *(Re).* Across the range of *Re* applied in this work, counterflow cooling systems increased the values of *NFF* than parallel flow cooling systems. The realization of *NFF* values higher than 3, as shown in Figures 5.8a and 5.8b, implies the tendency of CSPF in the fluid domain to raise the working fluid friction more than 3 times compared to the cooling systems with no insert [40]. For counterflow cooling systems, the placement of a single CSPF at *L/8* (NC_{MCF}) made it possible to lower *NFF* by 0.014% compared to *L/4* (NC_{JCF}) and by 0.067% to *L/2* (NC_{3CF}) at a specified *Re* 898.66 (Figure 5.8b). The parallel flow cooling system demonstrates a similar pattern of *NFF* reduction with an insert located at *L/8* compared to *L/4* and *L/2* (Figure 5.8a). Meanwhile, an increase in *NFF* values was documented with the decrease in the space between the CSPF in the channels of the cooling systems equipped with multiple (three) inserts as indicated in Figure 5.8b [200]. For instance, at *Re* 2054.08, $NC1.5M_{PF}$ raised the *NFF* values by 0.12% and 0.35% compared to $NC2.0M_{PF}$ and $NC2.5M_{PF,}$ respectively. A similar scenario of increased *NFF* values was observed with $NC1.5M_{CF}$ over $NC2.0M_{CF}$ and $NC2.5MC_{F}$. However, regardless of the spacing arrangement of multiple CSPFs and the locations of a single CSPF(s) in the channel, a higher value of *NFF* was obtained with cooling systems equipped with three CSPFs (Figure 5.8b) compared to one (Figure 5.8a) CSPF insert(s), demonstrating the effect of fluid domain complexity on the pressure drop and consequently *NFF*.

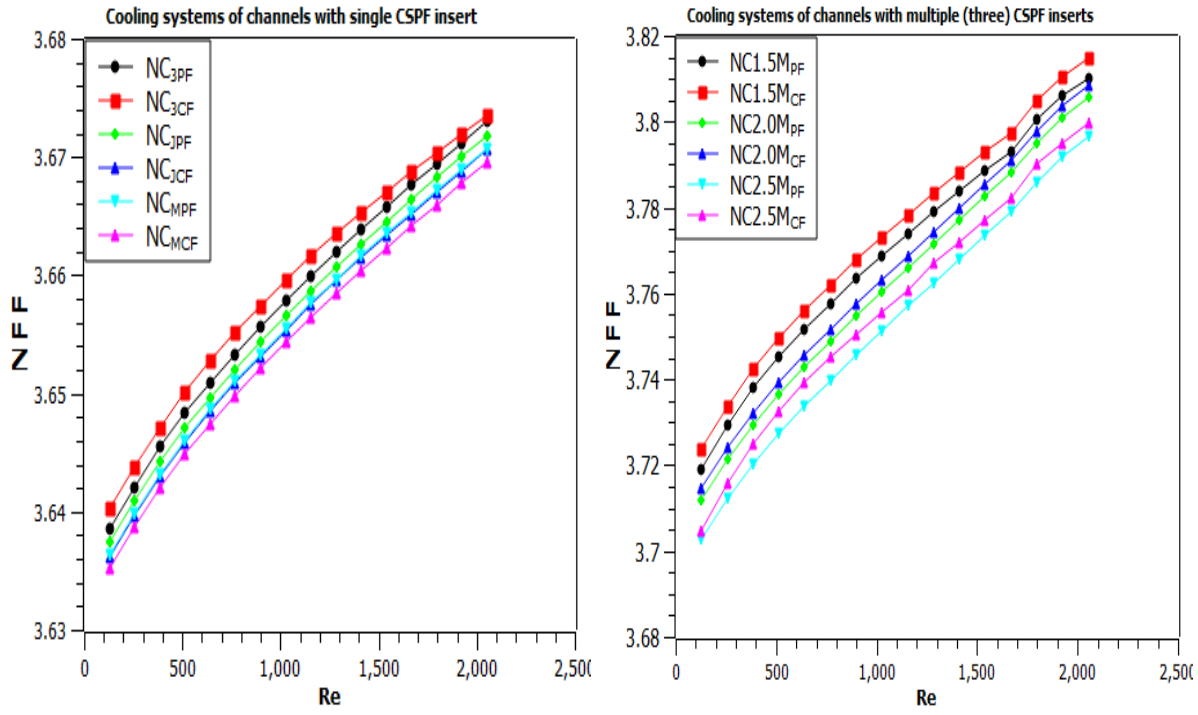

Figures 0.8. Normalized friction factor (*NFF*) vs. Reynolds number (*Re*) of the cooling system with a single (a) and three (b) circular solid pin fin (CSPF) insert(s). The color markers illustrate counterflow (CF) and parallel flow (PF) cooling systems with varying locations of a single CSPF and spacing arrangements of multiple CSPFs in the channels.

5.3.1.6 Comparison of thermal performance enhancement factor effect between the varying location of a single and varying spacing arrangement of three circular solid pin fin (CSPF)

Figure 5 .9 shows the variation of the thermal performance enhancement factor *(TPEF)* with Reynolds number *(Re)* for comparison between single and multiple CSPF insert(s) effects on the overall thermal performance of the cooling system. It can be noted from Figure 5.9 that *TPEF* increases with an increase in varying *Re*. Noticeably, the curve shows *TPEF* values greater than 1, suggesting that implementing CSPF(s) improved heat transfer at a reasonable increase in the friction factor [45]. Within the range of applied *Re* in this work, counterflow cooling systems were recorded with slightly higher *TPEF* values than the parallel flow cooling systems, regardless of the number and spacing arrangements of CSPF in the channels. Specifically, at *Re* 2054.08, $NC2.0M_{PF}$ is 4.3% better than $NC1.5M_{PF}$ and 5.4% better than $NC2.5M_{PF}$. In counterflow cooling systems, a similar improvement of system performance was realized by $NC2.0M_{CF}$ over $NC1.5M_{CF}$ and $NC2.5M_{CF}$. This shows that the frictional factor

effect is more tolerable to the augmentation of heat transfer in the channel of 2.0 mm than in 1.5 mm and 2.5 mm spacing arrangements. However, compared to the cooling system with three CSPF inserts regardless of the spacing arrangements, the cooling system with a single CSPF insert gives the highest value of *TPEF*. For instance, NC_{MCF} improves TPEF by 7.81%, 4.24%, and 8.3% compared to $NC1.5M_{CF}$, $NC2.0M_{CF,}$ and $NC2.5M_{PF,}$ respectively, at *Re* 2054.08. This implies that a single CSPF located at *L/8* in the channels can enhance the overall thermal performance of the cooling system with more than three CSPFs.

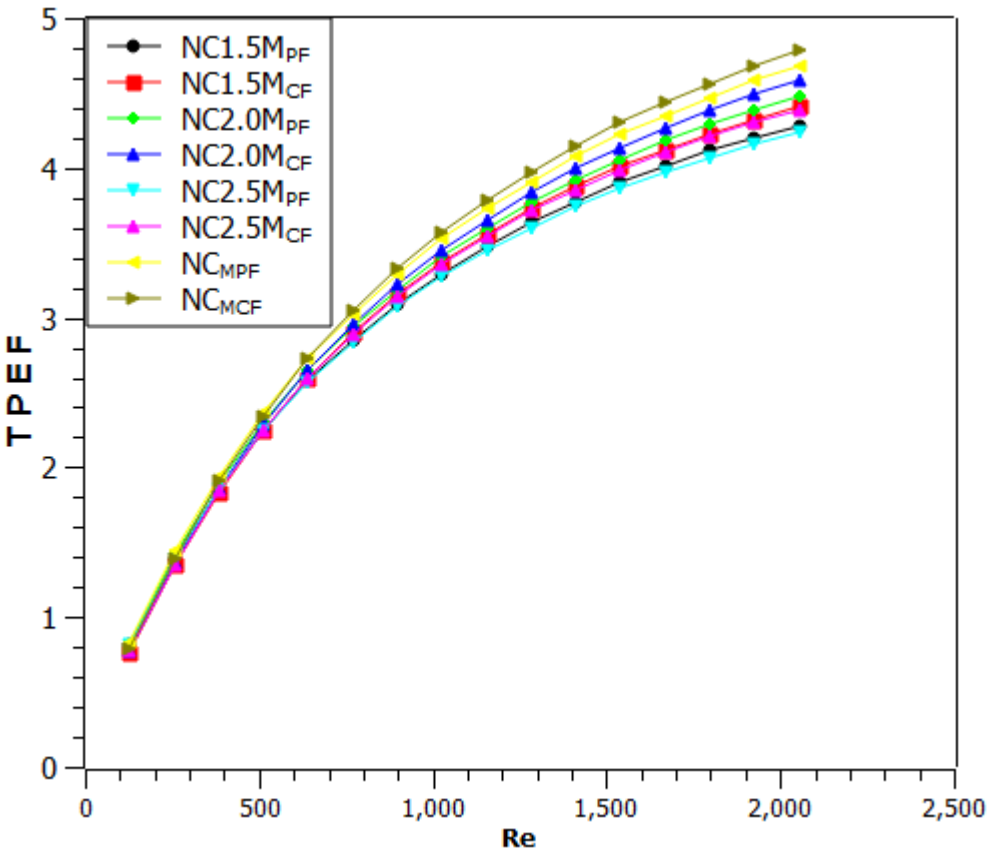

Figure 0.9. Thermal performance enhancement factor (*TPEF*) vs. Reynolds number (*Re*) of cooling system with circular solid pin fin (CSPF) insert(s). The color markers illustrate counterflow (CF) and parallel flow (PF) cooling systems equipped with a single CSPF *(NC_{MCF} and NC_{MPF}), and 1.5mm ($NC1.5M_{CF}$ and $NC1.5_{PF}$), 2.0mm ($NC2.0M_{CF}$ and $NC2.0M_{PF}$)* as well as 2.5mm *($NC2.5M_{CF}$ and $NC2.5M_{PF}$)* spacing arrangements of three CSPFs in the channels.

5.3.1.7 Temperature uniformity of the battery cells in the pack

This section disscuses the effect of the cooling system on the temperature uniformity of battery cells in the pack. As shown in Figures 5.10(a-c), increasing the Reynolds number improves

the battery cells' temperature uniformity regardless of the cooling system design. However, a temperature variation of less than 2℃ between cells was maintained within the applied *Re* number range, demonstrating the cooling system's ability to preserve temperature uniformity[13]. Lower temperature uniformity values indicate better cooling system performance. Figures 5.10(a) and (b) show that inserting a CSPF (circular solid pin fin) into the cooling system channels further lowers the temperature uniformity values compared to systems without inserts (Figures 4.11a and 4.11b). The coalescence of the curve is observed with Figures 5.10(a) and (b) compared to Figure 4.11(a) and (b) suggesting that insertion of the CSPF in the system channels can enhance the temperature uniformity of battery cells in the pack. Additionally, counterflow cooling systems (Figure 5.10b) provide slightly better temperature uniformity than the parallel flow system battery (Figure 5.10a), highlighting the influence of flow orientation on cooling system performance. Further improvement in temperature uniformity was observed when the CSPF was placed at *L/8* (Figure 5.10c) rather than at *L/2* (Figure 5.10b), indicating that the positioning of the CSPF also affects cooling system efficiency

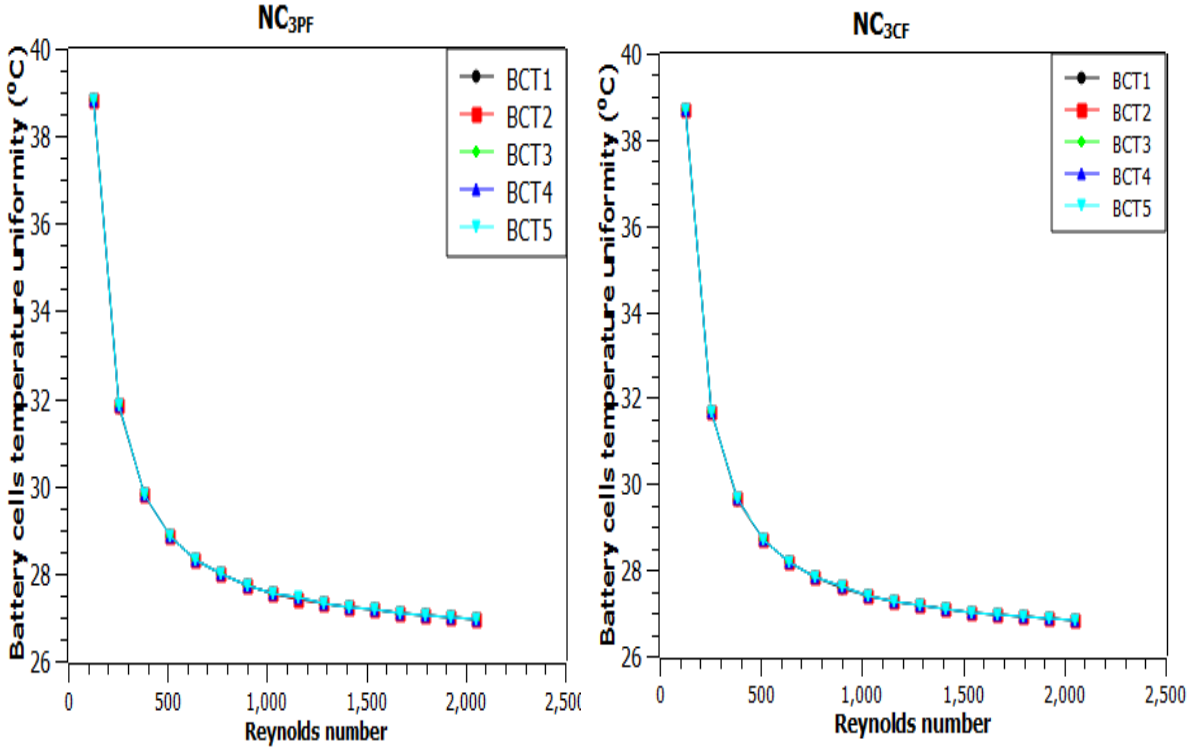

(a) (b)

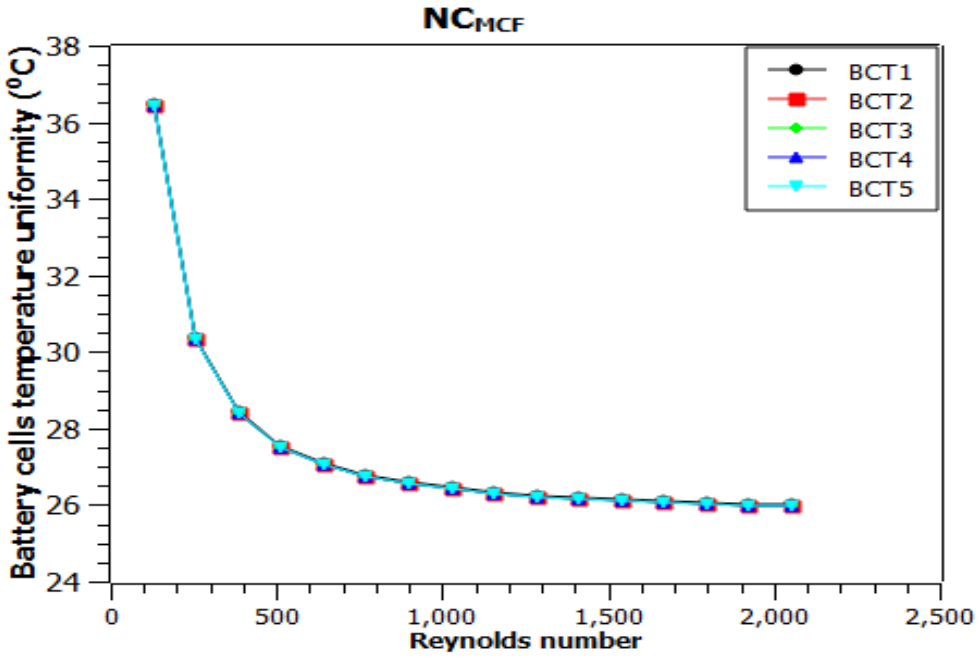

©

Figure 0.10. Battery cells temperature uniformity vs Reynolds number for cooling systems of three channels containing a single circular solid pin fin (CSPF) insert located at *L/2* (parallel flow (a) and counterflow (b) arrangement) as well as *L/8* (counterflow arrangement (c). The color makers represent the temperatures of each battery cell in a pack.

5.3.2 Case 2: Enhancement of the cooling system's performance by inserting insertion of circular aluminum foam(s) of varying porosities in the channel(s) under different flow orientations

5.3.2.1 Reynolds number effect on the cooling system characterization with centrally located (L/2) circular aluminum foam of 0.1 porosity under different flow orientations

5.3.2.1.1 Maximum rectangular frame wall temperature

Figure 5.11 reports the relationship between the maximum wall temperature (T_{max}) of the rectangular frame and the Reynolds number (Re) for the cooling systems with circular aluminum foam of 0.1 porosity $(CAF\varepsilon = 0.1)$ insert. An increase in Re reduces the T_{max}. Meanwhile, significant T_{max} reduction was realized with an increase in Re from 128.38 to 1283.8. When the Re increased beyond 1283.8, an insignificant T_{max} reduction was documented. At Re 2054.08, $NC_{5\varepsilon=0.1CF}$ respectively minimized T_{max} by 0.065%, 0.19%, 0.89%, and 2.9% compared to $NC_{4\varepsilon=0.1CF}$, $NC_{3\varepsilon=0.1CF}$, $NC_{2\varepsilon=0.1CF}$ and $NC_{1\varepsilon=0.1}$. Thus,

additional channels mounted on the rectangular frame provide a more pronounced T_{max} reduction. In addition, counterflow cooling systems were recorded with slightly lower T_{max} reduction than the parallel flow cooling systems. A significant reduction in T_{max} was demonstrated by the cooling systems of channel(s) with $CAF\varepsilon = 0.1$ insert (Figure 5.11) when compared with cooling systems of channels without insert (Figure 4.7), indicating the improved thermal performance provided by the insert.

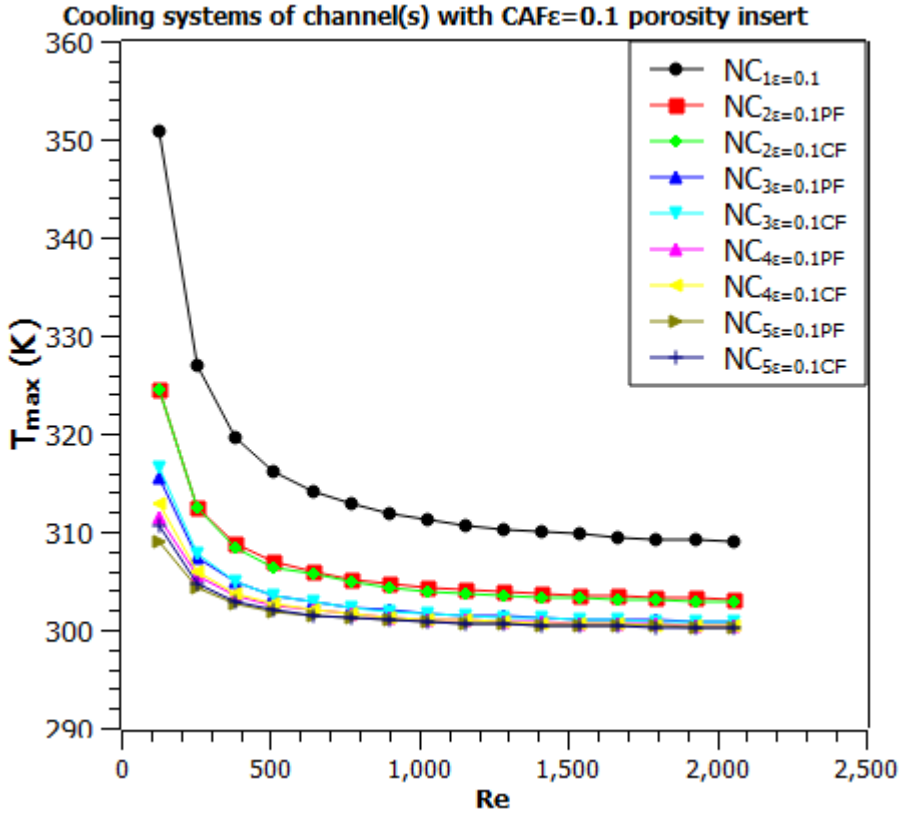

Figure 0.11. Maximum rectangular frame wall temperature (T_{max}) vs Reynolds number (*Re*) of the cooling system with a centrally located circular aluminum foam of 0.1 porosity ($CAF\varepsilon = 0.1$) insert in the channel(s). The color markers represent the cooling system of different numbers of channel(s) with a $CAF\varepsilon = 0.1$ insert mounted on the rectangular frame.

5.3.2.1.2 Dimensionless thermal resistance

Figure 5.12 shows a dimensionless thermal resistance *(R_{th})* reduction with an increase in Reynolds number *(Re).* Between *Re* 128.38 and 1283.8, a drastic drop in dimensionless R_{th} was realized regardless of the number of channels mounted on the rectangular frame, and above this, a negligible effect of *Re* on dimensionless R_{th} reduction was recorded. As indicated in the figure, the dimensionless R_{th} reduction improved with additional channels mounted on the

rectangular frame. Moreover, counterflow cooling systems achieved a slightly lower dimensionless R_{th} than parallel flow cooling systems. However, a significant reduction in dimensionless R_{th} was obtained in cooling systems with CAFε=0.1 insert (Figure 5.12) than those without insert (Figure 4.8), which implies the improved thermal performance achieved by applying the insert.

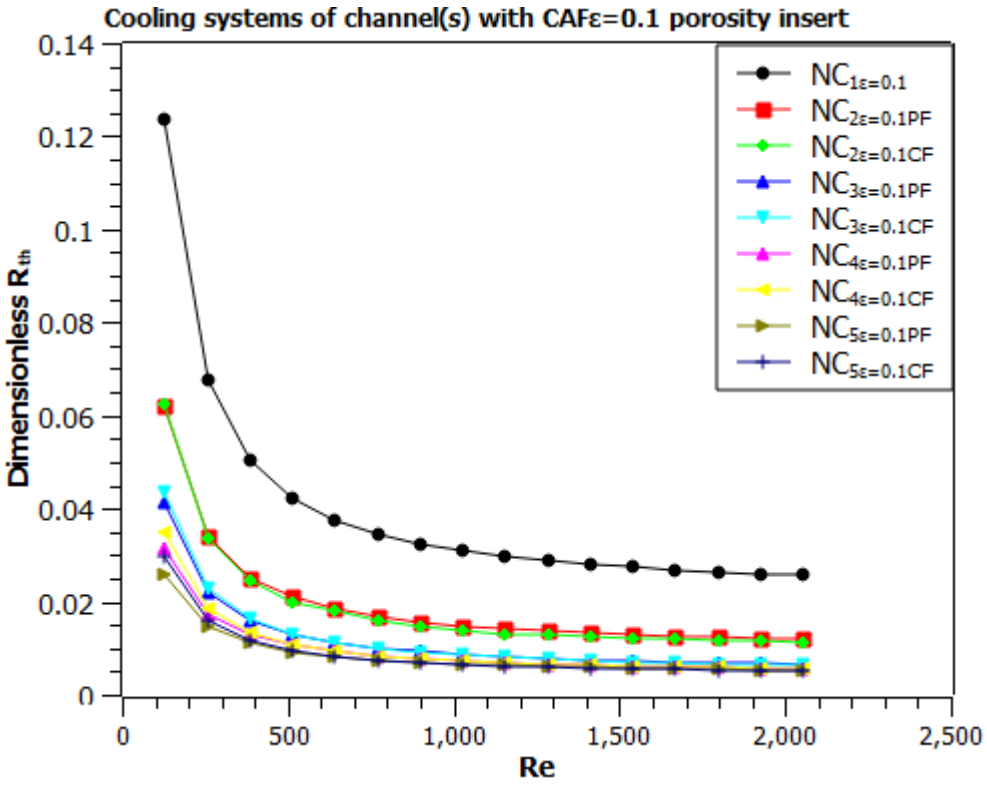

Figure 0.12. Dimensionless thermal resistance (R_{th}) vs Reynolds number (Re) of the cooling system with a centrally located circular aluminum foam of 0.1 porosity $(CAF\varepsilon = 0.1)$ insert in the channel(s). The color markers represent the cooling system of different numbers of channel(s) with a $CAF\varepsilon = 0.1$ insert mounted on the rectangular frame.

5.3.2.1.3 Cost of pumping power

Figure 5.13 shows an increase in the cost of pumping power *(Pp)* with an increase in Reynolds number *(Re),* regardless of the cooling system design. A slight rise in *Pp* was recorded when the *Re* increased from 283.83 to 641.9. However, a significant increase in *Pp* was recorded when *Re* increased beyond 898.66. As observed in this study, *Pp* increases with the number of channels mounted on the rectangular frame [197]. Meanwhile, counterflow cooling systems slightly incurred higher *Pp* values than parallel flow cooling systems. This was in agreement with the published work of [47]. The obtained results with cooling systems of channels with

the insertion of *CAFε=0.1* (Figure 5.13) demonstrate an outrageous increase in the *Pp* compared to cooling systems of channels without the insert (Figure 4.9) demonstrating the penalty of higher pressure drop incurred by the application of CAFε=0.1 insert.

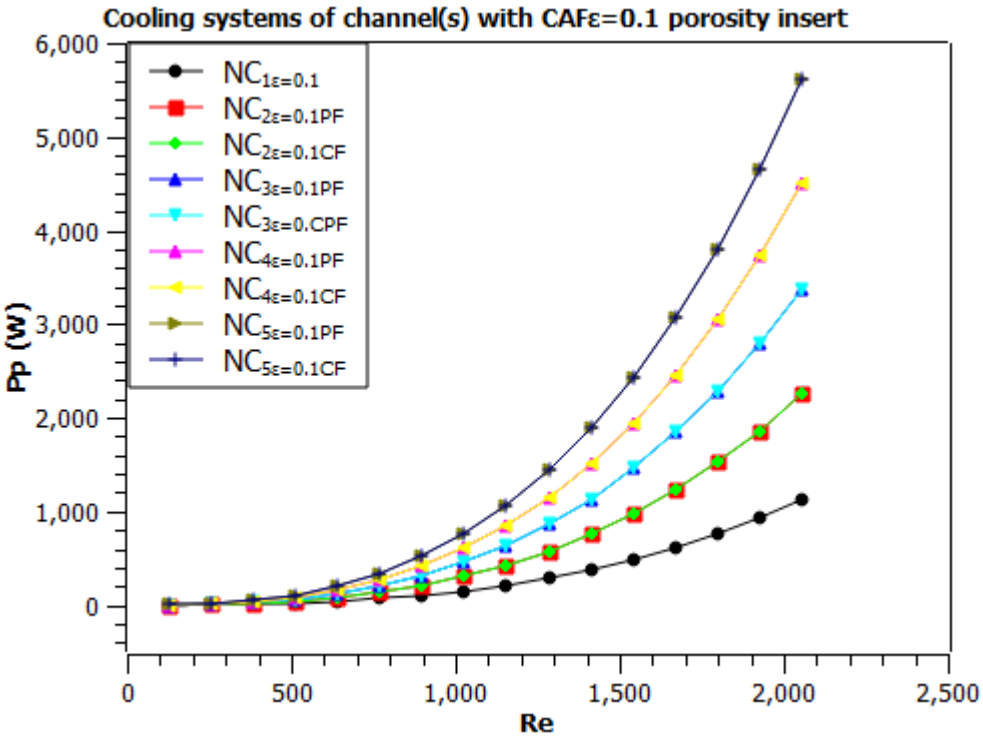

Figure 0.13. Cost of pumping power (*Pp*) vs Reynolds number (*Re*) of the cooling system with a centrally located circular aluminum foam of 0.1 porosity ($CAF\varepsilon = 0.1$) insert in the channel(s). The color markers represent the cooling system of different numbers of channel(s) with a $CAF\varepsilon = 0.1$ insert mounted on the rectangular frame.

5.3.2.2 Effect of channel number on dimensionless heat transfer rate density for the cooling systems with centrally located (L/2) circular aluminum foam of 0.1 porosity (CAFε=0.1) in the channel

Figures 5.14 reports the relationship between the dimensionless heat transfer rate density and the number of channels, with centrally located circular aluminum foam of 0.1 porosity (CAFε=0.1) inserts, mounted on the rectangular frame of a cooling system. An increased dimensionless heat transfer rate density indicates an improved system thermal performance (Equations (3.36-3.38)). Regardless of the flow orientations or number of channels, the figure shows that the dimensionless heat transfer rate increases with the Reynolds number (*Re*). Remarkably, the highest dimensionless heat transfer rate density was realized with three channels of CAFε=0.1 insert mounted on the rectangular frame. For instance, the counterflow

systems of three (3) channels achieved 27.7%, 17.5%, 15.1%, and 23.9% of increased dimensionless heat transfer rate density compared to 1, 2, 4, and 5 channels at *Re* 2054.08 (Figure 5.14b). This implies that three channels provide the best possible interaction between the working fluid and heat transfer surfaces. Meanwhile, a significant increase in the dimensionless heat transfer rate density of 93.94% (parallel flow) and 94.1% (counterflow) was obtained when CAFε=0.1 was inserted in the cooling systems of three channels mounted on the rectangular frame (Figures 5.18(a) and (b)) compared to the same configuration of no insert (Figures 4.10(a and (b)). The results demonstrate the cooling systems' thermal performance enhancement provided by the applications of CAFε=0.1. However, regardless of the cooling system design, the parallel flow cooling system (Figure 5.14a) shows a slightly lower dimensionless heat transfer rate density than the counterflow cooling systems (Figure 5.14b).

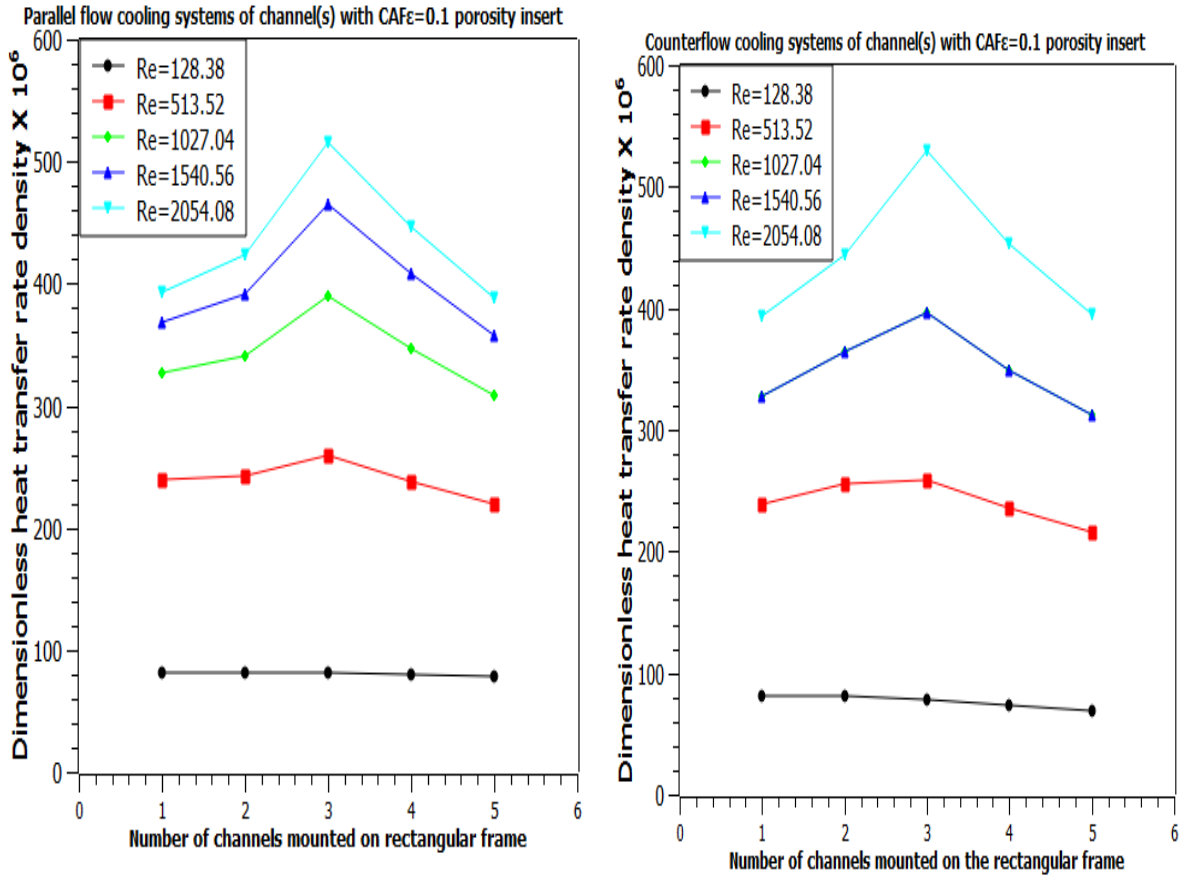

(a) (b)

Figure 0.14. Dimensionless heat transfer rate density vs. number of channels mounted on the rectangular frame in Parallel (a) and Counterflow (b) Cooling systems with circular aluminum foam of 0.1 porosity (CAFε=0.1) Inserts. Colored markers represent different Reynolds

numbers (Re): Re = 128.38 (black), Re = 513.52 (red), Re = 1027.04 (green), Re = 1540.56 (blue), and Re = 2054.08

5.3.2.3 Effects of the varying porosities of centrally located (L/2) circular aluminum foam in the channels on the thermal performance enhancement of the cooling system

According to the above results, it can be concluded that the highest thermal performance is achieved when three channels with circular aluminum foam of (low) 0.1 porosity insert (CAFε=0.1) are mounted on the rectangular frame of the cooling system. Further analysis to investigate the effect of varying porosities of circular aluminum foam of (medium) 0.5 porosity insert (CAFε=0.5) and circular aluminum foam of (high) 0.9 porosity insert (CAFε=0.9) on the performance of this cooling system is carried out in this section.

5.3.2.3.1 Dimensionless thermal resistance

As shown in Figure 5.15, an increase in Reynolds number (*Re*) leads to a decrease in the dimensionless thermal resistance (R_{th}), regardless of the porosity of the circular aluminum foam insert. A significant reduction in dimensionless R_{th} was observed when *Re* increased from 128.38 to 1283.8, with minimal impact on dimensionless R_{th} beyond this point. Specifically, at *Re* 1155.42, the cooling system with low porosity circular aluminum foam ($NC_{3\varepsilon=0.1CF}$) reduced dimensionless R_{th} values by 4.8% and 21.4% compared to the medium ($NC_{3\varepsilon=0.5CF}$) and high ($NC_{3\varepsilon=0.9CF}$) porosity inserts, respectively. This indicates that lower porosity circular aluminum foam inserts enhance the cooling system's ability to dissipate heat generated by the battery pack in an electric vehicle [201]. A similar reduction in dimensionless R_{th} was observed in the cooling system with the counterflow arrangement. However, regardless of the porosity of the circular aluminum foam insert, systems with a counterflow arrangement consistently achieved slightly lower dimensionless R_{th} values than those with a parallel flow arrangement.

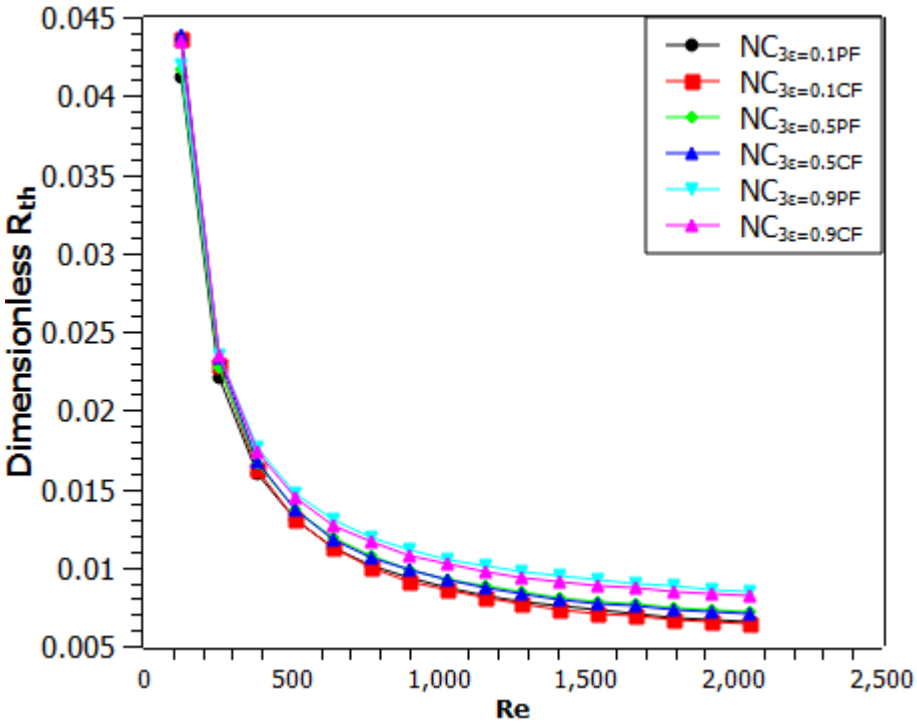

Figure 0.15. Dimensionless thermal resistance (R_{th}) vs Reynolds number (*Re*) of the cooling system with circular aluminum foam of varying porosities insert. The color markers illustrate counterflow (CF) and parallel flow (PF) cooling systems equipped with a single aluminum foam of 0.1 porosity ($NC_{3\varepsilon=0.1CF}$ and $NC_{3\varepsilon=0.1PF}$), 0.5 porosity ($NC_{3\varepsilon=0.5CF}$ and $NC_{3\varepsilon=0.5PF}$) as well as 0.9 porosity ($NC_{3\varepsilon=0.9CF}$ and $NC_{3\varepsilon=0.9PF}$)

5.3.2.3.2 Cost of pumping power

Figure 5.16 compares the cost of pumping power *(Pp)* for cooling systems inserted with different porosities of circular aluminum foam. An increase in *Pp* was recorded with an increase in Reynolds number *(Re)*, regardless of the porosity of the circular aluminum foam. However, an outrageous upward trend of *Pp* was observed when the cooling system was inserted with *CAFε=0.1*($NC_{3\varepsilon=0.1CF}$) compared to CAFε=0.5 ($NC_{3\varepsilon=0.5CF}$) and *CAFε=0.9* ($NC_{3\varepsilon=0.9CF}$). A similar pattern was observed with parallel flow cooling systems. Meanwhile, the lowest *PP* values occurred when CAFε=0.9 was inserted into the channels of the cooling systems. This shows that the resistance to the fluid flow (pressure drop) rises with the decrease in porosity [44]. Moreover, parallel flow cooling systems have slightly lower *Pp* values than counterflow cooling systems.

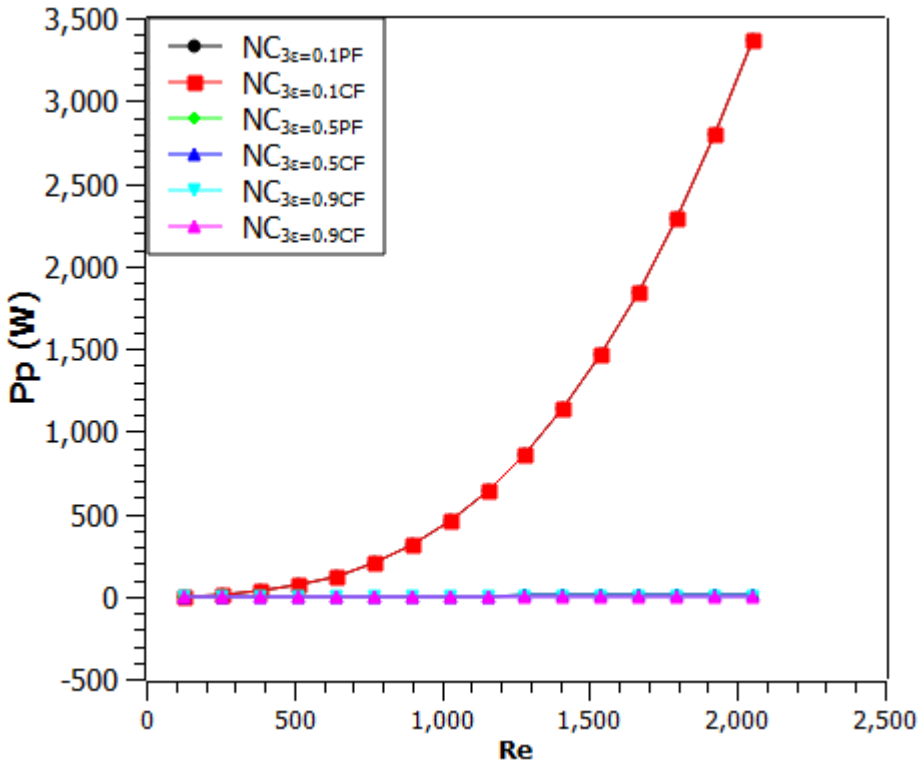

Figure 0.16. Cost of pumping power (*Pp*) vs Reynolds number (*Re*) of the cooling system with circular aluminum foam of varying porosities insert. The color markers illustrate counterflow (CF) and parallel flow (PF) cooling systems equipped with a single aluminum foam of 0.1 porosity ($NC_{3\varepsilon=0.1CF}$ *and* $NC_{3\varepsilon=0.1PF}$), 0.5 *porosity* ($NC_{3\varepsilon=0.5CF}$ and $NC_{3\varepsilon=0.5PF}$) as well as 0.9 porosity *(*$NC_{3\varepsilon=0.9CF}$ *and* $NC_{3\varepsilon=0.9PF}$*).*

5.3.2.3.3 Thermal performance enhancement factor

From Figure 5.17, an increase in the thermal performance enhancement factor *(TPEF)* with an increase in Reynolds number *(Re)*, regardless of the porosity of circular aluminum foams, was illustrated. Meanwhile, a direct relationship between the porosity and *TPEF* was realized. For instance, $NC_{3\varepsilon=0.9PF}$ respectively offer an increment of 82.7% and 93.1% *TPEF* over $NC_{3\varepsilon=0.5PF}$ and $NC_{3\varepsilon=0.9PF}$ precisely at *Re* 1155.42. This result suggests that the pressure drop influence is more tolerable to the augmentation of heat transfer in the channel inserted with circular aluminum foam of high *(CAFε=0.9)* than medium *(CAFε=0.5)* and low *(CAFε=0.1)* porosity. This was further substantiated by the cooling system of *CAFε=0.5 and CAFε=0.1* insert demonstrating *TPEF* values less than 1 as indicated in the figure. Hence, the implementation of *CAFε=0.*5 and *CAFε=0.1* for enhancing the cooling system thermal performance should be discouraged. In addition, the figure shows a slight increase in *TPEF* by the counterflow cooling systems over the parallel flow cooling systems regardless of the

porosity of circular aluminum foam, highlighting the influence of flow orientation on the system performance.

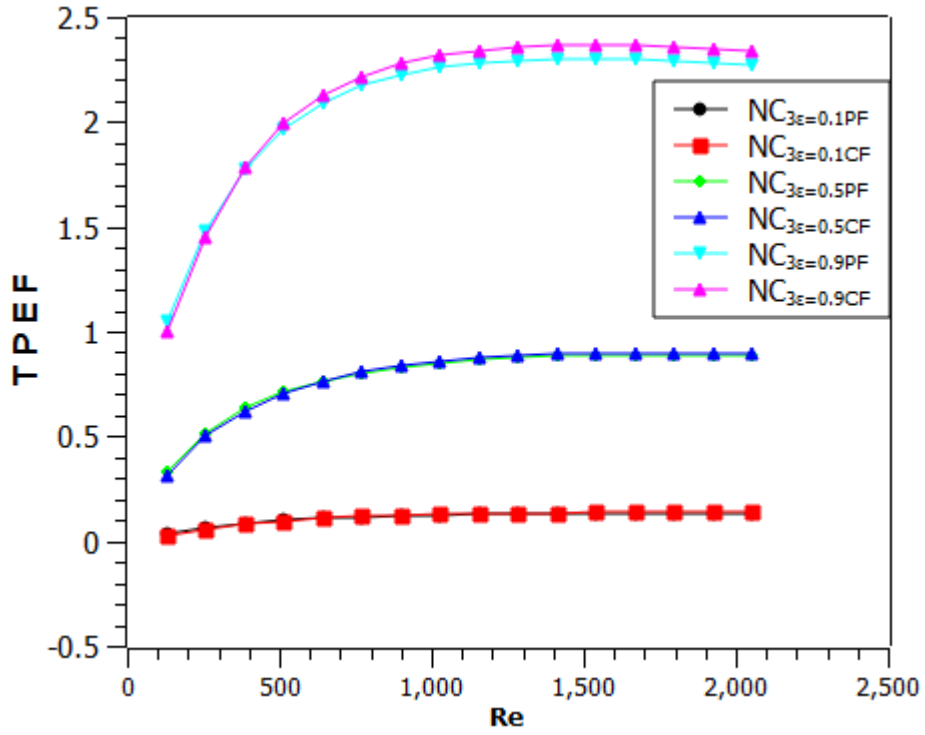

Figure 0.17. Thermal performance enhancement factor (*TPEF*) vs Reynolds number (*Re*) of the cooling system with circular aluminum foam of varying porosities insert. The color markers illustrate counterflow (CF) and parallel flow (PF) cooling systems equipped with a single aluminum foam of 0.1 porosity ($NC_{3\varepsilon=0.1CF}$ and $NC_{3\varepsilon=0.1PF}$), 0.5 porosity ($NC_{3\varepsilon=0.5CF}$ and $NC_{3\varepsilon=0.5PF}$) as well as 0.9 porosity ($NC_{3\varepsilon=0.9CF}$ and $NC_{3\varepsilon=0.9PF}$)

5.3.2.4 Effect of varying locations of a single circular aluminum foam of 0.9 porosity (CAFε=0.9) inserted in the channel(s) of the cooling system

The preceding section illustrates that a cooling system with three channels and a centrally located *CAFε=0.9* (at *L/2)* gives the highest dimensionless heat transfer rate density, demonstrating superior thermal performance for dissipating heat from the battery pack. This section further analyses the effect of alternative locations of *CAFε=0.9* within the cooling system's channels was further analyzed in this section to determine how different locations may influence thermal performance and heat dissipation effectiveness. This analysis explores

whether CAFε=0.9 alternative placements can further enhance cooling system performance beyond the best configuration identified earlier.

Figure 5.18 demonstrates the reduction of dimensionless thermal resistance *(R_{th})* with an increase in Reynolds number *(Re)* regardless of the point of placement of circular aluminum foam of 0.9 porosity (CAFε=0.9) in the cooling system's channels. A substantial decrease in dimensionless R_{th} was realized when the *Re* increased from 128.38 to 1283.8, and greater than this, a negligible effect of *Re* on dimensionless R_{th} was obtained. Meanwhile, a slight overperformance of counterflow cooling systems compared to the parallel flow cooling systems was observed regardless of the point of placement of *CAFε=0.9* in the channels. The result shows that the cooling system with *CAFε=0.9* located at L/8 ($NC_{M\varepsilon=0.9CF}$) further minimized the dimensionless R_{th} by 9.04% and 14.03% respectively at *Re* 1412.18 compared to the cooling system with CAFε=0.9 located at *L/4* ($NC_{J\varepsilon=0.9CF}$) and cooling system with *CAFε=0.9* located at *L/2* ($NC_{3\varepsilon=0.9CF}$). A similar performance was recorded with parallel flow cooling systems. Thus, the highest performance of the cooling systems is obtained with the placement of *CAFε=0.9* at *L/8* in the cooling system's channels.

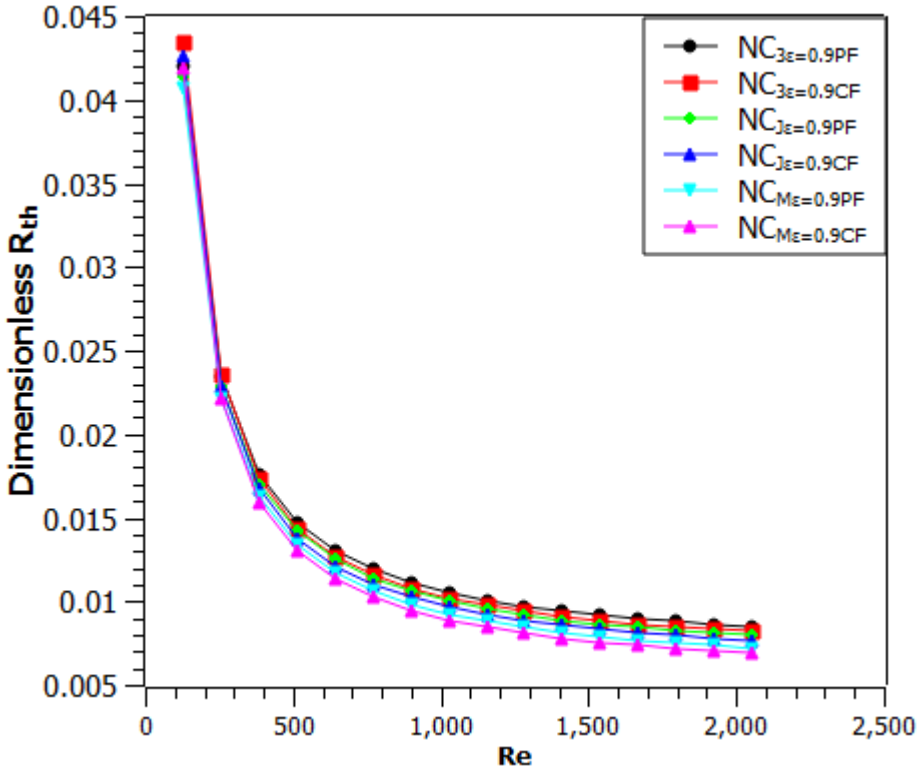

Figure 0.18. Dimensionless thermal resistance (R_{th}) vs Reynolds number (*Re*) of the cooling system with a single circular aluminum foam of 0.9 (CAFε=0.9) porosity insert. The colored markers illustrate counterflow (CF) and parallel flow (PF) cooling systems equipped with a

single CAFε=0.9 located at *L/2* ($NC_{3\varepsilon=0.9CF}$ and $NC_{3\varepsilon=0.9PF}$), ($NC_{J\varepsilon=0.9CF}$ and $NC_{J\varepsilon=0.9PF}$), and L/8 ($NC_{M\varepsilon=0.9CF}$ and $NC_{M\varepsilon=0.9PF}$).

5.3.2.5 Comparison of a single and varying spacing arrangement of three circular aluminum foam of high porosity (CAFε=0.9)

The CAFε=0.9 was increased to three from the best location of insert towards the inlet *(L/8),* to compare the influence of a single with multiple inserts in the channel(s) on the cooling systems' thermal performance enhancement. It is worth noting that [208] has earlier reported the precision of three-pin fin inserts for the optimal performance of the cooling configuration with no emphasis on the search for the best insert location in the channels. Hence, the reason for adopting three *CAFε=0.9* of varying in-line spacing arrangements (1.5 mm, 2.0 mm, and 2.5 mm) for comparison with a single *CAFε=0.9.*

Figure. 5.19, illustrates dimensionless thermal resistance *(R_{th})* reduction with an increase in Reynolds number *(Re)* regardless of the number of *CAFε=0.9* in the channels of the cooling systems. A significant reduction in dimensionless R_{th} was obtained when the *Re* increased from 128.38 to 1283.8. At a *Re* higher than 1283.8, an insignificant reduction in dimensionless R_{th} was documented. Counterflow cooling systems demonstrate slightly lower dimensionless R_{th} than parallel flow cooling systems. At *Re* 898.66, $NC1.5M_{\varepsilon=0.9PF}$ achieves the dimensionless R_{th} of 5.4% and 9.2% lower than $NC2.0M_{\varepsilon=0.9PF}$ and $NC2.5M_{\varepsilon=0.9PF}$ which implies that a shorter distance between the *CAFε=0.9* improves the cooling capacity of the cooling systems better than a larger distance between the *CAFε=0.9.* Nevertheless, regardless of the spacing arrangements, a single *CAFε=0.9* in the channels shows better cooling system enhancement than multiple (three) *CAFε=0.9.* For instance, $NC_{M\varepsilon=0.9CF}$ reduced the dimensionless R_{th} by 30.7%, 26.2%,, and 18.6% respectively compared to the $NC2.5M_{\varepsilon=0.9PF}$, $NC2.0M_{\varepsilon=0.9PF}$, and $NC1.5M_{\varepsilon=0.9PF}$ precisely at *Re* 2054.08. A similar pattern of the dimensionless Rth reduction was observed with counterflow cooling systems.

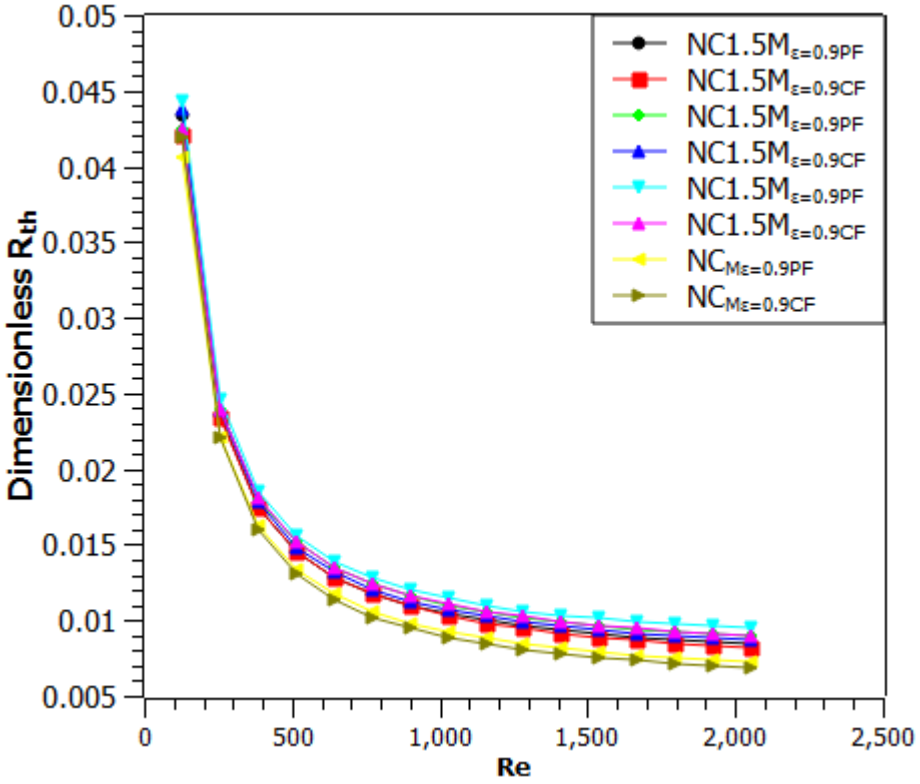

Figure 0.19. Dimensionless thermal resistance (R_{th}) vs. Reynolds number (*Re*) of the cooling system with circular aluminum foam of 0.9 (CAFε=0.9) porosity insert(s). The color markers illustrate counterflow (CF) and parallel flow (PF) cooling systems equipped with a single CAFε=0.9 ($NC_{M\varepsilon=0.9CF}$ and $NC_{M\varepsilon=0.9PF}$), and 1.5 mm ($NC1.5M_{\varepsilon=0.9CF}$ and $NC1.5M_{\varepsilon=0.9PF}$), 2.0 mm ($NC2.0M_{\varepsilon=0.9CF}$ and $NC2.0M_{\varepsilon=0.9PF}$), and 2.5 mm ($NC2.5M_{\varepsilon=0.9CF}$ and $NC2.5M_{\varepsilon=0.9PF}$) spacing arrangements of three CAFε=0.9 in the channels.

5.3.2.6 Normalized friction factor effect between the varying location of a single and spacing arrangement of three circular aluminum foam of 0.9 porosity (CAFε=0.9)

The direct relationship between the normalized friction factor *(NFF)* and the Reynolds number *(Re)* for the cooling system is illustrated in Figures 5.20. The influence of varying locations of CAFε=0.9 on the normalized friction factor was indicated in Figure 5.20a., while Figure 5.20b expressed the effect of different spacing of CAFε=0.9. As shown in Figures 5.20 (a) and (b) counterflow cooling systems provide higher values of *NFF* than parallel flow cooling systems regardless of the system design. It can be observed that both cases exhibited *NFF* greater than 2.5, indicating that the presence of CAFε=0.9 in the fluid domain can raise the working fluid friction more than 2.5 times compared to the cooling systems of channels with no insert. A similar observation was reported by Mohit and Gupta [40]. For counterflow cooling systems,

the placement of a single CAFε=0.9 at L/8 ($NC_{M\varepsilon=0.9CF}$) made it possible to reduce the *NFF* by 2.4% compared to *L/4* ($NC_{J\varepsilon=0.9CF}$) and by 4.5% to *L/2* ($NC_{3\varepsilon=0.9CF}$) at *Re* 898.66 (Figure 5.20a). The parallel flow cooling system exhibited a similar effect. Regardless of the flow orientation, 1.5mm and 2.5mm of CAFε=0.9 spacing arrangements, respectively, demonstrate the highest and lowest *NFF* values as indicated in Figure 5.20b. For instance, $NC2.5M_{\varepsilon=0.9CF}$ reduces the *NFF* values by 8.14% and 13.2% compared to $NC2.0M_{\varepsilon=0.9CF}$ and $NC1.5M_{\varepsilon=0.CPF}$ respectively at *Re* 2054.08. Parallel flow cooling systems exhibited a similar pattern. Thus, a cooling system with the shortest spacing arrangement between the CAFε=0.9 offers the highest *NFF* values and vice versa [200]. However, it was observed that the cooling system equipped with three CAFε=0.9, regardless of spacing arrangements, has the larger *NFF* which shows that the more the complexity of the fluid domain the more the normalized friction values.

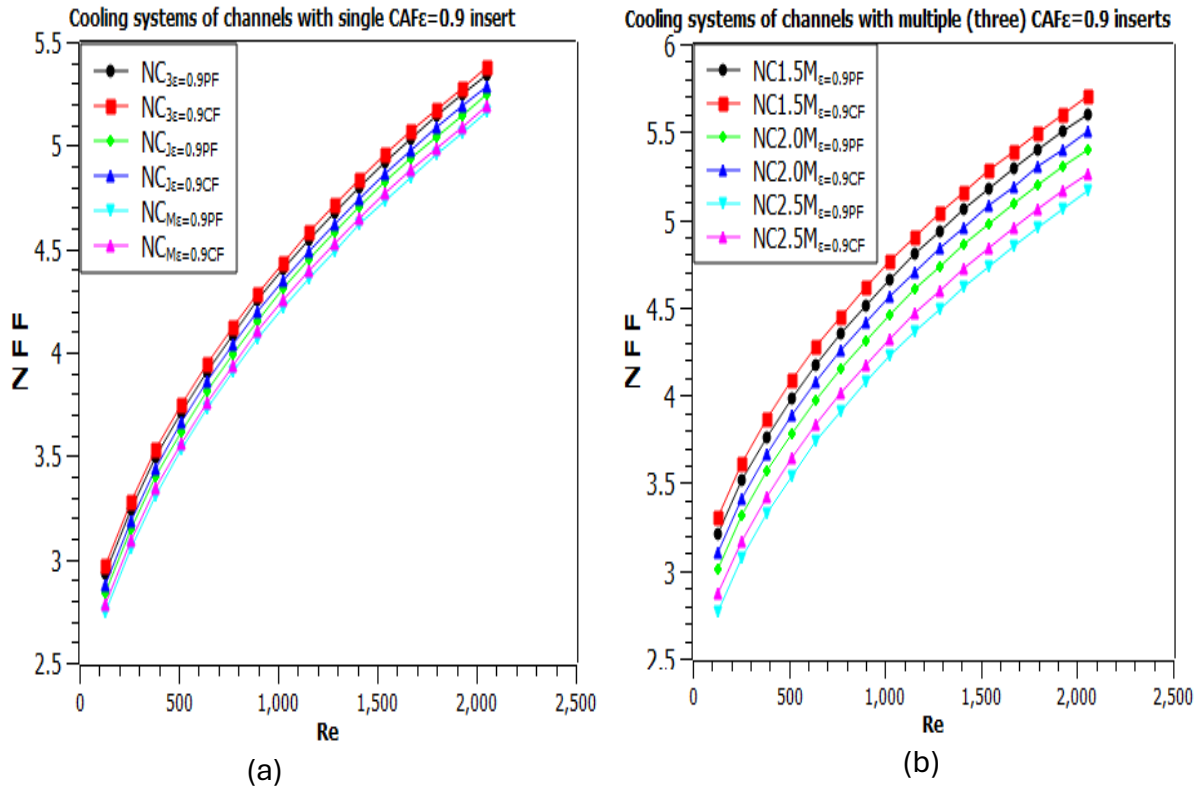

Figure 0.20. Normalized friction factor (*NFF*) vs. Reynolds number (*Re*) of the cooling system with a single (a) and three (b) circular aluminum foam of 0.9 (CAFε=0.9) porosity insert(s). The color markers illustrate counterflow (CF) and parallel flow (PF) cooling systems equipped with varying locations of a single and spacing arrangement of multiple CAFε=0.9 in the channels.

5.3.2.7 Comparison of thermal performance enhancement factor effect between the varying location of a single and the varying spacing arrangement of three circular aluminum foam of 0.9 porosity (CAFε=0.9)

As shown in Figure 5.21, an increase in Reynolds number *(Re)* increases the thermal performance enhancement factor *(TPEF)* regardless of the cooling system design. The figure shows a significant increase in *TPEF* when the *Re* increased from 128.38 to 898.66. However, a negligible increase in *TPEF* was noticed when the *Re* further increased beyond 898.66. Regardless of the number or spacing arrangements of the *CAFε=0.9* in the channels, counterflow cooling systems yield higher values of *TPEF* than parallel flow cooling systems. The graph demonstrates *TPEF* values greater than 1, implying that implementation of CAFε=0.9 in the fluid domain can augment heat transfer with a tolerably increased friction factor [45]. At *Re* 898.66, the system with 2.0 mm spacing arrangement ($NC2.0M_{\varepsilon=0.9CF}$) achieves 0.97% and 3.94% improved thermal performance than the system with a 1.5 mm spacing arrangement ($NC1.5M_{\varepsilon=0.9CF}$) and system with a 2.5 mm spacing arrangement ($NC2.5M_{\varepsilon=0.9CF}$) respectively. This implies that the frictional factor effect is more tolerable to the enhancement of heat transfer in the channel of 2.0 mm than in 1.5 mm and 2.5 mm spacing arrangements. However, the cooling system with a single CAFε=0.9 gave the maximum value of *TPEF* compared to the cooling system with multiple (three) CAFε=0.9 inserts, regardless of the spacing arrangements. Thus, $NC_{M\varepsilon=0.9CF}$ improves *TPEF* by 2.32%, 1.70%, and 6.07% compared to $NC1.5M_{\varepsilon=0.9CF}$, $NC2.0M_{\varepsilon=0.9CF}$ and $NC2.5M_{\varepsilon=0.9CF}$ respectively at *Re* 2054.08. This shows that a single *CAFε=0.9* located at *L/8* in the channels can augment the overall thermal performance of the cooling system better than three *CAFε=0.9* inserts. Therefore, considering the enhancement of the cooling system with the circular aluminum foam insert for the thermal management of the cylindrical lithium-ion battery $NC_{M\varepsilon=0.9CF}$ seems to be the most promising.

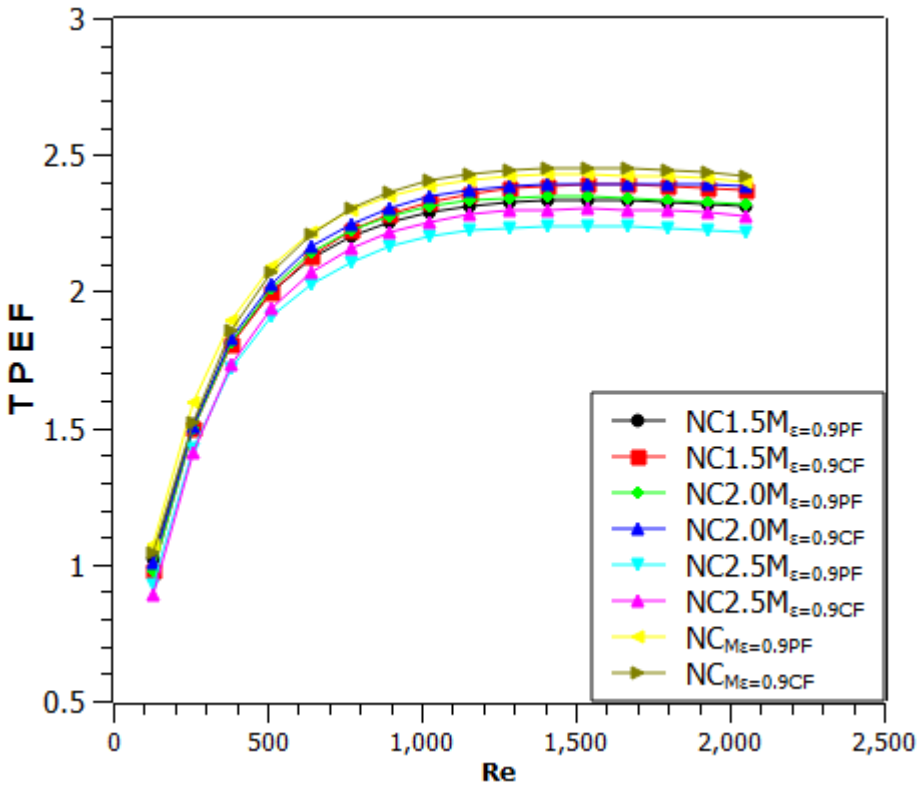

Figure 0.21. Thermal performance enhancement factor (*TPEF*) vs. Reynolds number (*Re*) of the cooling system with circular aluminum foam of 0.9 *(CAFε=0.9)* porosity insert(s). The color markers illustrate counterflow (CF) and parallel flow (PF) cooling systems equipped with a single CAFε=0.9 ($NC_{M\varepsilon=0.9CF}$ and $NC_{M\varepsilon=0.9PF}$), and 1.5 mm ($NC1.5M_{\varepsilon=0.9CF}$ and $NC1.5M_{\varepsilon=0.9PF}$), 2.0 mm ($NC2.0M_{\varepsilon=0.9CF}$ and $NC2.0M_{\varepsilon=0.9PF}$), and 2.5 mm ($NC2.5M_{\varepsilon=0.9CF}$ and $NC2.5M_{\varepsilon=0.9PF}$) spacing arrangements of three *CAFε=0.9* in the channels.

5.3.2.8 Temperature uniformity of the battery cells in the pack

Figures 5.22(a-d) displayed an inverse relationship between the temperature uniformity of the battery cells in a pack and the Reynolds number. The results show a variation of less than 2℃ of temperature from one battery cell to the other in the pack, reflecting the system's potential to manage the battery cells' temperature uniformity challenges [13]. A lower value of the battery cells' temperature uniformity shows an improved cooling system performance. The significance of circular aluminum foam in the fluid domain to improve system performance is noted as the system with low ($NC_{3\varepsilon=0.1PF}$) and high ($NC_{3\varepsilon=0.9CF}$) porosities insert (Figures 5.22 a and b) reflects lower values of battery cells' temperature uniformity as well as coalescence of graph compared to N_{3PF} and N_{3CF} (Figures 4.11a and b). In addition, a cooling system with counterflow arrangements (Figure 5.22b) gives the best result in minimizing the

battery cells' temperature uniformity compared to those with parallel flow arrangements (Figure 5.22a). However, Figure 5.22c with higher values of battery cells' temperature compared to Figure2.22b indicates the influence of porosity on the system's capacity to dissipate heat from the battery pack. Further enhancement in temperature uniformity was observed when the CAFε=0.9 was located at *L/8* (Figure 5.22d) rather than at *L/2* (Figure 5.11c), indicating that the location of the CAFε=0.9 also influenced the cooling system performance.

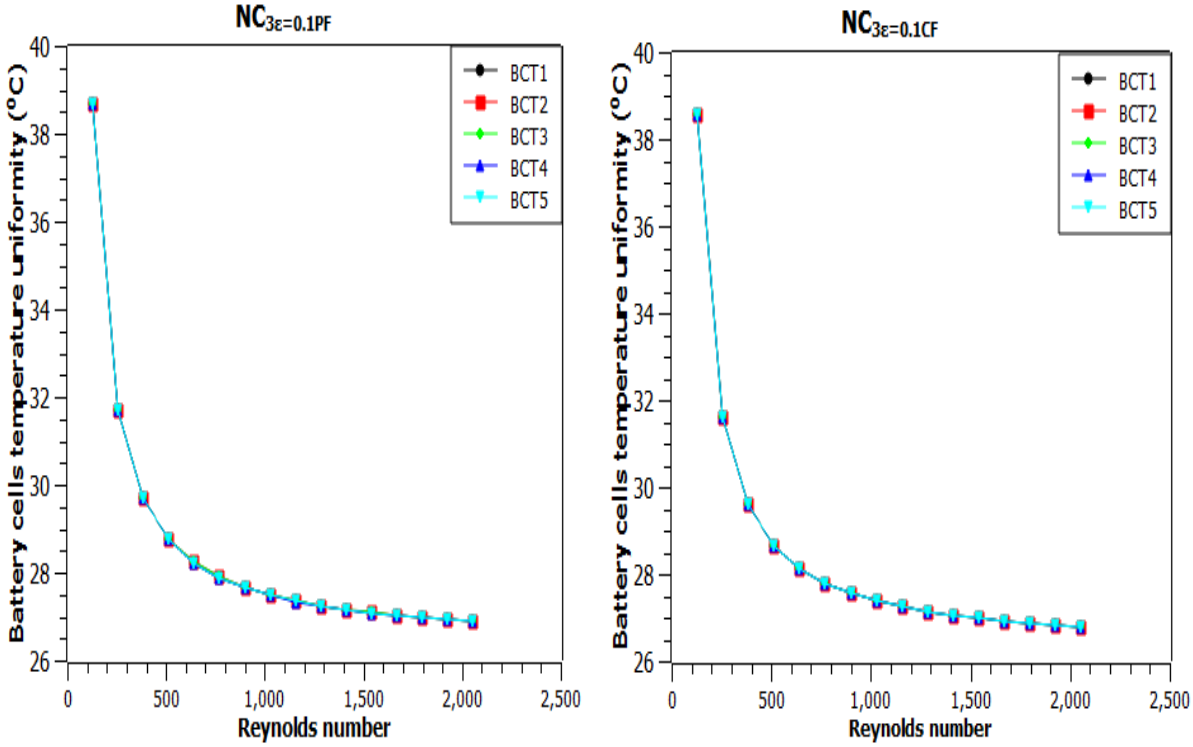

(a) (b)

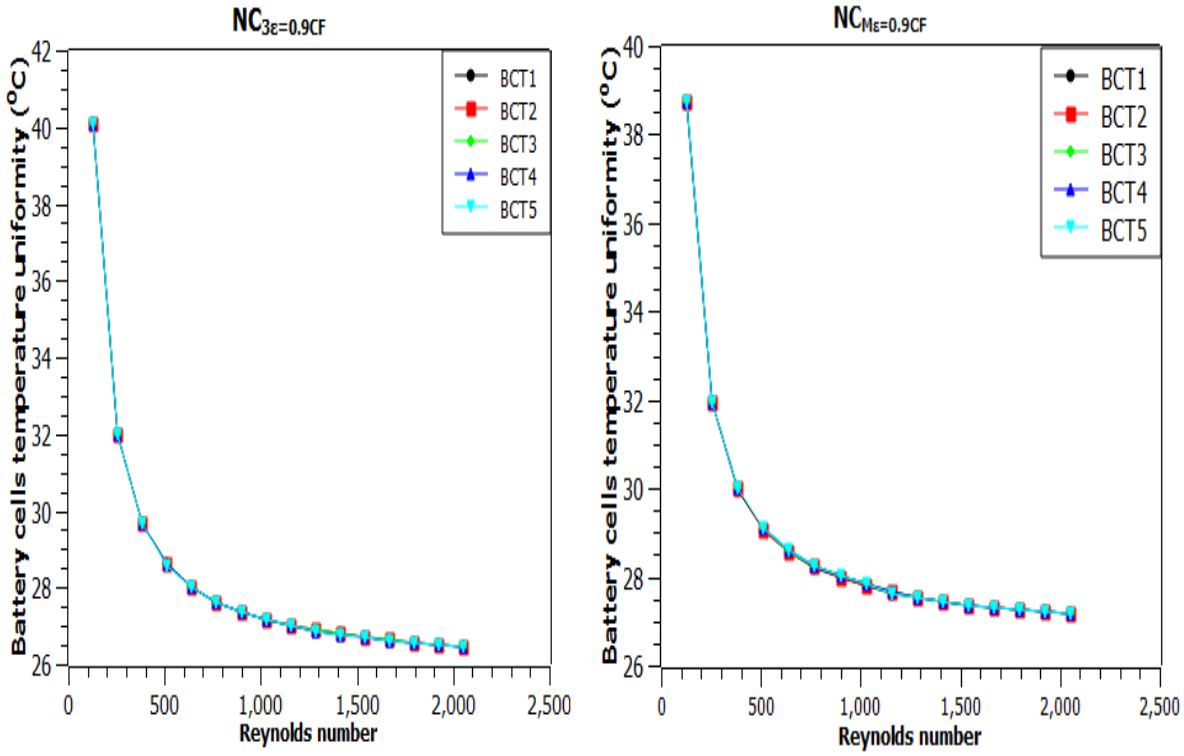

© (d)

Figure 0.22. Battery cells temperature uniformity vs Reynolds number for the cooling system of three channels containing single circular aluminum foam of 0.1*(CAFε=0.1)* and 0.9 *(CAFε=0.9)* porosities: Parallel (a) and counterflow (b) system with centrally located CAFε=0.1, as well as counterflow system with *CAFε=0.9* inserted at the center (c) and *L/8* (d). The color makers represent the temperatures of each battery cell in a pack.

5.3.3 Case 3: Comparison of the enhancement capacity of the circular solid pin fin with aluminum foam inserted in the channel(s) of the cooling system

5.3.3.1 Effect of Reynolds number on the thermal performance in the cooling system using circular solid pin fin and circular aluminum foam insert

This section analyzes the impact of Reynolds number (Re) on the maximum rectangular frame wall temperature, cost of pumping power, and the thermal performance enhancement factor for the two counterflow cooling systems: with the circular solid pin fin insert located at *L/8* (NC_{MCF}) in Case 1 and the circular aluminum foam insert with 0.9 porosity located at *L/8* ($NC_{M\varepsilon=0.9CF}$) in Case 2. These systems are the most promising configurations for effective battery pack thermal management.

5.3.3.1.1 Maximum rectangular frame wall temperature

As seen in Figure 5.23, both the cooling systems (NC_{MCF} and $NC_{M\varepsilon=0.9CF}$) exhibit a decrease in maximum wall temperature (T_{max}) with increasing Reynolds number (Re). A notable reduction in T_{max} is observed when Re rises from 128.38 to 1283.8, beyond which further increases in Re yield minimal effects on T_{max}. Specifically, the NC_{MCF} system achieves a 0.15% T_{max} reduction at the lowest Re of 128.38 and a 0.47% reduction at the highest Re of 2054.08, compared to $NC_{M\varepsilon=0.9CF}$. This suggests that the CSPF insert more effectively dissipates heat from the electric vehicle battery pack than the aluminum foam insert (CAFε=0.9), especially at higher Reynolds numbers.

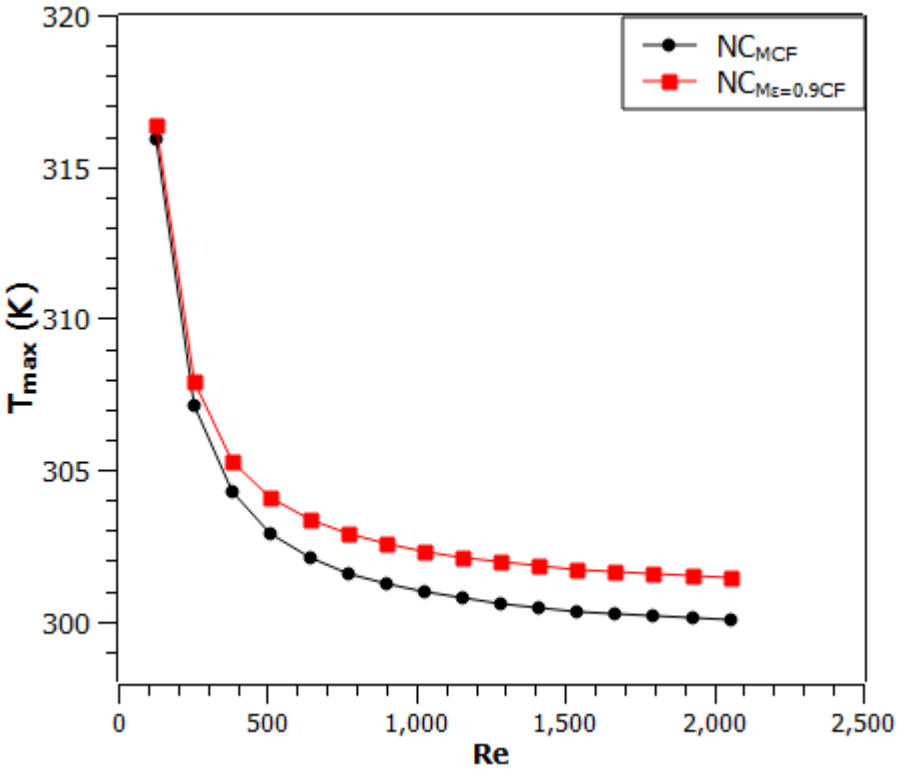

Figure 0.23. Maximum rectangular frame wall temperature (T_{max}) vs. Reynolds number (Re) for cooling systems with circular solid pin fin (CSPF) and aluminum foam of 0.9 porosity (CAFε=0.9) inserts. The graph shows T_{max} as a function of Re, comparing CSPF (black marker) and CAFε=0.9 (red marker) inserts located at $L/8$ in the channels of the cooling systems.

5.3.3.1.2 Dimensionless thermal resistance

Reduction in dimensionless thermal resistance *(R_{th})* with an increase in Reynolds number *(Re)* is observed in both cooling systems (NC_{MCF} and $NC_{M\varepsilon=0.9CF}$) as shown in Figure 5.24. A significant reduction in dimensionless R_{th} was realized when the Re changed from 128.38 to 1283.8 and above this, an insignificant effect of *Re* on the dimensionless R_{th} was observed. However, the cooling system with CSPF (NC_{MCF}) achieved a consistently improved cooling capacity by decreasing the dimensionless R_{th} than the one with CAFε=0.9 insert ($NC_{M\varepsilon=0.9CF}$). Thus, the application of CSPF enhanced the cooling system performance than CAFε=0.9.

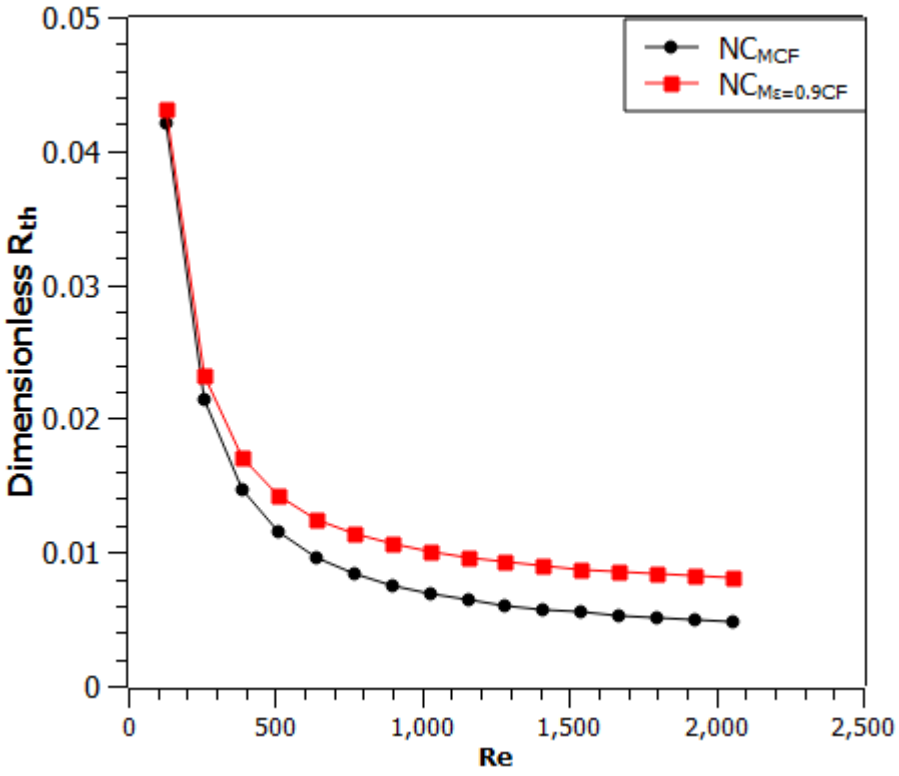

Figure 0.24. Dimensionless thermal resistance (R_{th}) vs. Reynolds number (*Re*) for cooling systems with circular solid pin fin (CSPF) and aluminum foam of 0.9 porosity (CAFε=0.9) inserts. The black and red colored markers represents CSPF and CAFε=0.9 inserts located at *L/8* in the channels of the cooling systems.

5.3.3.1.3 Cost of pumping power

Figure 5.25. shows that CSPF and CAFε=0.9 effect on the cooling system cost of pumping power (*Pp*) as a function of Reynolds number (*Re*). An upward trend of *Pp* was recorded with an increase in *Re*. A significant increase in *Pp* was noticed when *Re* exceeded 770.28. However, NC_{MCF} possesses a slight increase in *Pp* than $NC_{M\varepsilon=0.9CF}$ when the *Re* number increased from 128.38 to 513.52 and beyond this point, a further increase in *Re* was recorded with an

outrageous increase *Pp* by $NC_{M\varepsilon=0.9CF}$ than NC_{MCF}. In general, $NC_{M\varepsilon=0.9CF}$ shows a 65.7% increase in *Pp* compared to NC_{MCF} at the highest *Re* (2058.04) considered in this work.

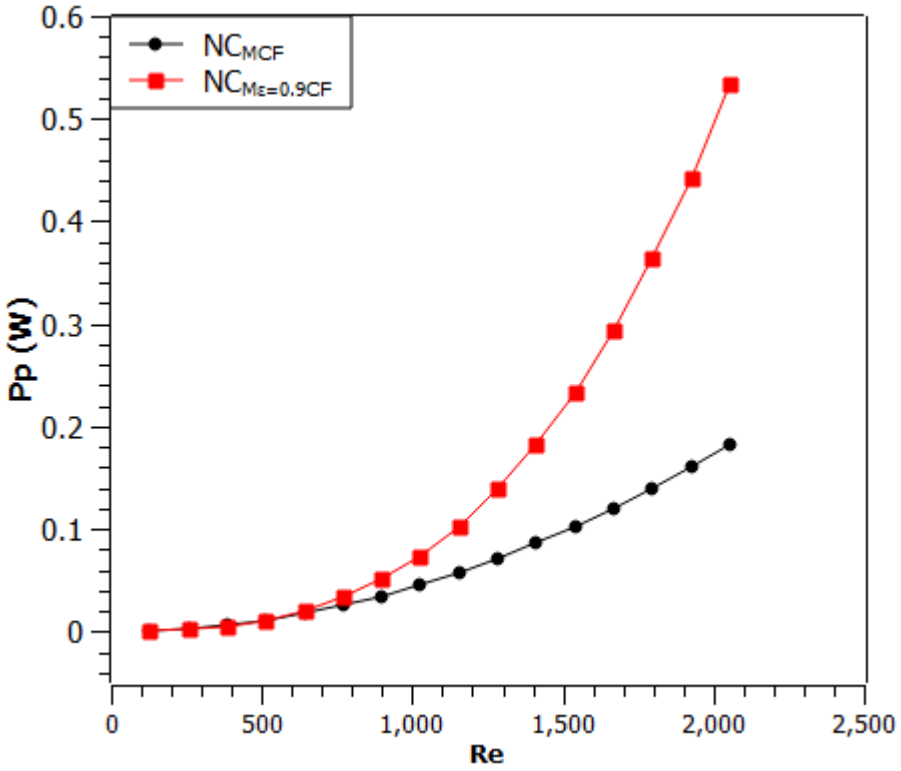

Figure 0.25. Cost of pumping power (*Pp*) vs. Reynolds number (*Re*) for cooling systems with circular solid pin fin (CSPF) and aluminum foam of 0.9 porosity (CAFε=0.9) inserts. The black and red colored markers represent CSPF and CAFε=0.9 inserts located at *L/8* in the channels of the cooling systems.

5.5.3.1.4 Thermal Performance Enhancement Factor

As shown in Figure 5.26, the thermal performance enhancement factor *(TPEF)* increases with Re for both cooling systems, regardless of the insert type. This study demonstrates that both $NC_{M\varepsilon=0.9CF}$ and NC_{MCF} yield a *TPEF* greater than 1, indicating enhanced thermal performance in the cooling system when using either CSPF or CAFε=0.9 inserts, albeit with some increase in friction factor. For *Re* between 128.38 and 385.14, $NC_{M\varepsilon=0.9CF}$ exhibits a higher *TPEF* than NC_{MCF}. However, as *Re* exceeds 385.14, NC_{MCF} achieves a substantially higher *TPEF* compared to $NC_{M\varepsilon=0.9CF}$. It appears that the CAFε=0.9 insert causes more significant pressure drop and friction factor impact on performance than the CSPF insert, particularly at higher *Re*. Notably, $NC_{M\varepsilon=0.9CF}$ reaches its peak *TPEF* at *Re* 1540.56, while NC_{MCF} achieves a similar effect at *Re* 2054.08, with a 46.1% and 49.3% increase in TPEF over $NC_{M\varepsilon=0.9CF}$ at *Re* values

of 1540.56 and 2054.08, respectively. This result indicates that CSPF insert outperforms CAFε=0.9 in thermal enhancement.

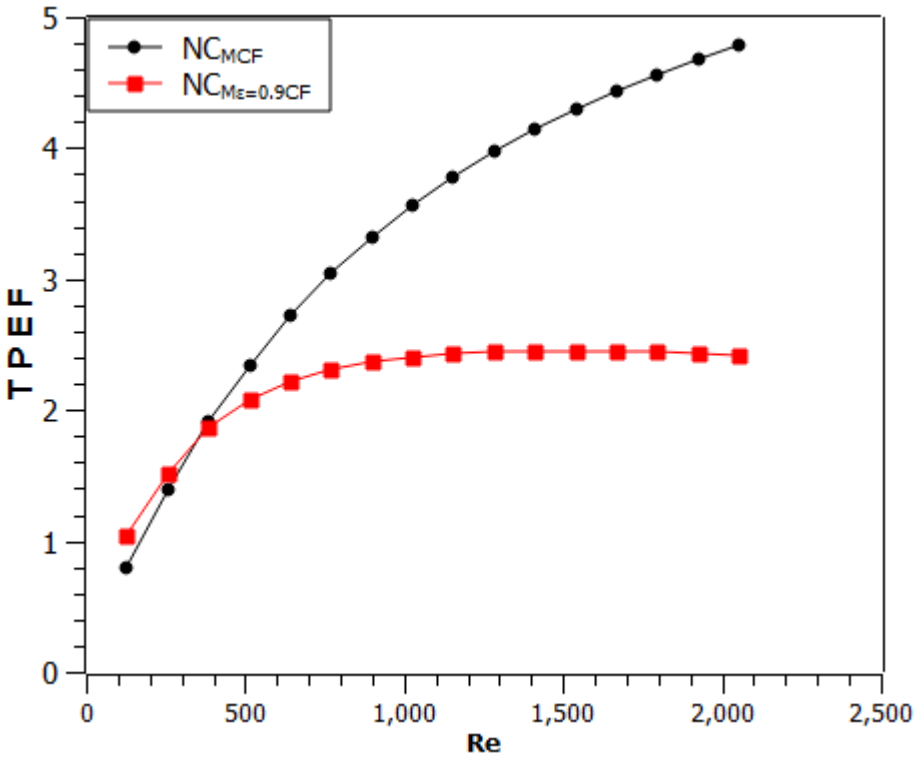

Figure 0.26. Thermal performance enhancement factor (*TPEF*) vs. Reynolds number (*Re*) for cooling systems with circular solid pin fin (CSPF) and aluminum foam of 0.9 porosity (CAFε=0.9) inserts. The black and red colored markers represents CSPF and CAFε=0.9 inserts located at *L/8* in the channels of the cooling systems.

5.3.3.2 Temperature contours

Figure. 5.27 (a and b) shows the temperature contours of the systems with either an insert of circular solid pin fin (CSPF) or aluminum foam of 0.9 porosity (CAFε=0.9) located at *L/8* towards the inlet. The contours are plotted at X plane 25mm and inlet velocity 1.1m/s (Reynolds number 1412.18). Notably, the system with CSPF (NC_{MCF}) achieved a lower temperature distribution than that of the CAFε=0.9 ($NC_{M\varepsilon=0.9CF}$). Thus, CSPF insert is more profitable than CAFε=0.9 for heat dissipation generated by the battery pack.

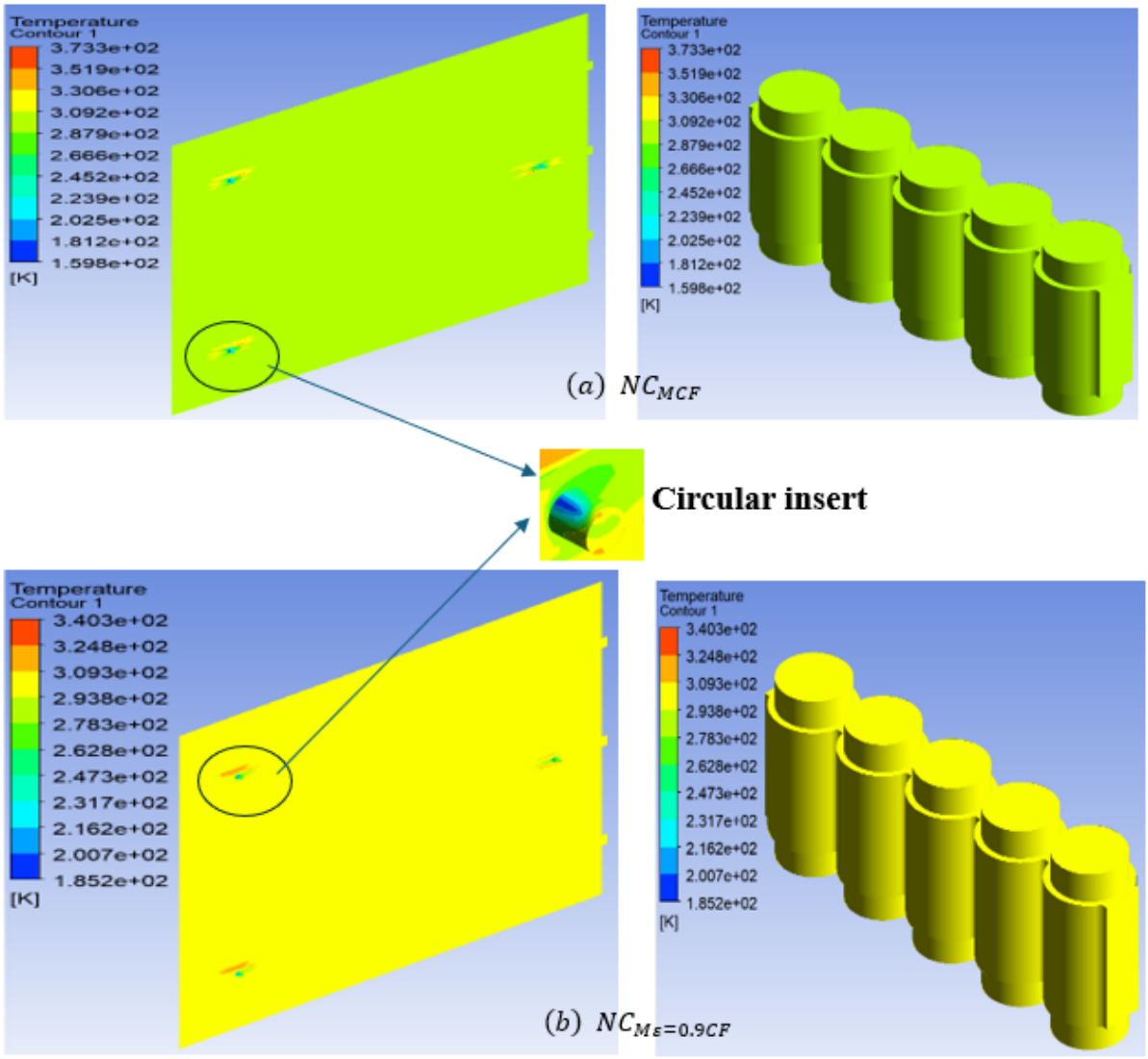

Figure 0.27. Temperature contour for counterflow cooling system of three channels with CSPF (a), and CAFε=0.9 (b) insert.

5.4 Conclusions

This chapter investigates the thermal enhancement potential of a cooling system designed for cylindrical lithium-ion batteries using circular solid pin fins or circular aluminum foam inserts with varying porosities. The effects of the number of channels, the placement of inserts, and *Re* on thermal performance was evaluated numerically for Re values between 128.38 and 2054.08. Key findings include:

1) **Number of mounted channels**: (a) Maximum dimensionless heat transfer rate density was observed in systems with three channels of centrally located circular solid pin fin (CSPF) or aluminum foam of 0.1 porosity (CAFε=0.1) inserts on the rectangular frame.

(b) At the highest applied Reynolds number, the parallel flow and counterflow systems of the three channels with CSPF respectively achieved 93.51% and 93.82% higher dimensionless heat transfer rate density in comparison to their counterparts with no insert. A similar pattern of the dimensionless heat transfer rate density increases of 93.94% and 94.1% were obtained with parallel flow and counterflow systems of the three channels with $CAF\varepsilon = 0.1$ inserts.

2) **Best insert location**: The best performance was achieved when the inserts (either CSPF or aluminum foam) were positioned at *L/8* towards the leading edge of the channels.

3) Impact of Porosity: High porosity (0.9) circular aluminum foam inserts showed acceptable performance, while lower porosities (0.1 and 0.5) resulted in high pumping power and friction factor, limiting their applicability.

4) Single versus Multiple Inserts: A single insert positioned at *L/8* towards the leading edge enhanced cooling performance more effectively than multiple inserts, regardless of spacing.

5) Counterflow versus Parallel Flow Systems: Counterflow cooling systems are slightly more beneficial in reducing the maximum wall temperature and thermal resistance than parallel flow systems.

The superior thermal performance enhancement factor (*TPEF*) of the NC_{MCF} system compared to $NC_{M\varepsilon=0.9CF}$ suggests that the CSPF insert is the optimal choice for effective temperature control of cylindrical lithium-ion battery packs in electric vehicles. Consequently, NC_{MCF} is recommended as the most suitable cooling system configuration for enhanced thermal management in electric vehicle applications.

CHAPTER SIX

ENHANCEMENT OF CYLINDRICAL LITHIUM-ION BATTERY PACK OF ELECTRIC VEHICLE COOLING SYSTEM WITH ELLIPTICAL SOLID PIN FIN / ALUMINIUM FOAM OF DIFFERENT POROSITIES INSERT(S)

6.1 Preview

This chapter analyzes the enhancement potential of the elliptical solid pin fin or aluminum foam of varying porosities inserted in the channels of the designed cooling systems from Chapter 4. With the centrally located insert in the channels, the cooling system performance will be compared with the previously obtained results in Chapter 4. The varying locations' effect of a single insert on the system performance was later considered and compared with varying spacing arrangements of three inserts in the channels. Meanwhile, the system performance will be evaluated with maximum rectangular frame wall temperature, thermal resistance, convective heat transfer coefficient, heat transfer rate density, and thermal performance enhancement factor. The discretization, mesh grid generation, and simulation process of the cooling systems were conducted with the Ansys® 2020 Fluent software package.

6.2 Physical and Computational Model

Figures. 6.1(a-d), indicates the cross-section of the computational domain of the cooling system inserted with a single or multiple (three) elliptical solid pin fins/aluminum foam. With fixed dimensions of the cooling system as stated in Chapter 4, varying locations of a single elliptical solid pin fin/aluminum foam insert in the fluid domain are first considered. The 1.5 mm, 2.0 mm, and 2.5 mm spacing arrangements of multiple (three) elliptical solid pin fins/aluminum foam in the cooling system’s fluid domain were later compared with the single insert at the finest location in the channels. The elliptical solid pin fin/aluminum foam used in this work is of dimension 1.1 mm × 0.6 mm × 0.18 mm while the considered porosities for the aluminum foam are low (0.1), medium 0.5, and high (0.9)

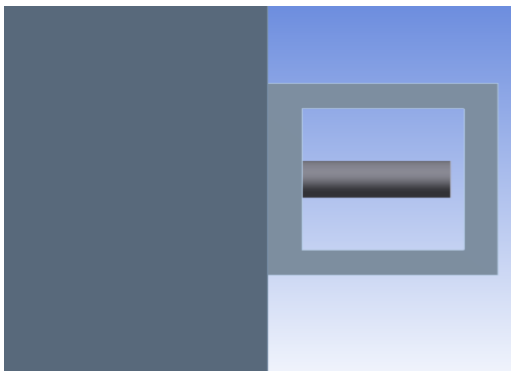

(a). Cooling system cross-section with elliptical solid pin fin or aluminum foam insert in the channel

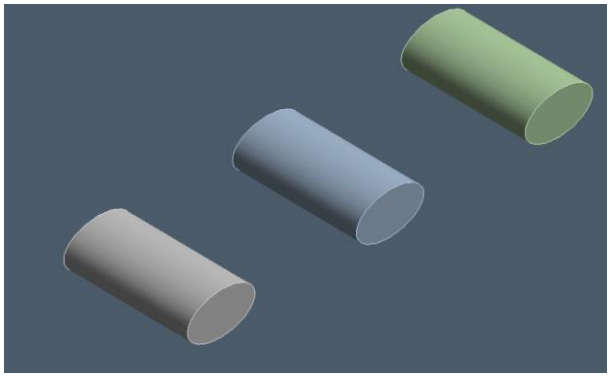

(b). Same size of elliptical solid pin fins or aluminum foam with a spacing of 1.5mm in the channel

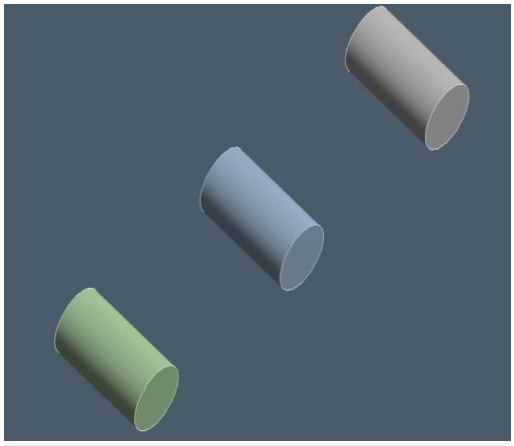

(c). Same size of elliptical solid pin fins or aluminum foam with a spacing of 2 mm in the channel

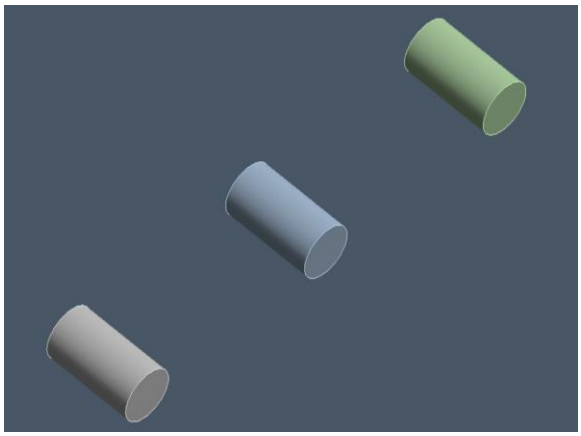

(d). Same size of elliptical solid pin fins or aluminum foam with a spacing of 2.5mm in the channel

Figures 0.1. Cooling system cross-section with single (a), 1.5 mm (b), 2.0 mm (c), and 2.5 mm (d) spacing arrangements of three elliptical solid pin fins insert(s) in the channel.

6.2.1 Grid refinement test analysis

For accurate comparative analysis, the same number of nodes and element sizes were considered for the cooling system with solid pin fin/aluminum foam (irrespective of porosity) inserted at the same point in the flow channel(s). A similar consideration was given to the cooling system with multiple (three) inserts with the same spacing arrangements in the channels.

Tables 6.1 and 6.2 respectively depict the conducted grid refinement test for counterflow cooling systems of three channels inserted with a single elliptical solid pin fin located at the

center of the flow channels (NE_{3CF}) and counterflow cooling system with three multiple (three) inserts of circular aluminum foam arranged with 2.0 mm spacing ($NE2.0M_{CF}$) as an example for all grid refinement analyses in this chapter.

Table 0.1. Grid refinement test for NE_{3CF}

Number of cells	Peak frame wall temperature (K)	Deviation $\left\|\frac{(\Delta T)_i - (\Delta T)_{i-1}}{(\Delta T)_i}\right\|$
151397	308. 0008	----------
182729	308.0379	0.00009708
165627	307.7055	0.0010790

Table 0.2. Grid refinement test for $NE2.0M_{CF}$

Number of cells	Peak frame wall temperature (K)	Deviation $\left\|\frac{(\Delta T)_i - (\Delta T)_{i-1}}{(\Delta T)_i}\right\|$
164397	307. 7215	----------
190729	307.7135	0.000025997
179627	306.9055	0.002625819

6.3 Results and Discussions

6.3.1 Case 1: Enhancement of the cooling system's thermal performance by inserting elliptical solid pin fin(s) in the channel(s) under different flow orientations

6.3.1.1 Reynolds number effect on the cooling system characterization with centrally located (L/2) elliptical solid pin fin (ESPF) under different low orientations

6.3.1.1.1 Maximum rectangular frame wall temperature

As seen in Figure 6.2, an increase in Reynolds number (*Re*) increases the maximum wall temperature (T_{max}) for the rectangular frame regardless of the cooling system design. A

significant drop in T_{max} occurred as *Re* increased from 128.38 to 1283.8. However, beyond this point, a further increase in *Re* had an insignificant effect on T_{max}. Further improvement of the cooling system was realized with additional channels mounted on the rectangular frame. Thus, NE_{5CF} reduced T_{max} by 0.049%, 0.17%, 0.99%, and 3.11% respectively compared to NE_{4CF}, NE_{3CF}, NE_{2CF}, and NE_1 at *Re* 2054.08. Parallel flow cooling systems show a similar pattern. However, counterflow cooling systems slightly reduced the T_{max} values than parallel flow cooling systems within the range of applied *Re* in this study. A substantial reduction in T_{max} was recorded with cooling systems of the channel(s) inserted with ESPF (Figure 6.2) compared to those without insert (Figure 4.7), reflecting the enhanced thermal performance provided by the implementation of an insert.

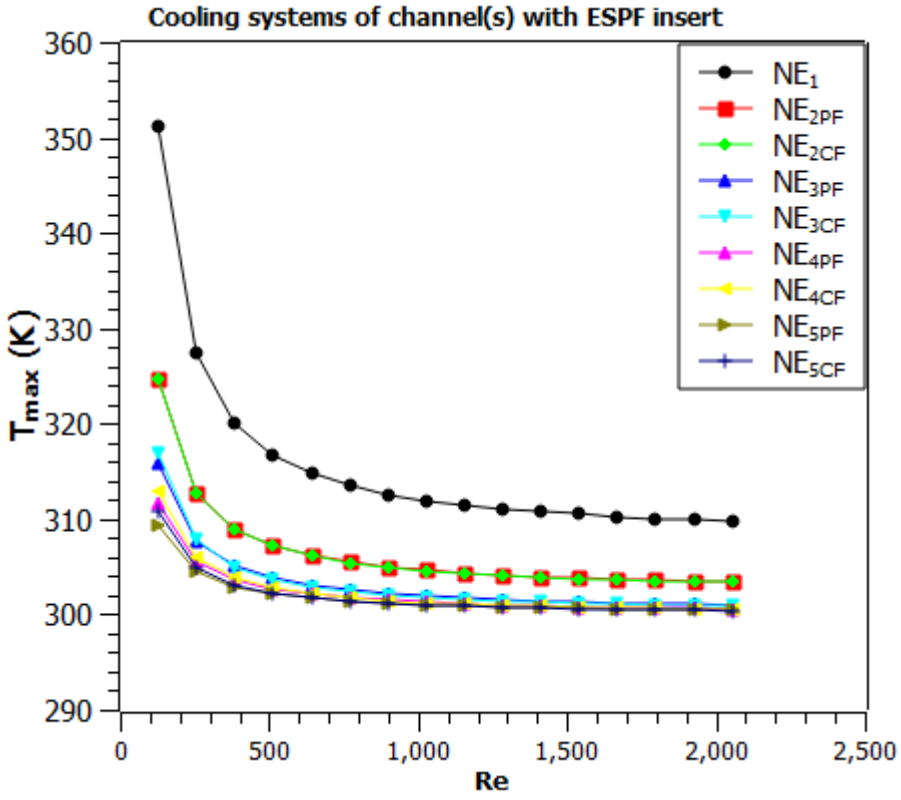

Figure 0.2. Maximum rectangular frame wall temperature (T_{max}) vs Reynolds number (*Re*) of the cooling system with a centrally located elliptical solid pin fin (ESPF) in the channel(s). The color markers represent the cooling system of different numbers of channel(s) with an ESPF insert mounted on the rectangular frame.

6.3.1.1.2 Dimensionless thermal resistance

An increase in Reynolds number (*Re*) leads to a decrease in dimensionless thermal resistance (R_{th}) of the cooling systems equipped with elliptical solid pin fin (ESPF) as reported in Figure

6.3. With an increase in *Re* from 128.38 to 1283.8, a significant reduction in dimensionless R_{th} was obtained. Beyond this point, the insignificant influence of *Re* on dimensionless R_{th} reduction was recorded. An improved dimensionless R_{th} reduction is achieved by mounting more channels on the rectangular frame. For instance, NE_{5CF} and NE_1 possess the lowest and highest dimensionless R_{th} within the range of Re considered in this study. A similar pattern of this behavior was observed with the parallel flow cooling systems. The dimensionless R_{th} values were slightly lower with counterflow cooling systems than with parallel flow cooling systems. Furthermore, Figure 6.3 shows that cooling systems with an ESPF insert had a significantly lower dimensionless R_{th} than cooling systems without inserts (Figure 4.8), indicating that using an insert improves thermal performance.

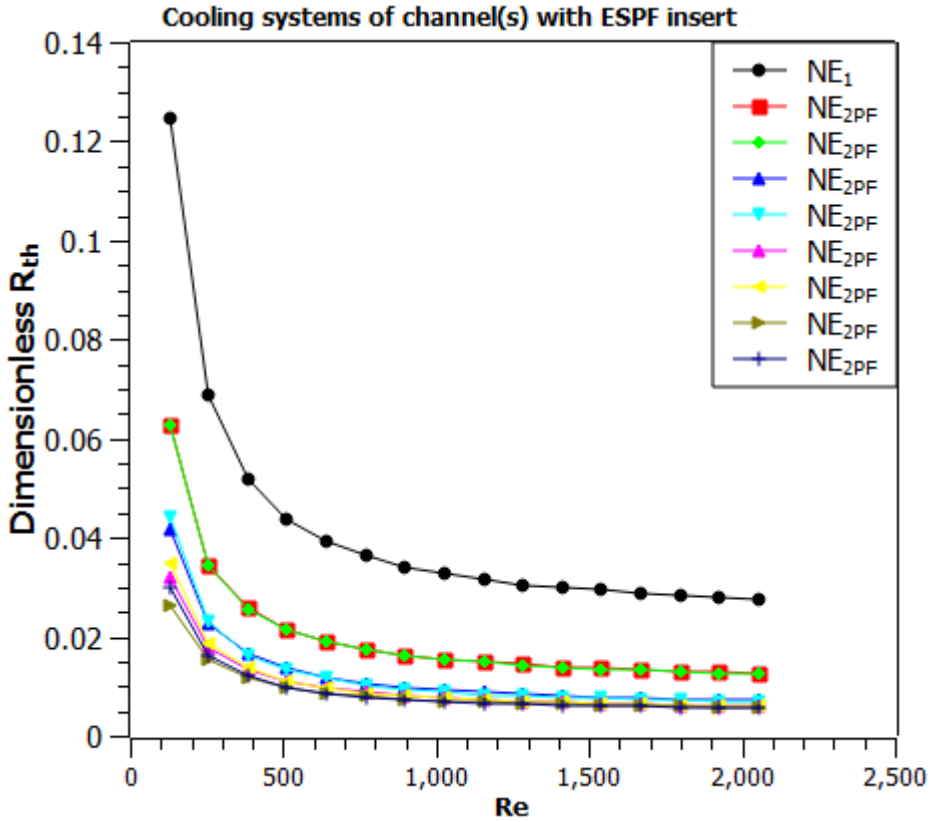

Figure 0.3. Dimensionless thermal resistance (R_{th}) vs Reynolds number (*Re*) of the cooling system with a centrally located elliptical solid pin fin (ESPF) in the channel(s). The color markers represent the cooling system of different numbers of channel(s) with an ESPF insert mounted on the rectangular frame.

6.3.1.1.3 Cost of pumping power

The relationship between the cost of pumping power (*Pp*) and the Reynolds number (*Re*) for the cooling system of channel(s) with elliptical solid pin fin (ESPF) insert is illustrated in Figure 6.4. An increase in Re increases the values of *Pp*. Meanwhile, a gradual increase in *Pp* was obtained when the *Re* increased from 128.38 to 641.9, and beyond this, a substantial increase in *Pp* was observed. A direct relationship between the *Pp* and the number of channels mounted on the rectangular frame was realized. For instance, 80%, 60%, 40%, and 20% of increased Pp were realized with NE_{5CF} compared to NE_1, NE_{2CF}, NE_{3CF}, and NE_{4CF} at *Re* 641.9. This result was in agreement with the published work of [197]. The cooling systems with a counterflow design possess slightly higher *Pp* values than those with a parallel flow arrangement [47]. The cooling systems of the channel(s) with ESPF (Figure 6.4) were found to have a higher *Pp* value than the cooling systems of the channels without ESPF (Figure 4.9). Thus, the insertion of ESPF in the flow channels comes with the penalty of higher pressure drop and consequently higher *Pp* values.

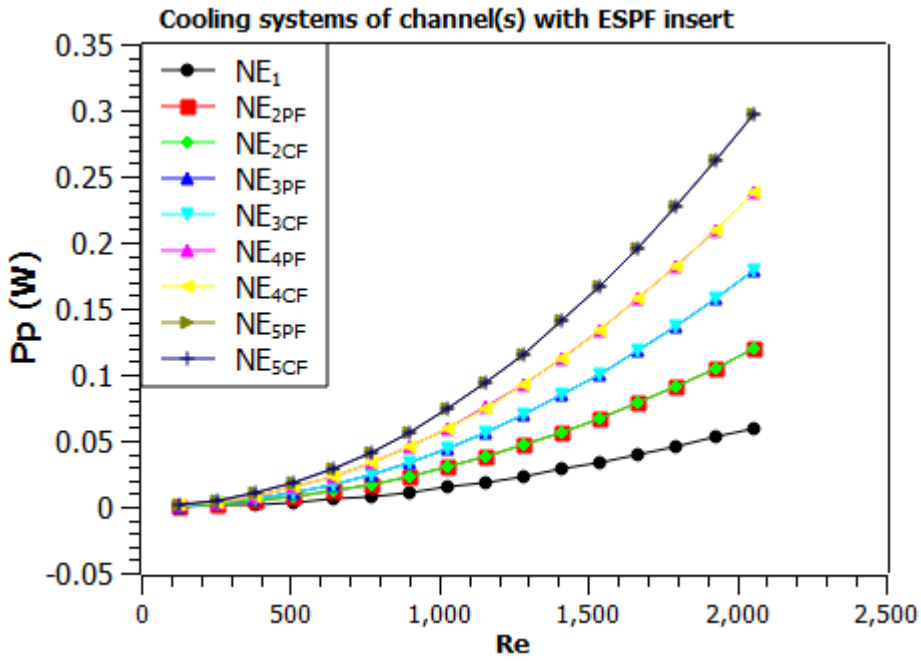

Figure 0.4. The cost of pumping power (*Pp*) vs Reynolds number (*Re*) of the cooling system with a centrally located elliptical solid pin fin (ESPF) in the channel(s). The color markers represent the cooling system of different numbers of channel(s) with an ESPF insert mounted on the rectangular frame.

6.3.1.2 Effect of channel number on the dimensionless heat transfer rate density for the cooling system with centrally located (L/2) elliptical solid pin fin (ESPF) in the channel(s)

The relationship between the dimensionless heat transfer rate density and the number of channels with an elliptical solid pin fin (ESPF) insert located at the center (L/2), mounted on the rectangular frame of the cooling systems, is shown in Figure 6.5. The expression of increased dimensionless heat transfer rate density shows an improved performance of the system (Equations (3.36-3.38)). Regardless of the number of channels mounted on the rectangular frame, the increasing dimensionless heat transfer rate density was recorded with an increase in Reynolds number (Re). A slightly lower thermal performance was obtained with the parallel flow cooling systems (Figure 6.5a) compared to the counterflow cooling systems (Figure 6.5b). The increased dimensionless heat transfer rate density of 22.36%, 15.73%, 29.17%, and 25.27% were achieved with three channels containing ESPF inserts compared to 1, 2, 4, and 5 channels at *Re* 2054.08 under the parallel flow orientation (Figure 4.10a) suggests that effective interaction between the working fluid and heat transfer surfaces is more pronounced with three channels [198, 199]. Also, at the highest *Re* considered in this work, the counterflow system of three channels with ESPF insert (Figure6.5b) achieves a 92.5% dimensionless heat transfer rate density increment compared to the cooling system of the same design with no insert (Figure 4.10a). Similarly, 92.21% of augmentation was realized with the parallel flow cooling systems. This scenario depicts the tendency of ESPF to restore thermal boundary layer development for the enhancement of heat transfer in the channels and, consequently, to improve cooling system performance.

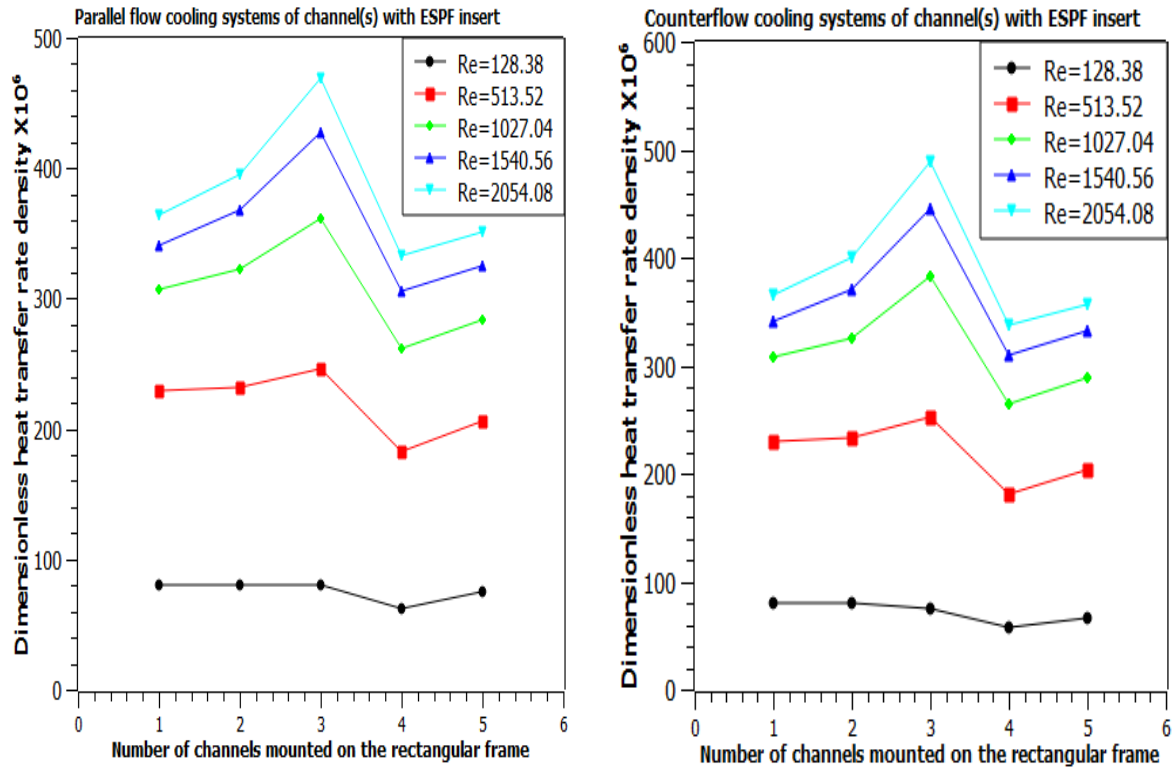

(a) (b)

Figures 0.5. Dimensionless heat transfer rate density vs. number of channels mounted on the rectangular frame in Parallel (a) and Counterflow (b) Cooling systems with elliptical solid pin fin (ESPF) Inserts. Colored markers represent different Reynolds numbers (Re): Re = 128.38 (black), Re = 513.52 (red), Re = 1027.04 (green), Re = 1540.56 (blue), and Re = 2054.08.

6.3.1.3 Effect of varying locations of a single elliptical solid pin fin (ESPF) inserted in the channel(s) of the cooling systems

From the previous section, the cooling system with three channels and centrally located ESPF (at *L/2)* was concluded to have the highest strength for dissipation of heat from the battery pack as it offers the highest dimensionless heat transfer rate density. Therefore, the effect of the varying locations of ESPF within the channels of this cooling system is further considered to evaluate the likely impacts of various placements on heat dissipation effectiveness and thermal performance. This analysis explores whether alternative ESPF placements can further augment cooling system performance beyond the best configuration identified earlier.

The reduction of the dimensionless thermal resistance (R_{th}) with an increased Reynolds number (*Re*), regardless of the ESPF location in the cooling systems' channels, is reported in Figure

6.6. A significant reduction in dimensionless R_{th} was obtained when the *Re* increased from 128.38 to 1283.8. An insignificant reduction in the dimensionless R_{th} was obtained when *Re* rises above 1283.8. Within the range of applied *Re*, counterflow cooling systems reduce the dimensionless R_{th} slightly than parallel flow cooling systems. Specifically, at *Re* 898.66 NE_{3PF} shows a significant improvement of 7.67% and 9.9% dimensionless R_{th} reduction compared to the NE_{JPF} and NE_{MPF} respectively. Counterflow cooling systems demonstrated a similar pattern of dimensionless R_{th} reduction Thus, the highest cooling capacity is achieved when the ESPF is located at *L/8* towards the leading edge of the cooling system's channels.

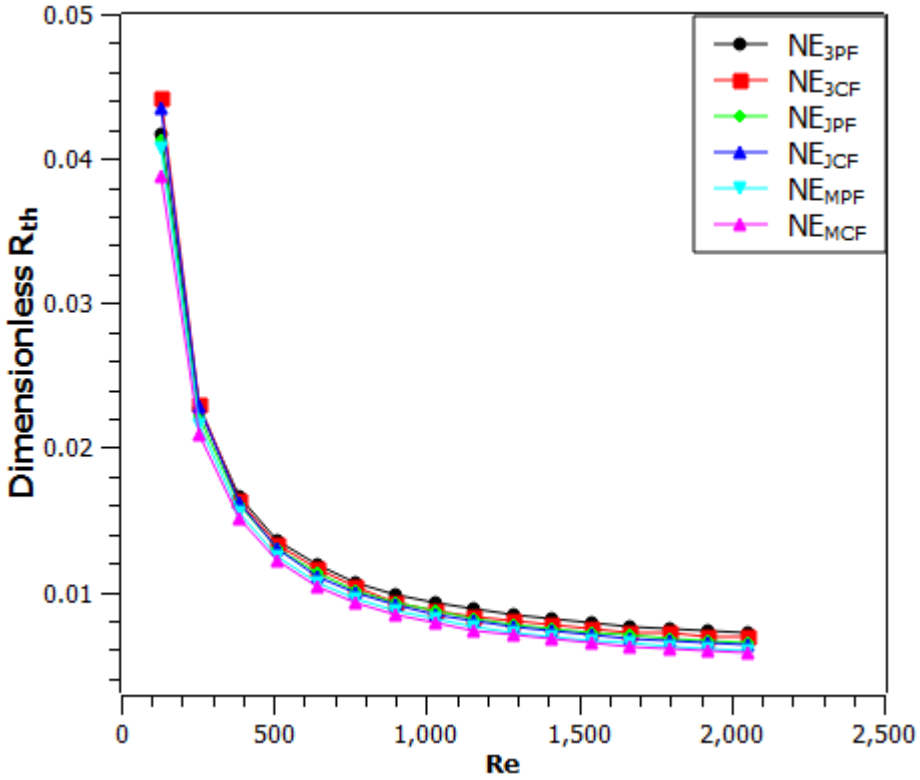

Figure 0.6. Dimensionless thermal resistance (R_{th}) vs Reynolds number (*Re*) of the cooling system with a single elliptical solid pin fin (ESPF) insert. The colored markers illustrate counterflow (CF) and parallel flow (PF) cooling systems equipped with a single ESPF located at *L/2 (NE_{3CF} and NE_{3PF})*, *L/4 (NE_{JCF} and NE_{JPF})*, and *L/8 (NE_{MCF} and NE_{MPF})*, in the channels.

6.3.1.4 Comparison of a single and varying spacing arrangement of three elliptical solid pin fin (ESPF) insert(s) in the channel(s) on the cooling system's performance

With no emphasis on finding the best insert location in the channel, earlier researchers [208] reported the realization of optimal performance of the cooling configuration with at most three-

pin fin inserts. Three ESPF were therefore, arranged from the best point of insert location *(L/8)* towards the inlet to compare the effect of a single with multiple insert(s) in the channels on the thermal performance enhancement of the cooling systems. The 1.5 mm, 2.0 mm, and 2.5 mm in-line spacing arrangements for the three ESPFs were considered for this analysis.

Figure 6.7 revealed the dimensionless thermal resistance (R_{th}) as the Reynolds number (*Re*) increased, regardless of the number and spacing arrangements of the elliptical solid pin fin (ESPF) in the cooling system's channels. A considerable dimensionless R_{th} reduction was noticed when the *Re* increased from 128.38 to 1283.8 with negligible effect on dimensionless R_{th} beyond this point. Compared to $NE2.0M_{PF}$ and $NE2.5M_{PF,}$ $NE1.5M_{PF}$ improved the dimensionless R_{th} reduction by 9.5% and 12.4% at *Re* 770.28. Counterflow cooling systems were also observed to exhibit similar behavior in dimensionless R_{th} reduction. This shows less space between ESPFs in the cooling system channels is better for the battery pack's heat dissipation. However, cooling systems with a single ESPF show the highest improvement of dimensionless R_{th} reduction compared to those with multiple (three) ESPFs regardless of the spacing arrangements. Thus, NE_{MCF} reduced the dimensionless R_{th} by 29%, 25.6%, and 15.1% compared to $NE2.5M_{CF}$, $NE2.0M_{CF,}$ and $NE1.5M_{CF}$ at the *Re* 770.28. However, the systems with counterflow arrangements provide slightly lower dimensionless R_{th} values compared to those with parallel flow arrangements.

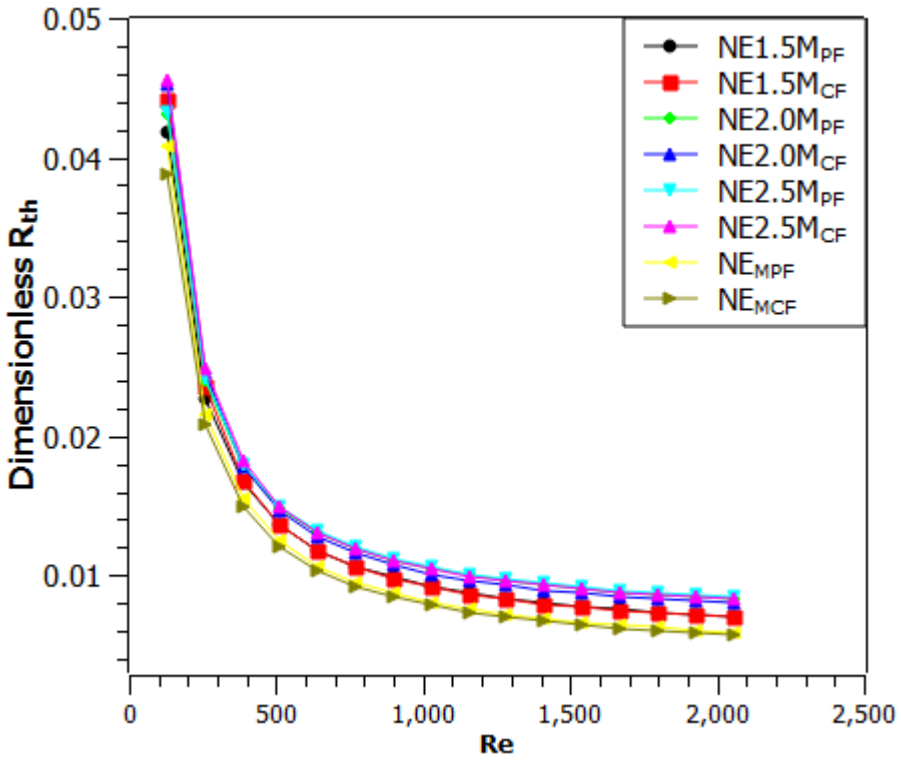

Figure 0.7. Dimensionless thermal resistance (R_{th}) vs. Reynolds number (*Re*) of cooling system with elliptical solid pin fin (ESPF) insert(s). The color markers illustrate counterflow (CF) and parallel flow (PF) cooling systems equipped with a single CSPF (NE_{MCF} and NE_{MPF}), and 1.5mm ($NE1.5M_{CF}$ and $NE1.5M_{PF}$), 2.0mm ($NE2.0M_{CF}$ and $NE2.0M_{PF}$) as well as 2.5mm ($NE2.5M_{CF}$ and $NE2.5M_{PF}$) spacing arrangements of three ESPFs in the channels

6.3.1.5 Normalized friction factor effect between the varying locations of a single and spacing arrangement of three elliptical solid pin fin (ESPF)

Figures 6.8 indicates the variation of the normalized friction factor (*NFF*) as a function of the Reynolds number (*Re*) for different cooling systems of single and multiple (three) ESPF insert(s). As the Re increases, the *NFF* also increases irrespective of the locations of a single ESPF (Figure 6.8a) or spacing arrangements of the multiple (three) ESPFs (Figure 6.8b) in the channels of the cooling system. From Figures 6.8 (a) and (b), counterflow cooling systems were observed with slightly higher *NFF* values than the parallel flow cooling systems. The tendency of the ESPF in the cooling system's channels to raise the working fluid more than three times compared to the cooling system with no insert in the channels was observed as both figures incurred *NFF* values higher than 3 [40]. However, Figure 6.8b (multiple ESPFs) with higher values of *NFF* compared to Figure 6.8a (single ESPF) suggests the implication of the complexity of the fluid domain on the working fluid friction factor. At *Re* 898.66, NE_{MCF} reduces *NFF* by 0.026% and 0.068% compared to NE_{JCF} and NE_{3CF} respectively (Figure 6.8a). A similar observation was recorded with the parallel flow cooling systems. Thus, the closer the ESPF is to the inlet, the lower the *NFF* values. In a like manner, $NE1.5M_{CF}$ increases *NFF* values by 0.14% and 0.17% compared to $NE2.0M_{CF}$ and $NE2.5M_{CF}$ respectively at the *Re* 2054.08 (Figure 6.8b). Parallel flow cooling systems show a similar pattern. Thus, a cooling system with the shortest spacing arrangement between the ESPF offers the highest *NFF* values and vice versa [200].

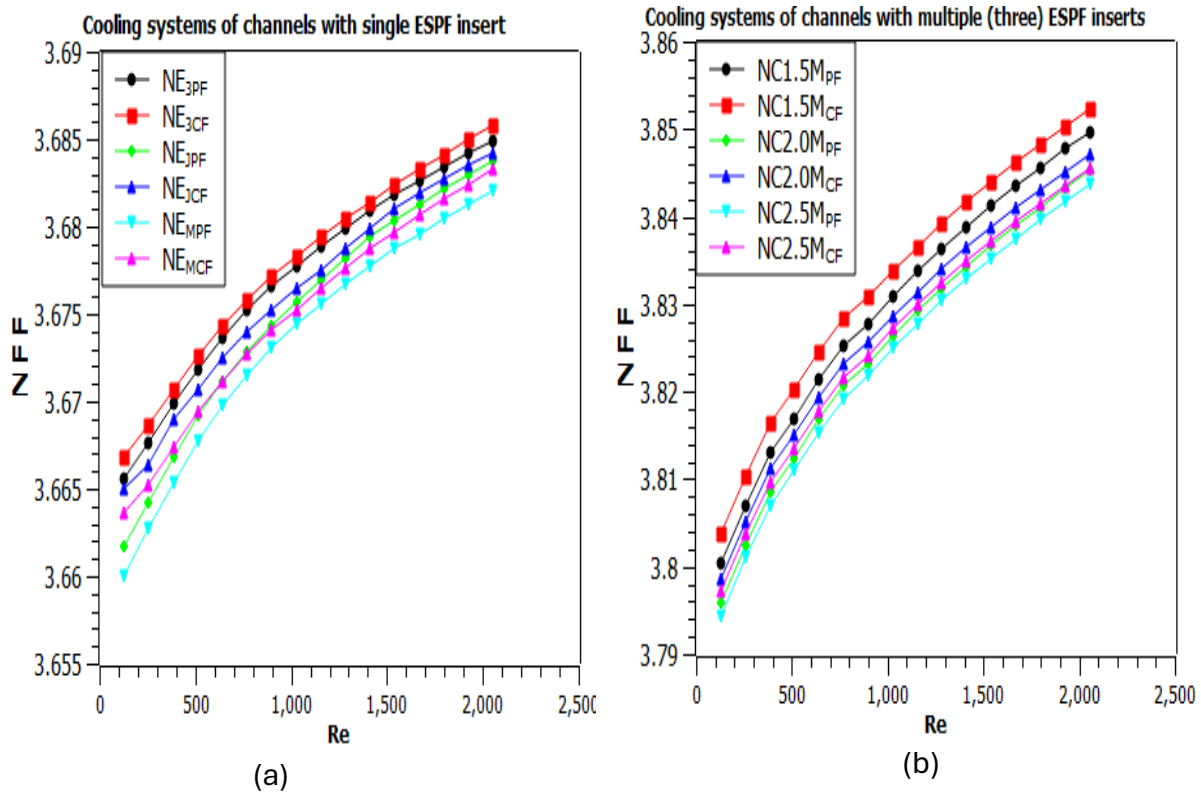

Figures 0.8. Normalized friction factor (*NFF*) vs. Reynolds number (*Re*) of the cooling system with a single (a) and three (b) elliptical solid pin fin (CSPF) insert(s). The color markers illustrate counterflow (CF) and parallel flow (PF) cooling systems equipped with varying locations of a single and spacing arrangement of multiple ESPFs in the channels.

6.3.1.6 Comparison of thermal performance enhancement factor effect between the varying locations of a single and varying spacing arrangement of three elliptical solid pin fin (ESPF)

The variation of the thermal performance enhancement factor (*TPEF)* with varying Reynolds number (*Re*) for comparison between single and multiple elliptical solid pin fin(s) ESPF(s) effect on the overall thermal performance of the cooling systems is represented in Figure 6.9. An increase in *Re* increases *TPEF* regardless of the number and spacing arrangement of ESPF in the channels. The realization of *TPEF* greater than 1 by all considered cooling systems indicates that insertion of ESPF in the fluid domain can result in heat transfer enhancement with a tolerable friction factor effect [45]. At the *Re* 2054.08, $NE2.0M_{PF}$ increases the *TPEF* by 0.33% and 2.1% compared to the $NE1.5M_{PF}$ and $NE2.5M_{PF,}$ respectively. A similar pattern of *TPEF* increase was observed with counterflow cooling systems. This result indicates that the frictional factor effect is more acceptable for the enhancement of heat transfer in the channel

of 2.0 mm than in 1.5 mm and 2.5 mm spacing arrangements. However, the cooling system with a single ESPF insert achieves the maximum value of *TPEF* compared to the one with multiple (three) ESPF inserts, regardless of the spacing arrangements. For instance, NE_{MCF} improves *TPEF* by 3.4%, 2.1%, and 4.2% compared to $NE1.5M_{CF}$, $NE2.0M_{CF,}$ and $NE2.5M_{PF}$ respectively at *Re* 2054.08 precisely. This implies that a single ESPF located at L/8 in the channels can enhance the overall thermal performance of the cooling system more than multiple ESPFs. Thus, one ESPF at *L/8* in the channels improved the cooling system's overall thermal performance better than multiple (three) ESPFs. Therefore, NE_{MCF} with the highest *TPEF* seems to be the best choice for temperature control of the electric vehicles' cylindrical lithium-ion battery pack, as considered in this section. However, with either single or multiple ESPF(s), parallel flow cooling systems offer slightly lower *TPEF* than the counterflow cooling systems

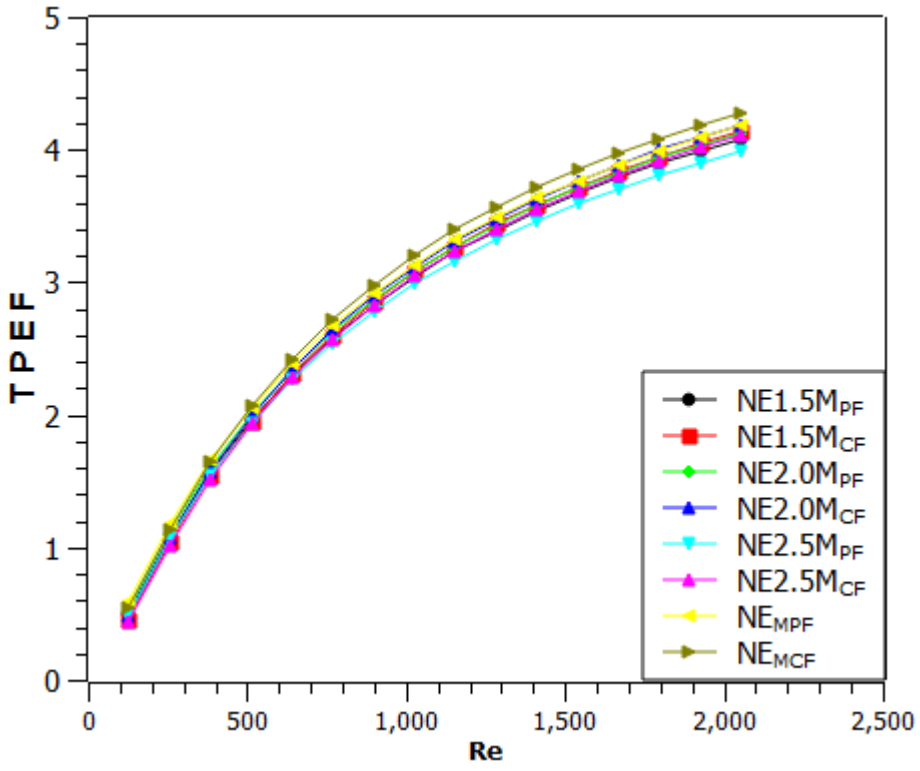

Figure 0.9. Thermal performance enhancement factor (*TPEF*) vs. Reynolds number (*Re*) of the cooling system with elliptical solid pin fin (ESPF) insert(s). The color markers illustrate counterflow (CF) and parallel flow (PF) cooling systems equipped with a single ESPF (NE_{MCF} and NE_{MPF}), and 1.5mm *($NE1.5M_{CF}$* and *$NE1.5_{PF}$)*, 2.0mm *($NE2.0M_{CF}$* and *$NE2.0M_{PF}$)* as well as 2.5mm *($NE2.5M_{CF}$* and *$NE2.5M_{PF}$)* spacing arrangements of three ESPFs in the channels.

6.3.1.7 Temperature uniformity of the battery cells in the pack

The cooling system's influence on maintaining the temperature uniformity of the battery cells in a pack is analyzed in this section. As expressed in Figures 6.10(a-c), an increased Reynolds number leads to decreased temperature uniformity of the battery cells in a pack. For the applied Reynolds number in this study, a variation of less than 2℃ of temperature from one battery cell to the other was obtained indicating the cooling system's capacity to maintain battery cells' temperature uniformity[13]. Regardless of the flow orientation, the observed lower values of battery cells temperature uniformity and the coalescence of the graph in Figs 6.10 (a) and (b) compared to Figures 4.11 (a) and (b) suggest that the insertion of ESPF can drastically lower and improve the temperature uniformity of the battery cells in the pack. This result is in agreement with the published work of [13]. In addition, NE_{3CF} (Figure 6.10b) offers a slightly lower battery cells' temperature uniformity than NE_{3PF} (Figure 6.10a), which implies the influence of flow orientation in dissipating heat generated in the battery pack. However, the placement of ESPF at *L/8* in the cooling system channels further reduced the battery cells' temperature uniformity, as shown in Figure 6.10c compared to Figure 6.10b.

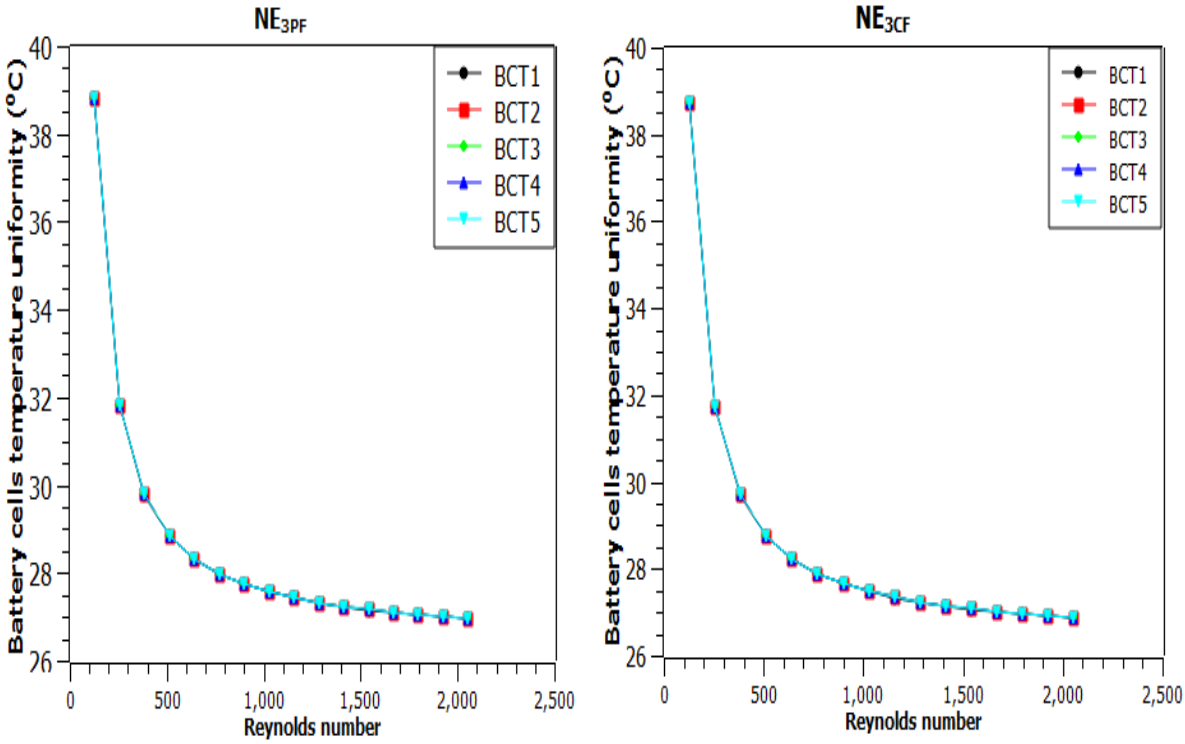

(a) (b)

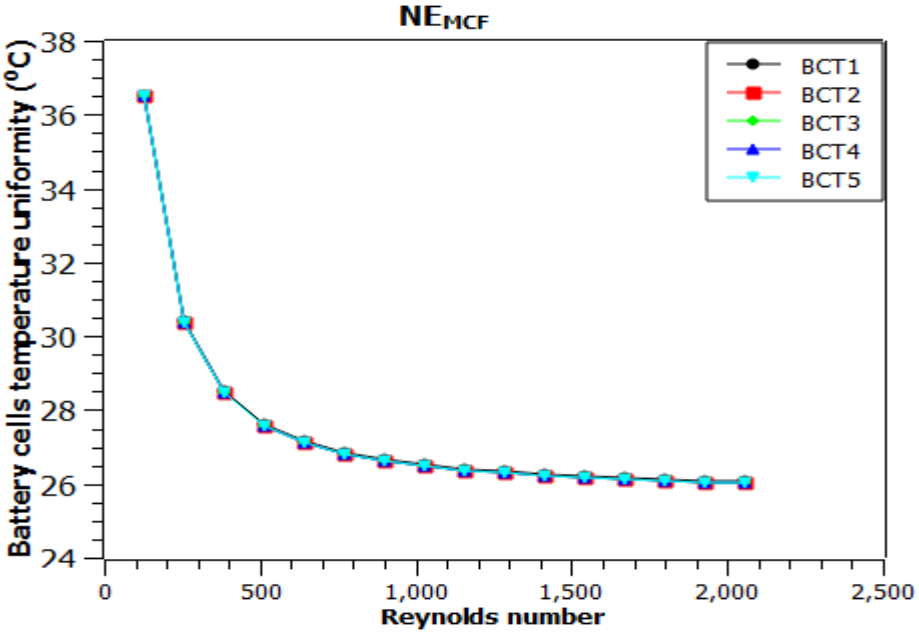

©

Figures 0.10. Battery cells temperature uniformity vs Reynolds number for cooling systems of three channels containing a single elliptical solid pin fin (ESPF) insert located at *L/2* (parallel flow (a) and counterflow (b) arrangement) as well as *L/8* (counterflow arrangement (c). The color makers represent the temperatures of each battery cell in a pack.

6.3.2 Case 2: Enhancement of the cooling system's performance by inserting elliptical aluminum foam(s) of varying porosities in the channel(s) under different flow orientations

6.3.2.1 Reynolds number effect on the cooling system characterization with centrally located (L/2) elliptical aluminum foam of 0.1 porosity ($EAF\varepsilon = 0.1$) *under different flow orientations*

6.3.2.1.1 Maximum rectangular frame wall temperature

From Figure 6.11, an increase in Reynolds number (*Re*) increases the maximum wall temperature (T_{max}) of the cooling systems with an elliptical aluminum foam of 0.1 porosity ($\text{EAF}\varepsilon = 0.1$) insert. A considerable reduction in T_{max} was noted when *Re* increased from 128.38 to 1283.8. However, a further increase in *Re* yields an insignificant effect on the T_{max} reduction. Counterflow cooling systems offer slightly lower values of T_{max} than parallel flow cooling systems. Meanwhile, an additional channel mounted on the rectangular frame offers

an improved T_{max} reduction. For instance, at *Re* 2054.08 $NE_{5\varepsilon=0.1PF}$ respectively achieved T_{max} reduction of 0.07%, 0.23%, 1.0%, and 3.13% compared to $NE_{4\varepsilon=0.1PF}$, $NE_{3\varepsilon=0.1PF}$, $NE_{2\varepsilon=0.1PF}$, and $NE_{1\varepsilon=0.1}$. The counterflow cooling systems exhibited a similar behavior. A substantial reduction in T_{max} was obtained by cooling systems of channel(s) with EAF$\varepsilon = 0.1$ insert (Figure 6.11) compared to those without insert (Figure 4.7), indicating the improved thermal performance provided by applying an insert.

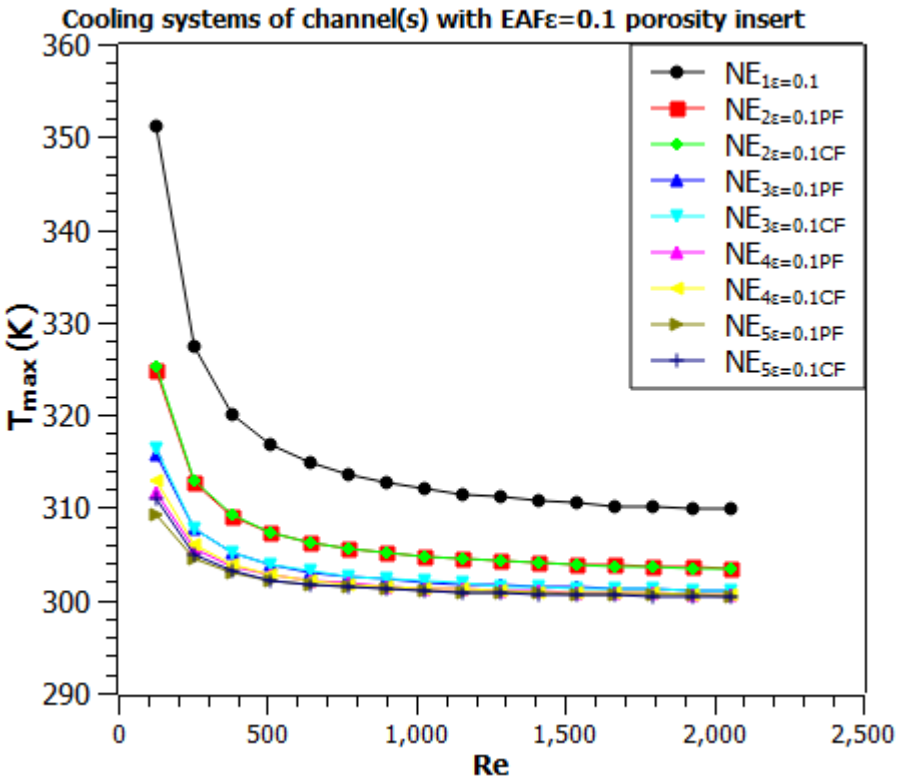

Figure 0.11. Maximum rectangular frame wall temperature (T_{max}) vs Reynolds number (*Re*) of the cooling system with a centrally located elliptical aluminum foam of 0.1 porosity ($EAF\varepsilon = 0.1$) insert in the channel(s). The color markers represent the cooling system of different numbers of channel(s) with a $EAF\varepsilon = 0.1$ insert mounted on the rectangular frame.

6.3.2.1.2 Dimensionless thermal resistance

Figure 6.12 shows a reduction of dimensionless thermal resistance (R_{th}) with an increased Reynolds number (*Re*) for the cooling system of EAF$\varepsilon = 0.1$ in the channel(s). The increase of *Re* from 128.38 to 1283.8 leads to a substantial reduction in the dimensionless R_{th} and greater than this *Re* effect on the T_{max} becomes inconsequential. For the range of applied Re in this work, counterflow cooling systems possess slightly lower dimensionless R_{th} values than

parallel flow cooling systems. An improved dimensionless R_{th} reduction was realized with additional channels mounted on the rectangular frame. The insertion of EAF$\varepsilon = 0.1$ in the channels achieves, a significant reduction of dimensionless R_{th}, as a substantial reduction in dimensionless Rth of cooling systems was recorded in Figure 6.12 compared to Figure 4.8. Thus, the enhancement of the cooling systems' thermal performance provided by the implementation of EAF$\varepsilon = 0.1$.

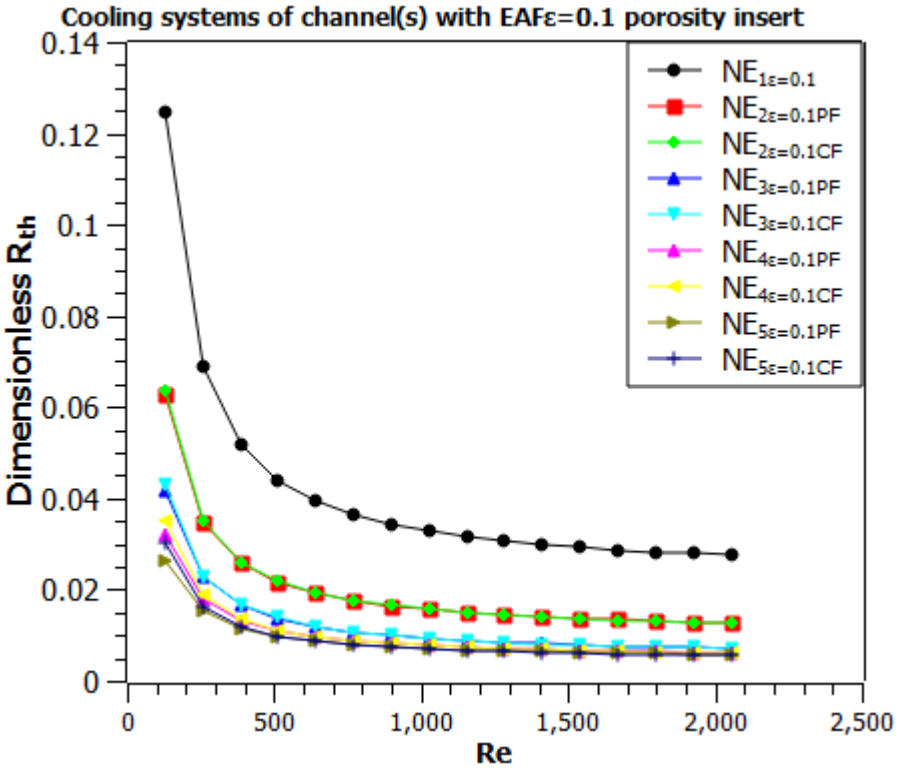

Figure 0.12. Dimensionless thermal resistance (R_{th}) Vs Reynolds number (Re) of the cooling system with a centrally located elliptical aluminum foam of 0.1 porosity ($EAF\varepsilon = 0.1$) insert in the channel(s). The color markers represent the cooling system of different numbers of channel(s) with a $EAF\varepsilon = 0.1$ insert mounted on the rectangular frame.

6.3.2.1.3 Cost of pumping power

Figure 6.13 illustrates the increase in the cost of pumping power (*Pp*) with an increased Reynolds number (*Re*) for the cooling systems equipped with an elliptical aluminum foam of 0.1 porosity (EAF$\varepsilon = 0.1$) insert. When the *Re* grew from 283.83 to 641.9, a gradual increase in *Pp* was realized, and a substantial gain of *Pp* was recorded when *Re* further increased beyond this point. In a like manner, an increase in the number of channels mounted on the rectangular frame significantly incurred higher values of *Pp*. [197]. However, counterflow cooling systems

slightly incurred higher *Pp* than parallel flow cooling systems. This was consistent with the published work of [47]. However, an outrageous value of *Pp* was recorded when EAFε=0.1 was inserted in the channels of cooling systems (Figure 6.13) compared to cooling systems with no insert in the channel(s) (Figure 4.9), suggesting a higher pressure drop associated with the inclusion of EAFε=0.1 in the fluid domain.

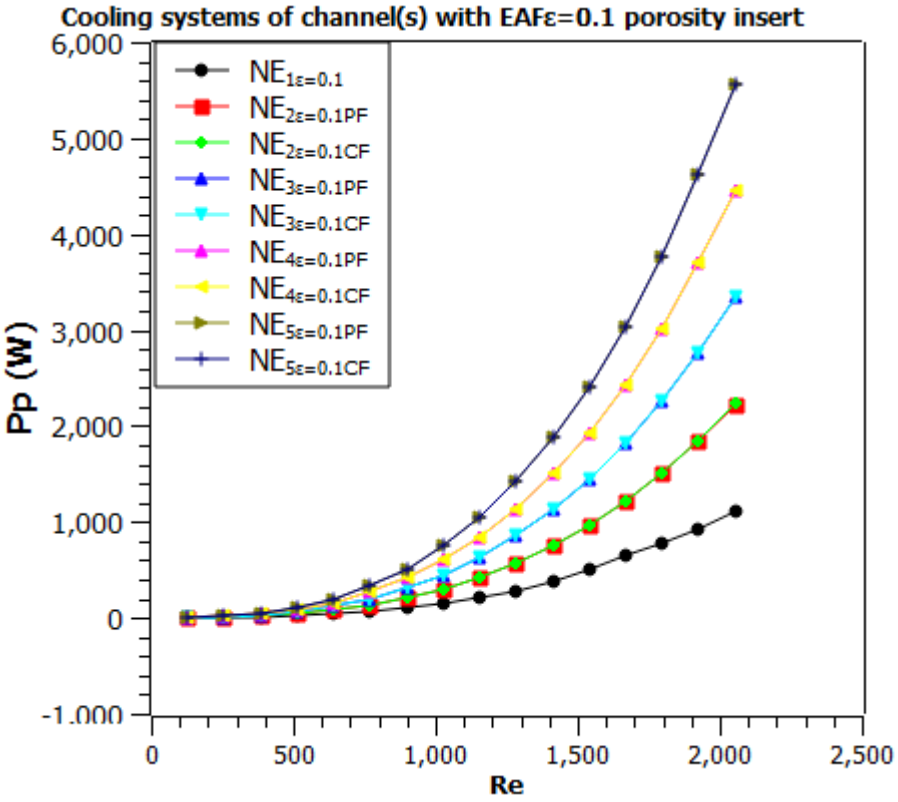

Figure 0.13. Cost of pumping power (*Pp*) vs Reynolds number (*Re*) of the cooling system with a centrally located elliptical aluminum foam of 0.1 porosity ($EAF\varepsilon = 0.1$) insert in the channel(s). The color markers represent the cooling system of different numbers of channel(s) with a $EAF\varepsilon = 0.1$ insert mounted on the rectangular frame.

6.3.2.2 Effect of channel number on dimensionless heat transfer rate density of the cooling systems with centrally located (L/2) elliptical aluminum foam of 0.1 porosity of insert in the channel

Figures 6.14 expresses the relationship between the dimensionless heat transfer rate density and the number of channels with EAFε=0.1 inserted located at the center (L/2), mounted on the rectangular frame of the cooling systems (Equations 3.36-3.38)). The figures show an increase in the dimensionless heat transfer rate density with an increased Reynolds number

(*Re*), regardless of the number of channels mounted on the rectangular frame. However, parallel flow cooling systems (Figure 6.14a) achieved slightly lower dimensionless heat transfer rate density than counterflow cooling systems (Figure 6.14b). The highest dimensionless heat transfer rate density was obtained with three channels of EAFε=0.1 insert. For instance, the parallel flow cooling systems of 3 channels mounted on the rectangular frame increased the dimensionless heat transfer rate density by 22.17%, 15.58%, 12.46%, and 25.14% respectively, compared to 1, 2, 4, and 5 channels at *Re* 2054.08 (Figure 6.14b). These results show that the interaction between the working fluid and solid elements of the cooling system is suspected to be more pronounced with three channels of EAFε=0.1 insert. However, the dimensionless heat transfer rate density was increased by 92.30% at *Re* 2054.08 by the parallel flow cooling system of three channels with EAFε=0.1 insert (Figure 6.14a) in comparison to cooling systems of the same design without insert (Figure 4.10a). A similar enhancement of 92.62% was obtained in counterflow cooling systems, indicating the major significance of EAFε=0.1 inserts in improving the cooling system performance.

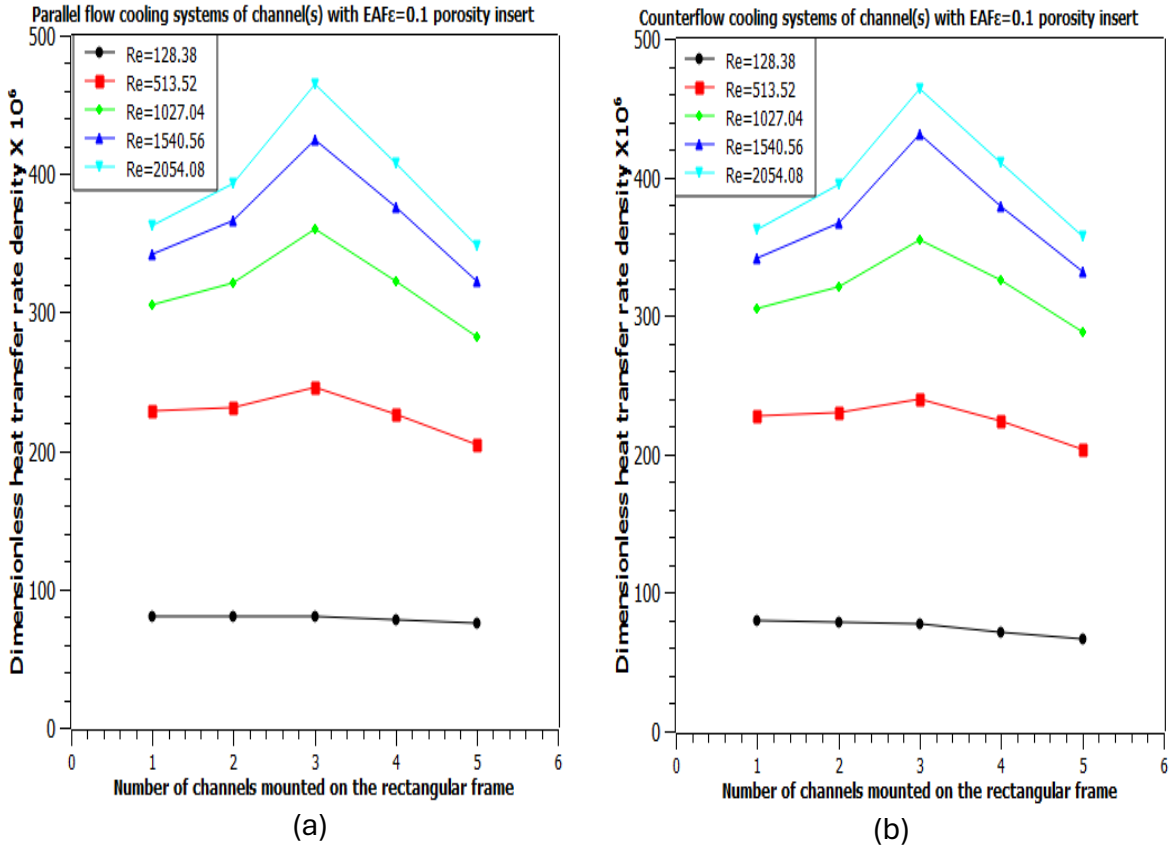

Figure 0.14. Dimensionless heat transfer rate density vs. number of channels mounted on the rectangular frame in Parallel (a) and Counterflow (b) cooling systems with elliptical aluminum

foam of 0.1 porosity (EAFε=0.1) inserts. Colored markers represent different Reynolds numbers (Re): Re = 128.38 (black), Re = 513.52 (red), Re = 1027.04 (green), Re = 1540.56 (blue), and Re = 2054.08.

6.3.2.3 Effects of the varying porosities of elliptical aluminum foam located at the center of the channel(s) on the thermal performance enhancement of the cooling system

Given the above results, it can be inferred that the highest thermal performance is obtained when three channels inserted with elliptical aluminum foam of (low) 0.1 porosity (EAFε=0.1) are mounted on the rectangular frame of the cooling system. Further analysis to investigate the effect of varying porosities of elliptical aluminum foam of (medium) 0.5 porosity insert (EAFε=0.5) and elliptical aluminum foam of (high) 0.9 porosity insert (EAFε=0.9) on the performance of this cooling system is conducted in this section.

6.3.2.3.1 Dimensionless thermal resistance

Figure 6.15 expresses the relationship between the Reynolds number and dimensionless thermal resistance (R_{th}) of cooling systems equipped with varying porosities of elliptical aluminum foam. An increase in *Re* leads to a decrease in dimensionless R_{th}. Changing the *Re* from 128.38 to 1283.8 offers a significant drop in dimensionless R_{th} and beyond this point, influence of *Re* on the dimensionless R_{th} was recorded insignificant. $NE_{3\varepsilon=0.1CF}$ reduced the dimensionless R_{th} by 7.7% and 19.3% compared to $NE_{3\varepsilon=0.5CF}$ and $NE_{3\varepsilon=0.9CF}$ respectively at *Re* 1155.42 Parallel flow cooling systems exhibit a similar pattern. Thus, the lesser the porosity of elliptical aluminum foam in the channel the higher the capacity of the cooling systems to remove heat from the battery pack. However, cooling systems with counterflow arrangements achieved slightly lower dimensionless R_{th} than those with parallel flow arrangements regardless of the porosity of the elliptical aluminum foam insert.

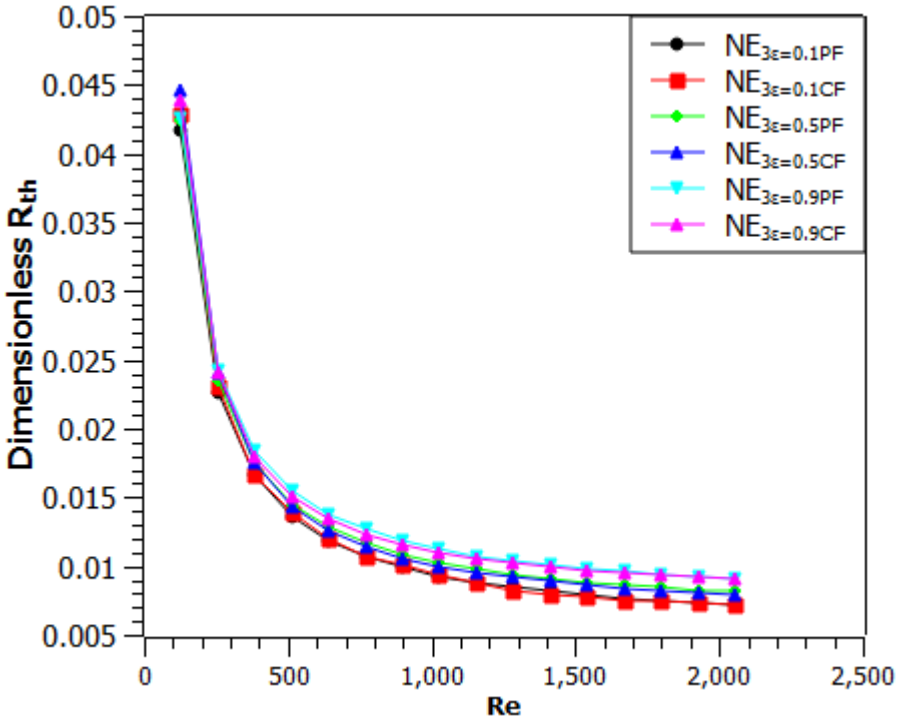

Figure 0.15. Dimensionless thermal resistance (R_{th}) vs Reynolds number (*Re*) of the cooling system with elliptical aluminum foam of varying porosities insert. The color markers illustrate counterflow (CF) and parallel flow (PF) cooling systems equipped with a single aluminum foam of 0.1 porosity ($NE_{3\varepsilon=0.1CF}$ and $NE_{3\varepsilon=0.1PF}$), 0.5 porosity ($NE_{3\varepsilon=0.5CF}$ and $NE_{3\varepsilon=0.5PF}$) as well as 0.9 porosity ($NE_{3\varepsilon=0.9CF}$ and $NE_{3\varepsilon=0.9PF}$).

6.3.2.3.2 Cost of pumping power

From Figure 6.16, an increase in the cost of pumping power (*Pp*) was observed with an increased Reynolds number (*Re*), regardless of the design of the cooling system. Compared to the *EAFε=0.5* and *EAFε=0.9*, the figure shows an outrageous increase of *Pp* when *EAFε=0.1* was inserted in the channels of the cooling systems, regardless of the flow orientations. Meanwhile, the cooling system equipped with *EAFε=0.9* gave the lowest value of *Pp*. This indicates that the resistance to the fluid flow (pressure drop) rises with the decrease in porosity [44]. Within the range of applied Re in this work, parallel flow cooling systems have slightly lower *Pp* values than counterflow cooling systems, regardless of the porosity of elliptical aluminum foam.

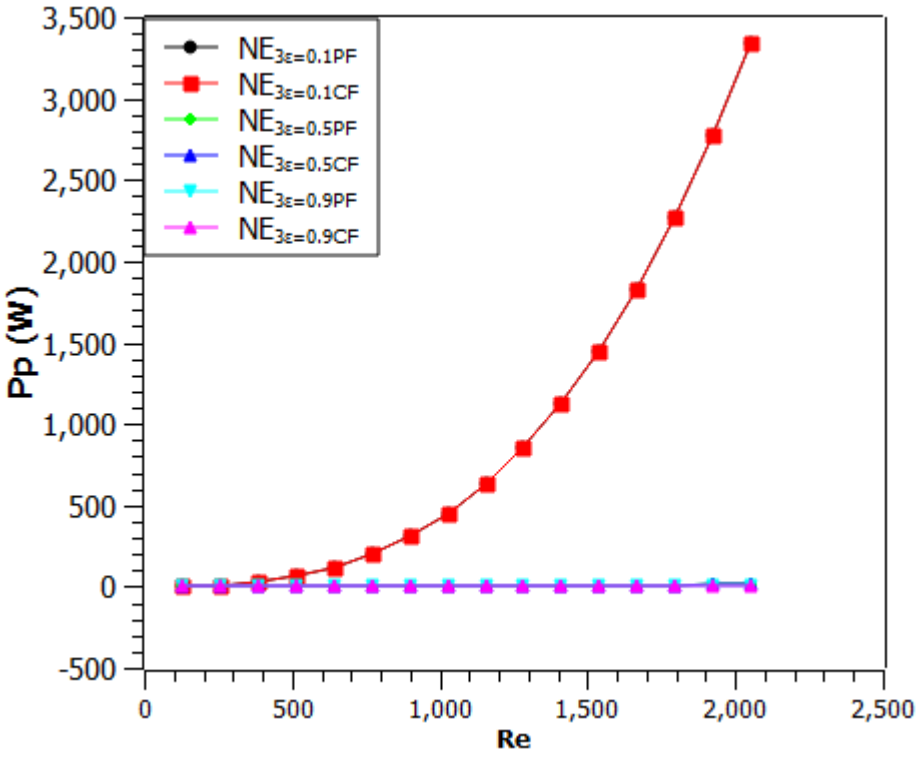

Figure 0.16. Cost of pumping power (*Pp*) vs Reynolds number (*Re*) of the cooling system with elliptical aluminum foam of varying porosities insert. The color markers illustrate counterflow (CF) and parallel flow (PF) cooling systems equipped with a single aluminum foam of 0.1 porosity ($NE_{3\varepsilon=0.1CF}$ and $NE_{3\varepsilon=0.1PF}$), 0.5 porosity ($NE_{3\varepsilon=0.5CF}$ and $NE_{3\varepsilon=0.5PF}$) as well as 0.9 porosity ($NE_{3\varepsilon=0.9CF}$ and $NE_{3\varepsilon=0.9PF}$).

6.3.2.3.3 Thermal Performance Enhancement Factor

Regardless of the porosity of the elliptical aluminum foam inserted in the cooling system channels, Figure 6.17 reports an increase in the Reynolds number *(Re)* with an increased thermal performance enhancement factor *(TPEF).* For the range of applied Re in this work, a slightly higher value of *TPEF* was obtained with the counterflow system than with the parallel flow cooling systems. However, an increase of 63.7% and 93.4% in *TPEF* was achieved with $NE_{3\varepsilon=0.9PF}$ over $NE_{3\varepsilon=0.5PF}$ and $NE_{3\varepsilon=0.1PF}$ respectively at *Re* 1155.4. The result implies that the tolerability of pressure drop to the obtained augmentation of heat transfer in the channels appreciates with an increased porosity of insert. This was further substantiated by the demonstration of *TPEF* less than 1 by the cooling system equipped with EAFε=0.5 and EAFε=0.1. Therefore, this study does not recommend the option of EAFε=0.5 and EAFε=0.1 for the thermal performance enhancement of the cooling system

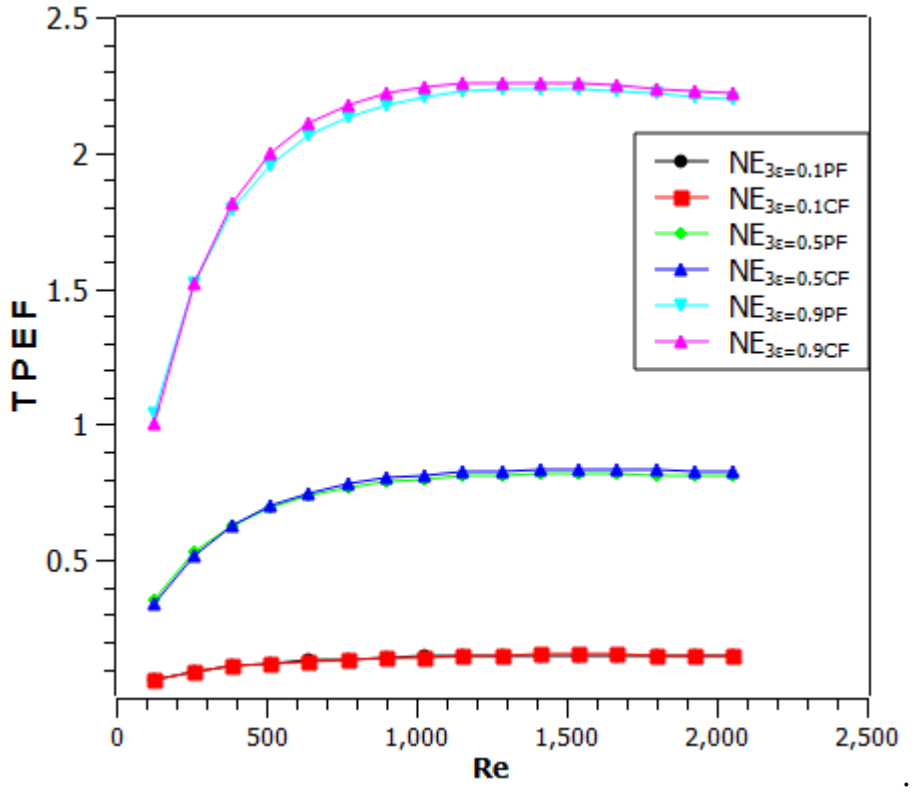

Figure 0.17. Thermal performance enhancement factor (*TPEF*) vs Reynolds number (*Re*) of the cooling system with elliptical aluminum foam of varying porosities inserted. The color markers illustrate counterflow (CF) and parallel flow (PF) cooling systems equipped with a single aluminum foam of 0.1 porosity ($NE_{3\varepsilon=0.1CF}$ and $NE_{3\varepsilon=0.1PF}$), 0.5 porosity ($NE_{3\varepsilon=0.5CF}$ and $NE_{3\varepsilon=0.5PF}$) as well as 0.9 porosity ($NE_{3\varepsilon=0.9CF}$ and $NE_{3\varepsilon=0.9PF}$).

6.3.2.4 Effect of varying locations of a single elliptical aluminum foam of 0.9 porosity (EAFε=0.9) inserted in the channel(s) on the cooling system's performance

The cooling system with three channels and a centrally positioned EAFε=0.9 (at L/2) was found to have the strongest capacity to dissipate heat from the battery pack in the preceding section given that it gives the maximum dimensionless heat transfer rate density. Therefore, the effect of the varying locations within the channels of this cooling system is further considered to evaluate the likely impacts of various EAFε=0.9 placements on heat dissipation effectiveness and thermal performance. This analysis explores whether alternative EAFε=0.9 placements can further augment cooling system performance beyond the best configuration identified earlier.

Figure 6.18 reveals that dimensionless R_{th} reduces noticeably when the Reynolds number (*Re*) increases regardless of the locations of EAFε=0.9 in the cooling system's channels. It can be noticed that significant dimensionless R_{th} reduction is observed when the *Re* increased from 128.38 to 1283.8. However, an insignificant *Re* effect on dimensionless R_{th} was noticed beyond this point. Within the range of *Re* applied in this work, counterflow cooling systems demonstrate slightly lower dimensionless R_{th} than those with parallel flow design. With *Re* 1412.18, $NE_{M\varepsilon=0.9CF}$ gave the best result in minimizing the dimensionless R_{th} by 11.6% and 15.3% respectively compared to $NE_{J\varepsilon=0.9CF}$ and $NE_{3\varepsilon=0.9CF}$. A similar performance was recorded with parallel flow cooling systems. Thus, the placement of EAFε=0.9 at L/8 in the channels appears to be the best location for the improved performance of the cooling systems.

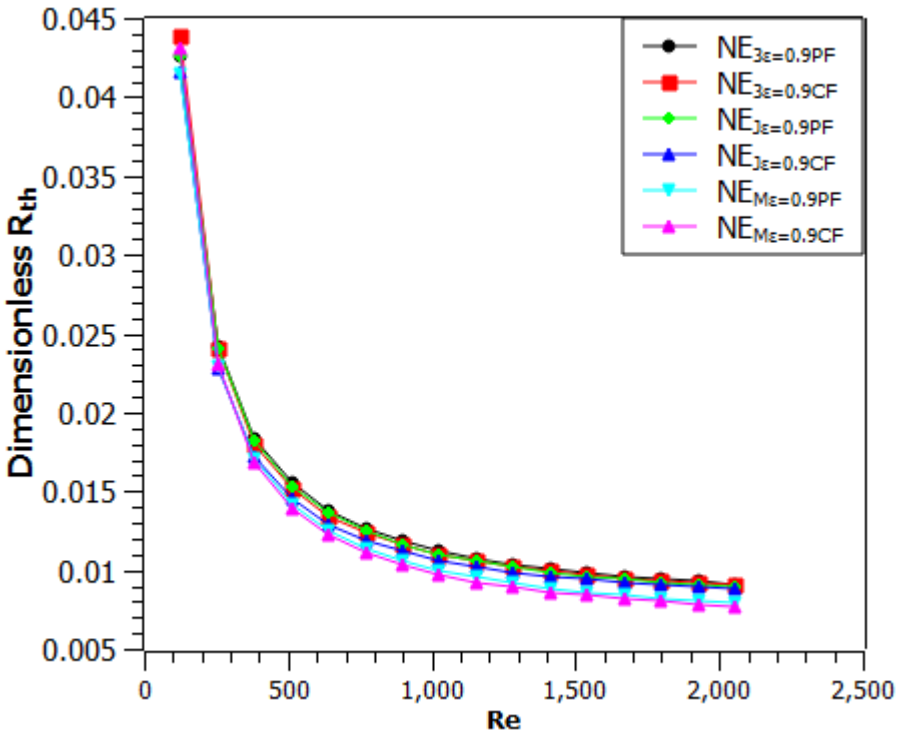

Figure 0.18. Dimensionless thermal resistance (R_{th}) vs Reynolds number (*Re*) of the cooling system with a single elliptical aluminum foam of 0.9 *(EAFε=0.9)* porosity insert. The colored markers illustrate counterflow (CF) and parallel flow (PF) cooling systems equipped with a single EAFε=0.9 located at L/2 ($NE_{3\varepsilon=0.9CF}$ and $NE_{3\varepsilon=0.9PF}$), ($NE_{J\varepsilon=0.9CF}$ and $NE_{J\varepsilon=0.9PF}$), and L/8 ($NE_{M\varepsilon=0.9CF}$ and $NE_{M\varepsilon=0.9PF}$).

6.3.2.5 Comparison of a single and varying spacing arrangement of three elliptical aluminum foam (EAFε=0.9) insert(s) in the channel(s) on the cooling system's performance

To compare the influence of a single with multiple insert(s) in the channels on the cooling system thermal performance, the *EAFε=0.9* was increased to three and arranged from *L/8* towards the inlet. It is worth noting that without emphasis on the search for the best insert location in the channels, [208] has previously demonstrated the precision of three-pin fin inserts for the optimal performance of the cooling configuration. Hence, the reason for adopting three *EAFε=0.9* of varying in-line spacing arrangements (1.5mm, 2.0mm, and 2.5mm) for comparison with a single *EAFε=0.9*.

Figure 6.19 shows the reduction in the dimensionless thermal resistance (R_{th}) with an increase in Reynolds number (*Re*) regardless of the number and spacing arrangements of the EAFε=0.9 in the channels. A substantial dimensionless R_{th} reduction occurred when the *Re* increased from 128.38 to 1283.8 and when the *Re* exceeded this, the dimensionless R_{th} reduction was negligible. Furthermore, the counterflow cooling system slightly improves in dimensionless R_{th} reduction compared to the parallel flow cooling systems. Meanwhile, the best spacing arrangement of multiple (three) EAFε=0.9 in the channels appears to be 1.5 mm as $NE1.5M_{\varepsilon=0.9CF}$ reduced the dimensionless R_{th} by 10.5% and 11.9% compared to $NE2.0M_{\varepsilon=0.9CF}$ and $NE2.5M_{\varepsilon=0.9CF}$ respectively at *Re* 898.66. Thus, minimizing of the space between the EAFε=0.9 in the channels leads to better enhancement of the cooling system thermal performance. On the other hand, $NE_{M\varepsilon=0.9PF}$ obtained a lower dimensionless R_{th} reduction of 19.5%. 18.8% and 4.7% compared to $NE2.5M_{\varepsilon=0.9PF}$, $NE2.0M_{\varepsilon=0.9PF}$, and $NE1.5M_{\varepsilon=0.9PF}$ respectively at *Re* 2054.08 demonstrating the overperformance of the cooling systems equipped with a single EAFε=0.9 than those with multiple (three) EAFε=0.9. Counterflow cooling systems exhibited a similar pattern.

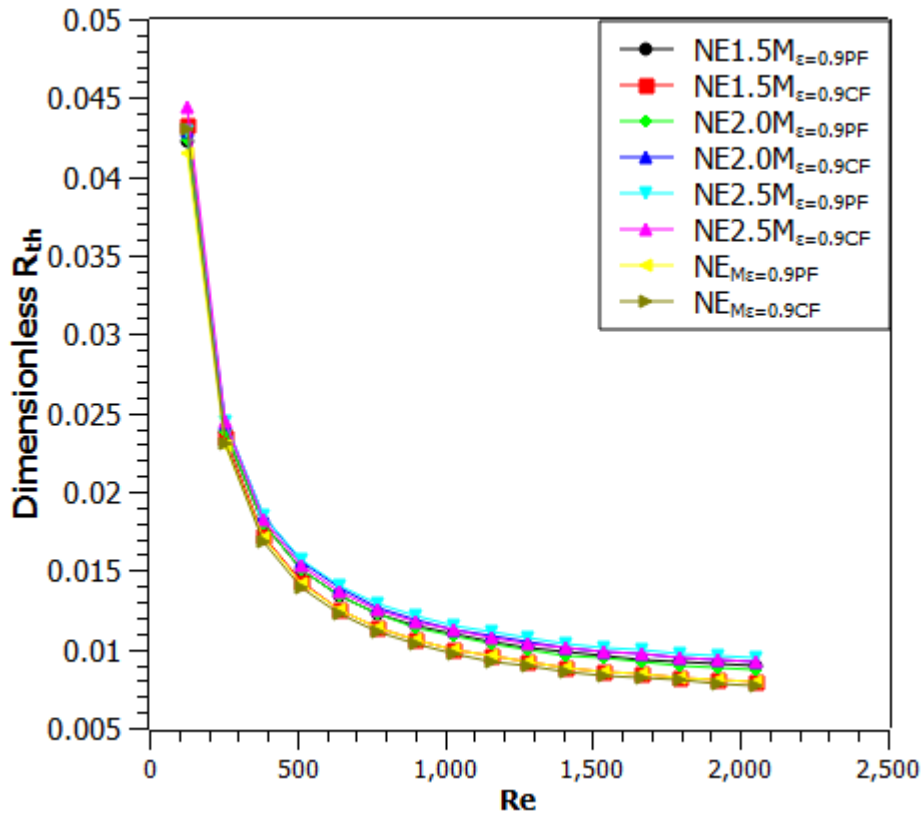

Figure 0.19. Dimensionless thermal resistance (R_{th}) vs. Reynolds number (*Re*) of the cooling system with elliptical aluminum foam of 0.9 (EAFε=0.9) porosity insert(s). The color markers illustrate counterflow (CF) and parallel flow (PF) cooling systems equipped with a single EAFε=0.9 ($NE_{M\varepsilon=0.9CF}$ and $NE_{M\varepsilon=0.9PF}$), and 1.5 mm ($NE1.5M_{\varepsilon=0.9CF}$ and $NE1.5M_{\varepsilon=0.9PF}$), 2.0 mm ($NE2.0M_{\varepsilon=0.9CF}$ and $NE2.0M_{\varepsilon=0.9PF}$), and 2.5 mm ($NE2.5M_{\varepsilon=0.9CF}$ and $NE2.5M_{\varepsilon=0.9PF}$) spacing arrangements of three EAFε=0.9 in the channels.

6.3.2.6 Normalized friction factor effect between the varying locations of a single and spacing arrangement of three elliptical aluminum foam of 0.9 porosity (EAFε=0.9)

In Figures 6.20, the upward trend of the normalized friction factor (*NFF*) was observed with an increase in Reynolds number (*Re*). The exhibition of *NFF* values higher than 3 by both figures suggests that the application of EAFε=0.9 to enhance of the cooling system performance can raise its working fluid friction more than 3 times compared to those without insert [40]. From Figure 6.20a, $NE_{M\varepsilon=0.9CF}$ reduced the *NFF* by 2.8% and 5.5% respectively compared to $NE_{J\varepsilon=0.9CF}$ and $NE_{3\varepsilon=0.9CF}$ at *Re* 898.66 indicating that the shorter the distance between a single EAFε=0.9 and the inlet the lesser the values of *NFF* and vice versa. Meanwhile, Figure 6.20b shows that the minimization of the space between one EAFε=0.9 to

the other increases the value of the *NFF* [200]. For instance, $NE2.5M_{\varepsilon=0.9CF}$ reduces the *NFF* values by 8.6% and 13.4% compared to $NE2.0M_{\varepsilon=0.9CF}$ and $NE1.5M_{\varepsilon=0.CPF}$ respectively at *Re* 2054.08. Moreover, a higher value of *NFF* was obtained in cooling systems with multiple EAFε=0.9 inserts (Figure 6.20b) compared to those with a single EAFε=0.9 (Figure 6.20a), demonstrating the effect of the fluid domain complexity on the pressure drop along the flow channels. With single or multiple EAFε=0.9 insert(s), the cooling systems with counterflow arrangement slightly increased the *NFF* values compared to those of parallel flow configurations.

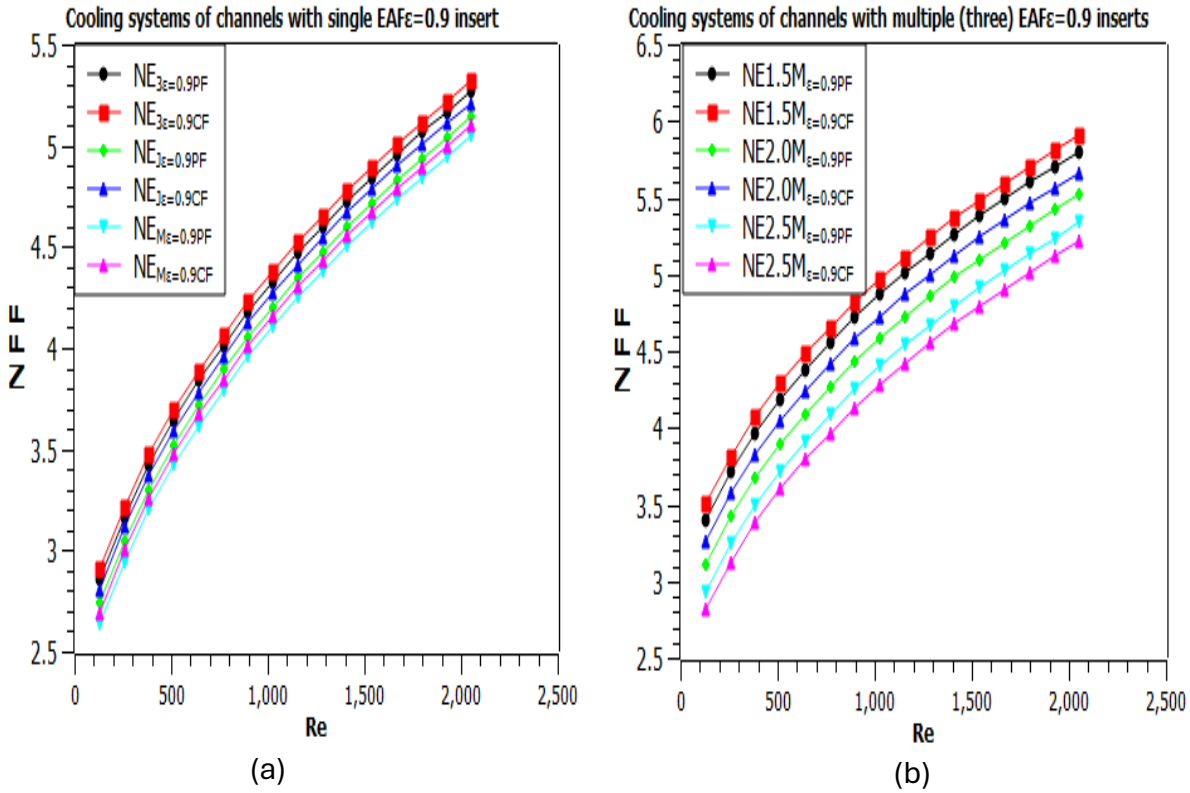

Figure 0.20. Normalized friction factor (*NFF*) vs. Reynolds number (*Re*) of the cooling system with a single (a) and three (b) elliptical aluminum foam of 0.9 (EAFε=0.9) porosity insert(s). The color markers illustrate counterflow (CF) and parallel flow (PF) cooling systems equipped with varying locations of a single and spacing arrangement of multiple EAFε=0.9 in the channels.

6.3.2.7 Comparison of thermal performance enhancement factor effect between the varying location of a single and varying spacing arrangement of three elliptical aluminum foam of 0.9 porosity (EAFε=0.9)

Figure 6.21 shows that an increase in Reynolds number (*Re*) increases the thermal performance enhancement factor (*TPEF*) regardless of the cooling system configuration. A significant rise

in *TPEF* occurred when the *Re* increased from 123.83 to 898.66. However, beyond this point, the effect of further increases in *Re* on *TPEF* became negligible. A slight increase in *TPEF* was achieved with cooling systems of counterflow arrangements compared to those parallel flow designs regardless of the number and spacing arrangements of EAFε=0.9 in the channels. However, the demonstration of *TPEF* higher than 1 observed with the considered cooling systems shows that the application of EAFε=0.9 can augment heat transfer with a tolerable increased friction factor [45]. The figure shows that the 2.0 mm spacing arrangement gives the highest *TPEF* compared to 1.5 mm and 2.5 mm. For instance, $NE2.0M_{\varepsilon=0.9CF}$ increased *TPEF* by 1.7% and 2.94% compared to $NE1.5M_{\varepsilon=0.9CF}$ and $NE2.5M_{\varepsilon=0.9CF}$ respectively at *Re* 898.66. Thus, the frictional factor effect on the enhancement of heat transfer appears more tolerable with cooling systems of 2.0 mm spacing arrangement of *EAFε=0.9* in the channels regardless of the flow orientations. Meanwhile, $NE_{M\varepsilon=0.9CF}$ demonstrates an improved *TPEF* of 2.9%, 1.5% and 2.1 over $NE2.5M_{\varepsilon=0.9CF}$, $NE2.0M_{\varepsilon=0.9CF}$, and $NE1.5M_{\varepsilon=0.9CF}$ respectively at *Re* 2054.08. A similar pattern was observed with the parallel flow cooling systems. This result indicates that a single *EAFε=0.9* located at *L/8* in the channels can enhance the overall thermal performance of the cooling system better than multiple (three) *EAFε=0.9* inserts.

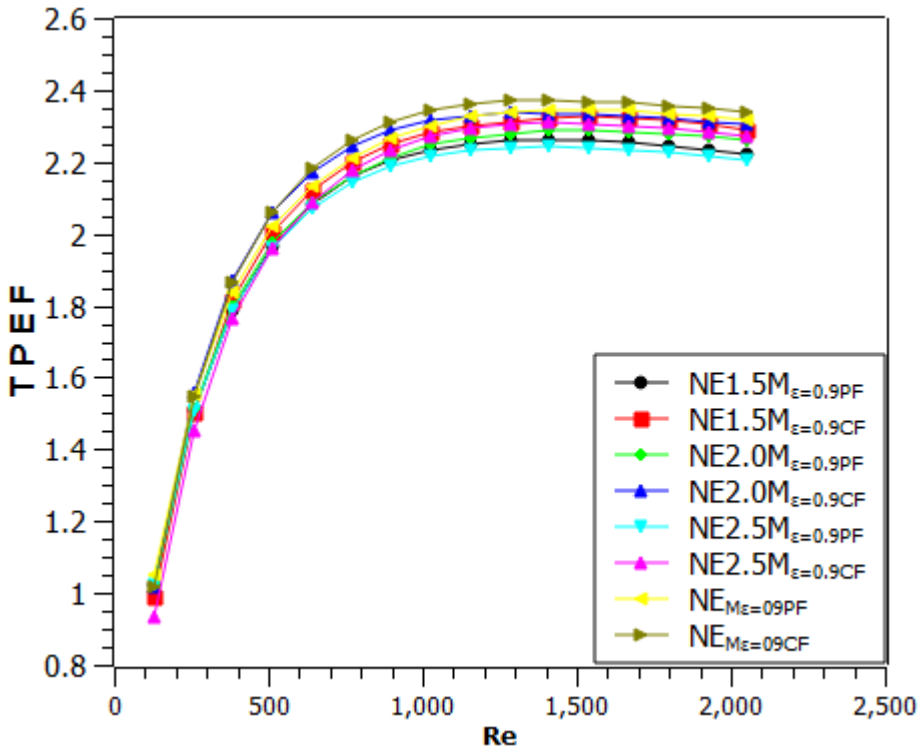

Figure 0.21. Thermal performance enhancement factor (*TPEF*) vs. Reynolds number (*Re*) of the cooling system with elliptical aluminum foam of 0.9 *(EAFε=0.9)* porosity insert(s). The color markers illustrate counterflow (CF) and parallel flow (PF) cooling systems equipped with

a single *EAFε=0.9* ($NE_{M\varepsilon=0.9CF}$ and $NE_{M\varepsilon=0.9PF}$), and 1.5 mm ($NE1.5M_{\varepsilon=0.9CF}$ and $NE1.5M_{\varepsilon=0.9PF}$), 2.0 mm ($NE2.0M_{\varepsilon=0.9CF}$ and $NE2.0M_{\varepsilon=0.9PF}$), and 2.5 mm ($NE2.5M_{\varepsilon=0.9CF}$ and $NE2.5M_{\varepsilon=0.9PF}$) spacing arrangements of three EAFε=0.9 in the channels.

6.3.2.8 Temperature uniformity of the battery cells in the pack

Figures. 6.22(a-d) describes the relationship between the Reynolds number and the temperature uniformity of the battery cells in the pack. At a specific *Re*, a temperature uniformity of less than 2℃ between one cell to the other in a pack was achieved. Thus, the capacity of the cooling systems to maintain the temperature uniformity of the lithium-ion battery cells in a pack is suspected [13]. The implementation of elliptical aluminum foam of 0.1 porosity (*EAFε=0.1*) provides a significant reduction in battery cells' temperature uniformity as indicated when Figure 6.22 (a) and (b) were compared to Figure 4.11(a) and (b). In addition, the coalescing of the graph observed in Figures 6.22 (a) and (b) compared to Figures 4.11(a) and (b) demonstrates the strength of the insertion of *EAFε=0.1* in the channels of the cooling system to improve the temperature uniformity of the battery cells in the pack. Meanwhile, counterflow cooling systems (Figure 6.22b) achieved a slightly lower battery cell temperature uniformity than the parallel flow cooling system (Figure 6.22a). $NE_{3\varepsilon=0.9CF}$ (Figure 6.22c) with higher values of battery cell temperature uniformity than $NE_{3\varepsilon=0.1CF}$ (Figure 6.22b) depicts the cooling system's response to different porosity of the elliptical aluminum foam insert. Nevertheless, EAFε=0.9 at L/8 in the channels further reduced the battery cells' temperature uniformity as shown in Figure 6.22d compared to Figure 6.22c.

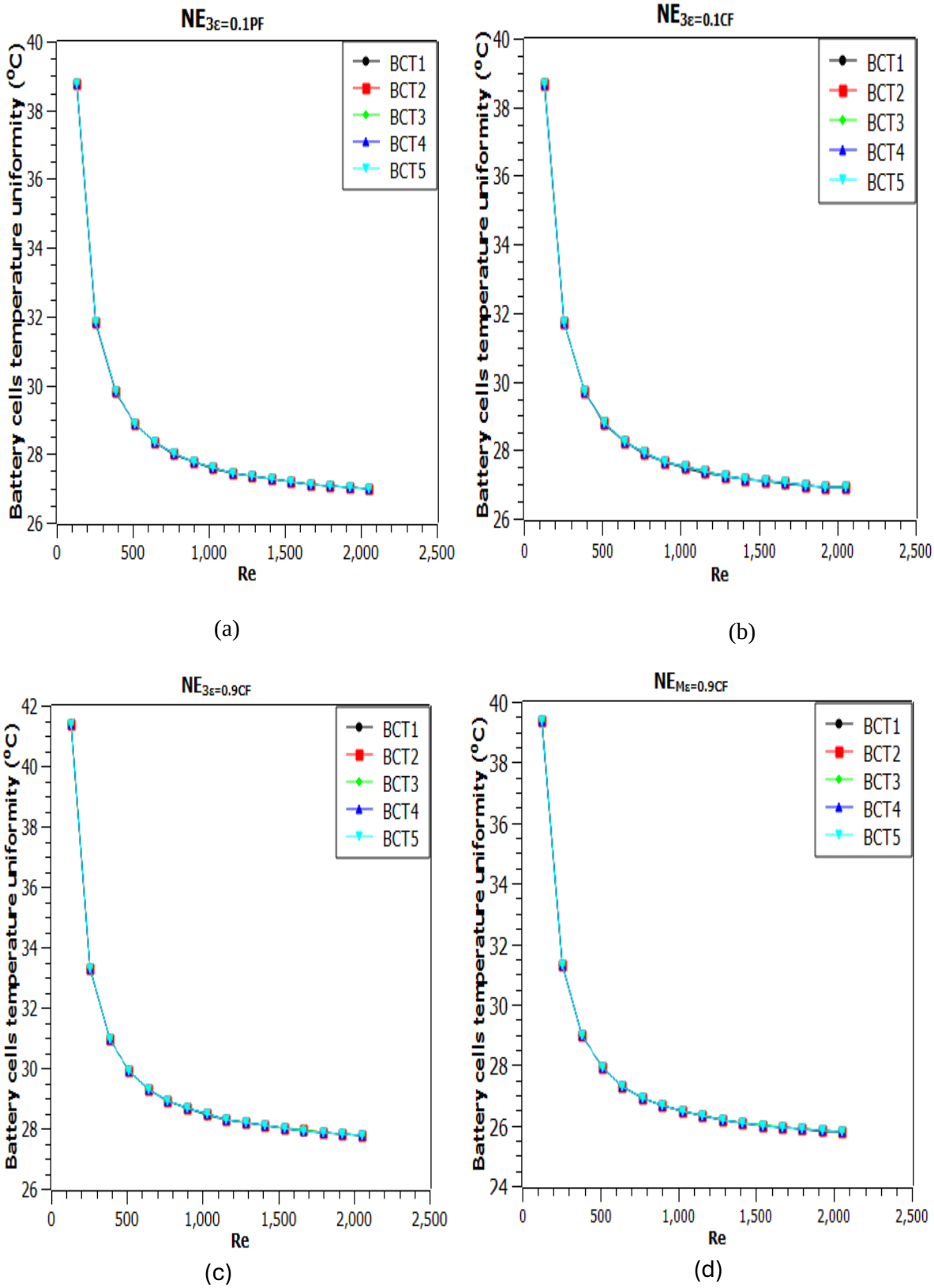

Figure 0.22. Battery cells temperature uniformity vs Reynolds number for the cooling system of three channels containing single elliptical aluminum foam of 0.1*(EAFε=0.1)* and 0.9

(CAFε=0.9) porosities: Parallel (a) and counterflow (b) system with centrally located *CAFε=0.1*, as well as counterflow system with *EAFε=0.9* inserted at the center (c) and *L/8* (d). The color makers represent the temperatures of each battery cell in a pack.

6.3.3 Case 3: Comparison of the enhancement capacity of the elliptical solid pin fin with aluminum foam inserted in the channel(s) of the cooling system

6.3.3.1 Effect of Reynolds number on the thermal performance of the cooling system based on circular solid pin fin and elliptical aluminum foam insert comparison

This section analyzed the influence of the Reynolds number on the maximum rectangular frame wall temperature, dimensionless thermal resistance, cost of pumping power, and thermal performance enhancement factor for the two counterflow cooling systems: with the elliptical solid pin fin insert located at *L/8 (NE_{MCF})* in Case 1 and the elliptical aluminum foam insert with 0.9 porosity located at *L/8* ($NE_{M\varepsilon=0.9CF}$) in Case 2. These systems have been identified as the most promising configurations for effective battery pack thermal management.

6.3.3.1.1 Maximum rectangular frame wall temperature

Figure 6.23, reports the reduction in maximum wall temperature (T_{max}) of the rectangular frame with Reynolds number (*Re*) regardless of the type of insert in the channels of the cooling systems. The figure shows a substantial reduction in T_{max} when the *Re* increased from 128.38 to 1283.8 and beyond this, the *Re* effect on T_{max} became insignificant. Meanwhile, NE_{MCF} gave the best result in minimizing the T_{max} than $NE_{M\varepsilon=0.9CF}$ within the applied *Re* in this work. For instance, at the extreme low (128.38) and high (2054.08) *Re* considered in this work, NE_{MCF} reduced T_{max} by 0.58% and 0.28 respectively compared to $NE_{M\varepsilon=0.9CF}$. Thus, the cooling system capacity is better enhanced by the application of ESPF than *EAFε=0.9*.

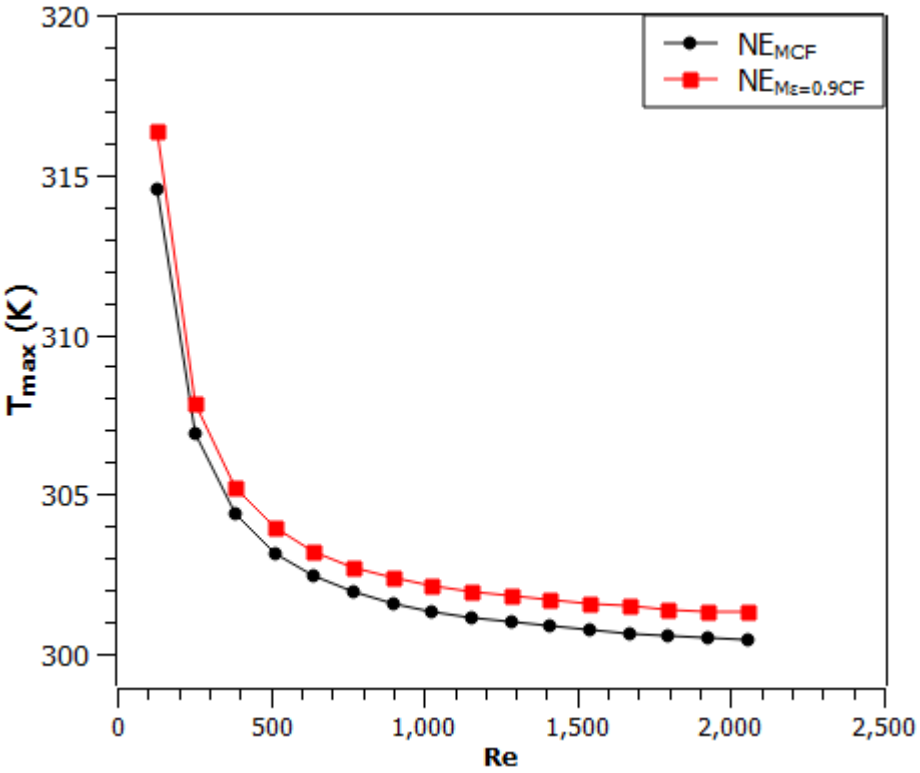

Figure 0.23. Maximum rectangular frame wall temperature (T_{max}) vs. Reynolds number (*Re*) for cooling systems with elliptical solid pin fin (ESPF) and aluminum foam of 0.9 porosity (EAFε=0.9) inserts. The graph shows T_{max} as a function of *Re*, comparing ESPF (black marker) and EAFε=0.9 (red marker) inserts located at *L/8* in the channels of the cooling systems.

6.3.3.1.2 Dimensionless thermal resistance

As shown in Figure 6.24, an increase in Reynolds number (*Re*) reduces the dimensionless thermal resistance (R_{th}) of both the cooling systems (NE_{MCF} and $NE_{M\varepsilon=0.9CF}$). When the *Re* increased from 128.38 to 1283.8, a substantial drop in the dimensionless R_{th} was realized. However, an insignificant dimensionless R_{th} was observed when the Re exceeded this point. For the range of the applied *Re* in this study, the application of ESPF *(NE_{MCF})* to enhance the system's performance achieves a consistently better cooling capacity in decreasing the dimensionless R_{th} than *$EAF\varepsilon=0.9$* ($NE_{M\varepsilon=0.9CF}$.). Thus, the application of ESPF provides an improved cooling system performance than the *$EAF\varepsilon=0.9$*.

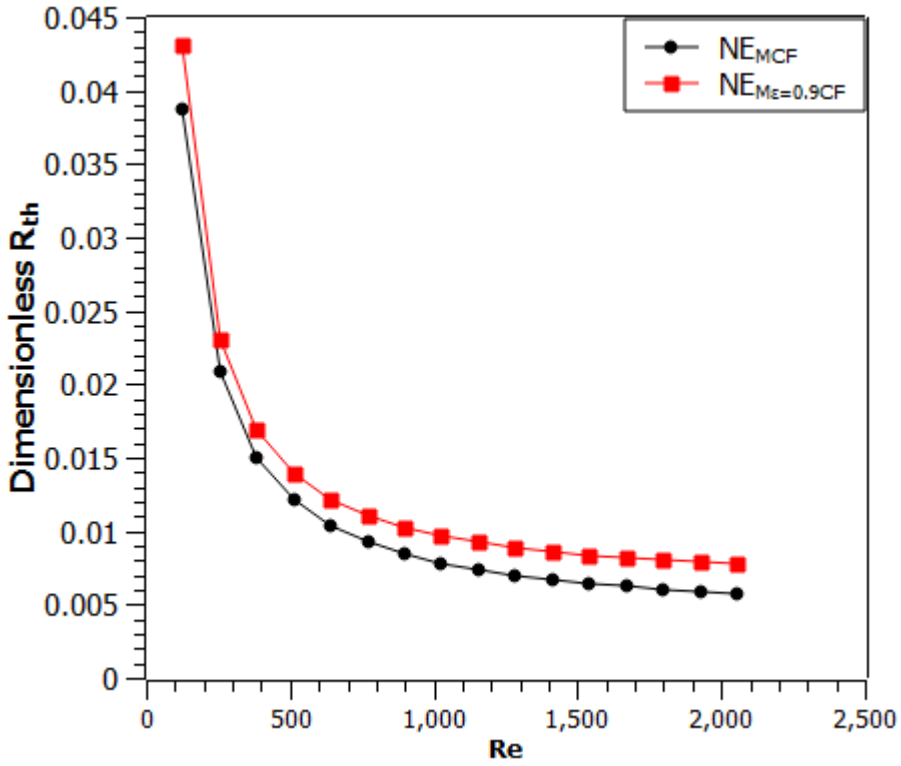

Figure 0.24. Dimensionless thermal resistance (R_{th}) vs. Reynolds number (*Re*) for cooling systems with elliptical solid pin fin (ESPF) and aluminum foam of 0.9 porosity *(EAFε=0.9)* inserts. The graph shows dimensionless R_{th} as a function of *Re*, comparing ESPF (black marker) and *EAFε=0.9* (red marker) inserts located at *L/8* in the channels of the cooling systems.

6.3.3.1.3 Cost of pumping power

Figure 6. 25, compares the effect of *EAFε=0.9* with ESPF on the cost of pumping power (*Pp*) of the cooling system as a function of the Reynolds number (*Re*). An increase in *Re* leads to an increase in *Pp*. However, a gradual increase in *Pp* was recorded below *Re* 770.28 and beyond this, a further increase in *Re* yields a significant upward trend of *Pp*. Meanwhile, NE_{MCF} achieves a slightly lower *Pp* compared to $NE_{M\varepsilon=0.9CF}$ when the *Re* increased from 12.38 to 513.52, a considerable increase in *Pp* was demonstrated by $NE_{M\varepsilon=0.9CF}$ over NE_{MCF} when the *Re* rises beyond 513.52. However, the figure shows an increase of 66.01% in *Pp* by $NE_{M\varepsilon=0.9CF}$ compared to the NE_{MCF} at the *Re* 2054.08. Thus, ESPF in the channels of the cooling systems appears to possess a significantly lesser value of *Pp* than *EAFε=0.9*, particularly at a higher *Re*.

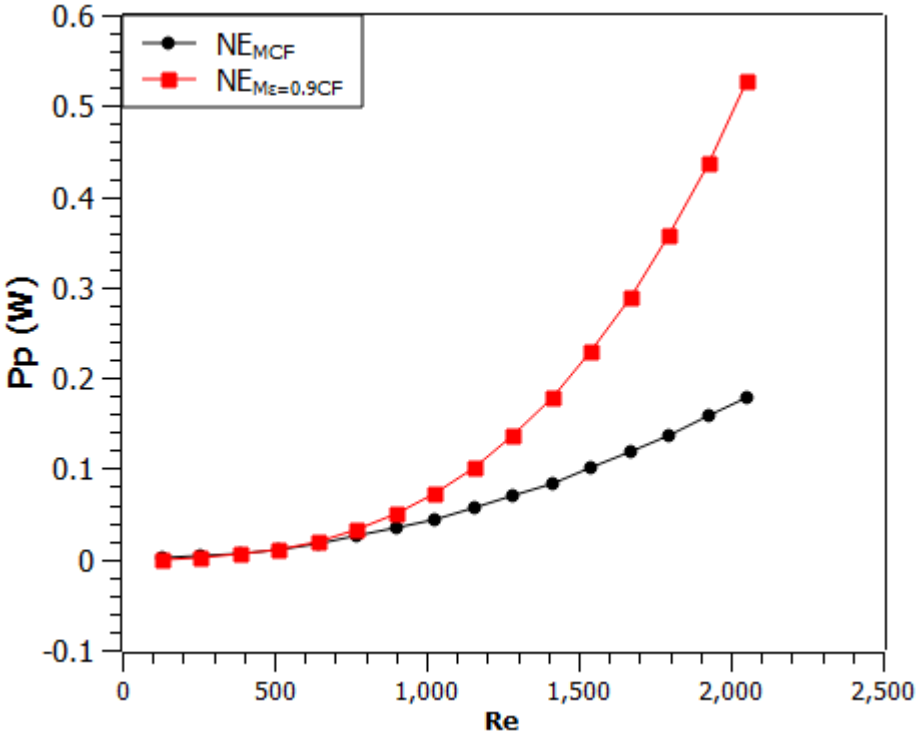

Figure 0.25. Cost of pumping power (*Pp*) vs. Reynolds number (*Re*) for cooling systems with elliptical solid pin fin (ESPF) and aluminum foam of 0.9 porosity *(EAFε=0.9)* inserts. The graph shows *Pp* as a function of *Re*, comparing ESPF (black marker) and *EAFε=0.9* (red marker) inserts located at *L/8* in the channels of the cooling systems.

6.3.3.1.4 Thermal performance enhancement factor

Figure 6.26 reveals that an increase in Reynolds number (*Re*) increases the thermal performance enhancement factor (*TPEF*) regardless of the type of insert (ESPF or *EAFε=0.9*) in the cooling system's channels. The figure shows that inserting either ESPF or *EAFε=0.9* in the channels can provide an enhancement of cooling system performance with a tolerable friction factor as both cooling systems ($NE_{M\varepsilon=0.9CF}$ or NE_{MCF}) archives *TPEF* higher than 1. Below the *Re* 513.52, $NE_{M\varepsilon=0.9CF}$ possess higher *TPEF* than NE_{MCF} and the reverse is the case when the *Re* increases beyond this point, as NE_{MCF} substantially increases the values of *TPEF* than $NE_{M\varepsilon=0.9CF}$. Thus, the effect of continuous increase in pressure drop along the flow path on cooling system performance appears to be more pronounced with the application of *EAFε=0.9* than with the ESPF insert, particularly at higher *Re* beyond 513.52. For the range of *Re* applied in this work, NE_{MCF} demonstrates continuous upward trending of *TPEF*, and at the same time, $NE_{M\varepsilon=0.9CF}$ shows a decline in *TPEF* values when the *Re* increases beyond 1412.18. Meanwhile, precisely at *Re* 1412.18 and 2054.08 NE_{MCF} gave the best result in

enhancing systems performance as it provides over 36.2% and 45.3% of increased *TPEF* compared to $NE_{M\varepsilon=0.9CF}$. Thus, ESPF appears to demonstrate better cooling system enhancement than EAFε=0.9.

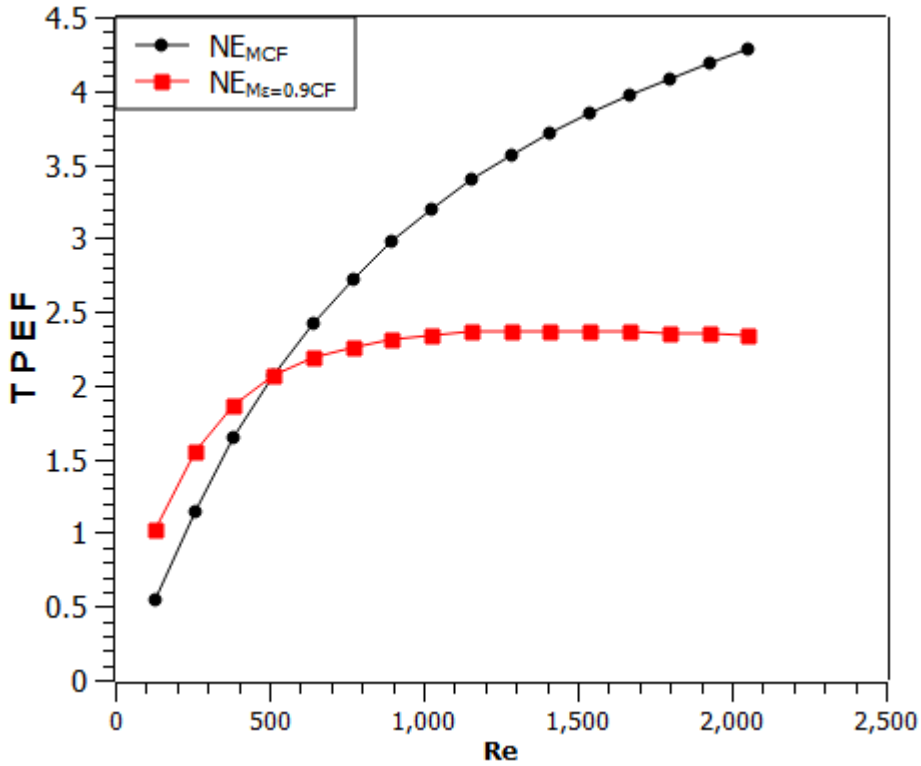

Figure 0.26. Thermal performance enhancement factor (*TPEF*) vs. Reynolds number (*Re*) for cooling systems with elliptical solid pin fin (ESPF) and aluminum foam of 0.9 porosity (EAFε=0.9) inserts. The graph shows *TPEF* as a function of *Re*, comparing ESPF (black marker) and *EAFε=0.9* (red marker) inserts located at *L/8* in the channels of the cooling systems.

6.3.3.2 Temperature contours

Figure 6.27 (a and b) depicts the temperature contours of the systems with either an insert of elliptical solid pin fin (ESPF) or aluminum foam of 0.9 porosity *(EAFε=0.9)* located at *L/8* towards the inlet. The contours are plotted at X plane 25mm and inlet velocity 1.1m/s (Reynolds number 1412.18). Notably, the system with ESPF *(NE_{MCF})* achieved a lower temperature distribution than that of the *EAFε=0.9* ($NE_{M\varepsilon=0.9CF}$) indicating the superiority of ESPF insert to dissipate heat from the batter pack than the *EAFε=0.9*.

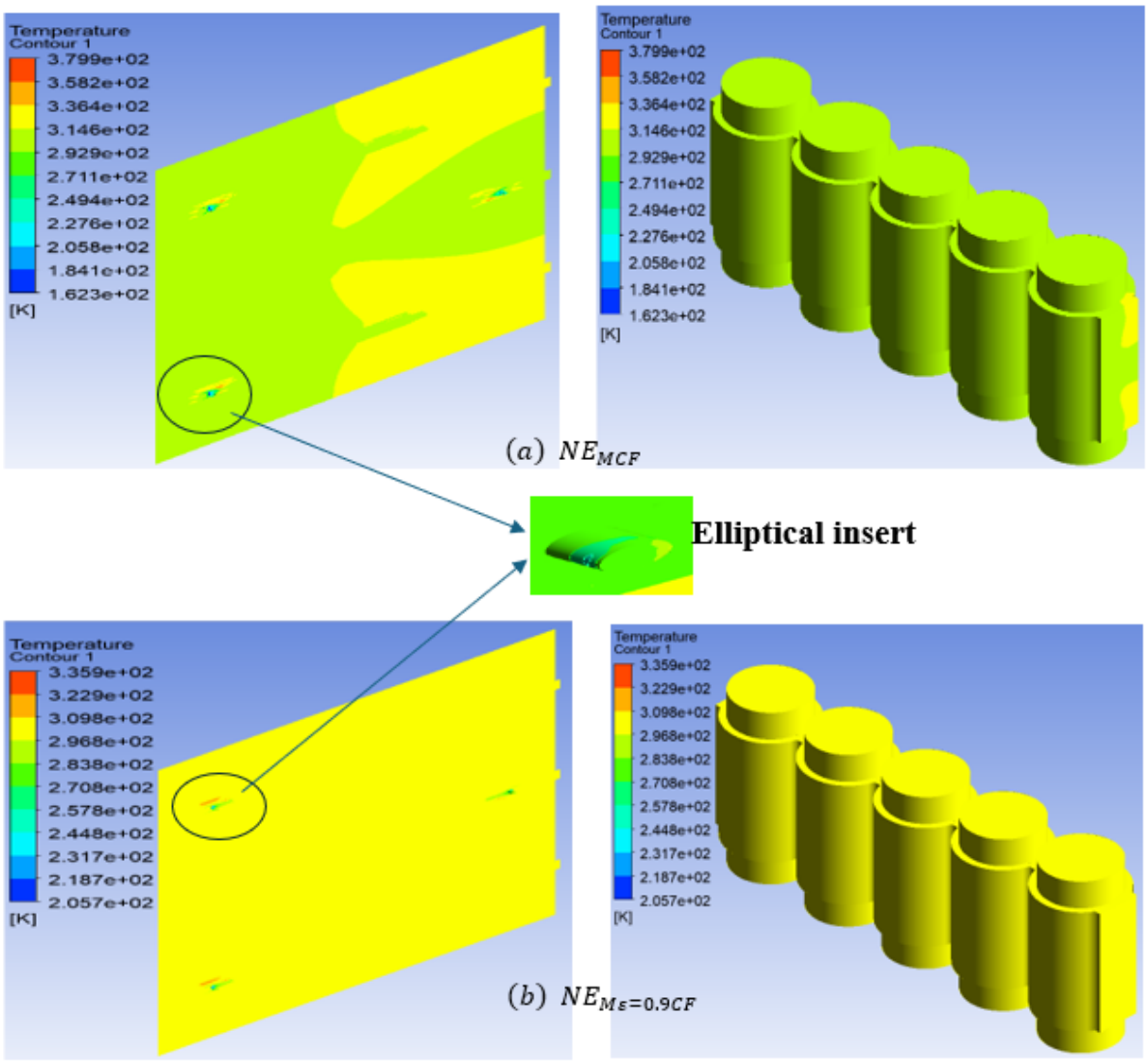

Figures 0.27. Temperature contour for counterflow cooling system of three channels with ESPF (a), and *EAFε=0.9* (b) insert.

6.4 Conclusions

This chapter details the effect of an elliptical solid pin fin and elliptical aluminum foam of varying porosities insert on the thermal performance of the cooling system for the thermal management of the cylindrical lithium-ion battery pack of an electric vehicle. For Re values ranging between 128.38 and 2054.08 as applied in this work, the response of the cooling system to the different number of channels mounted on the rectangular frame, the varying position of a single, and spacing arrangements of the multiple insert(s) in the channel(s) as well as varying porosities specifically for aluminum foam were numerically analyzed and reported. The Key findings are summarized below:

1) **Number of mounted channels**: (a) Maximum dimensionless heat transfer rate density was observed in systems with three channels of centrally located elliptical solid pin fin (ESPF) or aluminum foam of 0.1 porosity *(EAFε=0.1)* inserts on the rectangular frame. (b) At the highest applied Reynolds number, the parallel flow and counterflow systems of the three channels with ESPF respectively achieved 92.21% and 92.5% higher dimensionless heat transfer rate density in comparison to their counterparts with no insert. A similar pattern of the dimensionless heat transfer rate density increases of 92.30% and 92.62% were obtained with parallel flow and counterflow systems of the three channels with $EAF\varepsilon = 0.1$ inserts.

2) **Best insert location**: The best performance was achieved when the inserts (ESPF or aluminum foam) were positioned at *L/8* towards the leading edge of the channels.

3) **Impact of Porosity**: High porosity (0.9) elliptical aluminum foam inserts showed acceptable performance, while lower porosities (0.1 and 0.5) resulted in high pumping power and friction factor, limiting their applicability.

4) **Single versus Multiple Inserts**: A single insert positioned at *L/8* towards the leading edge- enhanced cooling performance more effectively than multiple inserts, regardless of spacing.

5) **Counterflow versus Parallel Flow Systems**: Counterflow cooling systems benefit slightly from reducing the maximum wall temperature and thermal resistance compared to parallel flow systems.

The superior thermal performance enhancement factor (*TPEF*) of the NE_{MCF} system compared to $NE_{M\varepsilon=0.9CF}$ suggests that the ESPF insert is the optimal choice for effective temperature control of cylindrical lithium-ion battery packs in electric vehicles. Therefore, NE_{MCF} is recommended in this chapter as the most effective cooling system for the cylindrical lithium-ion battery pack of electric vehicles.

CHAPTER SEVEN

ENHANCEMENT OF CYLINDRICAL LITHIUM-ION BATTERY PACK OF ELECTRIC VEHICLE COOLING SYSTEM WITH RECTANGULAR SOLID PIN FIN / ALUMINIUM FOAM OF DIFFERENT POROSITIES INSERT(S)

7.1 Preview

This chapter documents the enhancement potential analyses of the rectangular solid pin fin or aluminum foam of various porosities inserted in the channels of the designed cooling system from Chapter 4. With the centrally located insert in the channel, the cooling system performance is compared with previous obtained results from Chapter 4. The varying locations' effect of a single insert on the system performance was later considered and compared with varying spacing arrangements of three inserts in the channels. However, the performance will be evaluated with maximum rectangular frame wall temperature, thermal resistance, convective heat transfer coefficient, heat transfer rate density, and thermal performance enhancement factor. The discretization, mesh grid generation, and simulation process of the cooling systems were conducted with the Ansys® 2020 Fluent software package.

7.2 Physical and Computational Model

Figures 7.1(a-d), shows the cross-section of the computational domain of the cooling system inserted with single or multiple (three) rectangular solid pin fin/aluminum foam. With fixed dimensions of the cooling system as stated in Chapter 4, varying locations of a single rectangular solid pin fin/aluminum foam insert in the fluid domain are first considered. The 1.5 mm, 2.0 mm, and 2.5 mm spacing arrangements of three rectangular solid pin fins/aluminum foam in the fluid domain of the cooling system were further considered for comparison with a single insert at the finest location in the channels. The rectangular solid pin fin/aluminum foam used in this work is of dimensions $1.1\,\text{mm} \times 0.6\,\text{mm} \times 0.6\,\text{mm}$ while the considered porosities are low (0.1), medium 0.5, and high (0.9)

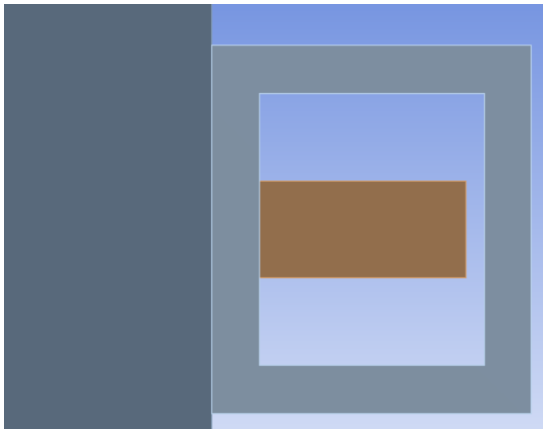

(a). Cooling system cross-section with a rectangular solid pin fin or aluminum foam insert in the channel

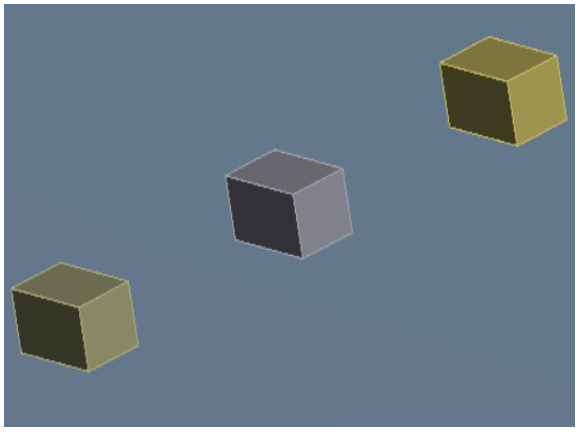

(b). Same size of rectangular solid pin fins or aluminum foam with a spacing of 1.5 mm in the channel

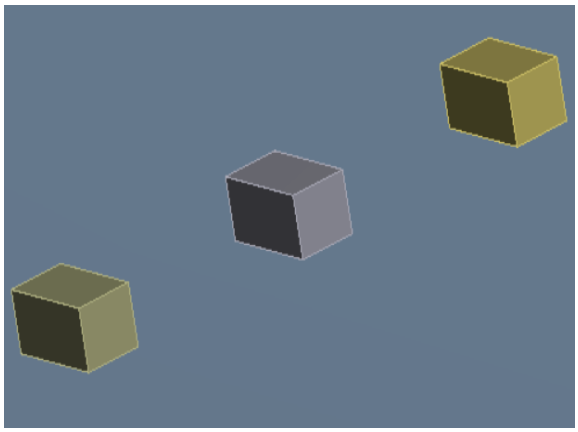

(c). Same size of rectangular solid pin fins or aluminum foam with a spacing of 2.0 mm in the channel

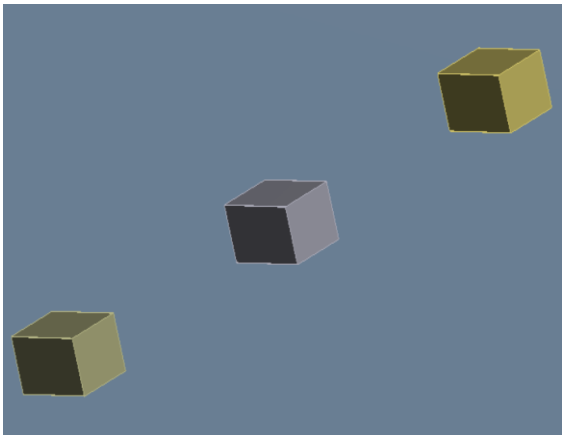

(d). Same size of rectangular solid pin fins or aluminum foam with a spacing of 2.5 mm in the channel

Figure 0.1. Cooling system cross-section with single (a), 1.5 mm (b), 2.0 mm (c), and 2.5 mm (d) spacing arrangements of three rectangular solid pin fins insert(s) in the channel.

7.2.1 Grid refinement test analysis

The same number of nodes and element sizes were considered for the cooling system with solid pin fin/aluminum foam (irrespective of porosity) inserted at the same point in the flow channel(s) for accurate comparative analysis. A similar consideration was given to the cooling system of multiple (three) inserts with the same spacing arrangements in the channels. Tables 7.1 and 7.2 respectively depict the conducted grid refinement test for counterflow cooling systems of three channels inserted with a single rectangular solid pin fin located at the center of the flow channels *(NR_{3CF})* and counterflow cooling system with three multiple (three) inserts

of circular aluminum foam arranged with 2.0 mm spacing ($NR2.0M_{CF}$) as an example for all grid refinement analyses carried out in this chapter.

Table 0.1. Grid refinement test for NR_{3CF}

Number of cells	Peak frame wall temperature (K)	Deviation $\left\|\frac{(\Delta T)_i - (\Delta T)_{i-1}}{(\Delta T)_i}\right\|$
131738	307. 5348	----------
127697	307.5573	0.00007316
133180	307.9055	0.00113215

Table 0.2. Grid refinement test for $NR2.0M_{CF}$

Number of cells	Peak frame wall temperature (K)	Deviation $\left\|\frac{(\Delta T)_i - (\Delta T)_{i-1}}{(\Delta T)_i}\right\|$
143738	307. 3916	----------
139697	307.3948	0.00001041
145180	307.7755	0.00123847

7.3 Results and Discussions

7.3.1 Case 1: Enhancement of the cooling system's thermal performance by inserting rectangular solid pin fin(s) in the channel(s) under different flow orientations.

7.3.1.1 Reynolds number effect on the cooling systems characterization with centrally located (L/2) rectangular solid pin fin (RSPF) under different flow orientation

7.3.1.1.1 Maximum rectangular frame wall temperature

Figure 7.2 shows the reduction in the maximum wall temperature (T_{max}) of the rectangular frame with an increased Reynolds number (*Re*) for the cooling systems equipped with RSPF

in the channel(s). Between the ranges of *Re* 128.38 to 1283.8 a substantial T_{max} reduction was realized. However, an insignificant T_{max} reduction occurred when the *Re* is further increased beyond 1283.8. Additional reductions in T_{max} were obtained as more channels were mounted on the rectangular frame of the cooling system. For instance, precisely at *Re* 2054.08, NR_{5CF} reduced T_{max} by 0.053%, 0.15%, 0.83%, and 2.89% respectively compared to NR_{4CF}, NR_{3CF}, NR_{2CF}, and NR_1. A similar pattern of T_{max} reduction was obtained with the parallel flow cooling systems. Within the range of applied *Re* in this study, counterflow cooling systems achieved a slightly lower T_{max} than parallel flow cooling systems. A considerable reduction in T_{max} was realized with cooling systems of the channel(s) inserted with RSPF (Figure 7.2) compared to those without insert (Figure4.7) indicating the enhanced thermal performance provided by the implementation of an insert.

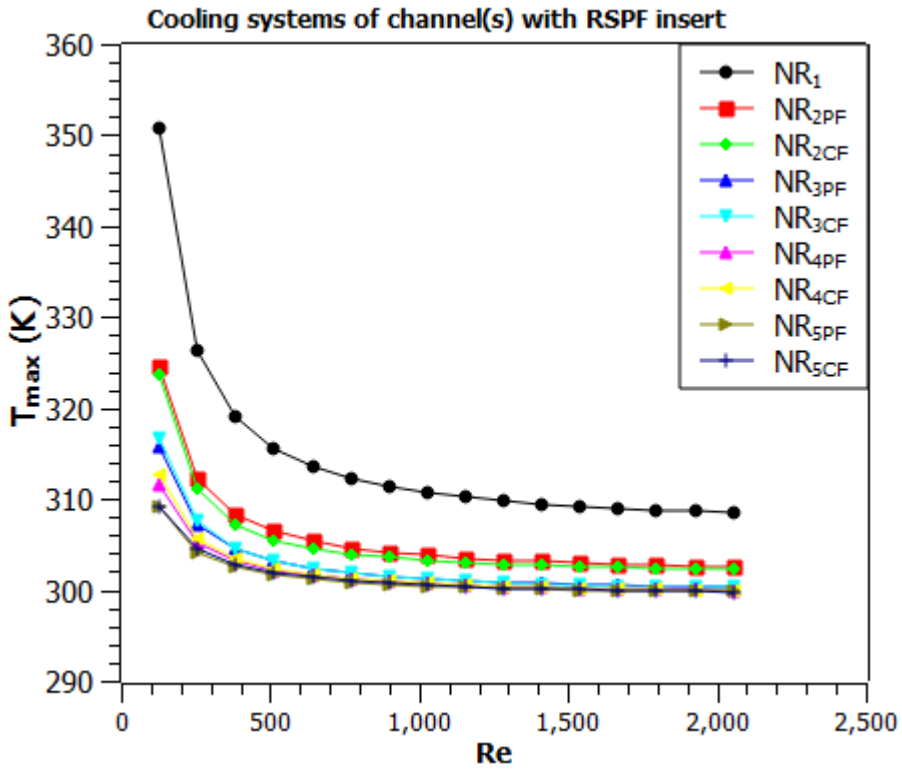

Figure 0.2. Maximum rectangular frame wall temperature (T_{max}) vs Reynolds number (*Re)* of the cooling system with a centrally located rectangular solid pin fin (RSPF) in the channel(s). The color markers represent the cooling system of different numbers of channel(s) with an RSPF insert mounted on the rectangular frame.

7.3.1.1.2 Dimensionless thermal resistance

From Figure 7.3, it is noticed that the dimensionless thermal resistance (R_{th}) decreases with the increase in Reynolds number (Re) for the cooling systems equipped with RSPF in the channel(s). When the Re increased from 128.38 to 1283.8, a substantial dimensionless R_{th} reduction was recorded and beyond this point, further increase in *Re* shows no significant effect on the dimensionless R_{th} reduction. An improved dimensionless R_{th} was obtained with increased channels mounted on the rectangular frame. Thus, NR_{5CF} and NR_1 achieved the best and poorest results in minimizing the dimensionless R_{th} in the category of counterflow cooling systems. A similar pattern of dimensionless R_{th} reduction was observed with parallel flow cooling systems. The figure shows a slight decrease of dimensionless R_{th} with counterflow cooling systems compared to parallel flow cooling systems. Moreover, the cooling systems with RSPF insert (Figure 7.3) demonstrate a significant decrease in the dimensionless R_{th} compared to those without insert (Figure 4.8), reflecting the improvement of thermal performance obtained by the use of an insert.

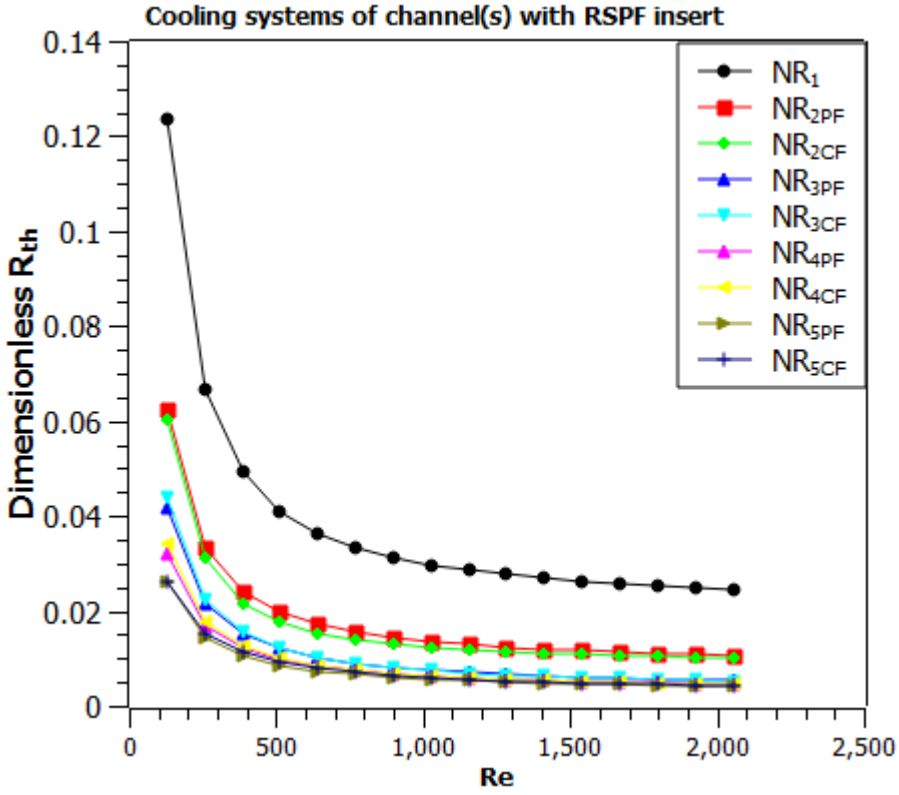

Figure 0.3. Dimensionless thermal resistance (R_{th}) vs Reynolds number (*Re*) of the cooling system with a centrally located rectangular solid pin fin (RSPF) in the channel(s). The color

markers represent the cooling system of different numbers of channel(s) with an RSPF insert mounted on the rectangular frame.

7.3.1.1.3 Cost of pumping power

The effect of the Reynolds number (*Re*) on the cost of pumping power (*Pp*) for the cooling systems with channels with RSPF is presented in Figure 7.4. Regardless of the number of channels mounted on the rectangular frame, the growth in *Pp* was recorded with an increased Re. However, a slight increase in *Pp* was obtained when the *Re* increased from 128.38 to 641.9, and beyond this, a further increase in *Re* significantly increased the values of *Pp*. Furthermore, the hike in *Pp* was more pronounced with an increased number of channels. For instance, at exactly Re, 641.9, NR_{5CF} increased *Pp* by 17.8%, 39.3%, 58.9%, and 80.8% compared to NR_{4CF}, NR_{3CF}, and NR_{2CF} and NR_1. A similar pattern of increased *Pp* values was observed with the parallel flow cooling system. This result was consistent with the published work of [197]. The figure demonstrates slightly increased *Pp* values with counterflow cooling systems compared to parallel flow cooling systems [47]. Meanwhile, the presence of the RSPF in the cooling systems' channels comes with a significant increase in the values of *Pp* values (Figure 7.4) compared to those without insert (Figure 4.9). Thus, the obstruction of the working fluid in the channels comes with a higher pressure drop and therefore a higher cost of pumping power.

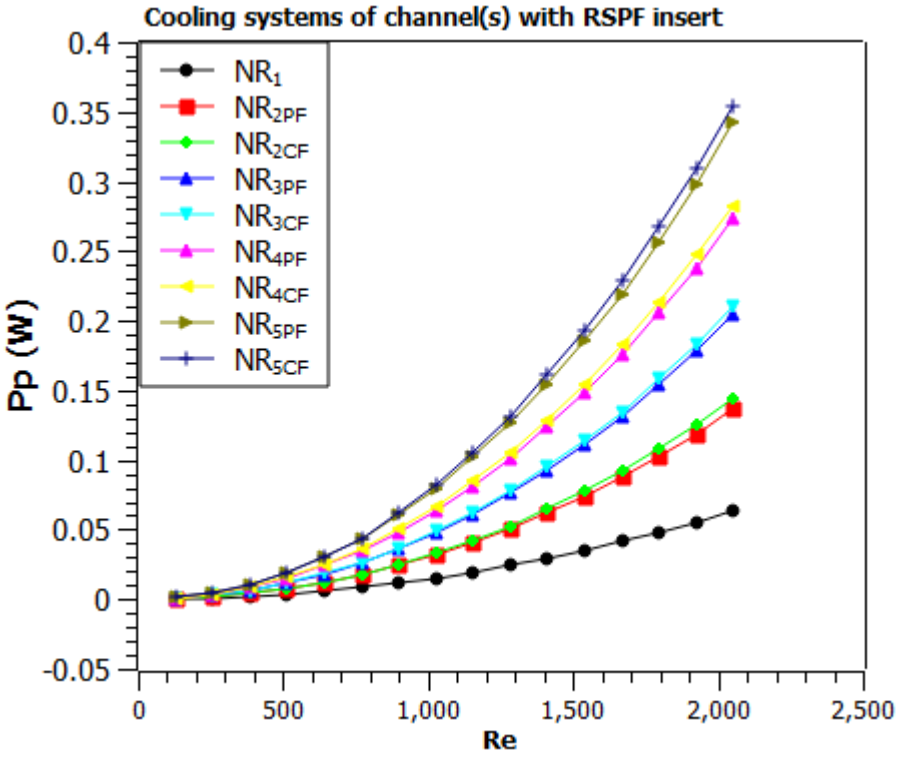

Figure 0.4. Cost of pumping power (*Pp*) vs Reynolds number (*Re*) of the cooling system with a centrally located rectangular solid pin fin (RSPF) in the channel(s). The color markers represent the cooling system of different numbers of channel(s) with an RSPF insert mounted on the rectangular frame.

7.3.1.2 Effect of channel number on the dimensionless heat transfer rate density for the cooling system with centrally located (L/2) rectangular solid pin fin (RSPF) in the channel(s)

Figure 7.5 illustrates the behavior of the cooling system in relation to the dimensionless heat transfer rate density, influenced by the varying number of channels, with rectangular solid pin fin (RSPF) inserts located at the center (L/2), mounted on the rectangular frame. A higher dimensionless heat transfer rate density indicates improved system thermal performance (Equations -3.36-3.38)). Regardless of flow orientation or the number of channels, an increase in *Re* leads to an increase in the dimensionless heat transfer rate density. Parallel flow cooling channels (Figure 7.5a) yielded slightly lower dimensionless heat transfer rate density than counterflow cooling channels (Figure 7.5b). In the parallel flow system, with three channels at *Re* 2054.08, the heat transfer rate density increased by 34.34%, 32.68%, 13.01%, and 23.57% compared to systems with 1, 2, 4, and 5 channels, respectively (Figure 7.5a). Thus, the highest dimensionless heat transfer rate density was achieved with three channels containing RSPF inserts indicating a system with the maximum interaction between the working fluid and heat transfer surfaces. A 94.91% and 95.01% increased dimensionless heat transfer rate density were respectively obtained by the parallel (Figure 7.5a) and counterflow systems (Figure 7.5b) of the three channels with RSPF at *Re* 2054.08 compared to their counterpart systems of no insert (Figure 4.10(a and b)). The result demonstrates the enhancement of the cooling system performance by applying the RSPF insert.

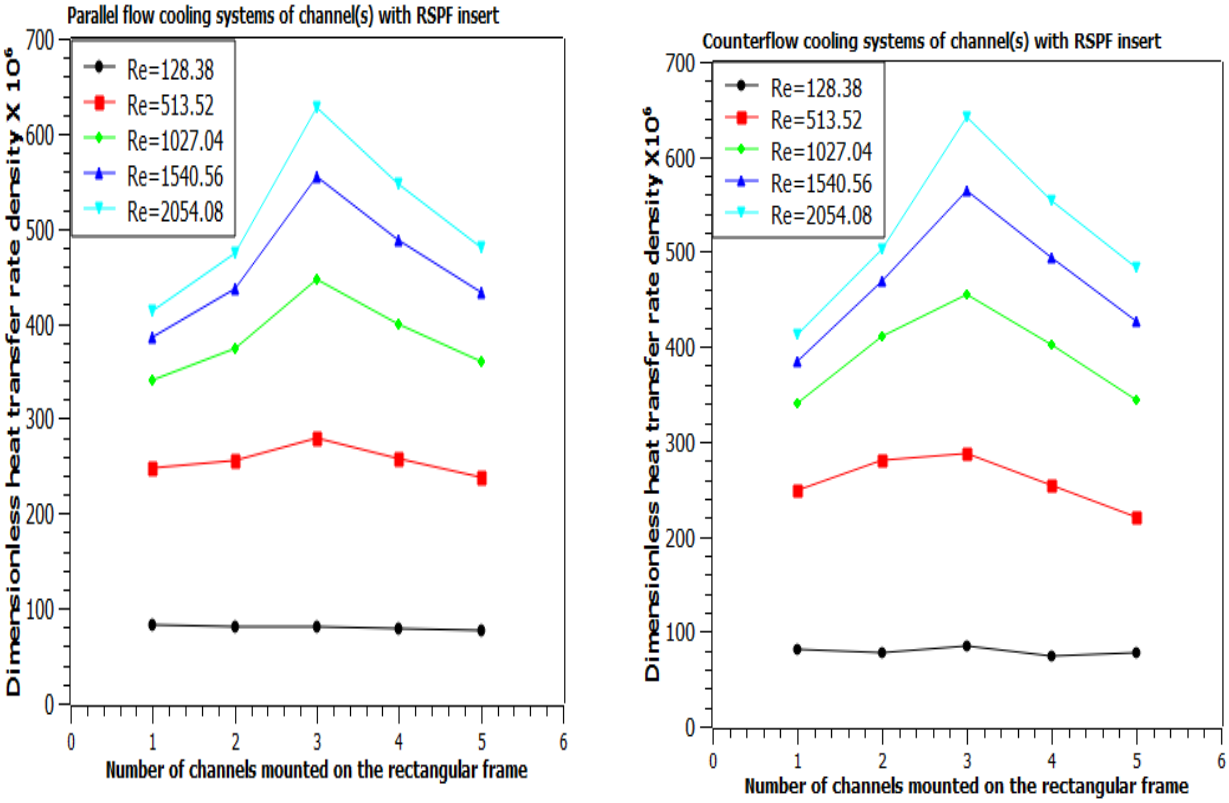

Figure 0.5. Dimensionless heat transfer rate density vs. number of channels mounted on the rectangular frame in Parallel (a) and Counterflow (b) cooling systems with rectangular solid pin fin (RSPF) Inserts. Colored markers represent different Reynolds numbers (Re): Re = 128.38 (black), Re = 513.52 (red), Re = 1027.04 (green), Re = 1540.56 (blue), and Re = 2054.08

7.3.1.3 Effect of varying locations of a single rectangular solid pin fin (RSPF) insert in the channel(s) on the cooling system's performance

From the above results, the highest dimensionless heat transfer rate density is achieved with three channels and a centrally located RSPF (at *L/2*), indicating superior thermal performance for dissipating heat from the battery pack. In this section, further analyses to study the possible effect of varying locations of the RSPF inserts within the channels of this cooling system to evaluate how different placements may influence thermal performance and heat dissipation efficiency were carried out. This analysis explores whether alternative RSPF placement can further enhance cooling system efficiency beyond the best identified system.

As shown in Figure 7.6 an increased Reynolds number (*Re*) decreases the dimensionless thermal resistance (R_{th}) regardless of the location of the rectangular solid pin fin (RSPF) in the channels of the cooling systems. The increase in *Re* from 128.38 to 1283.8 was observed with substantial dimensionless R_{th} reduction. Beyond this point, a further increase in the *Re* yields a negligible effect on the dimensionless R_{th} reduction. Meanwhile, the slight increase in dimensionless R_{th} values was demonstrated by the parallel flow cooling systems compared to the counterflow cooling systems, regardless of the point of placement of the RSPF insert in the channels. Precisely at *Re* 898.66, the cooling system equipped with RSPF located at *L/8* NR_{MCF} towards the leading edge reduced the dimensionless R_{th} by 11.38% and 18.5% respectively compared to when it was placed at *L/4* (NR_{JCF}) and *L/2* (NR_{3CF}) in the channels. Parallel flow cooling systems demonstrated a similar thermal resistance reduction with NR_{MPF} compared to NR_{JPF} and NR_{3CF}. Thus, minimizing the distance between the inlet and RSPF corresponds to an improved cooling system performance.

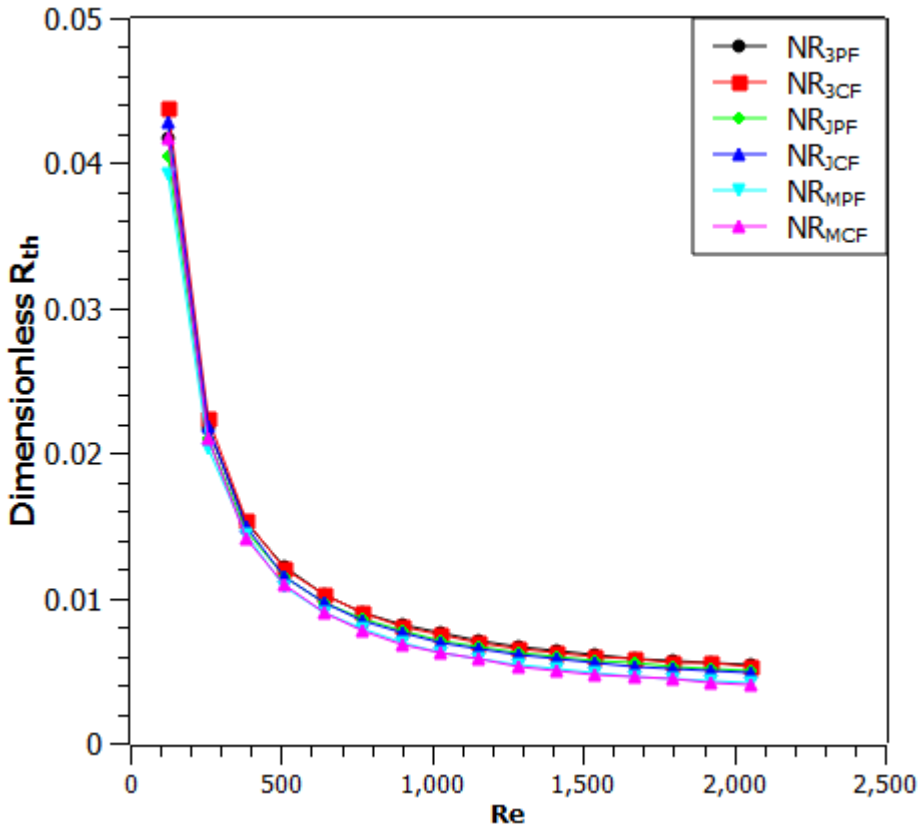

Figure 0.6. Dimensionless thermal resistance (R_{th}) vs Reynolds number (*Re*) of the cooling system with a single rectangular solid pin fin (RSPF) insert. The colored markers illustrate counterflow (CF) and parallel flow (PF) cooling systems equipped with a single RSPF located at *L/2* (NR_{3CF} *and* NR_{3PF}), *L/4* (NR_{JCF} *and* NR_{JPF}), and *L/8* (NR_{MCF} *and* NR_{MPF}), in the channel.

7.3.1.4 Comparison of a single and varying spacing arrangement of three rectangular solid pin fin (RSPF) insert(s) in the channel(s) on the cooling system's performance

From the best point of insert location *(L/8)* towards the inlet, the RSPF was increased to three to compare the effect of a single with multiple insert(s) in the channels on the thermal performance enhancement of the cooling systems. The realization of the optimum thermal performance of a designed cooling system with at most 3-pin fins in the channel was earlier reported by [208] with no emphasis on the search for the best insert location in the channels. Therefore, three RSPFs of varying spacing arrangements (1.5mm, 2.0mm, and 2.5mm) are employed in this work for comparison with a single RSPF located at *L/8*.

From Figure 7.7, the reduction in the dimensionless thermal resistance (R_{th}) with an increase in Reynolds number (*Re*) was observed for the cooling systems regardless of the number and the spacing arrangement of the RSPF in the channels. When the *Re* rises from 128.38 to 1283.8, a significant dimensionless R_{th} reduction is noted and when the *Re* exceeds 1283.8, the dimensionless R_{th} shows no significant decrease. Within the range of *Re* applied in this study, counterflow cooling systems show a slightly lower dimensionless R_{th} than parallel flow cooling systems. Compared to the 2.0 mm and 2.5 mm spacing arrangements, the lowest dimensionless R_{th} was obtained with the 1.5 mm spacing arrangement of the RSPF in the channel, regardless of the flow orientation. For instance, at exactly *Re* 770.28, $NR1.5M_{PF}$ achieves 3.4% and 9.8% of dimensionless R_{th} reduction compared to $NR2.0M_{PF}$ and $NR2.5_{PF}$ respectively. The result suggests that the shorter the distance between the RSPF, the better the heat dissipation capacity of the cooling system. Meanwhile, the cooling system with a single RSPF insert gives a better result in minimizing the dimensionless R_{th} to cooling systems equipped with three RSPFs regardless of the spacing arrangements. Thus, specifically at *Re* 770.28 NR_{MCF}, reduced dimensionless R_{th} by 12.7%, 17.0%, and 24.0% compared to $NR1.5M_{CF,}$ $NR2.0M_{CF,}$ and $NR2.5M_{CF}$ respectively. A similar pattern of dimensionless R_{th} reduction was observed with parallel flow cooling systems.

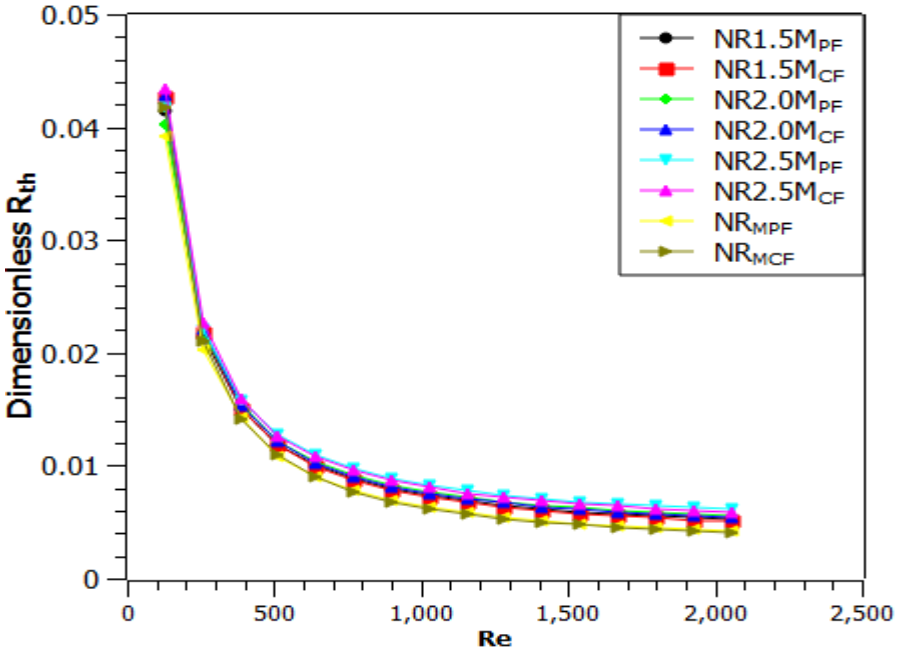

Figure 0.7. Dimensionless thermal resistance (R_{th}) vs. Reynolds number (*Re*) of cooling system with rectangular solid pin fin (RSPF) insert(s). The color markers illustrate counterflow (CF) and parallel flow (PF) cooling systems equipped with a single RSPF *(NR_{MCF} and NR_{MPF})*, and 1.5mm *($NR1.5M_{CF}$ and $NR1.5_{PF}$)*, 2.0mm *($NR2.0M_{CF}$ and $NR2.0M_{PF}$)* as well as 2.5mm *($NR2.5M_{CF}$ and $NR2.5M_{PF}$)* spacing arrangements of three RSPFs in the channels.

7.3.1.5 Normalized friction factor effect between the varying location of a single and spacing arrangement of three rectangular solid pin fins (RSPF)

From Figures 7.8, an increased Reynolds number (*Re*) leads to an increased normalized friction factor (*NFF*) for the cooling system with RSPF insert. The obtained *NFF* values higher than 3 with the cooling system equipped with either single (irrespective of location (Figure 7.8a) or multiple (regardless of the spacing arrangement (Figure 7.8b) RSPF indicate that the insertion of the RSPF in the flow channels can raise the working fluid friction more than 3 times compared to a cooling system without an insert [40]. Specifically, at *Re* 898.66 NR_{MCF} (RSPF at *L/8*) lowered the *NFF* values by 0.38% and 0.65% compared to NR_{JCF} (RSPF at *L/4*) and NR_{3CF} (RSPF at *L/2*) respectively (Figure 7.8a). A similar reduction of *NFF* values was observed with parallel flow cooling systems. Thus, the closer the RSPF to the inlet, the better the system performance. However, Figure 7.8b shows the increased values of *NFF* with the minimization of space from one RSPF to the other [200]. For instance, at the *Re* 2054.08 precisely, the cooling system with 2.5 mm spacing arrangements of three RSPF *($NR2.5M_{PF}$)*

reduced the *NFF* values by 0.96% and 1.63% compared to 2.0 mm *($NR2.0M_{PF}$)* and 2.5 mm *($NR1.5M_{PF}$)* spacing arrangements respectively (Figure 7.8b). Remarkably, the cooling systems containing three RSPFs incurred larger *NFF* values than the cooling channels with a single RSPF demonstrating the effect of increased fluid domain complexity on the pressure drop and consequently the *NFF*. Meanwhile, regardless of the number and spacing arrangements of RSPF, in the channels, cooling systems with counterflow arrangements yield slightly higher values of *NFF* than those with parallel flow arrangements.

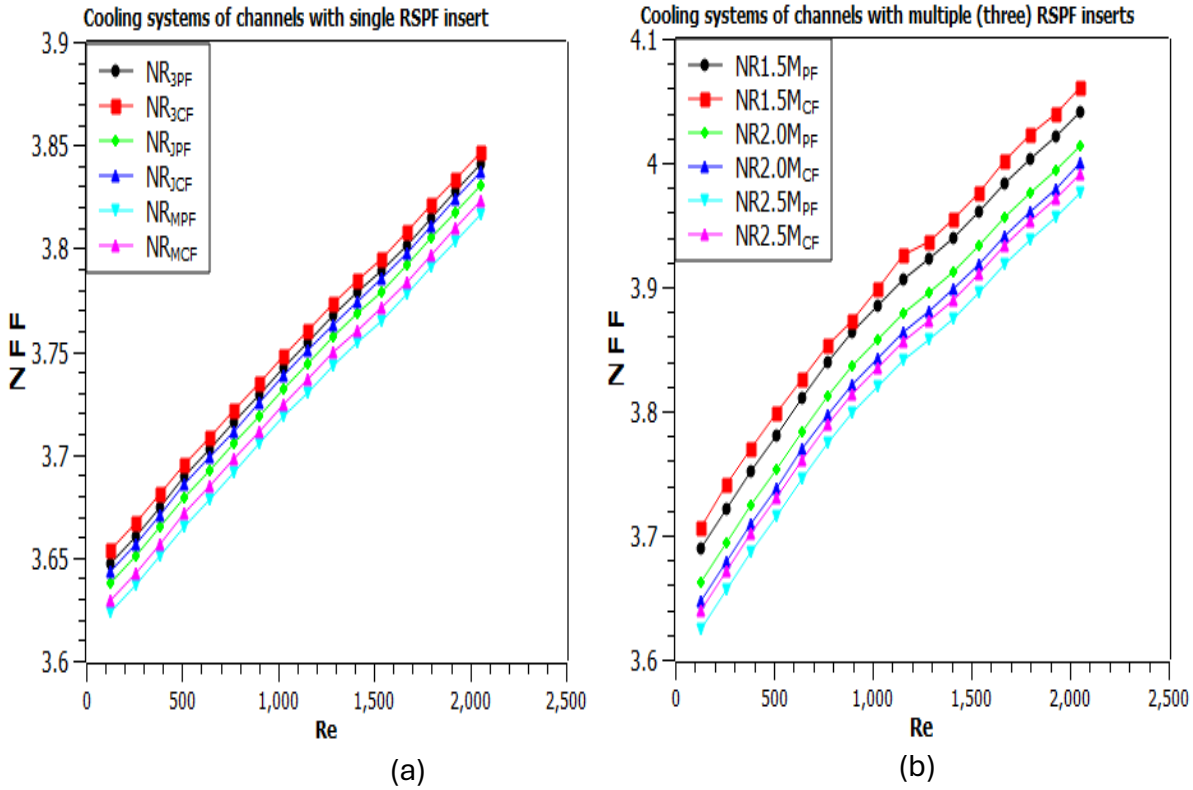

Figure 0.8. Normalized friction factor (*NFF*) vs. Reynolds number (*Re*) of the cooling system with a single (a) and three (b) rectangular solid pin fin (RSPF) insert(s). The color markers illustrate counterflow (CF) and parallel flow (PF) cooling systems equipped with varying locations of a single and spacing arrangement of multiple RSPFs in the channels.

7.3.1.6 Comparison of thermal performance enhancement factor effect between the varying location of a single and varying spacing arrangement of three rectangular solid pin fin (RSPF)

As shown in Figure 7.9 an increased Reynolds number (*Re*) increased the thermal performance enhancement factor (*TPEF*) regardless of the number and spacing arrangements of the RSPF in the cooling systems' channels. The obtained *TPEF* greater than 1, regardless of the cooling system configurations, shows that RSPF insertion in the channels can enhance the system

thermal performance with a tolerable increase of the friction factor in the channel [45]. Precisely at *Re* 2054.08, the cooling system with 2.0 mm spacing arrangements $NR2.0M_{CF}$ increased the *TPEF* by 1.46% and 7.19% respectively compared to 1.5 mm ($NR1.5M_{CF}$) and 2.5 mm $(NR2.5M_{CF})$ spacing arrangements reflecting that the frictional factor effect is more tolerable to the enhancement of heat transfer in the channel of 2.0 mm than in 1.5 mm and 2.5 mm spacing arrangements. The parallel flow cooling systems demonstrated a similar improvement in TPEF values. The figure further revealed that the cooling system equipped with a single RSPF achieved the highest *TPEF* than the three RSPFs regardless of the spacing arrangement. Thus, NR_{MPF} (system with a single RSPF at *L/8*) respectively raised the values of *TPEF* by 11.79%, 5.19%, and 6.98% compared to $NR2.5M_{PF}$, $NR2.0M_{PF}$, and $NR1.5M_{PF}$ at exactly *Re* 2054.08. Counterflow cooling systems exhibited a similar pattern of *TPEF* increase. Moreover, cooling systems with counterflow arrangements slightly increased *TPEF* values compared to those with the parallel flow arrangement, regardless of the number and spacing arrangement of the RSPF in the cooling system channels.

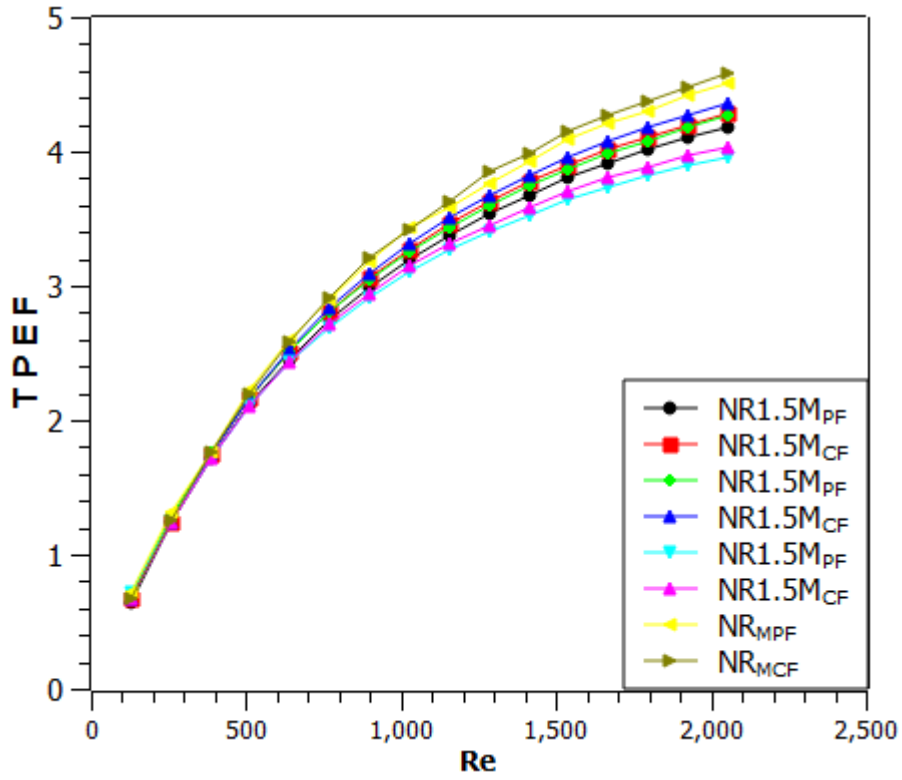

Figure 0.9. Thermal performance enhancement factor (*TPEF*) vs. Reynolds number (*Re*) of cooling system with rectangular solid pin fin (RSPF) insert(s). The color markers illustrate counterflow (CF) and parallel flow (PF) cooling systems equipped with a single RSPF $(NR_{MCF}$

and NR_{MPF}), and 1.5mm *($NR1.5M_{CF}$ and $NR1.5_{PF}$)*, 2.0 mm *($NR2.0M_{CF}$ and $NR2.0M_{PF}$)* as well as 2.5 mm *($NR2.5M_{CF}$ and $NR2.5M_{PF}$)* spacing arrangements of three RSPFs in the channels.

7.3.1.7 Temperature uniformity of the battery cells in the pack

Temperature uniformity of the battery cells in a pack of an electric vehicle as a function of the Reynolds number is shown in Figures 7.10(a-c). An increased Reynolds number reduced the battery cells' temperature uniformity. However, a battery cell temperature uniformity variation of less than 2℃ was realized. Thus, the capacity of the cooling system to maintain the temperature uniformity of the battery cells in a pack is depicted. The coalescing of the graph and lower values of the battery cells' temperature uniformity realized with the system containing RSPF in the channels (Figures 7.10(a) and (b)) compared to those without an insert (Figures 4.11(a) and (b)) reflects the effect of RSPF insert on the improvement of battery cells temperature uniformity in the pack. Meanwhile, the lower values of the battery cells' temperature uniformity by the NR_{3CF} (Figure 7.10b) compared with the NR_{3PF} (Figure 7.10a) reflect the influence of the flow orientation on the system performance. Furthermore, NR_{MCF} (Figure 7.10c) with lower values of the battery cells temperature uniformity compared to the NR_{3CF} (Figure 7.10b) indicates the influence of RSPF insert positioning in the system channels.

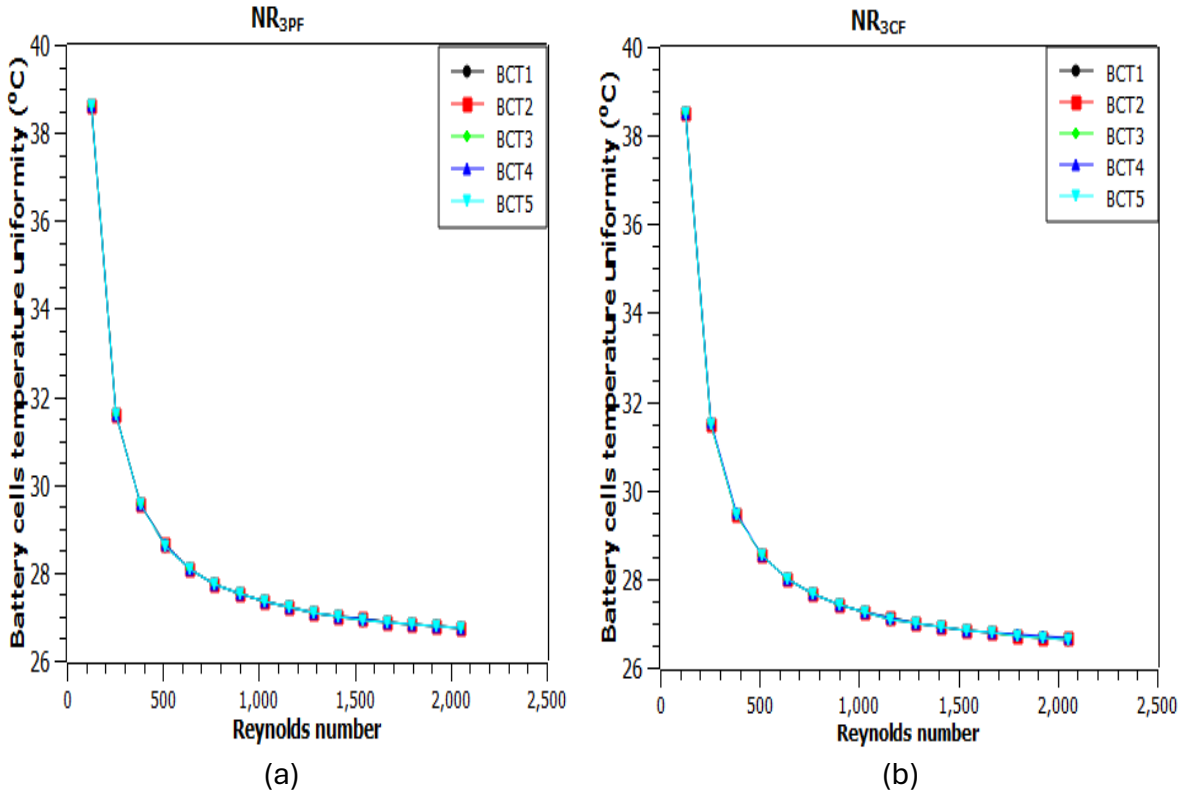

(a) (b)

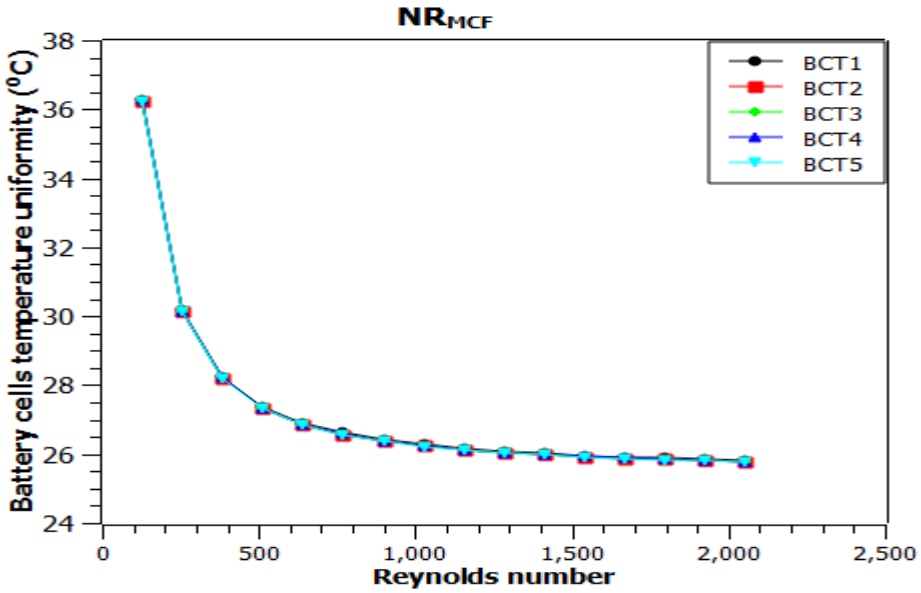

©

Figures 0.10. Battery cells temperature uniformity vs Reynolds number for cooling systems of three channels containing a single rectangular solid pin fin (RSPF) insert located at *L/2* (parallel flow (a) and counterflow (b) arrangement) as well as *L/8* (counterflow arrangement (c). The color makers represent the temperatures of each battery cell in a pack.

7.3.2 Case 2: Enhancement of the cooling system's performance with the insertion of rectangular aluminum foam(s) of varying porosities in the channel(s) under different flow orientations

7.3.2.1 Reynolds number effect on the cooling system characterization with centrally located (L/2) rectangular aluminum foam of 0.1 porosity ($RAF\varepsilon = 0.1$) under different flow orientations

7.3.2.1.1 Maximum rectangular frame wall temperature

As shown in Figure 7.1, an increase in Reynolds number (*Re*) reduces the maximum wall temperature (T_{max}) of the rectangular frame for the cooling systems with the rectangular aluminum foam of 0.1 porosity ($RAF\varepsilon = 0.1$) insert. A significant reduction in T_{max} was realized when *Re* increased from 128.38 to 1283.8. However, a further increase in *Re* yields an insignificant effect on the T_{max} reduction. Meanwhile, an improved T_{max} reduction was recorded with additional channels mounted on the rectangular frame. Thus, specifically at *Re* 2054.08, $NR_{5\varepsilon=0.1PF}$ reduced T_{max} by 0.05%, 0.15%, 0.83%, and 2.89% compared to $NR_{4\varepsilon=0.1PF}$,

$NR_{3\varepsilon=0.1PF}$, $NR_{2\varepsilon=0.1PF}$, and $NR_{1\varepsilon=0.1}$ respectively. Counterflow flow cooling systems exhibited a similar pattern of T_{max} reduction. For the applied *Re* in this study, counterflow cooling systems achieved slightly lower T_{max} values than parallel flow cooling systems. Moreover, the cooling systems inserted with $RAF\varepsilon = 0.1$ (Figure7.11) obtained a significant T_{max} reduction compared to those with no insert (Figure 4.7) indicating the improved thermal performance provided by applying an insert.

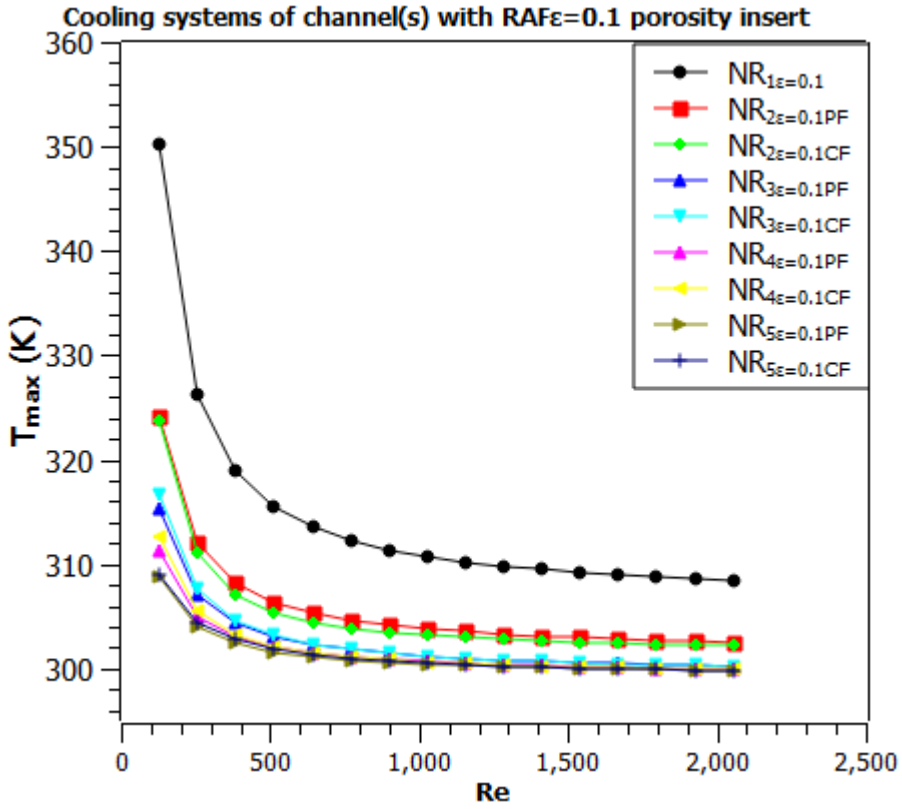

Figure 0.11. Maximum rectangular frame wall temperature (T_{max}) vs Reynolds number (*Re*) of the cooling system with a centrally located rectangular aluminum foam of 0.1 porosity ($RAF\varepsilon = 0.1$) insert in the channel(s). The color markers represent the cooling system of different numbers of channel(s) with a $RAF\varepsilon = 0.1$ insert mounted on the rectangular frame.

7.3.1.1.2 Dimensionless thermal resistance

As represented in Figure 7.12, the dimensionless thermal resistance (R_{th}) reduction was recorded with an increase in Reynolds number (*Re*) regardless of the cooling system design. The increase in *Re* from 128.38 to 1283.8 achieved a significant dimensionless R_{th} reduction. However, when the Re number exceeded this point, a continuous increase in *Re* shows a negligible effect on the T_{max} reduction. The figure shows an improved dimensionless R_{th}

reduction with additional channels mounted on the rectangular frame. Thus, cooling systems with five channels and one channel obtained the lowest and the highest dimensionless R_{th} reduction regardless of the flow orientation. A slightly lower dimensionless R_{th} was observed with the cooling systems of counterflow arrangement compared to those of parallel flow arrangement. Meanwhile, a substantial reduction in the dimensionless R_{th} was exhibited by the cooling systems equipped with $RAF\varepsilon = 0.1$ (Figure 7.12) compared to those without inserts (Figure 4.8) which implies the augmentation of performance brought about by the use of an insert.

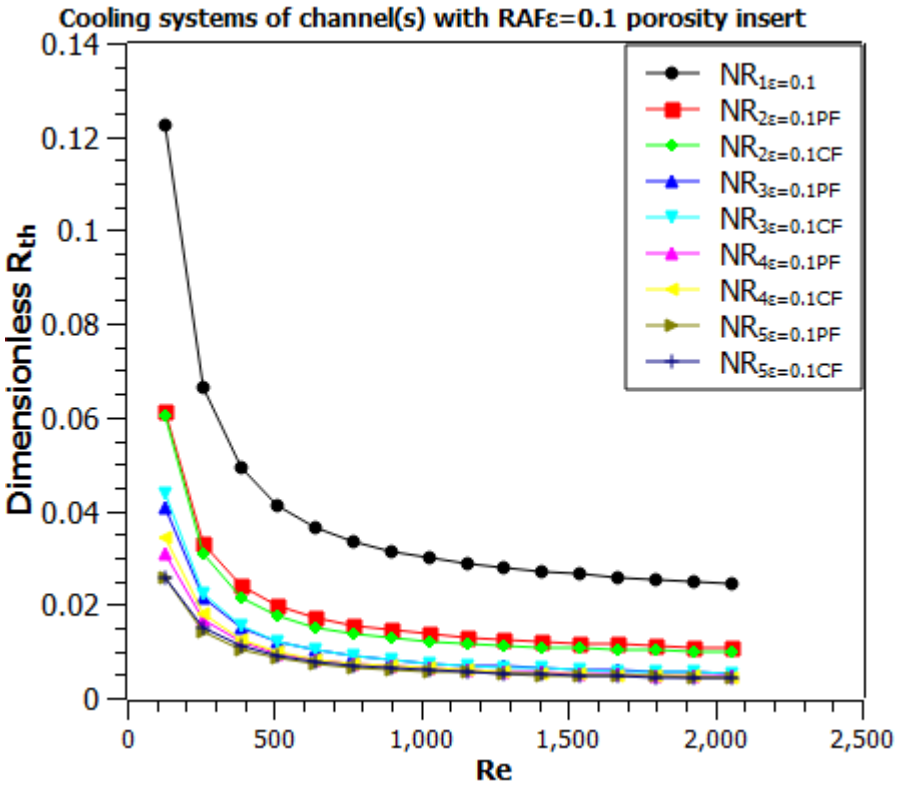

Figure 0.12. Dimensionless thermal resistance (R_{th}) vs Reynolds number (Re) of the cooling system with a centrally located rectangular aluminum foam of 0.1 porosity ($RAF\varepsilon = 0.1$) insert in the channel(s). The color markers represent the cooling system of different numbers of channel(s) with a $RAF\varepsilon = 0.1$ insert mounted on the rectangular frame.

7.3.1.1.3 Cost of pumping power

As shown in Figure 7.13, an increase in Reynolds number (Re) increases the cost of pumping power (Pp) of the cooling systems equipped with the rectangular aluminum foam of 0.1 porosity ($RAF\varepsilon = 0.1$). A slight hike in the Pp occurred when the Re increased from 283.83 to 641.9 and beyond this point, a further increase in Re leads to a significant increase in Pp.

However, an increase in the number of channels mounted on the rectangular frame significantly incurred higher values of *Pp* [197]. Within the range of applied *Re* in this study, counterflow cooling systems possess a slightly higher value of *Pp* compared to parallel flow cooling systems [47]. Meanwhile, a great increase in *Pp* was exhibited by the cooling systems equipped with $RAF\varepsilon = 0.1$ (Figure 7.13) compared to those without insert (Figure 4.9) indicating that the presence of *RAFε=0.1* in the fluid domain hikes the pressure drop and consequently the cost of pumping power.

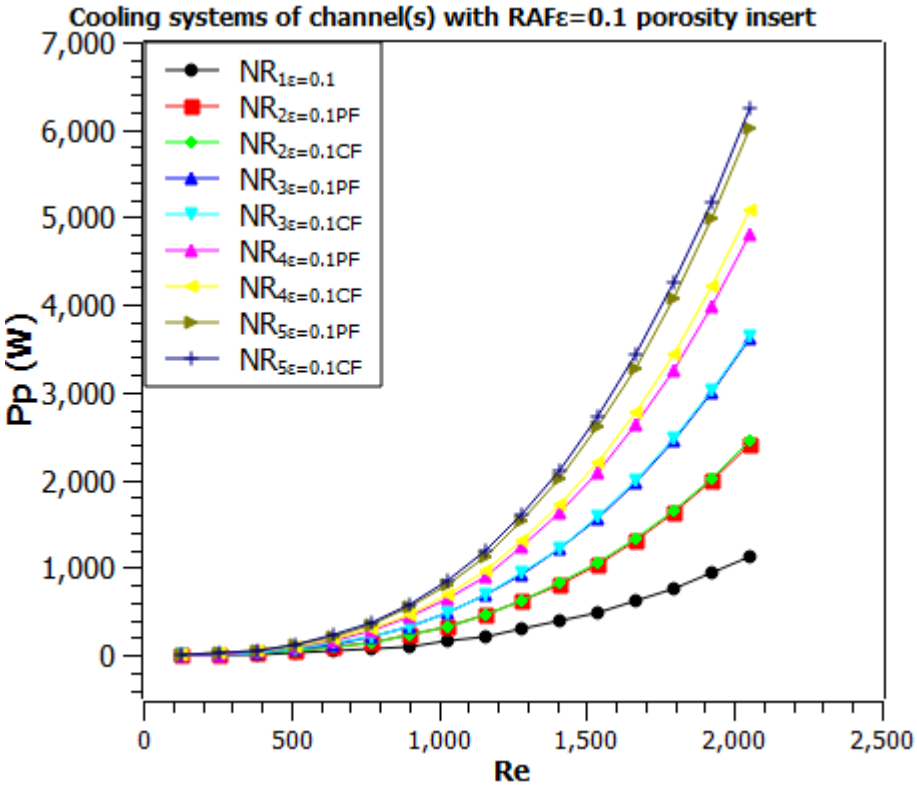

Figure 0.13. Cost of pumping power (*Pp*) vs Reynolds number (*Re*) of the cooling system with a centrally located rectangular aluminum foam of 0.1 porosity ($RAF\varepsilon = 0.1$) insert in the channel(s). The color markers represent the cooling system of different numbers of channel(s) with a $RAF\varepsilon = 0.1$ insert mounted on the rectangular frame.

7.3.2.2 Effect of channel number on the dimensionless heat transfer rate density for the cooling system with centrally located (L/2) rectangular aluminum foam of 0.1 porosity ($RAF\varepsilon = 0.1$) in the channel(s)

Figure 7.14 shows the response of the cooling system to the dimensionless heat transfer rate density, influenced by the varying number of channels, with rectangular aluminum foam of *0.1*($RAF\varepsilon = 0.1$) inserts located at the center *(L/2)*, mounted on the rectangular frame

(Equations (3.36-3.38)). The figures show an increased dimensionless heat transfer rate density with an increase in Reynolds number (*Re*), regardless of the number of channels mounted on the rectangular frame. Within the range of applied *Re*, parallel flow cooling systems (Figure 7.14b) slightly reduced the dimensionless heat transfer rate density than counterflow cooling systems (Figure 7.14a), regardless of the number of channels. Interestingly, the highest dimensionless heat transfer rate density was documented with the three channels of $RAF\varepsilon = 0.1$ inserts mounted on the rectangular frame. In the parallel flow system, 35.15%, 25.37%, 12.70%, and 25.22% of increased dimensionless heat transfer rate density were recorded with the three (3) channels of RAFε = 0.1 inserts compared to 1, 2, 4, and 5 channels, respectively at *Re* 2054.08 (Figure 7.14a). This implies that three channels provide the best possible interaction between the heat transfer surfaces and the working fluid. Meanwhile, at *Re* 2054.08, the parallel (Figure 7.14a) and counterflow (Figure 7.14b) systems of the three channels with $RAF\varepsilon = 0.1$ achieved, respectively, a 94.96% and 95.07% higher dimensionless heat transfer rate density in comparison to their counterpart systems of no insert (Figure 4.10(a and b)). Thus, the enhanced thermal performance of the cooling system provided by using $RAF\varepsilon = 0.1$ inserts is demonstrated.

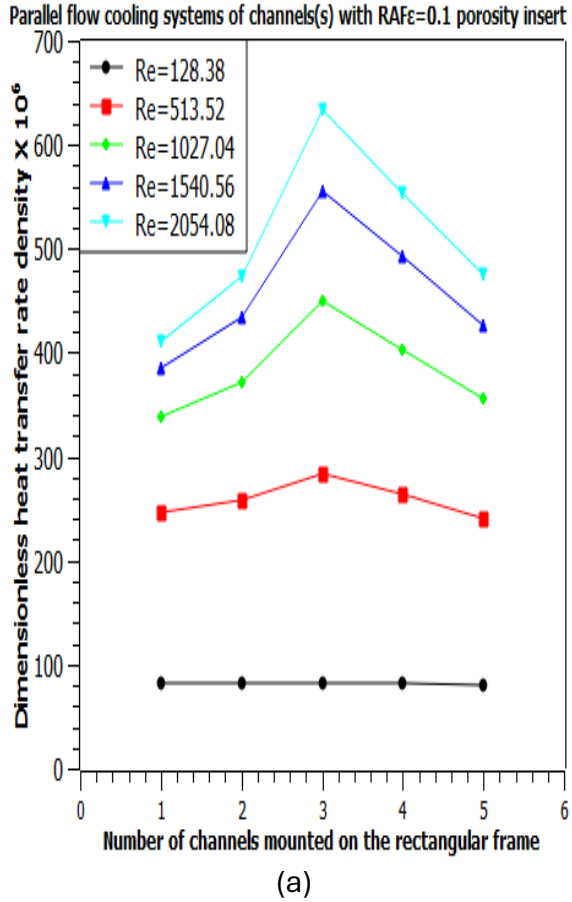

(a)

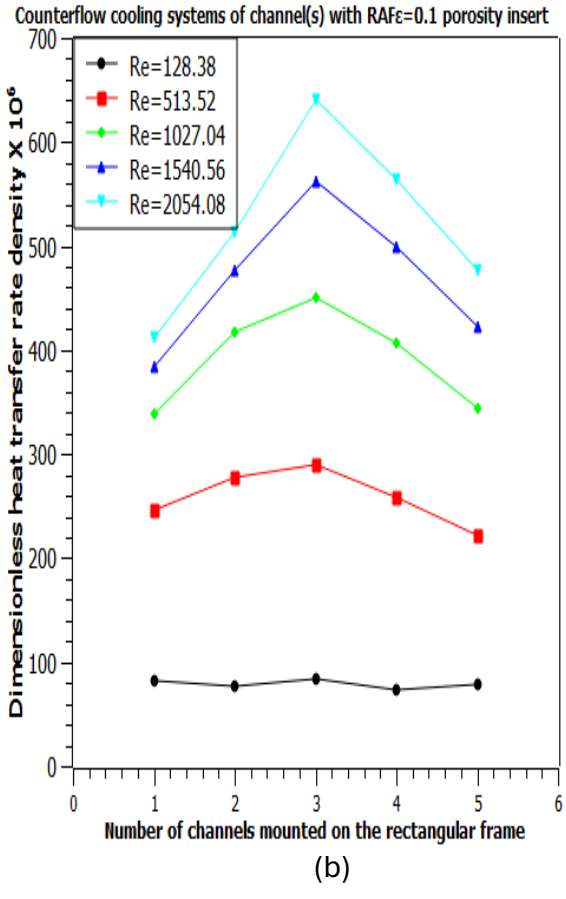

(b)

Figure 0.14. Dimensionless heat transfer rate density vs. number of channels mounted on the rectangular frame in Parallel (a) and Counterflow (b) cooling systems with rectangular aluminum foam of 0.1 porosity (RAFε=0.1) inserts. Colored markers represent different Reynolds numbers (Re): Re = 128.38 (black), Re = 513.52 (red), Re = 1027.04 (green), Re = 1540.56 (blue), and Re = 2054.08

7.3.2.3 Effects of varying porosities of the rectangular aluminum foam on the thermal performance of the cooling system

The highest thermal performance is obtained when three channels with rectangular aluminum foam inserts of low porosity (*EAFε=0.1*) are mounted on the rectangular frame of the cooling system as earlier narrated in the previous section. In this section, a further analysis is carried out to study the effect of varying porosities on cooling system performance. Precisely, the performance of rectangular aluminum foam inserts with medium porosity (*EAFε=0.5*) and high porosity (*EAFε=0.9*) is examined to determine how different porosity levels influence the system's thermal efficiency.

7.3.2.3.1 Dimensionless thermal resistance

As seen in Figure 7.15, an increased Reynolds number (*Re*) reduces the dimensionless thermal resistance (R_{th}) regardless of the type of rectangular aluminum foam porosities. A remarkable drop in the dimensionless R_{th} was recorded when the *Re* increased from 128.38 to 1283.8. An insignificant dimensionless R_{th} reduction was noted when the *Re* was further increased beyond this point. In general, the lowest and the highest dimensionless R_{th} were respectively found with the insertion of low (0.1) and high (0.9) porosities of rectangular aluminum foam ($\mathrm{RAF}\varepsilon = 0.1$ and $\mathrm{RAF}\varepsilon = 0.5$) in the channels of the cooling systems regardless of the flow orientation. For instance, at a fixed *Re* 1155.42, $NR_{3\varepsilon=0.1PF}$ reduced the dimensionless R_{th} by 12.1% and 13.8% compared to $NR_{3\varepsilon=0.5PF}$ and $NR_{3\varepsilon=0.9PF}$ respectively [201]. Thus, the higher the porosity, the less heat is trapped in the porous matrix. However, counterflow cooling systems give slightly lower dimensionless R_{th} values than parallel flow cooling systems.

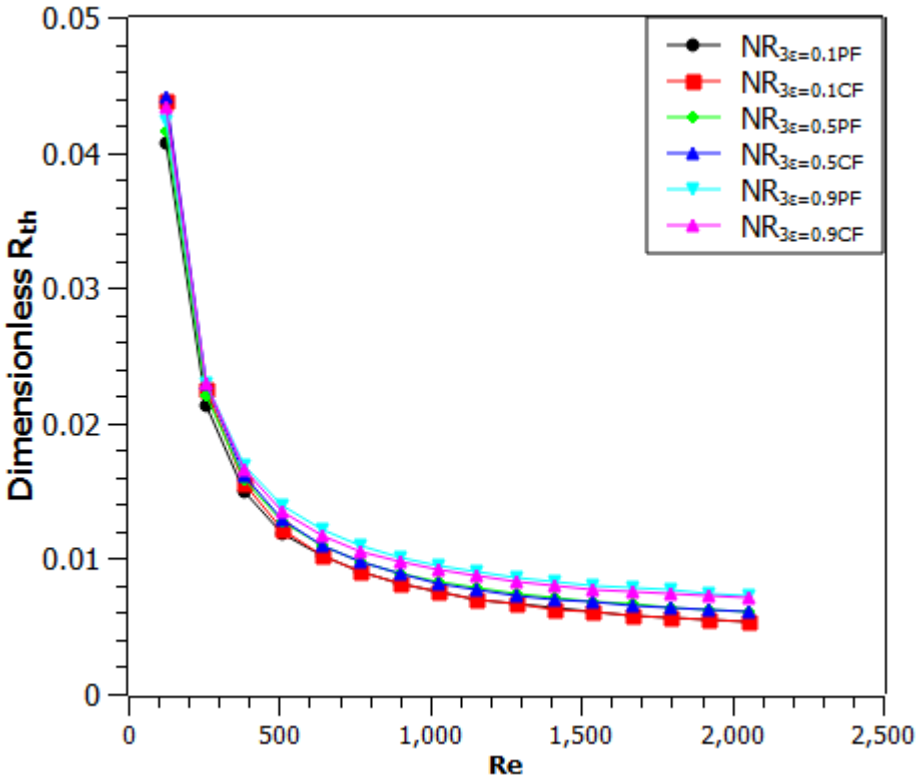

Figure 0.15. Dimensionless thermal resistance (R_{th}) vs Reynolds number (Re) of the cooling system with rectangular aluminum foam of varying porosities inserted. The color markers illustrate counterflow (CF) and parallel flow (PF) cooling systems equipped with a single aluminum foam of 0.1 porosity ($NR_{3\varepsilon=0.1CF}$ and $NR_{3\varepsilon=0.1PF}$), 0.5 porosity ($NR_{3\varepsilon=0.5CF}$ and $NR_{3\varepsilon=0.5PF}$) as well as 0.9 porosity ($NR_{3\varepsilon=0.9CF}$ and $NR_{3\varepsilon=0.9PF}$).

7.3.2.3.2 Cost of pumping power

Figure 7.16 displayed an increase in the cost of pumping power (Pp) with an increased Reynolds number (Re) regardless of the type of rectangular aluminum foam porosities inserted into the cooling systems' channels. As shown in the figure, the insertion of the RAF$\varepsilon = 0.1$ in the cooling systems' channels, generating an outrageous Pp compared to RAF$\varepsilon = 0.5$ and RAF$\varepsilon = 0.9$ regardless of the flow orientation. However, the cooling system equipped with the RAF$\varepsilon = 0.9$ achieved the lowest values of Pp indicating the indirect relationship between the pressure drop and insert porosity [44]. Regardless of the type of rectangular aluminum foam porosity insert counterflow cooling systems, Pp values were recorded slightly higher than those of parallel flow configurations.

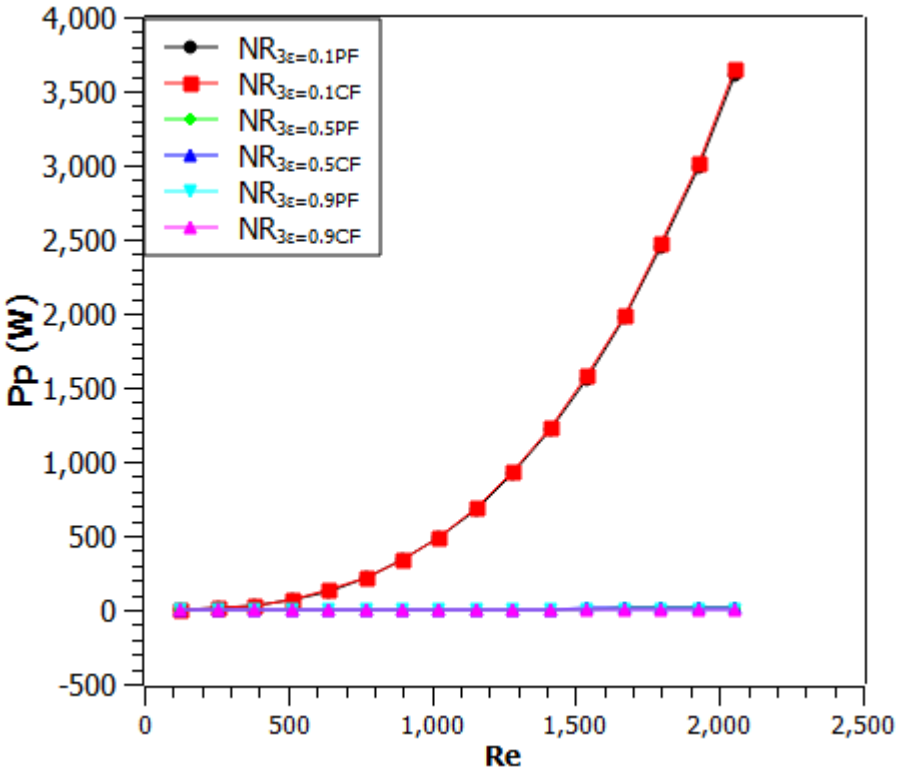

Figure 0.16. Cost of pumping power (*Pp*) vs Reynolds number (*Re*) of the cooling system with rectangular aluminum foam of varying porosities insert. The color markers illustrate counterflow (CF) and parallel flow (PF) cooling systems equipped with a single aluminum foam of 0.1 porosity ($NR_{3\varepsilon=0.1CF}$ and $NR_{3\varepsilon=0.1PF}$), 0.5 porosity ($NR_{3\varepsilon=0.5CF}$ and $NR_{3\varepsilon=0.5PF}$) as well as 0.9 porosity ($NR_{3\varepsilon=0.9CF}$ and $NR_{3\varepsilon=0.9PF}$).

7.3.2.3.3 Thermal performance enhancement factor

Regardless of the porosity of rectangular aluminum foam inserted in the cooling system channels, Figure 7.17 reports an increase in the Reynolds number *(Re)* with an increased thermal performance enhancement factor *(TPEF)*. Precisely at *Re* 1155.4, $NR_{3\varepsilon=0.9CF}$ increased the *TPEF* by 60.6% and 93.4% compared to the $NR_{3\varepsilon=0.5CF}$ and $NR_{3\varepsilon=0.1CF}$ respectively. Parallel flow cooling systems exhibited a similar *TPEF* increase. The result shows that the tolerability of pressure drop to the obtained augmentation of heat transfer in the channels deteriorates with a decrease in the porosity of the insert. The demonstration of *TPEF* lesser than 1 by the cooling system equipped with *EAFε=0.5* and *EAFε=0.1* further substantiates this result. Thus, the implementation of *EAFε=0.5* and *EAFε=0.1* for the augmentation of the cooling system performance should be discouraged. Meanwhile, cooling

systems with counterflow arrangement offer slightly higher *TPEF* values than those with parallel flow arrangement regardless of the rectangular aluminum porosities.

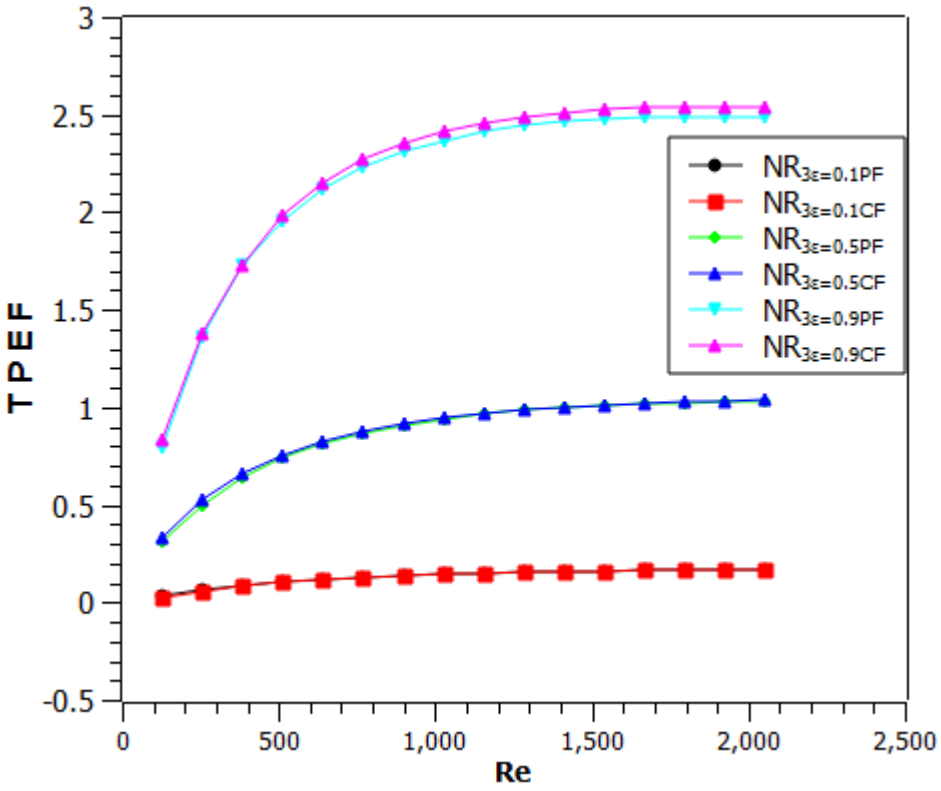

Figure 0.17. Thermal performance enhancement factor (*TPEF*) vs Reynolds number (*Re*) of the cooling system with rectangular aluminum foam of varying porosities insert. The color markers illustrate counterflow (CF) and parallel flow (PF) cooling systems equipped with a single aluminum foam of 0.1 porosity ($NR_{3\varepsilon=0.1CF}$ and $NR_{3\varepsilon=0.1PF}$), 0.5 porosity ($NR_{3\varepsilon=0.5CF}$ and $NR_{3\varepsilon=0.5PF}$) as well as 0.9 porosity ($NR_{3\varepsilon=0.9CF}$ and $NR_{3\varepsilon=0.9PF}$).

7.3.2.4 Effect of varying locations of a single rectangular aluminum foam of 0.9 porosity (RAFε=0.9) inserted in the channel(s) on the cooling system's performance

From the preceding section, a cooling system with three channels and a centrally located RAFε=0.9 (at L/2) yields the highest dimensionless heat transfer rate density, demonstrating superior thermal performance for dissipating heat from the battery pack. This section further analyses the effect of alternative locations of *RAFε=0.9* within the cooling system channels to determine how different locations may influence thermal performance and heat dissipation effectiveness. This analysis explores whether *RAFε=0.9* alternative placements can further improve cooling system performance beyond the best configuration identified earlier.

Figure 7.18 illustrates the reduction in the dimensionless thermal resistance (R_{th}) with an increased Reynolds number (Re) regardless of the point of placement of *RAFε=0.9* cooling systems' channels. When the *Re* increased from 128.38 to 1283.8, a significant dimensionless R_{th} reduction was realized, and beyond this point, a further increase in *Re* had no significant effect on the dimensionless R_{th} reduction. Meanwhile, regardless of flow orientation, the lowest and the highest dimensionless R_{th} were achieved with the placement of *RAFε=0.9* at *L/8* ($NR_{M\varepsilon=0.9PF}$ *and* $NR_{M\varepsilon=0.9CF}$) and *L/2* ($NR_{3\varepsilon=0.9PF}$ *and* $NR_{3\varepsilon=0.9CF}$) in the cooling systems' channels indicating that the closer the insert to the inlet, the better the cooling system capacity. In addition, counterflow cooling systems obtained a slightly lower dimensionless R_{th} than the parallel flow cooling systems.

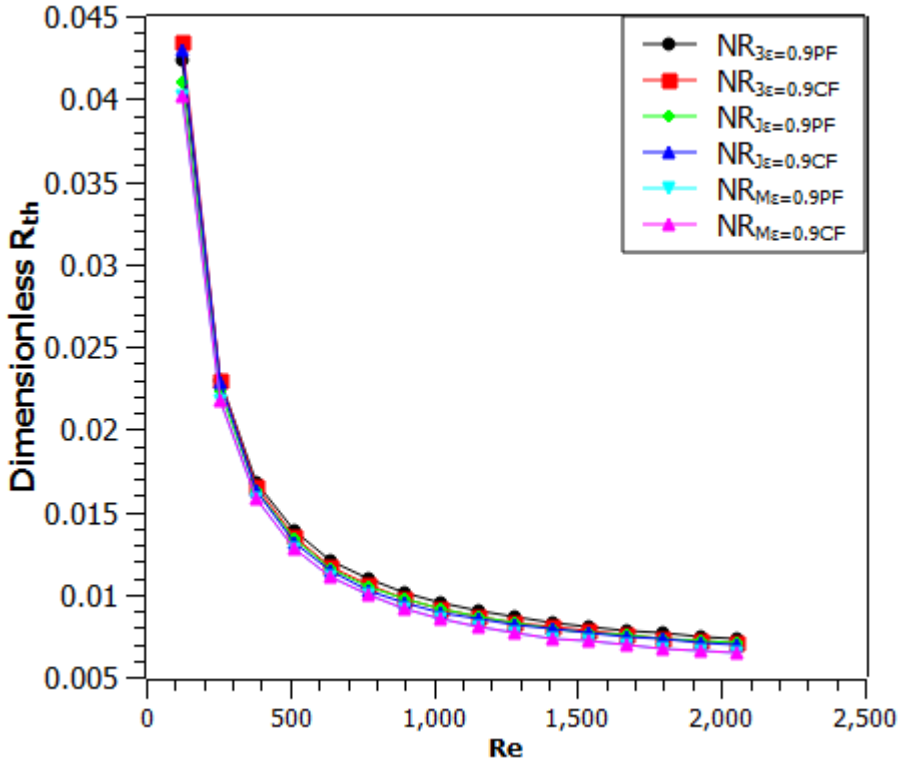

Figure 0.18. Dimensionless thermal resistance (R_{th}) vs Reynolds number (*Re*) of the cooling system with a single rectangular aluminum foam of 0.9 (*RAFε=0.9*) porosity insert. The colored markers illustrate counterflow (CF) and parallel flow (PF) cooling systems equipped with a single *RAFε=0.9* located at *L/2* ($NR_{3\varepsilon=0.9CF}$ and $NR_{3\varepsilon=0.9PF}$), ($NR_{J\varepsilon=0.9CF}$ and $NR_{J\varepsilon=0.9PF}$), and *L/8* ($NR_{M\varepsilon=0.9CF}$ and $NR_{M\varepsilon=0.9PF}$).

7.3.2.5 Comparison of a single and varying spacing arrangement of three rectangular aluminum foam (RAFε=0.9) insert(s) in the channel(s) on the cooling system's performance

To compare the effect of a single with multiple insert(s) in the channels on the thermal performance enhancement of the cooling systems, the *RAFε=0.9* was increased to three from the best insert location (*L/8*) towards the inlet. The realization of the optimum thermal performance of a designed cooling system with at most 3-pin fins in the channel was earlier reported by [208] with no emphasis on the search for the best insert location in the channels. Hence, the reason for employing three *RAFε=0.9* of varying in-line spacing arrangements (1.5mm, 2.0mm, and 2.5mm) for comparison with a single *RAFε=0.9*.

Figure 7.19, illustrates an inverse relationship between the dimensionless thermal resistance (R_{th}) and the Reynolds number (*Re*). A drastic dimensionless R_{th} reduction was obtained when *Re* increased from 128.38 to 1283.8. However, an insignificant dimensionless R_{th} occurred when the *Re* is further increased beyond this point. Precisely at *Re* 898.66, $NR1.5M_{\varepsilon=0.9PF}$ possessed a lower dimensionless R_{th} of 7.8% and 8.2% respectively compared to the $NR2.0M_{\varepsilon=0.9PF}$ and $NR2.5M_{\varepsilon=0.9PF}$ the minimization of the distance between the three RAFε=0.9 leads to improved cooling system performance. In the counterflow cooling systems, a similar pattern of 11.43% and 13.01% of dimensionless R_{th} reduction was also demonstrated by $NR1.5M_{\varepsilon=0.9CF}$ compared to $NR2.0M_{\varepsilon=0.9CF}$ and $NR2.5M_{\varepsilon=0.9CF}$ at same *Re*. Remarkably, cooling systems with a single *RAFε=0.9* gave the lowest dimensionless R_{th} compared to cooling systems of three *RAFε=0.9* inserts. For instance, $NE_{M\varepsilon=0.9CF}$ reduced the system dimensionless R_{th} by 13.9%, 13.0%, and 2.7% compared to $NR2.5M_{\varepsilon=0.9CF}$, $NR2.0M_{\varepsilon=0.9CF}$, and $NR1.5M_{\varepsilon=0.9CF}$ at *Re* 2054.08. A similar pattern in the reduction of dimensionless Rth was observed with parallel flow cooling systems. Moreover, cooling systems with counterflow arrangements achieved a slightly lower dimensionless R_{th} than those with the parallel flow arrangements regardless of the number and spacing arrangements of *RAFε=0.9* in the cooling systems' channels.

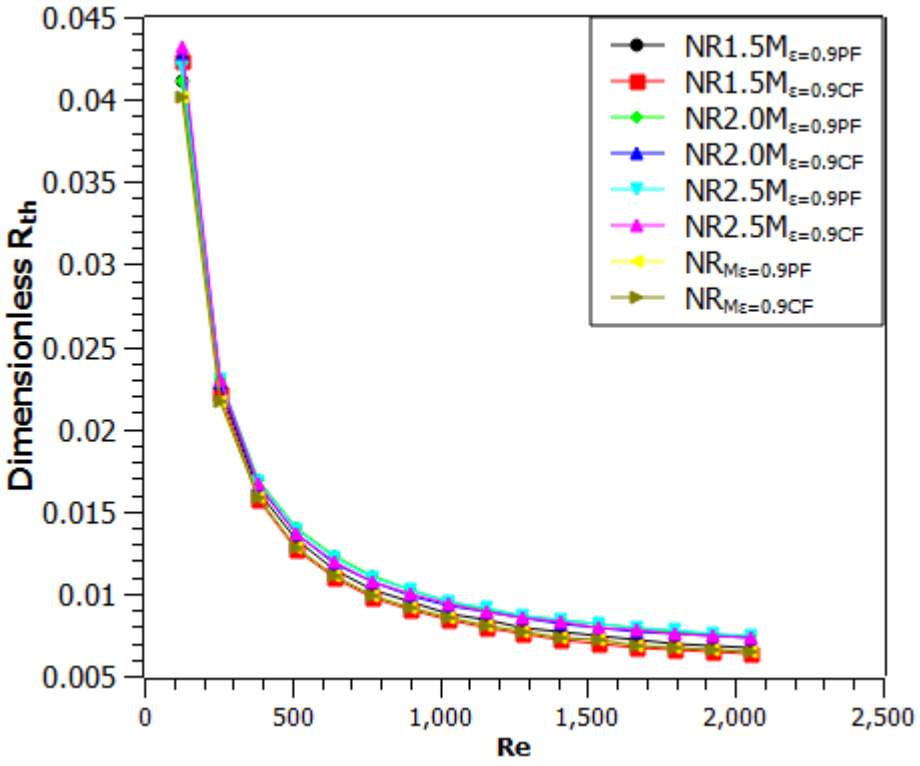

Figure 0.19. Dimensionless thermal resistance (R_{th}) vs. Reynolds number (*Re*) of the cooling system with rectangular aluminum foam of 0.9 (RAFε=0.9) porosity insert(s). The color markers illustrate counterflow (CF) and parallel flow (PF) cooling systems equipped with a single RAFε=0.9 ($NR_{M\varepsilon=0.9CF}$ and $NR_{M\varepsilon=0.9PF}$), and 1.5 mm ($NR1.5M_{\varepsilon=0.9CF}$ and $NR1.5M_{\varepsilon=0.9PF}$), 2.0 mm ($NR2.0M_{\varepsilon=0.9CF}$ and $NR2.0M_{\varepsilon=0.9PF}$), and 2.5 mm ($NR2.5M_{\varepsilon=0.9CF}$ and $NR2.5M_{\varepsilon=0.9PF}$) spacing arrangements of three RAFε=0.9 in the channels.

7.3.2.6 Normalized friction factor effect between the varying locations of a single and spacing arrangement of three rectangular aluminum foam of 0.9 porosity (RAFε=0.9)

As indicated in Figure 7.20 (a) and (b), the increase in Reynolds number (Re) increases the Normalized friction factor (*NFF*). The obtained *NFF* values higher than 3 exhibited by both figures suggest that *RAFε=0.9* in the fluid domain can raise the working fluid friction higher than three compared to the cooling systems without an insert. Specifically, at *Re* 2054.08, $NR_{M\varepsilon=0.9CF}$ respectively reduced *NFF* by 2.93% and 5.25% compared $NR_{J\varepsilon=0.9CF}$ and $NR_{3\varepsilon=0.9CF}$ reflecting a direct relationship between the *NFF* values and the distance of the insert to the inlet. In a like manner, 2.1% and 4.7% *NFF* reduction was obtained with $NR_{M\varepsilon=0.9PF}$ compared to $NR_{J\varepsilon=0.9PF}$ and $NR_{3\varepsilon=0.PCF}$ at the same *Re* (Figure 7.20a). Similarly,

at *Re*, 2054.08, $NR2.5M_{\varepsilon=0.9CF}$ reduced NFF by 3.62% and 7.14% respectively, compared to $NR2.0M_{\varepsilon=0.9CF}$ and $NR1.5M_{\varepsilon=0.9CF}$ (Figure 7.20b) Also, precisely at the same *Re* 3.40% and 6.93% *NFF* values, reduction was recorded by $NR2.5M_{\varepsilon=0.9PF}$ compared to $NR2.0M_{\varepsilon=0.9PF}$ *and* $NR1.5M_{\varepsilon=0.9PF}$ suggesting that a larger space between the inserts results in an increased value of *NFF*. However, regardless of the varying locations of a single and spacing arrangements of three *RAFε=0.9* in the systems' channels, counterflow cooling systems incurred *NFF* slightly higher than the parallel flow cooling systems. Cooling systems with three *RAFε=0.9* (Figure 7.20b) gave higher values of *NFF* compared to those with a single *RAFε=0.9* (Figure 7.20a) indicating the direct effect of increased fluid domain complexity on the working fluid friction in the channels.

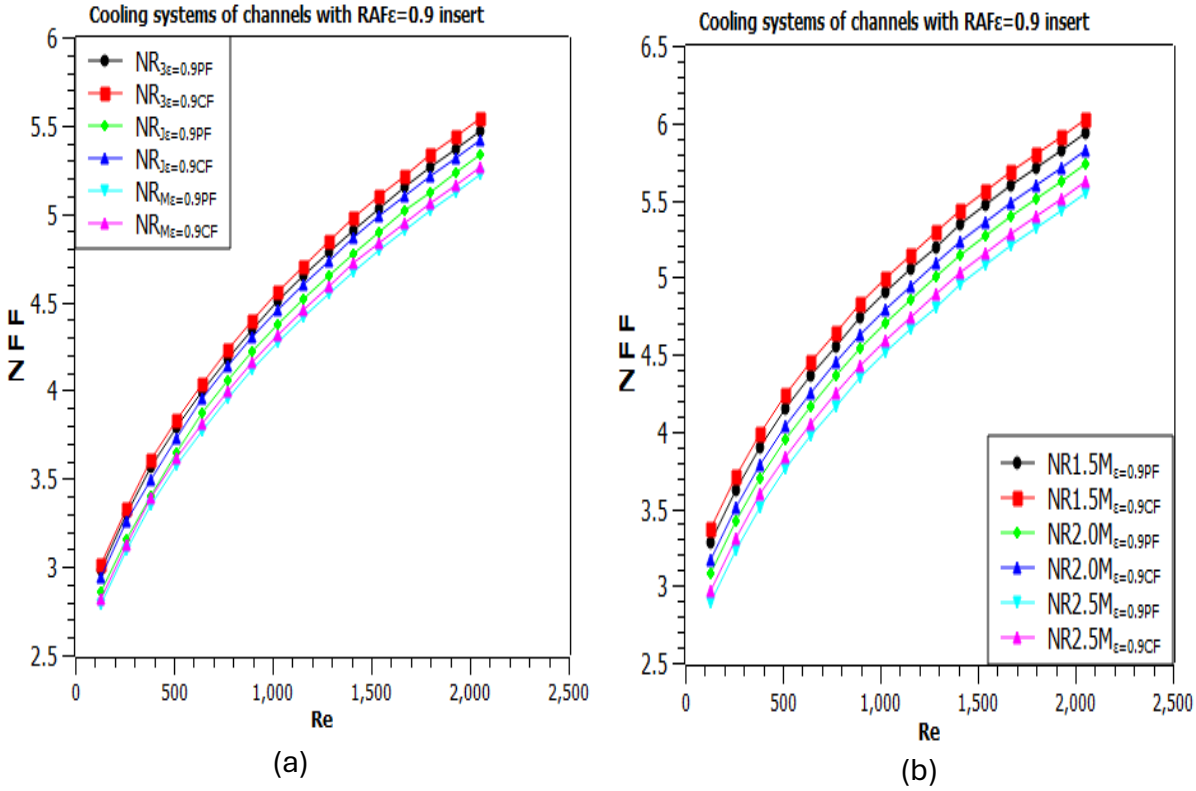

Figure 0.20. Normalized friction factor (NFF) vs. Reynolds number (Re) of the cooling system with a single (a) and three (b) elliptical aluminum foam of 0.9 (RAFε=0.9) porosity insert(s). The color markers illustrate counterflow (CF) and parallel flow (PF) cooling systems equipped with varying locations of a single and spacing arrangement of multiple RAFε=0.9 in the channels.

7.3.2.7 Comparison of the thermal performance enhancement factor effect between the varying location of a single and varying spacing arrangement of three rectangular aluminum foam of 0.9 porosity (RAFε=0.9)

Figure 7.21 shows an increase in the thermal performance enhancement factor (*TPEF*) with the growth of the Reynolds number (*Re*) for the cooling systems regardless of the number and spacing arrangements of the rectangular aluminum foam of 0.9 porosity (*RAFε=0.9*) inserted in the channels. A significant *TPEF* occurred when the *Re* increased from 128.38 to 1155.42 above this point, the *Re* effect on *TPEF* becomes negligible. However, the display of a *TPEF* higher than 1 by all considered systems depicts that an application of *RAFε=0.9* can augment heat transfer with a tolerable increased friction factor in the cooling systems' channel [45]. Precisely at *Re* 898.66, to $NR2.0M_{\varepsilon=0.9PF}$ increased the *TPEF* by 5.61% and 1.67% compared to $NR2.5M_{\varepsilon=0.9PF}$ and to $NR1.5M_{\varepsilon=0.9PF}$ respectively indicating that the tolerability of increased friction factor effect on improved heat transfer enhancement in the cooling system channels is more pronounced with 2.0 mm than 2.5 mm and 1.5 mm spacing arrangement of RAFε=0.9. A similar *TPEF* increase of 4.81% and 1.36% was exhibited by $NR2.0M_{\varepsilon=0.9CF}$ compared to $NR2.5M_{\varepsilon=0.9CF}$ and $NR1.5M_{\varepsilon=0.9CF}$ at the same *Re*. Meanwhile, the figure shows that the placement of a single RAFε=0.9 at L/8 in the cooling system channels achieved higher *TPEF* values than when three *RAFε=0.9* were implemented. For instance, $NR_{M\varepsilon=0.9CF}$ improved the *TPEF* by 12.58%, 4.13% and 8.12% respectively compared to $NR2.5M_{\varepsilon=0.9CF}$, $NR2.0M_{\varepsilon=0.9CF}$ and $NR1.5M_{\varepsilon=0.9CF}$ at the fixed *Re* 2054.08. In a like manner, at the same *Re*, 12.29%, 4.46% and 7.60% TPEF improvement were also obtained by $NR_{M\varepsilon=0.9PF}$ compared $NR2.5M_{\varepsilon=0.9PF}$, $NR2.0M_{\varepsilon=0.9PF}$ and $NR1.5M_{\varepsilon=0.9PF}$. Thus, the systems with a single RAFε=0.9 give the best results in enhancing the cooling systems' thermal performance compared to all systems with three *RAFε=0.9* inserts. Moreover, regardless of the number and the spacing arrangement of the *RAFε=0.9* in the channels, cooling systems with counterflow arrangements give slightly higher values of *TPEF* than those with the parallel flow arrangements.

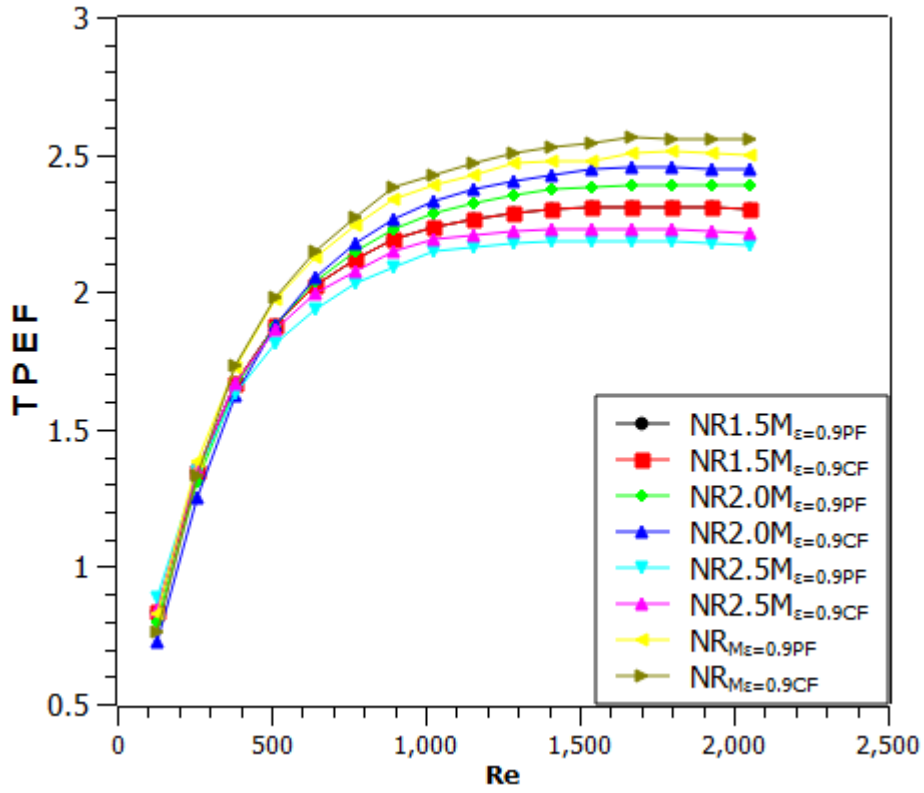

Figure 0.21. Thermal performance enhancement factor (*TPEF*) vs. Reynolds number (*Re*) of the cooling system with rectangular aluminum foam of 0.9 (RAFε=0.9) porosity insert(s). The color markers illustrate counterflow (CF) and parallel flow (PF) cooling systems equipped with a single RAFε=0.9 ($NR_{M\varepsilon=0.9CF}$ and $NR_{M\varepsilon=0.9PF}$), and 1.5 mm ($NR1.5M_{\varepsilon=0.9CF}$ and $NR1.5M_{\varepsilon=0.9PF}$), 2.0 mm ($NR2.0M_{\varepsilon=0.9CF}$ and $NR2.0M_{\varepsilon=0.9PF}$), and 2.5 mm ($NR2.5M_{\varepsilon=0.9CF}$ and $NR2.5M_{\varepsilon=0.9PF}$) spacing arrangements of three *RAFε=0.9* in the channels.

7.3.2.8 Temperature uniformity of the battery cells in the pack

As shown in Figures 7.22(a-d), the battery cells' temperature uniformity decreased with an increased Reynolds number regardless of the cooling systems designed. This study achieved a temperature uniformity variation of less than 2℃ from one battery cell to another, reflecting the cooling systems' capacity to maintain the temperature uniformity of the lithium-ion battery cells in a pack [13]. Insertion of the rectangular aluminum foam of 0.1 porosity (*RAFε=0.1*) provides a significant reduction and improved battery cells' temperature uniformity as indicated in Figure 7.22 (a) and (b) compared to Figure 4.11(a) and (b). Meanwhile, cooling systems with counterflow arrangement (Figure 7.22b) achieved a slightly lower battery cells' temperature uniformity than those with the parallel flow arrangement (Figure 7.22a). The

graph's convergence and decreased battery cell temperature uniformity values exhibited by $NR_{3\varepsilon=0.1CF}$ (Figure 7.22c) compared to $NR_{3\varepsilon=0.9CF}$ (Figure 7.22b) depicts that the cooling system's capacity to dissipate heat from the battery pack improves with a decreased porosity of the rectangular aluminum foam insert. In addition, the location of RAFε=0.9 at L/8 in the channels further reduced the battery cells' temperature uniformity, as shown in Figure 7.22d compared to Figure 7.22c.

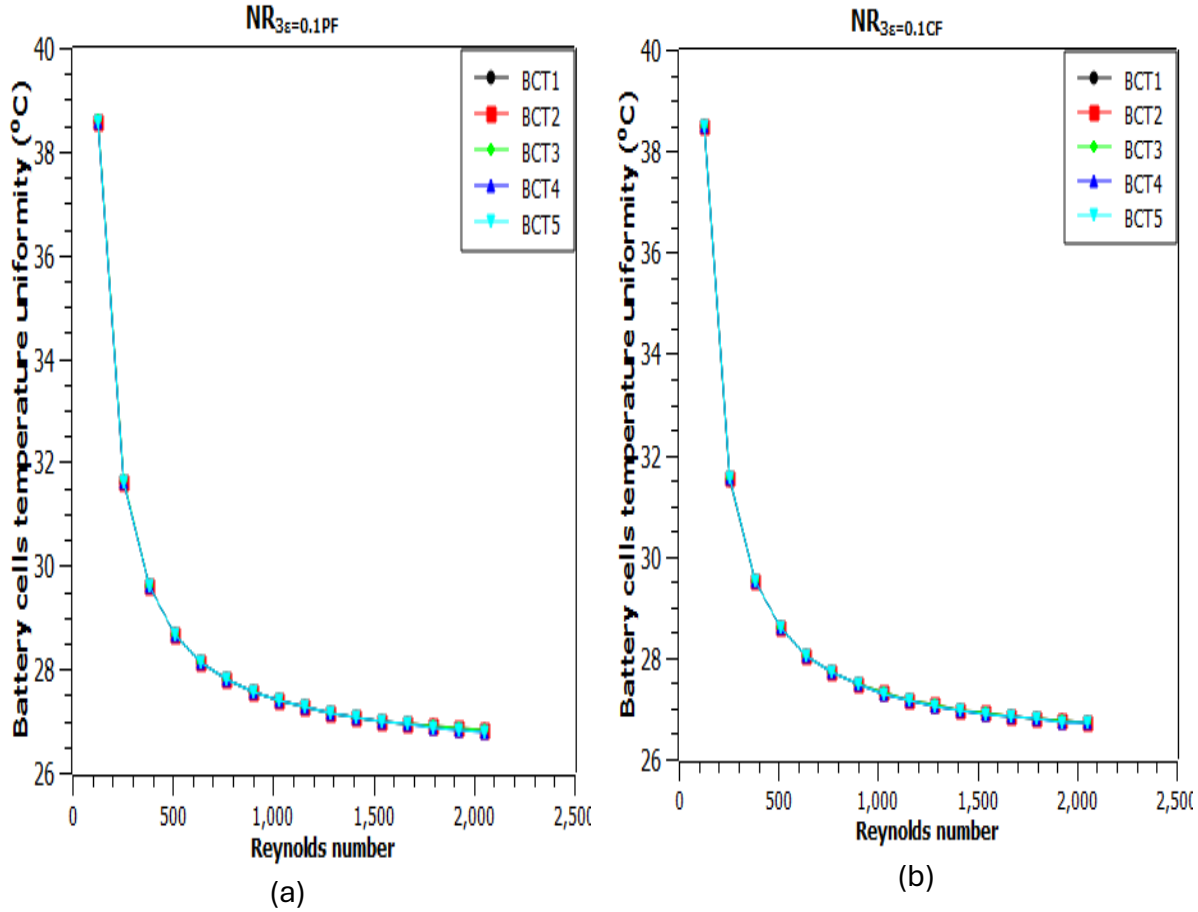

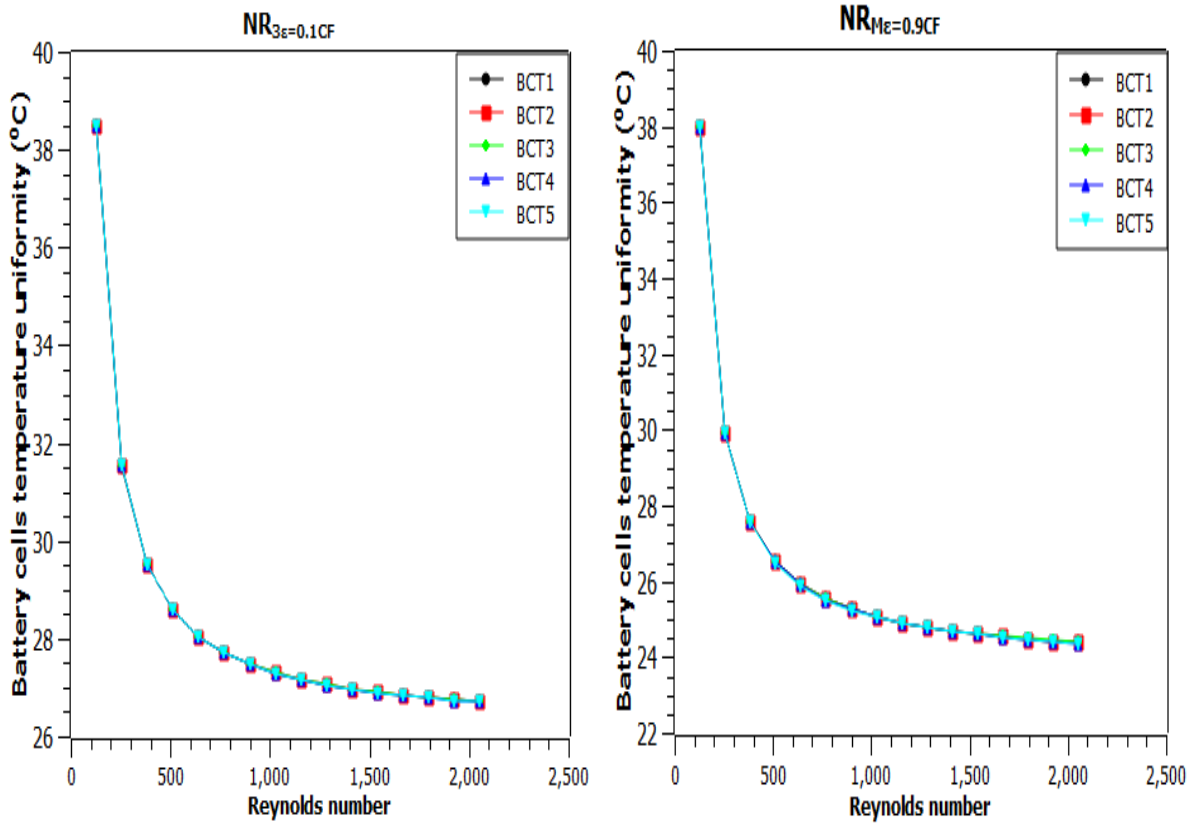

Figures 0.22. Battery cells temperature uniformity vs Reynolds number for the cooling system of three channels containing single rectangular aluminum foam of 0.1(*RAFε=0.1*) and 0.9 (*RAFε=0.9*) porosities: Parallel (a) and counterflow (b) system with centrally located *RAFε=0.1*, as well as counterflow system with *RAFε=0.9* inserted at the center (c) and *L/8* (d). The color makers represent the temperatures of each battery cell in a pack.

7.3.3 Case 3: Comparison of the enhancement capacity of the rectangular solid pin fin with aluminum foam inserted in the channel(s) of the cooling system.

7.3.3.1 Effect of Reynolds number on the thermal performance of the cooling system based on rectangular solid pin fin and rectangular aluminum foam insert comparison

This section investigates the effect of the Reynolds number on the maximum rectangular frame wall temperature, dimensionless thermal resistance, cost of pumping power, and thermal performance enhancement factor of the two counterflow cooling systems: with the rectangular solid pin fin insert located at L/8 (NR_{MCF}) in Case 1 and the rectangular aluminum foam insert with 0.9 porosity located at L/8 ($NR_{M\varepsilon=0.9CF}$) in Case 2. These systems are the most promising configurations for effective battery pack thermal management.

7.3.3.1.1 Maximum rectangular frame wall temperature

As shown in Figure 7.23, an increased Reynolds number (*Re*) reduces in the maximum wall temperature (T_{max}) of the rectangular frame regardless of the type of cooling system. The graph displayed a substantial T_{max} reduction when the *Re* increased from 128.38 to 1283.8 and beyond this, a further increase in *Re* yields an insignificant T_{max} reduction. Beyond *Re*, 128.38, NR_{MCF} consistently demonstrates lower T_{max} values compared to $NR_{M\varepsilon=0.9CF}$. Thus, specifically at *Re* 2054.08, NR_{MCF} reduced T_{max} by 0.3% compared to $NR_{M\varepsilon=0.9CF}$. This suggests that RSPF can enhance the system's cooling capacity better than $RAF\varepsilon=0.9$.

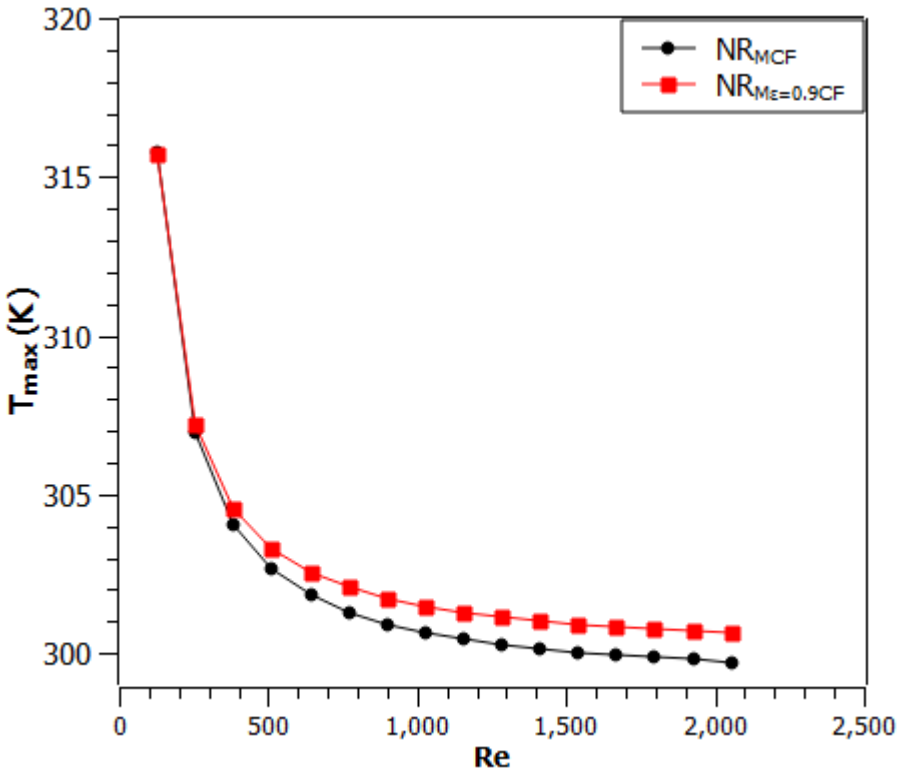

Figure 0.23. Maximum rectangular frame wall temperature (T_{max}) vs. Reynolds number (*Re*) for cooling systems with rectangular solid pin fin (RSPF) and aluminum foam of 0.9 porosity ($RAF\varepsilon=0.9$) inserts. The graph shows T_{max} as a function of *Re*, comparing RSPF (black marker) and $RAF\varepsilon=0.9$ (red marker) inserts located at *L/8* in the channels of the cooling systems.

7.3.3.1.2 Dimensionless thermal resistance

Figure 7.24 reports the influence of increased Reynolds number (*Re*) on the dimensionless thermal resistance (R_{th}) of both the cooling systems (NR_{MCF} and $NR_{M\varepsilon=0.9CF}$) The figure shows dimensionless R_{th} reduction with the growth of *Re*. However, significant dimensionless R_{th} reduction occurred when *Re* increased from 128.38 to 1283.8 and beyond this point, a further

increase in *Re* had an insignificant effect on dimensionless R_{th}. NR_{MCF} exhibited a steadily improved cooling capacity in decreasing the dimensionless R_{th} than $NR_{M\varepsilon=0.9CF}$ as the *Re* rises beyond 128.38 indicating that the application of RSPF enhances the cooling systems better than *RAFε=0.9*.

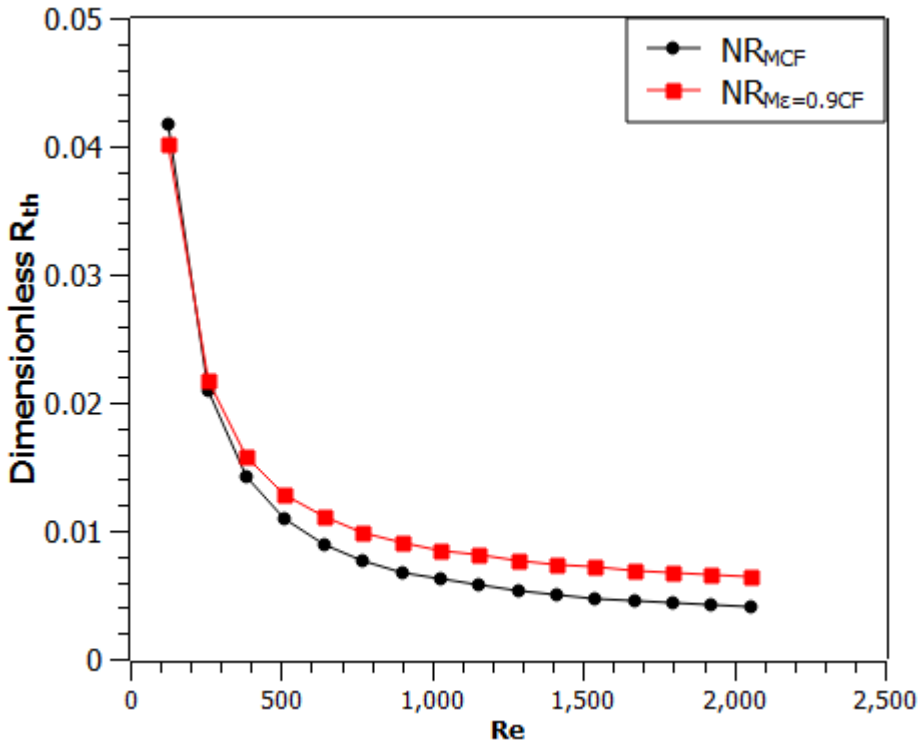

Figure 0.24. Dimensionless thermal resistance (R_{th}) vs. Reynolds number (*Re*) for cooling systems with rectangular solid pin fin (RSPF) and aluminum foam of 0.9 porosity (*RAFε=0.9*) inserts. The graph shows dimensionless R_{th} as a function of *Re*, comparing RSPF (black marker) and *RAFε=0.9* (red marker) inserts located at *L/8* in the channels of the cooling systems.

7.3.3.1.3 Cost of pumping power

The effect of the RSPF and *RAFε=0.9* on the cooling system cost of pumping power (*Pp*) as a function of Reynolds number (*Re*) is expressed in Figure 7.25. Regardless of the type of insert in the channel an increased *Pp* was obtained with an increased *Re*. However, a substantial increase in *Pp* was realized with both cooling systems when *Re* exceeded 385.14. Beyond *Re* 128.38, $NR_{M\varepsilon=0.9CF}$ incurred a significantly higher value of the *Pp* compared to NR_{MCF}. For instance, $NR_{M\varepsilon=0.9CF}$ raised the *Pp* by 53.4% compared to NR_{MCF} precisely at *Re* 2054.08, suggesting the realization of higher values of pressure drop along the flow path with the presence of *RAFε=0.9* than RSPF in the fluid domain.

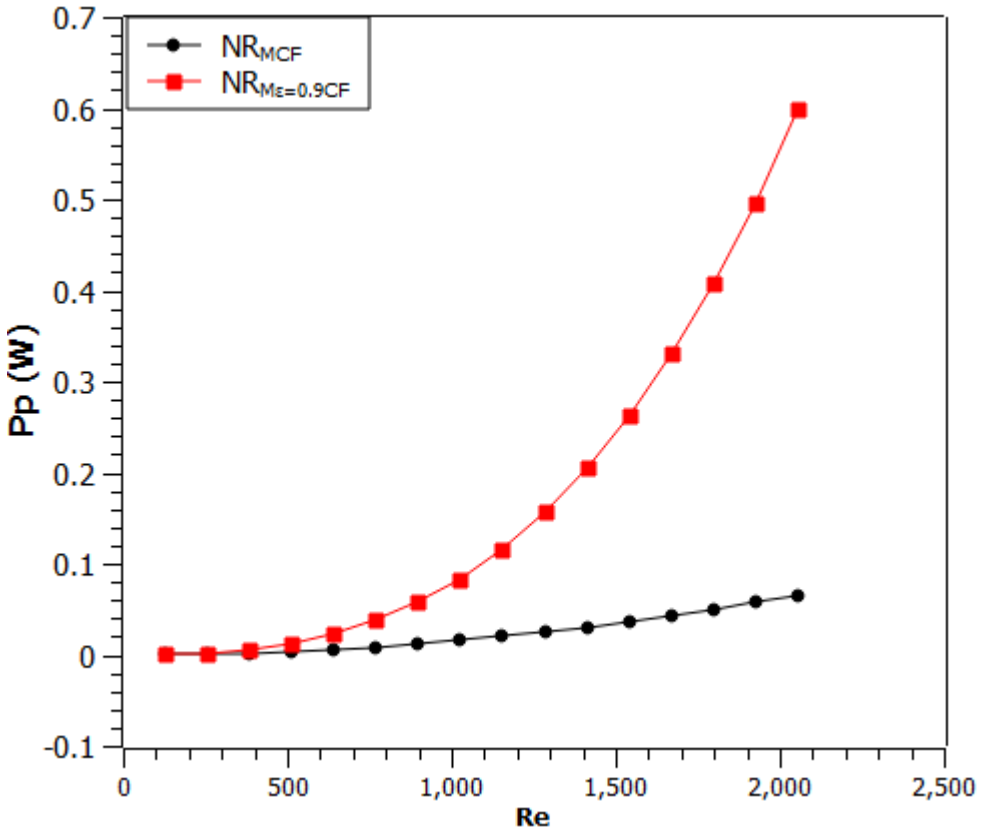

Figure 0.25. Cost of pumping power (*Pp*) vs. Reynolds number (*Re*) for cooling systems with rectangular solid pin fin (RSPF) and aluminum foam of 0.9 porosity (*RAFε=0.9)* inserts. The graph shows *Pp* as a function of *Re*, comparing RSPF (black marker) and *RAFε=0.9* (red marker) inserts located at *L/8* in the channels of the cooling systems.

7.3.3.1.4 Thermal performance enhancement factor

An increased Reynolds number (*Re*) yields an increased thermal performance enhancement factor (TPEF) regardless of the cooling system designed as shown in Figure 7.26. The figure demonstrates a *TPEF* value greater than 1 with either $NR_{M\varepsilon=0.9CF}$ (cooling system equipped with *RAFε=0.9)* or NR_{MCF} (cooling system equipped with RSPF) indicating that inserting RSPF or *RAFε=0.9* in the fluid domain can enhance the cooling system's performance with a tolerably increased friction factor. Below the *Re* 385.14, $NR_{M\varepsilon=0.9CF}$ demonstrates higher values of TPEF than $NR_{MCF,}$ and beyond this point, NR_{MCF} significantly achieved an increase in *TPEF* than $NR_{M\varepsilon=0.9CF}$. This result suggests that the implementation of *RAFε=0.9* appears to incur a considerable impact of increased pressure drop and consequently friction factor on the system performance than RSPF insert particularly when the *Re* exceeded 385.14. Meanwhile. NR_{MCF} achieved a consistent rising trend in *TPEF* value within the range of the *Re* applied in this work while a decline in the *TPEF* value was observed with $NR_{M\varepsilon=0.9CF}$ at *Re*

beyond 1668.94. Specifically, at Re 1668.94 and 2054.08 NR_{MCF} increased the TPEF values by 39.40% and 44.40% respectively indicating that RSPF is more promising for the cooling system thermal performance enhancement than the *RAFε=0.9* insert.

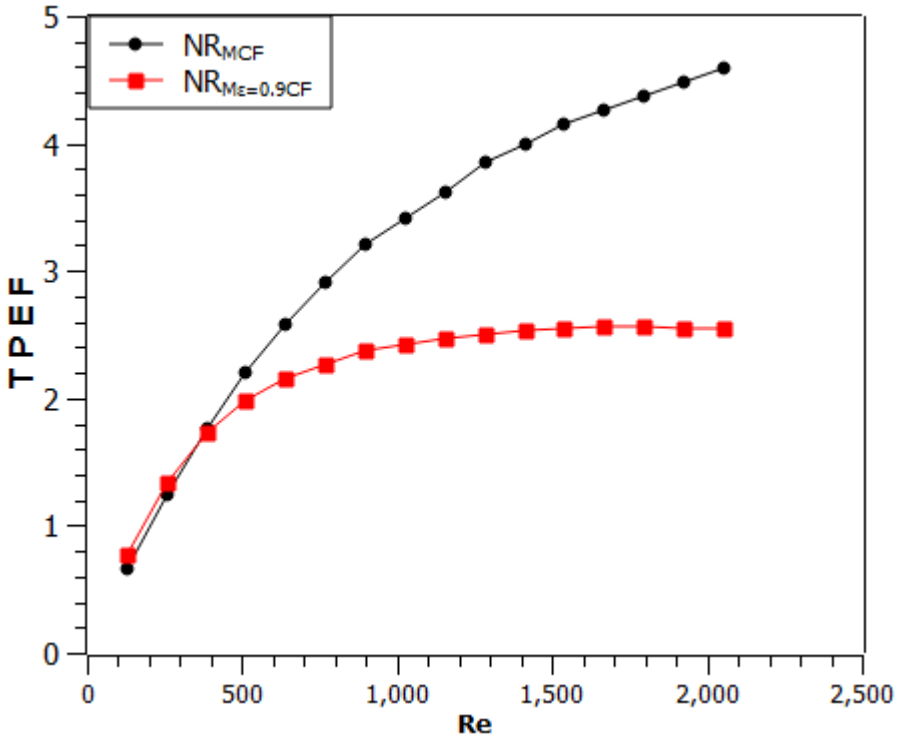

Figure 0.26. Thermal performance enhancement factor (*TPEF*) vs. Reynolds number (*Re*) for cooling systems with rectangular solid pin fin (RSPF) and aluminum foam of 0.9 porosity (*RAFε=0.9*) inserts. The graph shows *TPEF* as a function of *Re*, comparing RSPF (black marker) and *RAFε=0.9* (red marker) inserts located at *L/8* in the channels of the cooling systems.

7.3.3.2 Temperature contours

Figure 7.27 (a and b) displays the temperature contours of the systems with either an insert of rectangular solid pin fin (ESPF) or aluminum foam of 0.9 porosity (*RAFε=0.9)* located at *L/8* towards the inlet. The contours are plotted at X plane 25mm and inlet velocity 1.1m/s (Reynolds number 1412.18). Notably, the system with RSPF (NR_{MCF}) achieved a lower temperature distribution than that of the RAFε=0.9 ($NR_{M\varepsilon=0.9CF}$) reflecting the superiority of the RSPF insert to dissipate heat from the battery pack over the *RAFε=0.9*.

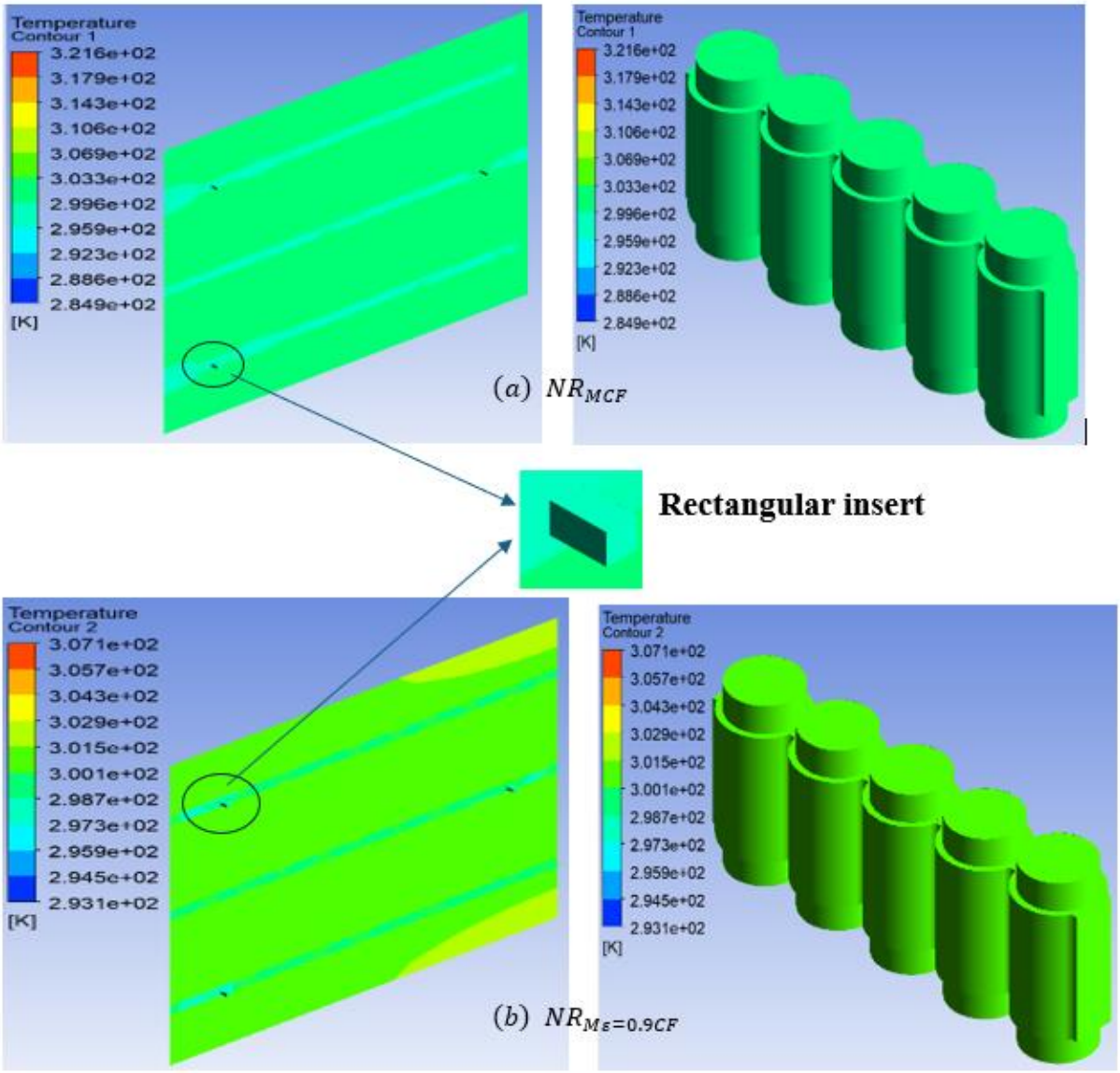

Figures 0.27. Temperature contour for counterflow cooling system of three channels with RSPF (a), and *RAFε=0.9* (b) insert.

7.4 Conclusions

This chapter analyzed the thermal enhancement potential of a cooling system designed for cylindrical lithium-ion batteries using either rectangular solid pin fins or aluminum foam inserts with varying porosities. The effects of the number of channels, the locations of inserts, and the Reynolds number (*Re*) on thermal performance were evaluated numerically for *Re* values between 128.38 and 2054.08. Key findings include:

1) **Number of mounted channels**: (a) Maximum dimensionless heat transfer rate density was observed in systems with three channels of centrally located rectangular solid pin fin (RSPF) or aluminum foam of 0.1 porosity (*RAFε=0.1*) inserts on the rectangular

frame. (b) At the highest applied Reynolds number, the parallel flow and counterflow systems of the three channels with RSPF, respectively achieved 94.91% and 95.01% higher dimensionless heat transfer rate density in comparison to their counterpart with no insert. A similar pattern of the dimensionless heat transfer rate density increases of 94.96% and 95.07% were obtained with parallel flow and counterflow systems of the three channels with $RAF\varepsilon = 0.1$ inserts.

2) **Best insert location**: The best performance was achieved when the inserts (RSPF or aluminum foam) were positioned at *L/8* towards the leading edge of the channels.

3) Impact of Porosity: High porosity (0.9) rectangular aluminum foam inserts showed acceptable performance, while lower porosities (0.1 and 0.5) resulted in high pumping power and friction factor, limiting their applicability.

4) Single versus Multiple Inserts: A single insert positioned at *L/8* towards the leading-edge enhanced cooling performance more effectively than multiple inserts, regardless of spacing.

5) Counterflow versus Parallel Flow Systems: Counterflow cooling systems demonstrated a slight advantage in reducing maximum wall temperature and thermal resistance compared to parallel flow systems.

The superior thermal performance enhancement factor (*TPEF*) of the NR_{MCF} system compared to $NR_{M\varepsilon=0.9CF}$ suggests that the RSPF insert is the optimal choice for effective temperature control of cylindrical lithium-ion battery packs in electric vehicles. Hence, this chapter finds NR_{MCF} to be the most promising cooling system for the thermal management of the battery pack of an electric vehicle.

CHAPTER EIGHT

COMPARATIVE ANALYSIS OF DIFFERENT CONFIGURATIONS' INSERT EFFECT ON THE ENHANCEMENT OF THE THERMAL PERFORMANCE OF THE COOLING SYSTEM

8.1 Preview

Chapters 5 through 7 demonstrated that a counterflow cooling system with three channels and inserts—circular solid pin fins (CSPF), elliptical solid pin fins (ESPF), or rectangular solid pin fins (RSPF)—positioned at *L/8* on the rectangular frame provided the highest thermal performance. This chapter compares the effects of these inserts on the cooling system's thermal performance.

8.2 Effect of Reynolds number on the thermal performance of the cooling system with circular, elliptical, and rectangular solid pin fin inserts comparison

8.2.1 Maximum rectangular frame wall temperature

Figure 8.1 illustrates the reduction in the rectangular frame's maximum wall temperature (T_{max}) as a function of the Reynolds number (*Re*). Regardless of the insert configuration, T_{max} decreases with increasing *Re*. However, a significant reduction in T_{max} occurs between *Re* 128.38 and 1283.8, beyond which further increases in *Re* have a negligible impact. Among the configurations, the cooling system with RSPF inserts (NR_{MCF}) achieved the most significant T_{max} reduction. For instance, at *Re* 2054.08, the NR_{MCF} configuration reduced T_{max} by 0.24% and 0.1% compared to the NE_{MCF} and NC_{MCF} configurations, respectively

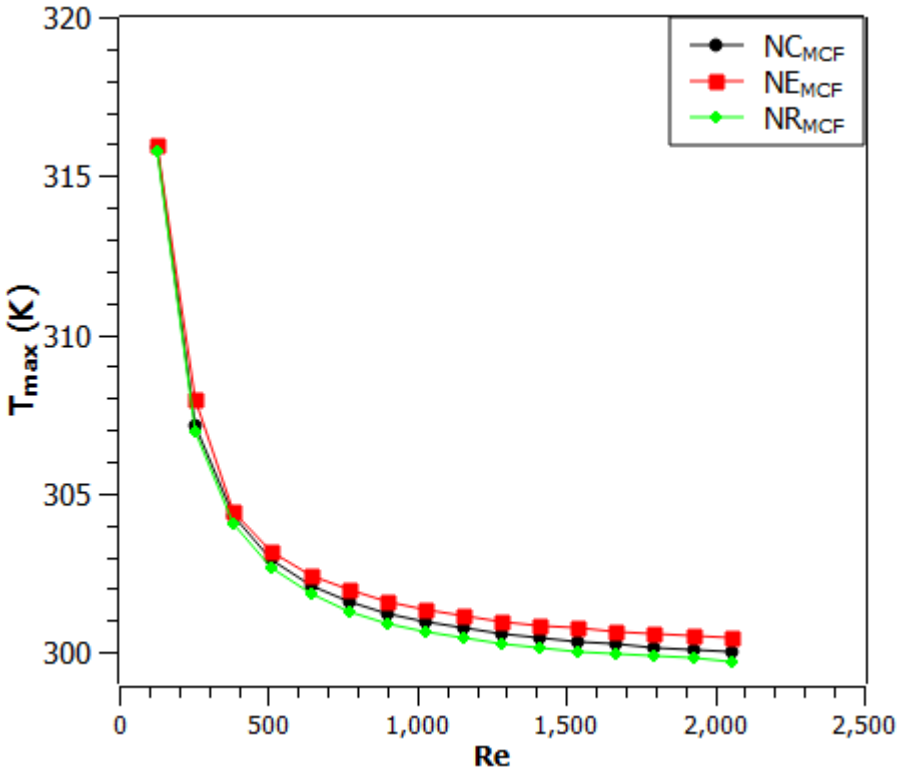

Figure 0.1. Maximum rectangular frame wall temperature (T_{max}) vs Reynolds number (Re) of the cooling system with CSPF, ESPF, and RSPF insert located at $L/8$. The graph illustrates the T_{max} as a function of Re comparing the potential enhancement of the CSPF (black maker), ESPF (red marker), and RSPF (green marker) inserts located at $L/8$ in the channels of the cooling system.

8.2.2 Dimensionless thermal resistance

An inverse relationship between the dimensionless thermal resistance (R_{th}) and the Reynolds number (Re) was observed in Figure 8.2 indicating the strength of the cooling system to dissipate heat from the battery of an electric vehicle, regardless of the insert configuration in the channel. The figure presents a similar trend of dimensionless R_{th} reduction with all considered cooling systems: NE_{MCF}, $NC_{MCF,}$ and NR_{MCF}. However, a significant dimensionless R_{th} reduction occurred when the Re increased from 128.38 to 1283.8, and beyond this point, a further increased in Re had an insignificant effect on the dimensionless R_{th} reduction. For the range of the applied Re in this work, the highest and the lowest dimensionless R_{th} were obtained from NR_{MCF} and $NE_{MCF,}$ respectively. Thus, the dissipation of heat from the battery pack is more pronounced with the insertion of RSPF in the cooling system channels than CSPF or ESPF.

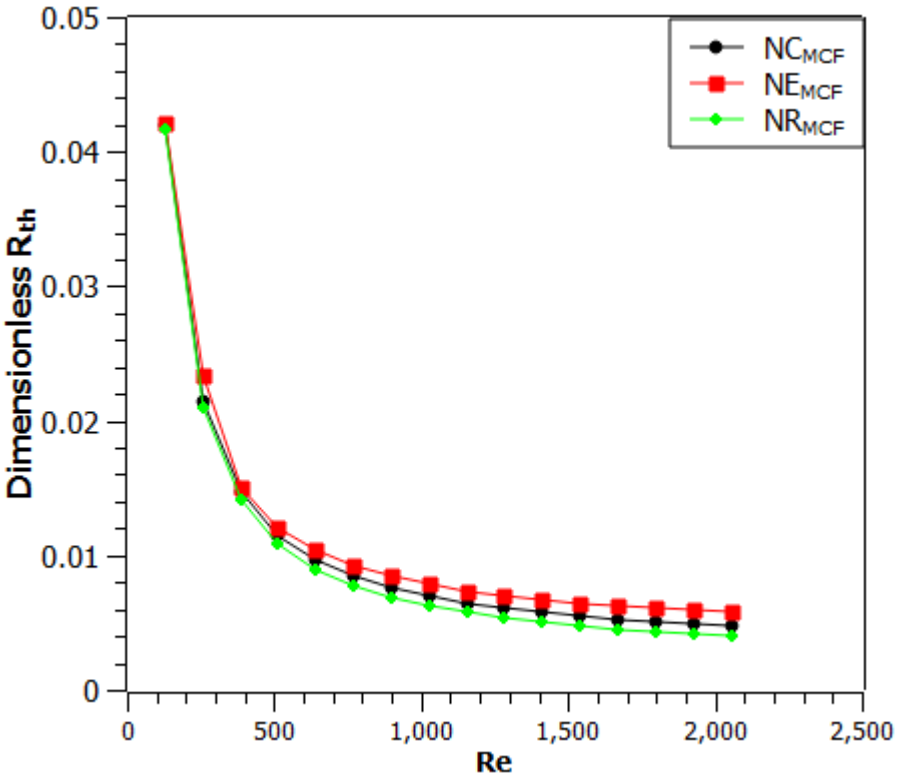

Figure 0.2. Dimensionless thermal resistance (R_{th}) vs Reynolds number (*Re*) of the cooling system with CSPF, ESPF, and RSPF insert located at *L/8.* The graph illustrates the dimensionless *Rth* as a function of *Re,* comparing the potential enhancement of the CSPF (black marker), ESPF (red marker), and RSPF (green marker) inserts located at *L/8* in the channels of the cooling system.

8.2.3 Cost of pumping power

From Figure 8.3, an increased Reynolds number (*Re*) increases the cost of pumping power (*Pp*) regardless of the cooling systems' design. However, a consistent upward trend of the Pp values was realized with the examined cooling systems: NE_{MCF} (cooling system inserted with ESPF), NC_{MCF} (cooling system inserted with CSPF), and NR_{MCF} (cooling system inserted with RSPF). Meanwhile, the figure shows that NR_{MCF} incurred the highest Pp compared to NE_{MCF} and NC_{MCF}. For example, NR_{MCF} increased Pp values by 6.8% and 4.3% respectively, compared to NE_{MCF} and $NC_{MCF,}$ precisely at Re 2054.08. Thus, the insertion of the RSPF in the channels comes with the highest generation of pressure drop and consequently higher value of cost of pumping power than CSPF and ESPF.

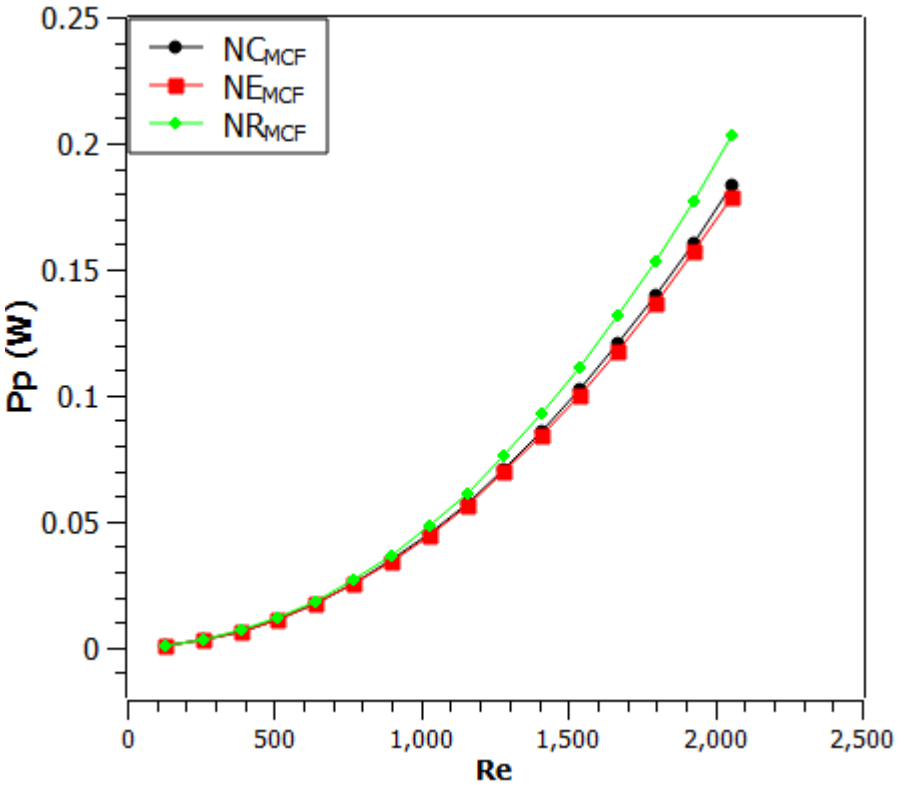

Figure 0.3. Cost of pumping power (*Pp*) vs Reynolds number (*Re*) of the cooling system with CSPF, ESPF, and RSPF insert located at *L/8*. The graph illustrates the *Pp* as a function of *Re* comparing the potential enhancement of the CSPF (black marker), ESPF (red marker), and RSPF (green marker) inserts located at *L/8* in the channels of the cooling system.

8.2.4. Thermal performance enhancement factor

Figure 8.4 reports an increased thermal performance enhancement factor (*TPEF*) with an increased Reynolds number (Re) regardless of the insert configuration in the cooling system's channel. The graph shows the *TPEF* values higher than 1 regardless of the cooling system's design indicating that the insertion of RSPF, CSPF, or ESPF in the channel can enhance the system performance with tolerably increased working fluid friction. However, a consistent upward trend of *TPEF* was recorded with all the systems: NE_{MCF} (cooling system inserted with ESPF), NC_{MCF} (cooling system inserted with CSPF), and NR_{MCF} (cooling system inserted with RSPF). The cooling system with the ESPF insert performed the worst compared to those with CSPF and RSPF. Meanwhile, the realization of 10.6% and 4.2% of increased *TPEF* by NC_{MCF} compared to NE_{MCF} and $NR_{MCF,}$ specifically at *Re* 2058.04, implies that tolerability of increased pressure drop on the heat transfer enhancement is more pronounced with the implementation

of CSPF than RSPF and ESPF insert. Thus, NC_{MCF} is more promising for the thermal management of electric vehicles' cylindrical lithium-ion battery pack.

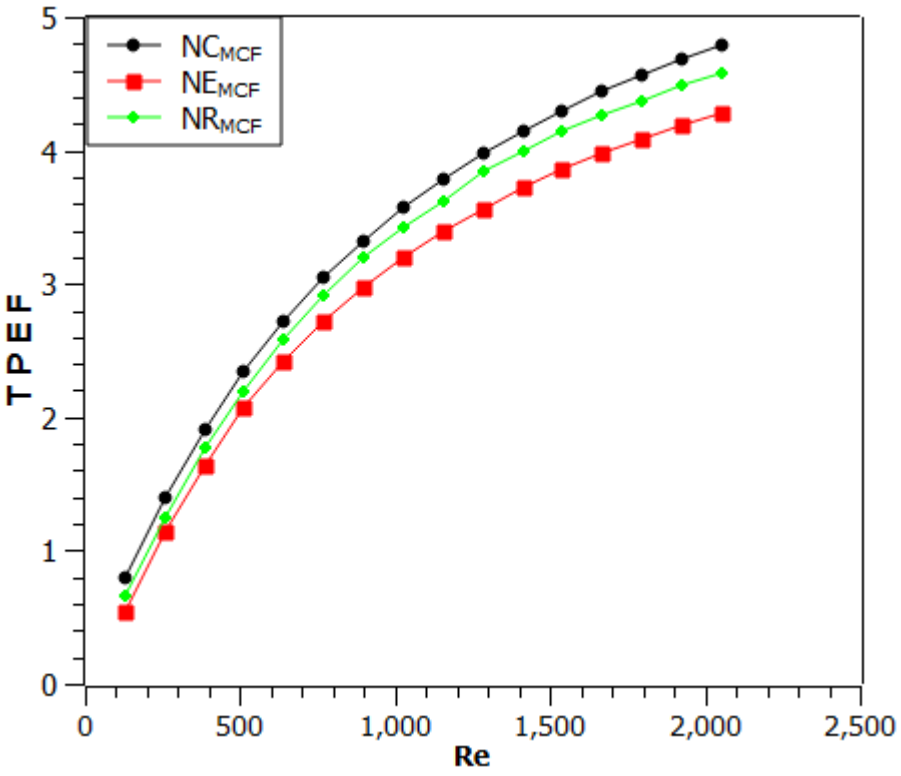

Figure 0.4. Thermal performance enhancement factor (*TPEF*) vs Reynolds number (*Re*) of the cooling system with CSPF, ESPF, and RSPF insert located at *L/8*. The graph illustrates *TPEF* as a function of *Re*, comparing the potential enhancement of the CSPF (black marker), ESPF (red marker), and RSPF (green marker) inserts located at *L/8* in the channels of the cooling system.

8.3 Conclusions

This chapter reports the comparison effects of different shapes of solid pin fins located at the L/8 towards the inlet on the thermal performance enhancement of the cooling system designed for temperature control of the cylindrical lithium-ion battery pack of electric vehicles. The results show that the RSPF and ESPF inserts, respectively, show the highest and lowest strength in dissipation of heat from the battery pack. However, the system with RSPF insert incurred the highest pressure drop value (cost of pumping power) along the flow path, which has an adverse effect on the overall thermal performance of the cooling system. Specifically, at the highest Reynolds number applied in this work, NC_{MCF} obtained 10.6% and 4.2% of the system performance enhancement compared to the NE_{MCF} and $NR_{MCF,}$ indicating

that CSPF located in the channels appears to be the most promising insert for the enhancement of the system performance designed for thermal management of the cylindrical lithium-ion battery pack of an electric vehicle.

CHAPTER NINE

CONSTRUCTAL DESIGN AND OPTIMIZATION OF THE COOLING SYSTEM

9.1 Preview

Optimizing the cooling system to achieve maximum thermal performance under specific manufacturing constraints is critical for efficient thermal management of electric vehicle battery packs. In this chapter, the counterflow cooling system with three channels (N_{3CF}) mounted on a rectangular frame, which demonstrated superior heat dissipation in previous analyses, is selected for optimization. Special attention is given to configurations with circular solid pin fin (CSPF) inserts positioned at one-eighth of the channel length from the inlet (*L/8*) referred to as $NC_{MCF,}$ as detailed in Chapters 4 and 8. The optimized cooling system with CSPF inserts ($(NC_{MCF})_{opt}$) is compared against the unoptimized version (NC_{MCF}) to identify the most cost-effective and efficient design for managing the thermal performance of electric vehicle battery packs.

9.2 Grid analysis and code validation

The grid analysis and model validation carried out for the optimization process are illustrated in section 4.3.

9.3 Optimization procedures and design variables

The constructal theory and design approach was applied by fixing the length and volume of the cooling system's channels mounted on the rectangular frame (N_{3CF}) as shown in Figure 9.1. For the first stage of the optimization process, the channel length (L) and volume (Vol) were fixed at 59.4 mm and 2.23 mm^3, thereafter, the optimization process was repeated with fixed channel volume of 2.43 mm^3 and 2.63 mm^3. Subject to the manufacturing constraints, the system's internal structure is allowed to vary. The Bejan number (dimensionless pressure drop) of 7×10^8, 6×10^9 and 9×10^9 equivalent to Reynolds numbers 128.38, 1027.04, and 1540.56 were employed for all the conducted optimization processes. However, $1.14\ mm \leq W_c \leq 1.56\ mm$, $0.55\ mm \leq H_c \leq 1.72\ mm$, and $0.07\ mm \leq z_1 \leq 0.34\ mm$ were set for the response surface spacing in this study. It is important to note that the rectangular frame of dimensions $60\ mm \times 59.4mm \times 3mm$ imposed with the volumetric heat transfer of $3340135\ W/m^3$ equivalent to the total heat generated by the battery pack, remained fixed throughout the optimization process. The optimized system is later inserted with a circular solid

pin fin (CSPF) at *L/8* in the channel for performance enhancement. As stated in Equation (9.6), the inserted CSPF aspect ratio is also subject to manufacturing constraints. Meanwhile, the design space for the CSPF insert was set as $0.9 \leq H_f \leq 1.2$ mm and $0.5 \leq D_f \leq 0.73$ mm

$$\text{Bejan number (Be)} = \frac{\Delta P L^2}{\alpha \mu} \tag{9.1}$$

$$LWH = \text{Vol= constant} \tag{9.2}$$

$$z_2 = z_3 \leq 0.095\text{mm} \tag{9.3}$$

$$\frac{H_c}{W_c} \leq 1.8 \tag{9.4}$$

$$D_h \leq 1.6 \text{ mm} \tag{9.5}$$

$$1.5 \leq \frac{H_f}{D_f} \leq 1.7 \tag{9.6}$$

System performance is measured using the maximum rectangular frame wall temperature (T_{max}) and dimensionless thermal resistance (R_{th}).

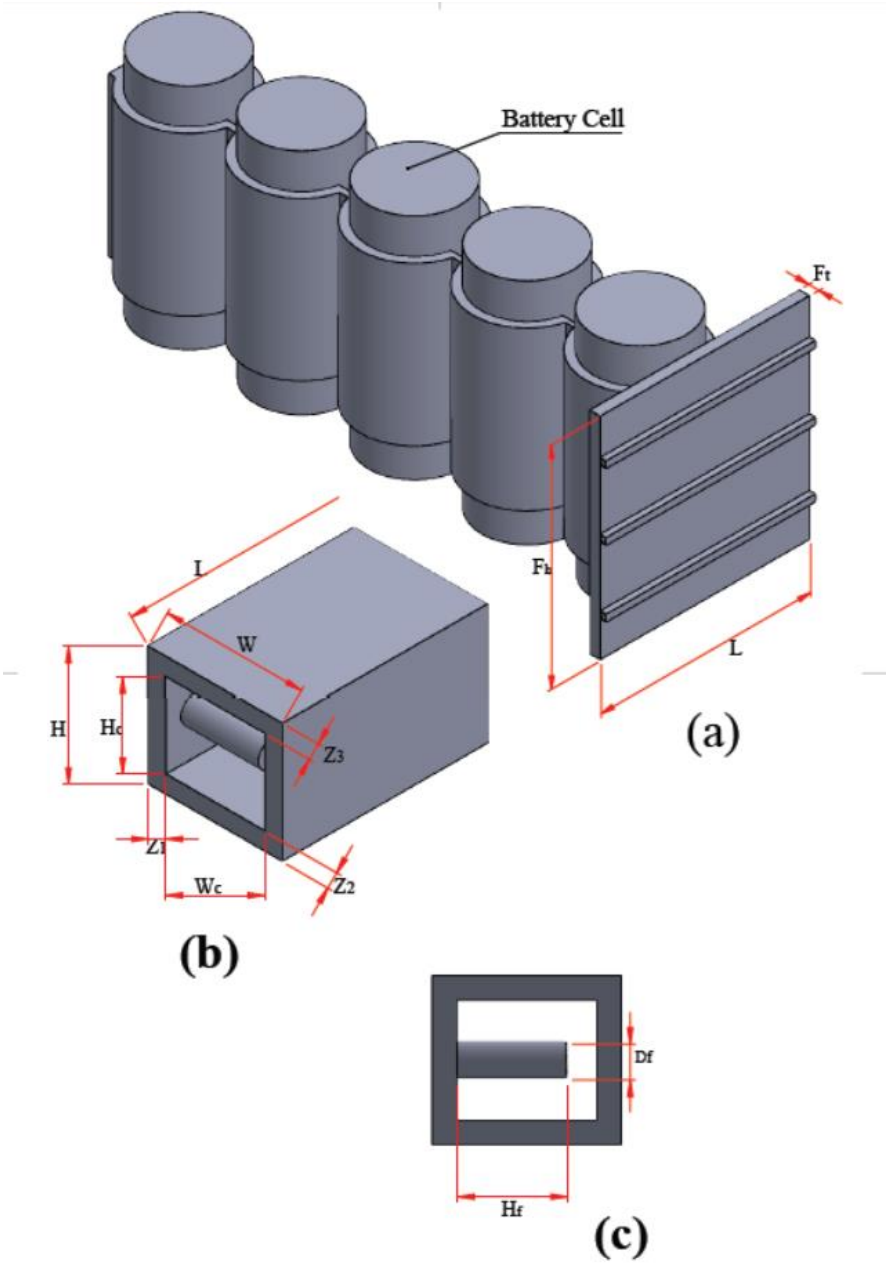

Figures 0.1. Cooling system with mounted three channels (a), 3D of the computational domain of the cooling system (b), cross-section of the channel with circular solid pin fin located at *L/8* towards the leading edge (c)

9.4 Case 1: Optimization of the cooling system of three channels without an insert (N_{3CF})

9.4.1 Effects of aspect ratio and hydraulic diameter on the thermal performance of cooling systems without an insert at a fixed Bejan number

9.4.1.1 Relationship between aspect ratio and optimized maximum rectangular frame wall temperature

For a fixed Benjan number (*Be*) of 7×10^8 (Reynolds number 128.38) and the channel volume of 2.23 mm^3 (equivalent to the volume of each N_{3CF} channel), the relationship between the aspect ratio $\left(\frac{H_c}{W_c}\right)$ and the maximum rectangular frame wall temperature (T_{max}) is illustrated in Figure 9.2. The results revealed the existence of an optimal channel aspect ratio $\left(\left(\frac{H_c}{W_c}\right)_{opt}\right)$ which minimized the T_{max}. As the aspect ratio increases, T_{max} decreases until $\left(\left(\frac{H_c}{W_c}\right)_{opt}\right)$ is reached; further increases result in significant T_{max} rises beyond this point. The system's thermal performance degrades more noticeably when $\frac{H_c}{W_c} > \left(\frac{H_c}{W_c}\right)_{opt}$ compared to when $\frac{H_c}{W_c} < \left(\frac{H_c}{W_c}\right)_{opt}$ indicating that oversizing the aspect ratio is particularly detrimental

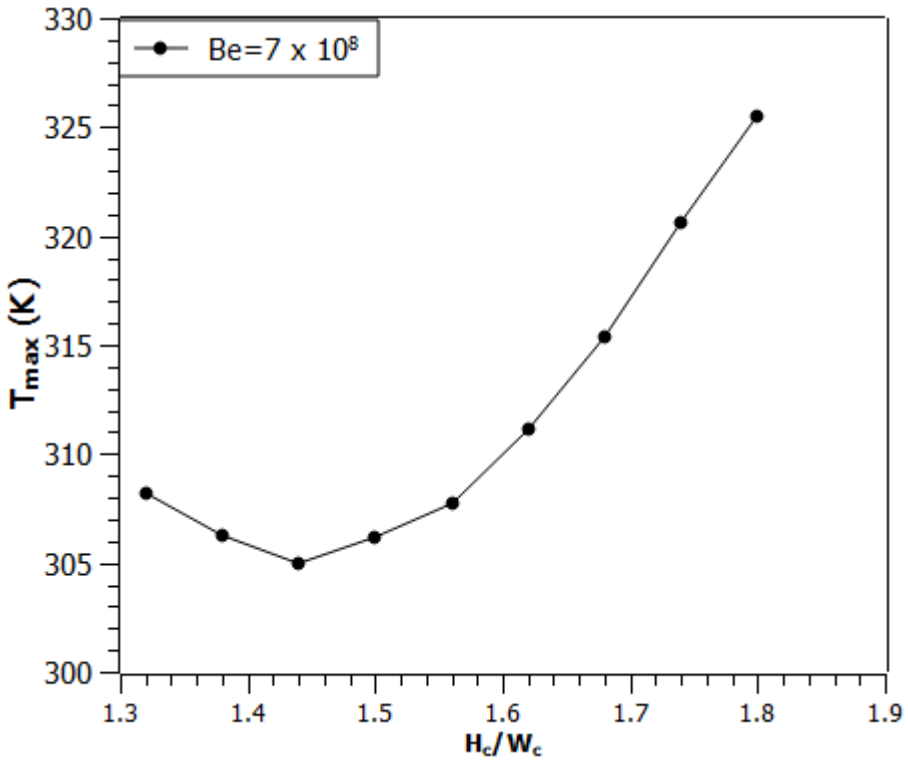

Figure 0.2. Maximum rectangular frame wall temperature (T_{max}) vs. aspect ratio ($\frac{H_c}{W_c}$) for the optimized N_{3CF} cooling system.

9.4.1.2. Relationship between aspect ratio and optimized dimensionless thermal resistance (R_{th})

In a like manner, Figure 9.3 displayed the relationship between the varying aspect ratio $\left(\frac{H_c}{W_c}\right)$ and the optimized dimensionless thermal resistance (R_{th}) of the cooling systems. It shows that $\frac{H_c}{W_c}$ has a significant influence on the minimized dimensionless R_{th}. The graph demonstrates the existence of the $\left(\frac{H_c}{W_c}\right)_{opt}$ that minimized dimensionless R_{th} which lies in the range of $1.32 \leq \frac{H_c}{W_c} \leq 1.8$. It was observed that the optimized dimensionless R_{th} decreased until it reached the $\left(\frac{H_c}{W_c}\right)_{opt}$ and beyond this point, a further increase in aspect ratio yields a drastic increase in the dimensionless R_{th}. Hence increasing or reducing the aspect ratio beyond the $\left(\frac{H_c}{W_c}\right)_{opt}$ is detrimental to the cooling system's performance. The simulation results show that the optimized cooling system $(N_{3CF})_{opt}$ (Figure 9.3) achieved an improved 14.64% in minimizing the dimensionless R_{th} compared to the unoptimized N_{3CF} (Figure 4.8).

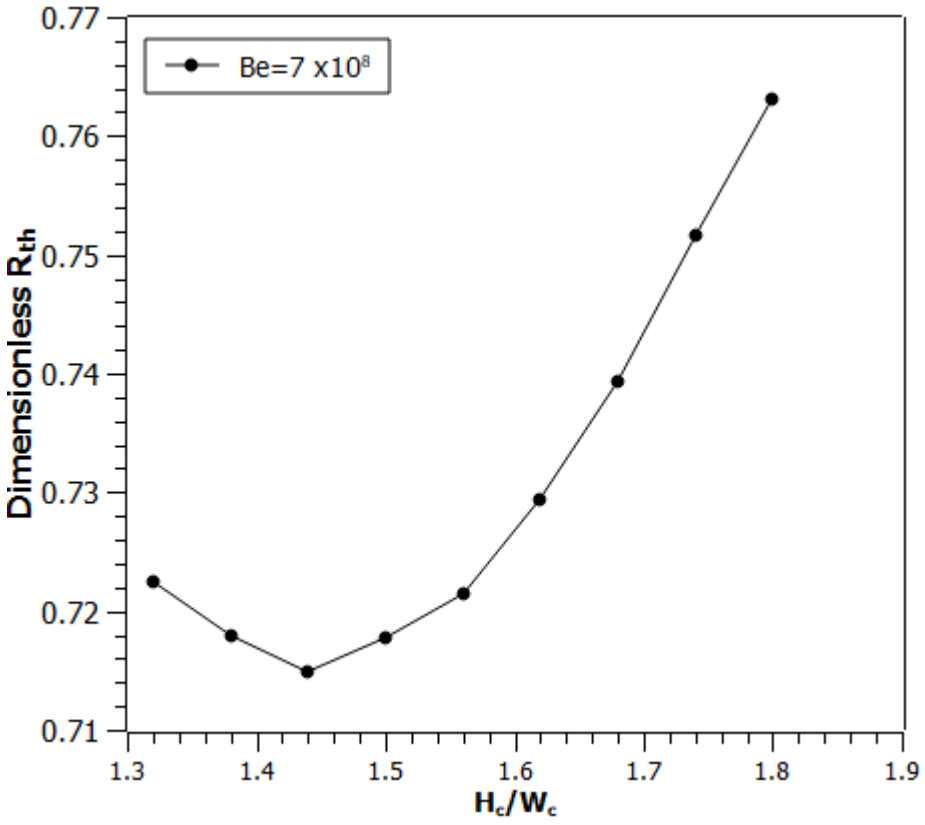

Figure 0.3. Dimensionless thermal resistance (R_{th}) vs Aspect ratio ($\frac{H_c}{W_c}$) for the optimized N_{3CF} cooling system.

9.4.1.3. Relationship between hydraulic diameter and optimized maximum rectangular frame wall temperature

Figure 9.4 shows the effect of the varying hydraulic diameter (D_h) on the optimized maximum wall temperature (T_{max}) of the rectangular frame at a fixed Benjan number (Be) of 7×10^8. The results show an optimal hydraulic diameter $(D_h)opt$ for the realization of the optimized value of T_{max}. From the graph, the minimum T_{max} was obtained with $(D_h)opt$ of 1.33. The figure further shows a significant increase in T_{max} values when $(D_h < (D_h)opt)$ which is damaging to the cooling systems' thermal performance compared to when $(D_h > (D_h)opt)$, as the T_{max} increases slightly. Thus, as the channel's characteristic dimensions become smaller, the working fluid is compressed by the channel's wall and becomes overworked, leading to an increase in T_{max} values [156]

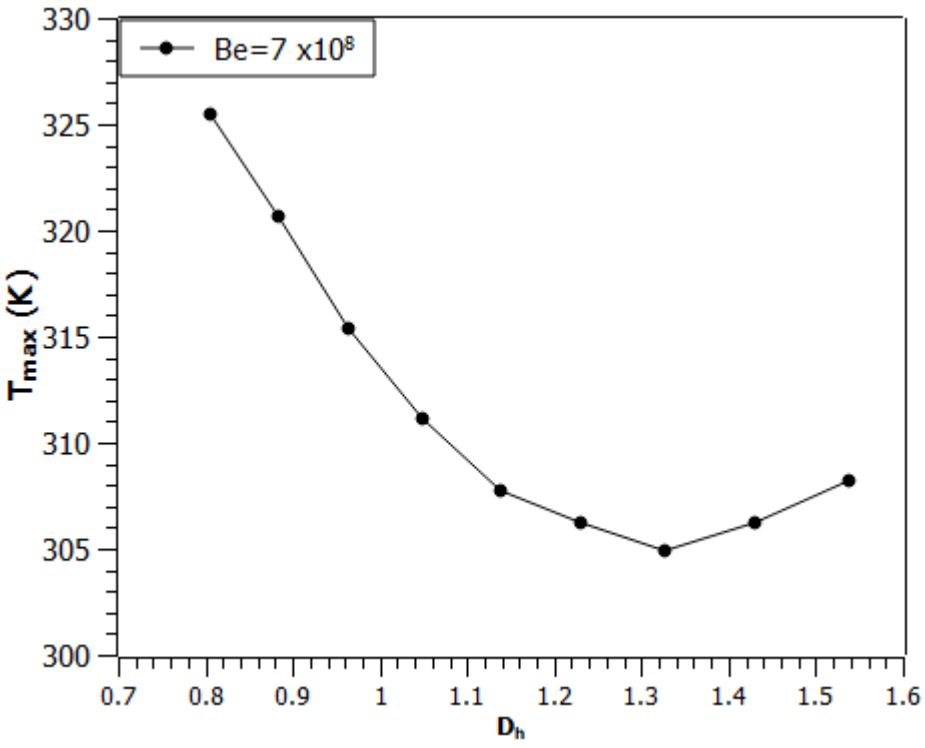

Figure 0.4. Maximum rectangular frame wall temperature (T_{max}) vs hydraulic diameter $(D_h)$for the optimized N_{3CF} cooling system.

9.4.2 Effect of varying Bejan numbers on cooling systems optimization

The optimization process was later repeated with an increased Bejan number as narrated below.

9.4.2.1 Relationship between optimized maximum rectangular frame wall temperature and increased Bejan number

Figure 9.5 shows the effect of varying Bejan numbers (*Be*) on the maximum wall temperature (T_{max}) of the rectangular frame of the cooling system with a fixed-mounted channel's volume of $2.23\,mm^3$ and a fixed length of $59.4\,mm$. An increased *Be* consistently decreased the optimized T_{max}. Thus, the cooling system performance improved with increasing flow velocity and thereafter increased dimensionless pressure drop (Be). The results are consistent with the published work of Adewumi et al. [41].

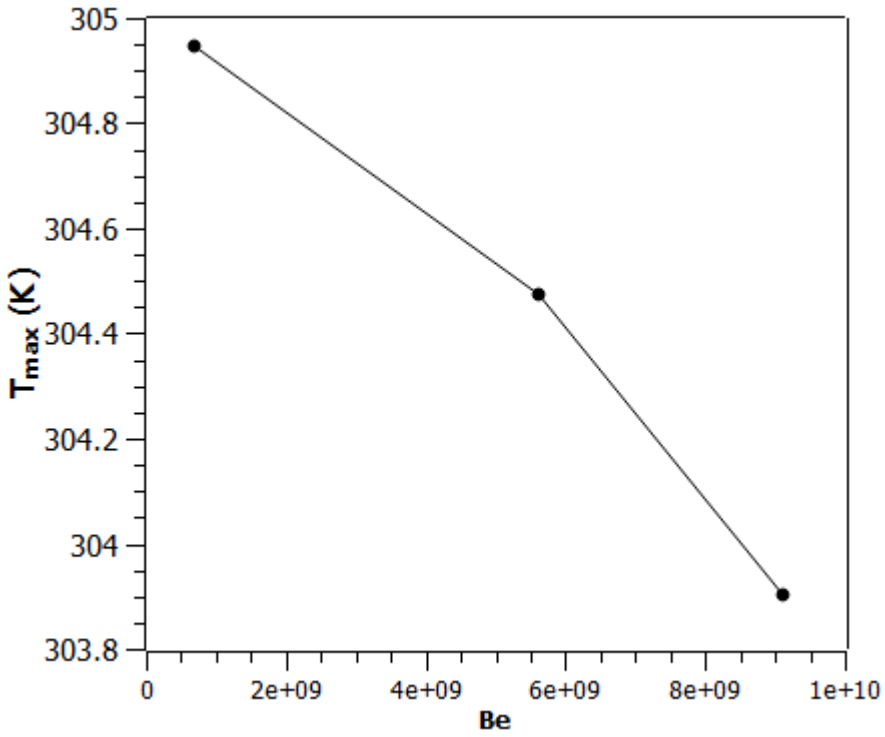

Figure 0.5. Maximum rectangular frame wall temperature (T_{max}) vs Bejan number (*Be*) for the optimized N_{3CF} cooling system.

9.4.2.2. Relationship between optimized dimensionless thermal resistance and increased Bejan number

In Figure 9.6, the optimized dimensionless thermal resistance (R_{th}) decreased with an increased Bejan number (*Be*) for a fixed-mounted channel volume of $2.23mm^3$ and a fixed length of $59.4mm$. This implies the influence of the increased dimensionless pressure drop on the improved system thermal performance. The optimized system provides improved heat

exchange enhancement with a reduced dimensionless R_{th} of 12.7% at $Be = 9 \times 10^9$ (Re =1540.56) compared to the unoptimized system (Figure 4.8).

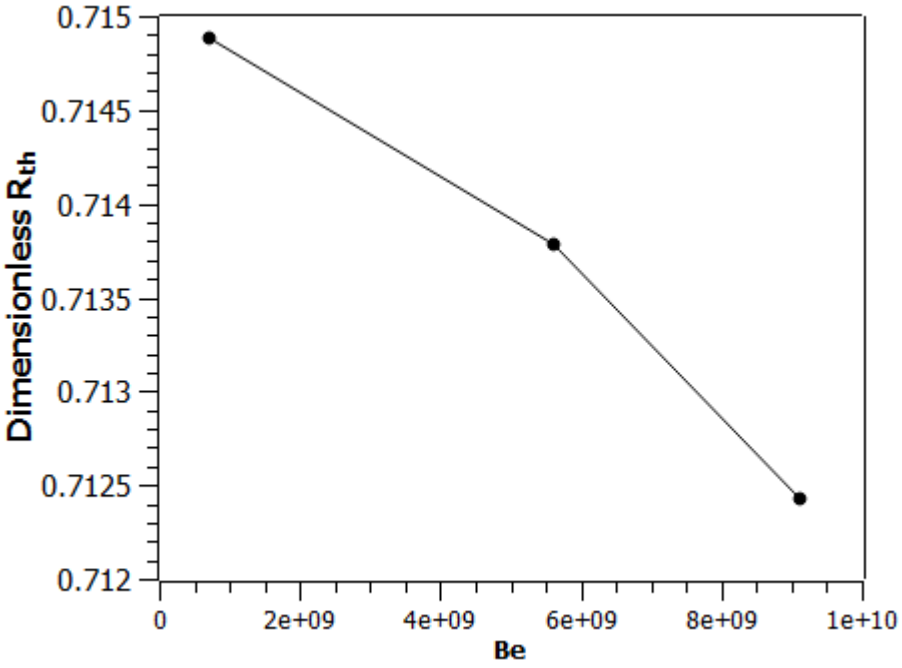

Figure 0.6. Dimensionless thermal resistance (R_{th}) vs Bejan number (Be) for the optimized N_{3CF} cooling system.

9.4.2.3 Relationship between optimized aspect ratio and increased Bejan number

Figure 9.7 reports the effects of the varying Bejan number (Be) on the optimal aspect ratio $\left(\left(\frac{H_c}{W_c}\right)_{opt}\right)$ of the cooling system with a fixed-mounted channel's volume of $2.23\ mm^3$ and a fixed length of $59.4\ mm$. For the range of applied Be in this work, a monotonic increase in the $\left(\frac{H_c}{W_c}\right)_{opt}$ was obtained with an increased Be. This result is consistent with the published work of Bello-Ochende [48].

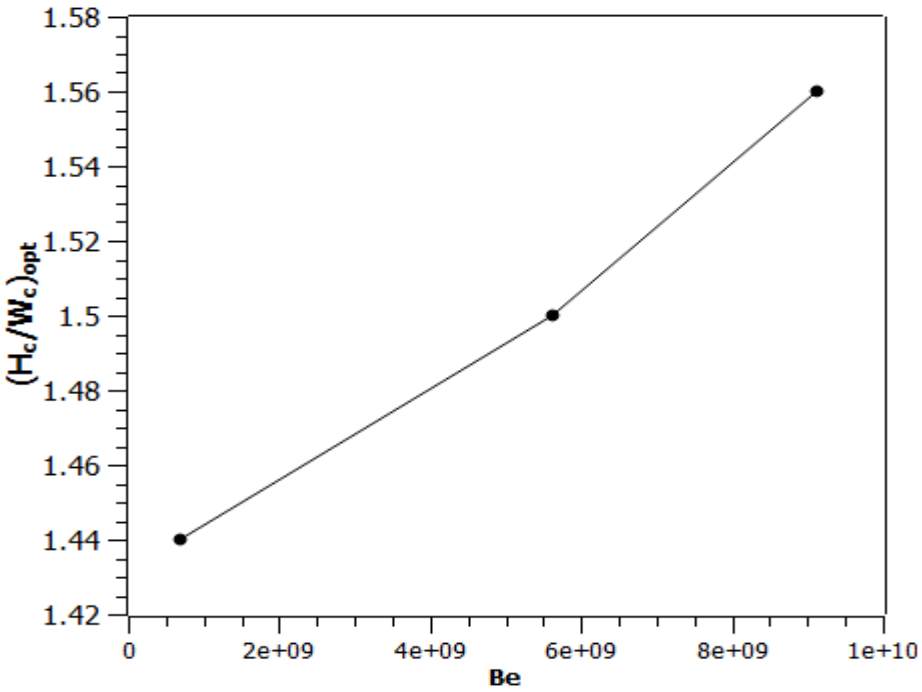

Figure 0.7. Optimized aspect ratio $\left(\left(\frac{H_c}{W_c}\right)_{opt}\right)$ Vs Bejan number (*Be*) for the optimized N_{3CF} cooling system.

9.4.3 Effect of different channels' fixed volume on the cooling system performance under varying Bejan numbers

The optimization process was further applied to different fixed channels' volumes of a fixed of length of 59.4 mm under varying Bejan numbers.

9.4.3.1 Optimized maximum rectangular frame wall temperature

Figure 9.8 shows the relationship between the optimized maximum wall temperature (T_{max}) for the rectangular frame. It is observed that the optimized T_{max} reduces with an increased *Be*. The figure further shows that the optimized T_{max} reduces as the volume increases. This result agreed with the published work of [49].

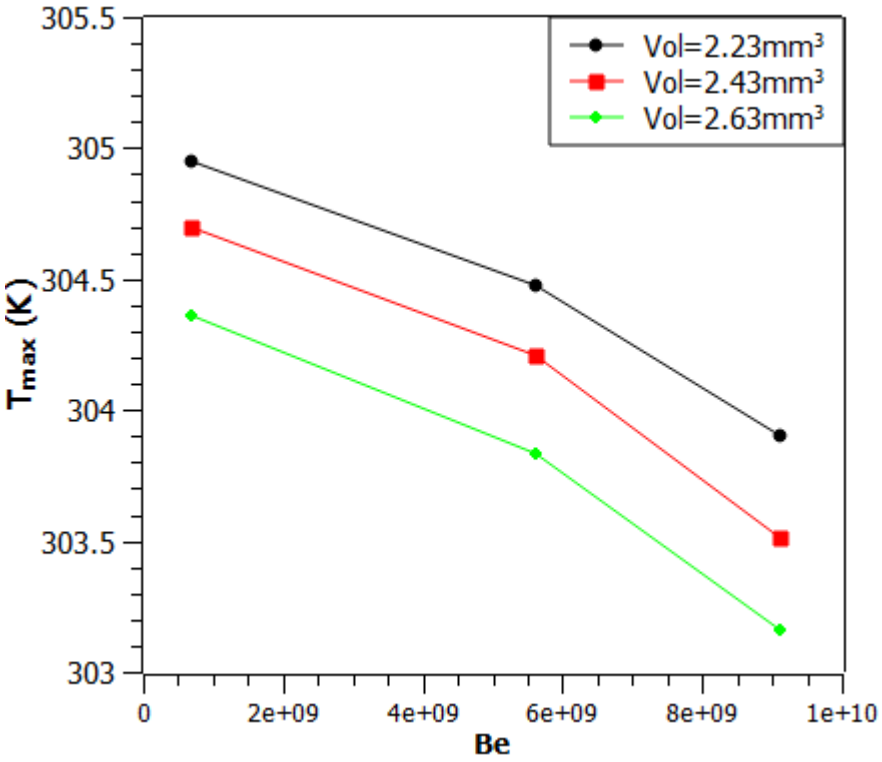

Figure 0.8. Maximum rectangular frame wall temperature (T_{max}) vs Bejan number (*Be*) for the N_{3CF} cooling system without an insert. Colored markers represent different volumes (Vol): Vol = 2.23 mm^3 (black), Vol = 2.43 mm^3 (red), and Vol = 2.63 mm^3 (green).

9.4.3.2. Optimized dimensionless thermal resistance

Figure 9 .9 reports the reduction of the optimized dimensionless thermal resistance (Rth) with an increased Bejan number (Be) regardless of the channel's fixed volume (V). For the range of applied Be, a common trend of optimized dimensionless Rth reduction was observed for different fixed channels' volumes. It is also observed that the optimized dimensionless Rth reduces as the volume increases.

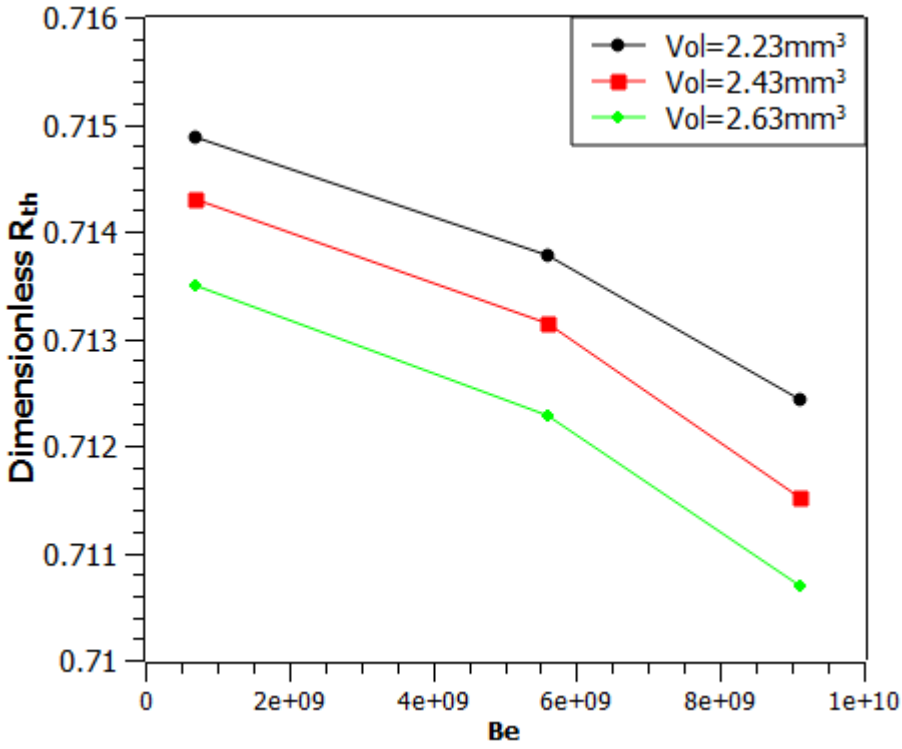

Figure 0.9. Dimensionless thermal resistance (R_{th}) vs Bejan number (Be) for the optimized N_{3CF} cooling system without an insert. Colored markers represent different Volumes (Vol): Vol = 2.23 mm^3 (black), Vol = 2.43 mm^3 (red), and Vol = 2.63 mm^3 (green).

9.4.3.3. Aspect ratio and hydraulic diameter

From Figure 9.10, the optimal aspect ratio and hydraulic diameter were observed to grow with the increased volume of the mounted channels indicating the direct relationship between the internal and external structure of the channels. A similar observation was reported in the literature [48].

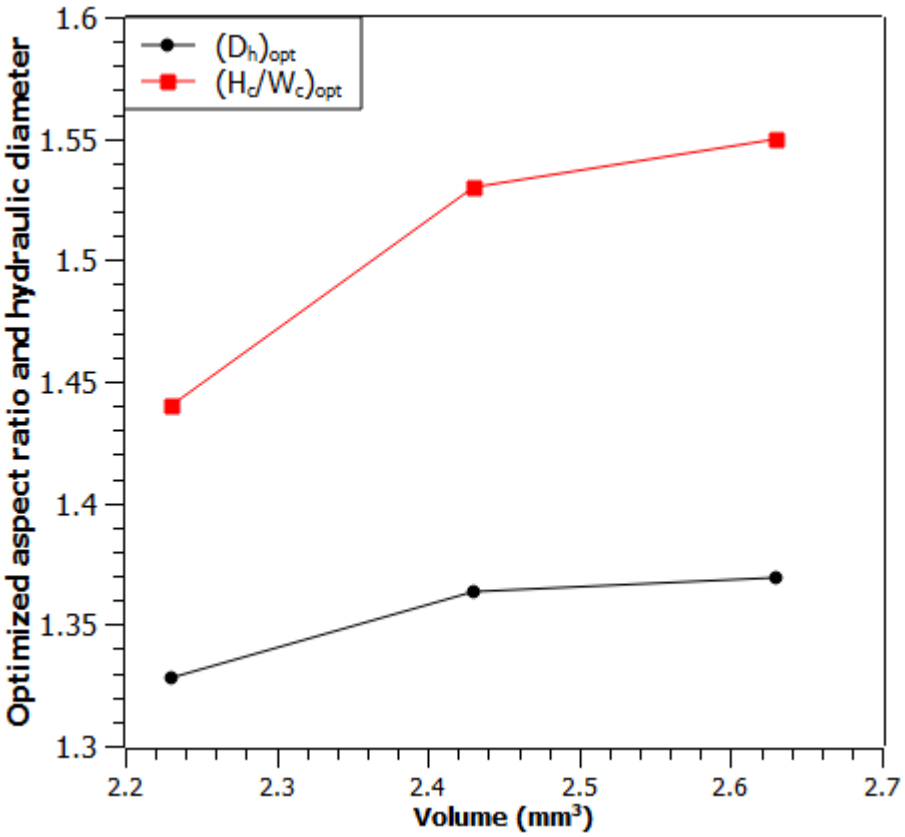

Figure 0.10. Optimized aspect ratio and hydraulic diameter vs Bejan number (*Be*) for the N_{3CF} cooling system without an insert. The black and red colored markers represent the optimized hydraulic diameter $(D_h)opt$ and aspect ratio $\left(\left(\frac{H_c}{W_c}\right)_{opt}\right)$.

9.5 Case 2: Optimization for the cooling system of three channels with circular solid pin fin (CSPF) insert located at *L/8* towards the inlet (NC_{MCF})

The optimized cooling system from case 1 $((N_{3CF})_{opt})$ is later inserted with a circular solid pin (CSPF) at *L/8* in the fluid domain towards the inlet to study the effect of the insert on enhancing the optimized system performance. Meanwhile, the optimization results for the cooling system with the fixed channel's global volume of 2.43 mm³ and 2.63 mm³ were not reported as both systems give 1.74 and 1.77 of CSPF aspect ratios, which do not meet manufacturer specifications as defined in Equation (9.6).

9.5.1 Effect of the CSPF insert on optimized system performance

9.5.1.1 Maximum rectangular frame wall temperature

Figure 9.11 shows the obtained results for the system with and without the CSPF for a fixed global volume of 2.23 mm^3 and fixed length of 59.4mm . An increased *Be* reduces the optimized T_{max}. For the ranges of applied *Be* in this work, it is observed that the insertion of CSPF in the optimized system channels further minimizes the values of T_{max}. For instance, the optimized system with CSPF achieved a 2.3% minimized T_{max} compared to the system without CSPF at the lowest *Be* 7×10^8 applied in this work. The CSPF optimal aspect ratio $\left({}^{H_P}/_{D_P}\right)opt$ for the system with a fixed channel's global volume of 2.23 mm^3 was 1.63.

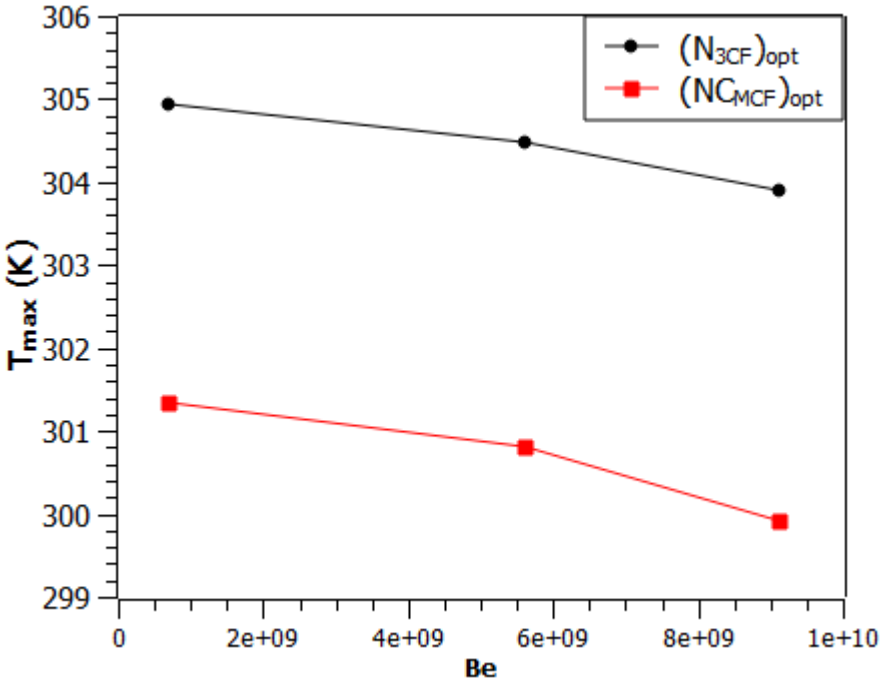

Figure 0.11. Maximum rectangular frame wall temperature (T_{max}) vs Bejan number (*Be*) for the optimized N_{3CF} and NC_{MCF} cooling systems. The graph compares the performance of systems with (red marker) and without (black marker) CSPF insert.

9.5.1.2 Dimensionless thermal resistance

Figure 9.12 summarises the effect of Bejan number (Be) on the dimensionless thermal resistance (R_{th}) for the optimized system with and without CSPF insert. Results indicate a significant reduction in the dimensionless R_{th} as *Be* increases. The insertion of CSPF

($(NC_{MCF})_{opt}$) provided substantial performance enhancement compared to the system without inserts ($(N_{3CF})_{opt}$). Precisely at *Be* 9×10^9, the optimized system with CSPF achieved a 12.3% reduction in minimized dimensionless R_{th}, demonstrating its superior ability to minimize thermal resistance and enhance heat dissipation.

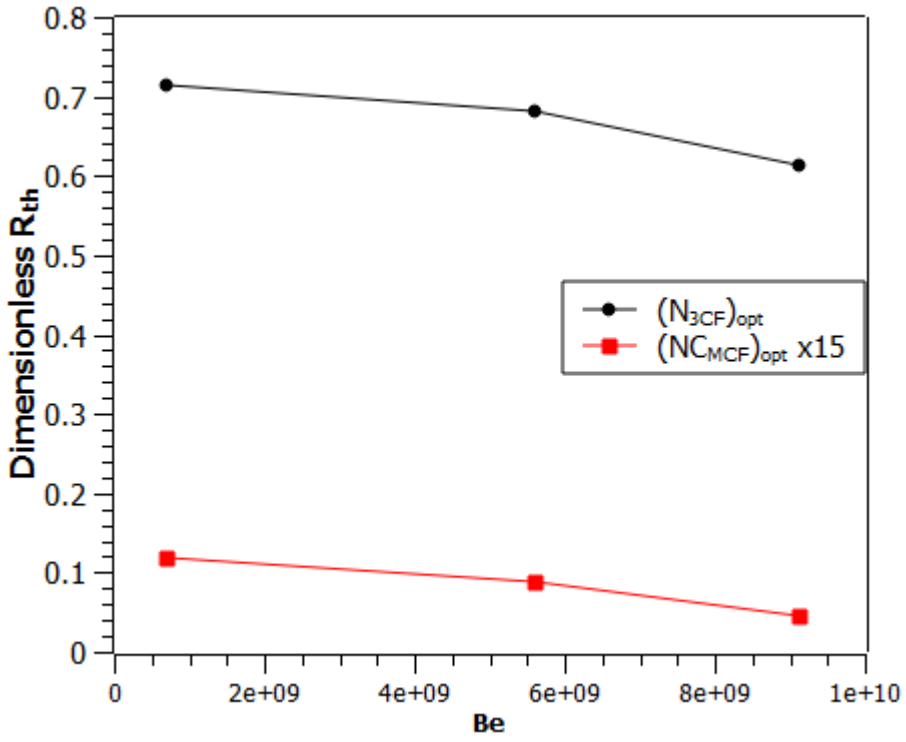

Figure 0.12. Dimensionless thermal resistance (R_{th}) vs Bejan number (*Be*) for the optimized N_{3CF} and NC_{MCF} cooling systems. The graph compares the performance of systems with (red marker) and without (black marker) CSPF insert.

9.5.2 Comparison of the optimized cooling systems with an unoptimized cooling system

In this section, the optimized ($(NC_{MCF})_{opt}$) and an unoptimized (NC_{MCF}) counterflow cooling system of three channels with a circular solid pin fin (CSPF) insert located at *L/8*, mounted on the rectangular frame, were compared. The systems (both optimized and unoptimized) are of fixed channels global volume 2.23 mm^3 and length 59.4 mm.

9.5.2.1 Maximum rectangular frame wall temperature

As seen in Figure 9.13, the minimized maximum wall temperature (T_{max}) of the rectangular frame decreases with increasing Bejan number (*Be*) for both the cooling systems, because increasing dimensionless pressure drops yields an improved cooling system thermal performance. This result agrees with previously published research in the open literature [41,

49]. For the range of *Be* applied in this study, the optimized system *(NC_{MCF})$_{opt}$* achieved the best cooling capacity in decreasing the optimized T_{max} than the unoptimized one *(NC_{MCF})* indicating the enhanced system performance provided by the optimization application.

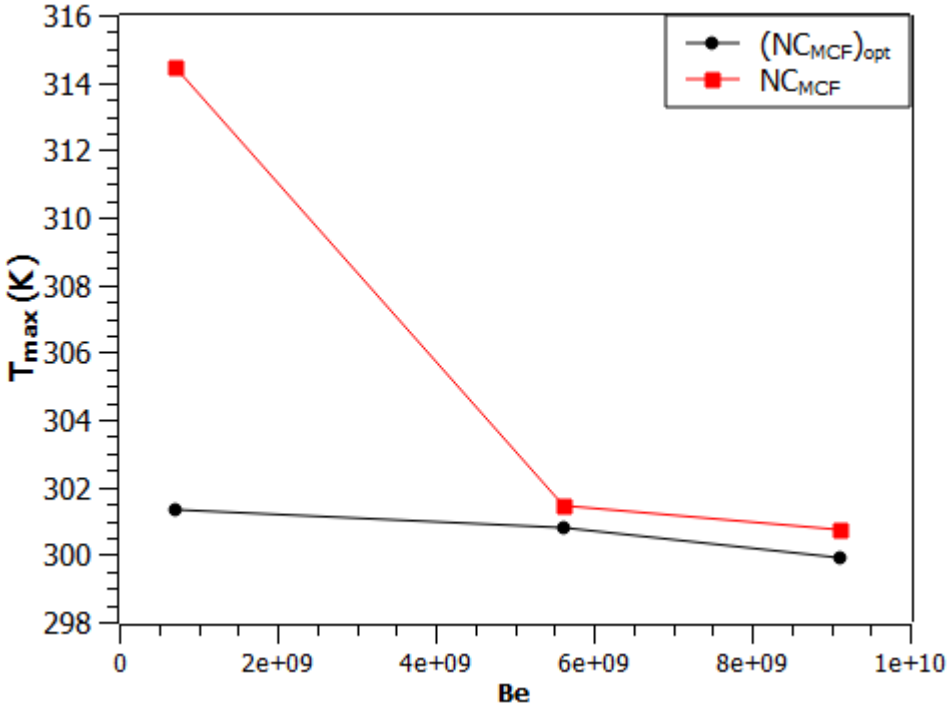

Figure 0.13. Maximum rectangular frame wall temperature (T_{max}) vs Bejan number (*Be*) for the optimized *(NC_{MCF})$_{opt}$* and unoptimized *(NC_{MCF})* cooling systems. The graph compares the performance of the optimized (black marker) with an unoptimized (red marker) system.

9.5.2.2 Dimensionless thermal resistance

Figure 9.14 depicts the relationship between the varying Bejan number (*Be*) and the dimensionless thermal resistance (R_{th}) for the optimized *(NC_{MCF})$_{opt}$* and an unoptimized *(NC_{MCF})* counterflow cooling system of three channels with a circular solid pin fin (CSPF) insert located at *L/8*, mounted on the rectangular frame. The result shows the inverse relationship between the *Be* and dimensionless R_{th} regardless of the cooling system. However, the *(NC_{MCF})$_{opt}$* significantly reduced the minimized dimensionless R_{th} compared to the $NC_{MCF.}$ For instance, *(NC_{MCF})$_{opt}$* improved the minimized dimensionless R_{th} reduction of 43.4% at *Be* 9×10^9 and over 390% at *Be* 7×10^8 compared to $NC_{MCF.}$ Thus, the optimized cooling system $(NC_{MCF})_{opt}$ demonstrates a better capacity for dissipating heat from the battery pack.

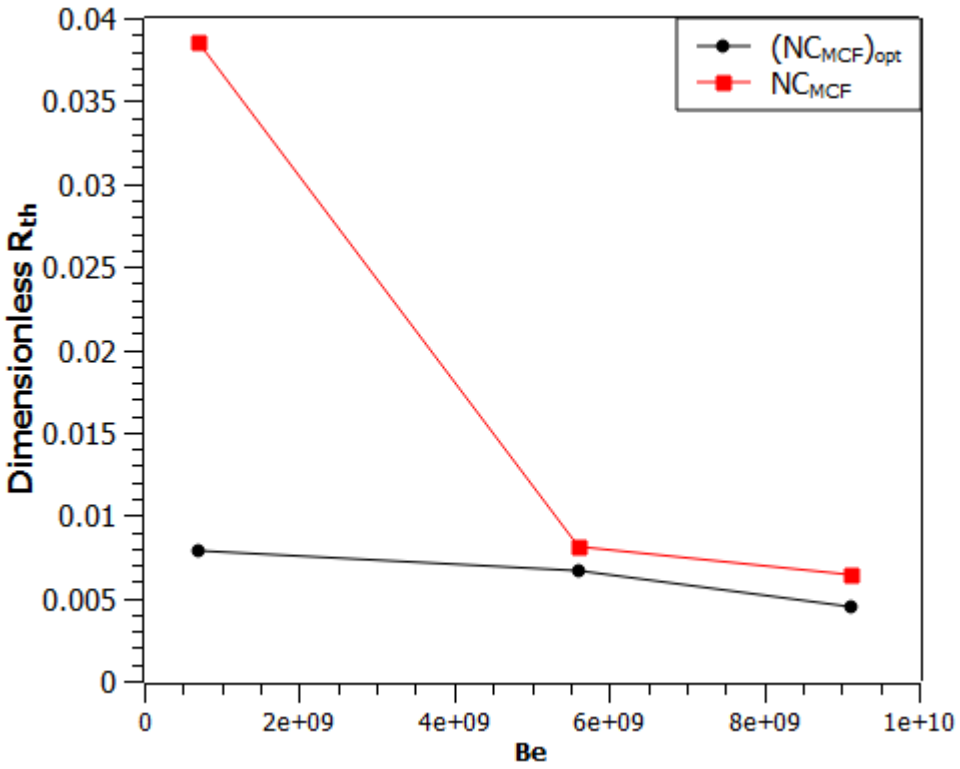

Figure 0.14. Dimensionless thermal resistance (R_{th}) vs Bejan number (Be) for the optimized $(NC_{MCF})_{opt}$ and unoptimized (NC_{MCF}) cooling systems. The graph compares the performance of the optimized (black marker) with an unoptimized (red marker) system.

9.6 Temperature contours

Figure 9.15 (a and b) displays the temperature contours of the unoptimized and optimized systems with an insert of circular solid pin fin (CSPF) located at *L/8* towards the inlet. The contours are plotted at X plane 25mm and inlet velocity 0.1m/s (Reynolds number 128.38). The optimized $(NC_{MCF})_{opt}$ system achieved a significantly lower temperature distribution than the unoptimized configuration (NC_{MCF}) showing that the optimized system can dissipate heat from the battery pack better than the unoptimized design.

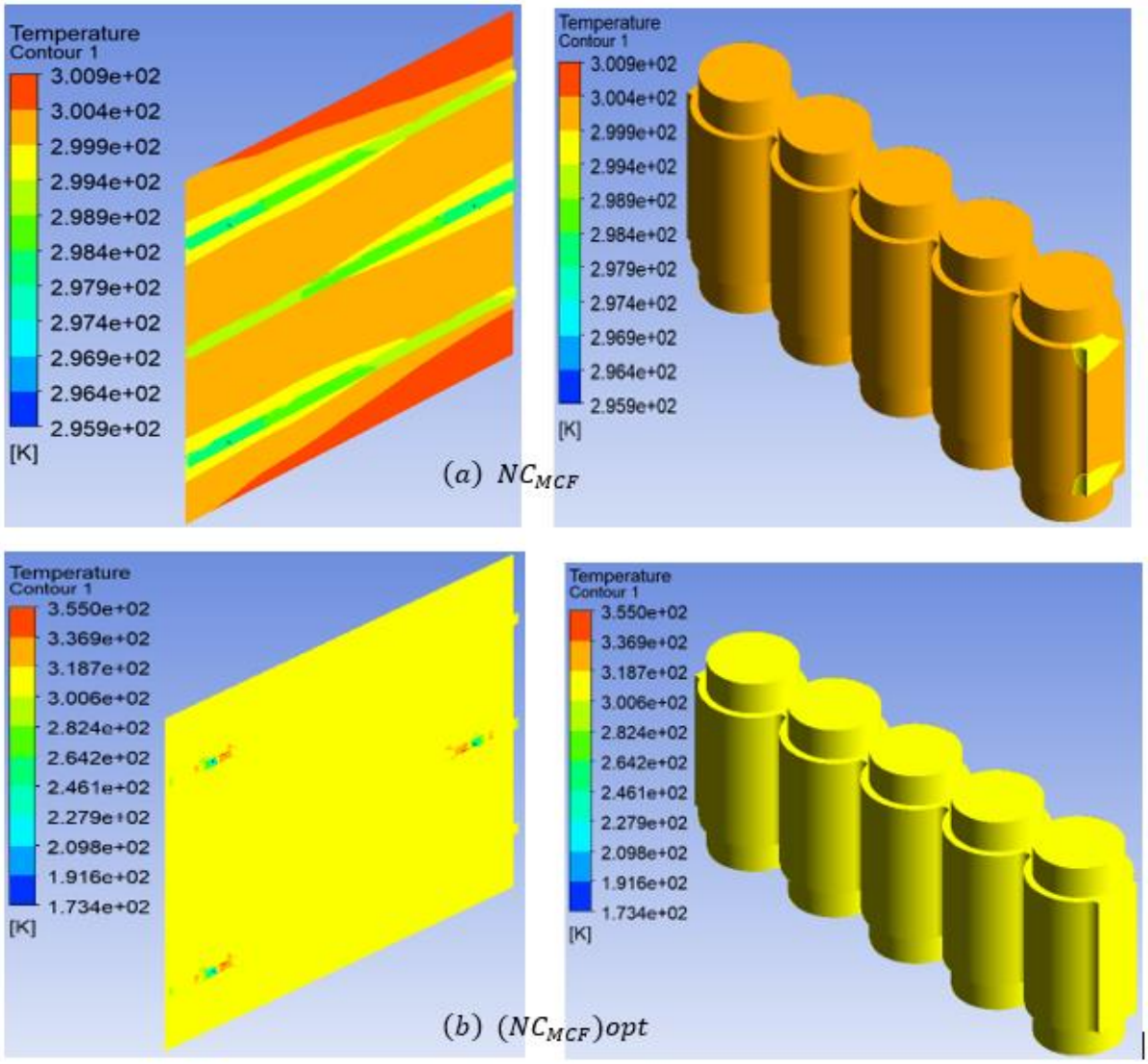

Figures 0.15. Temperature contours of the unoptimized (a) and optimized (b) cooling systems.

9.7 Conclusions

In this chapter, the numerical analysis was conducted to optimize the aspect ratio and hydraulic diameter of the cooling system for fixed channel length and global volumes with the circular solid pin fin (CSPF) insert. For the applied Bejan number, it was observed that a unique optimal cooling system internal structure exists that minimizes the maximum rectangular frame wall temperature and the dimensionless thermal resistance. It was found that the optimal aspect ratio and hydraulic diameter increased with increased Bejan number and channel's global volume. With or without a CSPF insert the system performance in minimizing the maximum rectangular frame wall temperature and dimensionless thermal resistance improves with an increased Bejan number. However, compared to the unoptimized, this study demonstrates a better battery pack cooling capacity with an optimized system particularly when inserted with CSPF at *L/8* in the

channels. For the lowest and the highest applied Bejan number $(NC_{MCF})_{opt}$ the optimized cooling system gave the best cooling results as it achieved an improvement of over 390% and 43.4% enhanced capacity for dissipating heat from the battery pack compared to NC_{MCF} (unoptimized cooling system).

CHAPTER TEN

CONCLUSIONS AND RECOMMENDATIONS

10.1 Preview

The thermal management of the electric vehicle battery pack is numerically developed and analyzed in this study using the computational fluid dynamic code of ANSYS® Fluent 20R1 as a tool. ANSYS® fluent 20R1 code validation was conducted with available data from experimental and numerical work of open literature and a good agreement of results was documented. The battery pack of 5 identical cylindrical lithium-ion batteries operating at a very high discharge rate of $6\,\mathrm{C}$ and generating a volumetric heat transfer of $3340135\ \mathrm{W/m^3}$ is coupled with a liquid cooling system. Newly developed cooling systems with an insert(s) in the channel(s) mounted on the rectangular frame, were modeled and their thermal performance was compared with those without an insert. Circular, elliptical, and rectangular shapes of solid pin fins as well as aluminum foam of low (0.1), medium (0.5), and high (0.9) porosities were considered as inserts for the enhancement of the cooling system in this study. The numerical procedures and assumptions made for analyzing the cooling system model were extensively documented in this dissertation. Optimization of the cooling system with superior thermal performance was later carried out. The specific conclusions are detailed in each chapter.

10.2 Conclusions

This study investigated the thermal performance of cooling systems for electric vehicle battery packs by imposing fixed volumetric heat transfer on a rectangular frame. Key performance metrics such as maximum rectangular frame wall temperature, dimensionless thermal resistance, cost of pumping power, convective heat transfer, dimensionless heat transfer rate density, and thermal performance enhancement factor were shown to depend on increasing Reynolds numbers. However, beyond a Reynolds number of 1027.04, changes in wall temperature and thermal resistance became negligible, and a similar trend was observed for systems with inserts (solid pin fins or aluminum foam) at Reynolds numbers above 1283.8. The cost of pumping power increased with the addition of channels on the rectangular frame, but counterflow arrangements consistently outperformed parallel flow arrangements in thermal performance. The highest dimensionless heat transfer rate density was recorded for systems with three channels. The study modeled cooling systems with inserts of solid pin fins and aluminum foam at low (0.1), medium (0.5), and high (0.9) porosities. Inserts significantly

improved system performance compared to systems without inserts. The placement of inserts also played a critical role: shorter distances between the insert and the inlet enhanced performance. However, low and medium-porosity aluminum foam inserts caused excessive pressure drops, making them impractical. A 2.0 mm spacing arrangement offered the best balance between friction factor and heat transfer enhancement for multiple-insert cooling systems, outperforming 1.5 mm and 2.5 mm spacing arrangements. Despite this, systems with a single insert located at *L/8* consistently outperformed those with three inserts, regardless of spacing or insert shape (circular, elliptical, or rectangular).

Aluminum foam inserts with 0.9 porosity at lower Reynolds numbers outperformed solid pin fins. However, as Reynolds numbers increased, solid pin fins demonstrated continuous performance improvements. In contrast, the performance of aluminum foam inserts declined at Reynolds numbers of 1797.32, 1412.18, and 1668.94 for circular, elliptical, and rectangular shapes, respectively. At the peak performance of the system with a circular, elliptical, and rectangular aluminum foam of 0.9 porosity insert, 46.1%, 36.2%, and 39.40% of improved enhancement factors were achieved respectively, by the cooling system with solid pin fin counterparts. Overall, a cooling system with a circular solid pin fin insert positioned at *L/8* demonstrated superior performance, exceeding elliptical and rectangular inserts by 10.6% and 4.2%, respectively. At the highest Reynolds number (2054.08), solid pin fins improved performance by 49.3%, 45.3%, and 44.4% compared to their aluminum foam counterparts. Overall, solid pin fins proved more effective for heat dissipation in electric vehicle battery packs.

The comparative analysis in Chapter 8 revealed that circular solid pin fins at *L/8* outperformed their rectangular and elliptical counterparts by 10.6% and 4.2% respectively. Chapter 9 demonstrated that optimizing the counterflow cooling system using constructal theory and design further enhanced performance. The optimized system, with a fixed channel length and global volume, improved of over 390% and 43.4% in thermal performance at the lowest and highest Bejan numbers, respectively, compared to its unoptimized counterpart.

This research highlights the importance of heat transfer enhancement techniques in improving the thermal performance of cooling systems for electric vehicle battery packs. Among the configurations studied, a circular solid pin fin located at *L/8* near the inlet provided the highest thermal performance. When optimized using constructal theory, this configuration

demonstrated exceptional potential for practical application in electric vehicle battery cooling systems.

10.3 Recommendations

In this study, the development and enhancement of the cooling system for the thermal management of the battery pack of an electric vehicle were numerically analyzed. The enhancement techniques were based on applying circular, elliptical, and rectangular shapes of solid pin fin and aluminum foam of varying porosity inserts. The following recommendations are suggested:

- The obtained numerical results in this study should be subjected to experimental investigation for effective comparison and extension to the thermal management of the electric vehicle battery pack operating in non-steady conditions.
- The numerical and experimental investigation of further points of insert location towards the inlet in the flow channels for maximum heat transfer enhancement should be carried out.
- Water was adopted as a working fluid in this study, future investigation should numerically consider the use of nanofluids or air as an alternative working fluid in comparison with water and extend to experimental investigation.
- The analysis of the other passive potential heat transfer enhancement techniques for the augmentation of battery cooling system performance should be explored.
- The cooling system with insert of circular solid pin fin located at L/8 towards the inlet, found in this study with superior performance is therefore recommended as the best for the dissipation of heat from the pack of electric vehicles.

REFERENCES.

[1] D. Wang *et al.*, "Life cycle analysis of internal combustion engine, electric and fuel cell vehicles for China," *Energy,* vol. 59, pp. 402-412, 2013.

[2] O. A. Towoju and F. A. Ishola, "A case for the internal combustion engine powered vehicle," *Energy Reports,* vol. 6, pp. 315-321, 2020.

[3] W. h. organisation, "Air pollution: The invisible health treat," 2022. [Online]. Available: https://www.who.int/news-room/feature-stories/detail/air-pollution--the-invisible-health-threat. Accessed;10/10/2023

[4] X. Tian, C. An, Z. Chen, and Z. Tian, "Assessing the impact of COVID-19 pandemic on urban transportation and air quality in Canada," *Science of the Total Environment,* vol. 765, pp. 144270-144270, 2021, doi: 10.1016/j.scitotenv.2020.144270.

[5] S. Gocmen and E. Cetkin, "Emergence of elevated battery positioning in air cooled battery packs for temperature uniformity in ultra-fast dis/charging applications," *Journal of Energy Storage,* vol. 45, no. November 2021, pp. 103516-103516, 2022, doi: 10.1016/j.est.2021.103516.

[6] B. Berman, "Better place pulled down Isreal and Denmark electric car markets, say local drivers," *Consulté le October,* vol. 7, p. 2021, 2013.

[7] L. H. Saw, Y. Ye, M. C. Yew, W. T. Chong, M. K. Yew, and T. C. Ng, "Computational fluid dynamics simulation on open cell aluminium foams for Li-ion battery cooling system," *Applied Energy,* vol. 204, pp. 1489-1499, 2017, doi: 10.1016/j.apenergy.2017.04.022.

[8] R. Liu, J. Chen, J. Xun, K. Jiao, and Q. Du, "Numerical investigation of thermal behaviors in lithium-ion battery stack discharge," *Applied Energy,* vol. 132, pp. 288-297, 2014, doi: 10.1016/j.apenergy.2014.07.024.

[9] H. Park, "A design of air flow configuration for cooling lithium ion battery in hybrid electric vehicles," *Journal of Power Sources,* vol. 239, pp. 30-36, 2013, doi: 10.1016/j.jpowsour.2013.03.102.

[10] F. F. Liu, F. C. Lan, J. Q. Chen, and Y. G. Li, "Experimental investigation on cooling/heating characteristics of ultra-thin micro heat pipe for electric vehicle battery thermal management," *Chinese Journal of Mechanical Engineering (English Edition),* vol. 31, no. 3, 2018, doi: 10.1186/s10033-018-0255-0.

[11] L. Bodenes, R. Dedryvère, H. Martinez, F. Fischer, C. Tessier, and J.-P. Pérès, "Lithium-ion batteries working at 85 C: Aging phenomena and electrode/electrolyte interfaces studied by XPS," *Journal of the Electrochemical Society,* vol. 159, no. 10, p. A1739, 2012.

[12] G. Gachot *et al.*, "Thermal behaviour of the lithiated-graphite/electrolyte interface through GC/MS analysis," *Electrochimica acta,* vol. 83, pp. 402-409, 2012.

[13] K. Benabdelaziz, B. Lebrouhi, A. Maftah, and M. Maaroufi, "Novel external cooling solution for electric vehicle battery pack," *Energy Reports,* vol. 6, no. September 2019, pp. 262-272, 2020, doi: 10.1016/j.egyr.2019.10.043.

[14] Y. Huo, Z. Rao, X. Liu, and J. Zhao, "Investigation of power battery thermal management by using mini-channel cold plate," *Energy Conversion and Management,* vol. 89, pp. 387-395, 2015, doi: 10.1016/j.enconman.2014.10.015.

[15] K. H. L. Y. Y. W. C. C. W. M.S. Wu, "No Title," *J. Power Sources,* vol. 109, pp. 160-166, 2002.

[16] Z. Rao, S. Wang, M. Wu, Z. Lin, and F. Li, "Experimental investigation on thermal management of electric vehicle battery with heat pipe," *Energy Conversion and Management,* vol. 65, pp. 92-97, 2013, doi: 10.1016/j.enconman.2012.08.014.

[17] R. Zhao, J. Gu, and J. Liu, "An experimental study of heat pipe thermal management system with wet cooling method for lithium ion batteries," *Journal of Power Sources,* vol. 273, pp. 1089-1097, 2015, doi: 10.1016/j.jpowsour.2014.10.007.

[18] A. Mills, M. Farid, J. R. Selman, and S. Al-Hallaj, "Thermal conductivity enhancement of phase change materials using a graphite matrix," *Applied Thermal Engineering,* vol. 26, no. 14-15, pp. 1652-1661, 2006, doi: 10.1016/j.applthermaleng.2005.11.022.

[19] P. Goli, S. Legedza, A. Dhar, R. Salgado, J. Renteria, and A. A. Balandin, "Graphene-enhanced hybrid phase change materials for thermal management of Li-ion batteries," *Journal of Power Sources,* vol. 248, pp. 37-43, 2014, doi: 10.1016/j.jpowsour.2013.08.135.

[20] R. Karami and B. Kamkari, "Investigation of the effect of inclination angle on the melting enhancement of phase change material in finned latent heat thermal storage units," *Applied Thermal Engineering,* vol. 146, no. March 2018, pp. 45-60, 2019, doi: 10.1016/j.applthermaleng.2018.09.105.

[21] K. Yu, X. Yang, Y. Cheng, and C. Li, "Thermal analysis and two-directional air flow thermal management for lithium-ion battery pack," *Journal of Power Sources,* vol. 270, pp. 193-200, 2014, doi: 10.1016/j.jpowsour.2014.07.086.

[22] R. D. Widyantara *et al.*, "Electric Vehicle," 2021.

[23] X. M. Xu and R. He, "Research on the heat dissipation performance of battery pack based on forced air cooling," *Journal of Power Sources,* vol. 240, pp. 33-41, 2013, doi: 10.1016/j.jpowsour.2013.03.004.

[24] J. Zhao, Z. Rao, and Y. Li, "Thermal performance of mini-channel liquid cooled cylinder based battery thermal management for cylindrical lithium-ion power battery," *Energy Conversion and Management,* vol. 103, pp. 157-165, 2015, doi: 10.1016/j.enconman.2015.06.056.

[25] C. Lan, J. Xu, Y. Qiao, and Y. Ma, "Thermal management for high power lithium-ion battery by minichannel aluminum tubes," *Applied Thermal Engineering,* vol. 101, pp. 284-292, 2016, doi: 10.1016/j.applthermaleng.2016.02.070.

[26] M. Shahjalal *et al.*, "A Numerical Thermal Analysis of a Battery Pack in an Electric Motorbike Application," *Designs,* vol. 6, no. 4, 2022, doi: 10.3390/designs6040060.

[27] S. Basu, K. S. Hariharan, S. M. Kolake, T. Song, D. K. Sohn, and T. Yeo, "Coupled electrochemical thermal modelling of a novel Li-ion battery pack thermal management system," *Applied Energy,* vol. 181, pp. 1-13, 2016, doi: 10.1016/j.apenergy.2016.08.049.

[28] J. G. Vián and D. Astrain, "Development of a heat exchanger for the cold side of a thermoelectric module," *Applied Thermal Engineering,* vol. 28, no. 11-12, pp. 1514-1521, 2008, doi: 10.1016/j.applthermaleng.2007.08.014.

[29] P. Bichkar, O. Dandgaval, P. Dalvi, R. Godase, and T. Dey, "Study of Shell and Tube Heat Exchanger with the Effect of Types of Baffles," *Procedia Manufacturing,* vol. 20, pp. 195-200, 2018, doi: 10.1016/j.promfg.2018.02.028.

[30] A. Bejan, S. Lorente, L. Martins, and J. P. Meyer, "The constructal size of a heat exchanger," *Journal of Applied Physics,* vol. 122, no. 6, 2017, doi: 10.1063/1.4991014.

[31] D. B. Tuckerman and R. F. W. Pease, "High-Performance Heat Sinking for VLSI," *IEEE Electron Device Letters,* vol. EDL-2, no. 5, pp. 126-129, 1981, doi: 10.1109/EDL.1981.25367.

[32] S. D. Thakre, V. B. Swami, and P. D. Malwe, "Cooling System of Electronic Devices using Microchannel Heat Sink," vol. 4, no. 2, pp. 58-60, 2014.

[33] X. Zhang and Y. Jaluria, "Optimization of microchannel-based cooling systems," *Numerical Heat Transfer; Part A: Applications,* vol. 74, no. 3, pp. 1053-1067, 2018, doi: 10.1080/10407782.2018.1513285.

[34] J. Xu, C. Lan, Y. Qiao, and Y. Ma, "Prevent thermal runaway of lithium-ion batteries with minichannel cooling," *Applied Thermal Engineering,* vol. 110, pp. 883-890, 2017, doi: 10.1016/j.applthermaleng.2016.08.151.

[35] Y. Chen, K. Chen, Y. Dong, and X. Wu, "Bidirectional symmetrical parallel mini-channel cold plate for energy efficient cooling of large battery packs," *Energy,* vol. 242, pp. 122553-122553, 2022, doi: 10.1016/j.energy.2021.122553.

[36] S. Panchal, R. Khasow, I. Dincer, M. Agelin-Chaab, R. Fraser, and M. Fowler, "Thermal design and simulation of mini-channel cold plate for water cooled large sized prismatic lithium-ion battery," *Applied Thermal Engineering,* vol. 122, pp. 80-90, 2017, doi: 10.1016/j.applthermaleng.2017.05.010.

[37] A. Manoj, U. V. Goddumarri, R. A, and S. Chakraborty, "Heat transfer and fluid flow characteristics of a microchannel heat sink with microplates - A critical computational study," *Applied Thermal Engineering,* vol. 226, no. November 2022, pp. 120309-120309, 2023, doi: 10.1016/j.applthermaleng.2023.120309.

[38] Z. Feng *et al.*, "Combined influence of rectangular wire coil and twisted tape on flow and heat transfer characteristics in square mini-channels," *International Journal of Heat and Mass Transfer,* vol. 205, 2023, doi: 10.1016/j.ijheatmasstransfer.2023.123866.

[39] A. R. Al-Obaidi and J. Alhamid, "Investigation of the effect of various corrugated pipe configurations on thermo-hydraulic flow and enhancement of heat transfer performance with the development of different correlations," *International Journal of Thermal Sciences,* vol. 176, no. February, pp. 107528-107528, 2022, doi: 10.1016/j.ijthermalsci.2022.107528.

[40] M. K. Mohit and R. Gupta, "Numerical investigation of the performance of rectangular micro-channel equipped with micro-pin-fin," *Case Studies in Thermal Engineering,* vol. 32, no. October 2021, pp. 101884-101884, 2022, doi: 10.1016/j.csite.2022.101884.

[41] O. O. Adewumi, T. Bello-Ochende, and J. P. Meyer, "Constructal design of combined microchannel and micro pin fins for electronic cooling," *International Journal of Heat and Mass Transfer,* vol. 66, pp. 315-323, 2013, doi: 10.1016/j.ijheatmasstransfer.2013.07.039.

[42] S. K. Mohammadian and Y. Zhang, "Cumulative effects of using pin fin heat sink and porous metal foam on thermal management of lithium-ion batteries," *Applied Thermal Engineering,* vol. 118, pp. 375-384, 2017, doi: 10.1016/j.applthermaleng.2017.02.121.

[43] V. Mali, R. Saxena, K. Kumar, A. Kalam, and B. Tripathi, "Review on battery thermal management systems for energy-efficient electric vehicles," *Renewable and Sustainable Energy Reviews,* vol. 151, no. February, pp. 111611-111611, 2021, doi: 10.1016/j.rser.2021.111611.

[44] S. O. Fatukasi and T. Bello-Ochende, "Numerical development of effective cooling system for battery pack of electric vehicles," *Materials Today: Proceedings,* no. xxxx, 2022, doi: 10.1016/j.matpr.2022.06.070.

[45] Z. Guo, Q. Xu, S. Zhao, S. Zhai, T. Zhao, and M. Ni, "A new battery thermal management system employing the mini-channel cold plate with pin fins," *Sustainable Energy Technologies and Assessments,* vol. 51, no. September 2021, pp. 101993-101993, 2022, doi: 10.1016/j.seta.2022.101993.

[46] S. K. Mohammadian, S. M. Rassoulinejad-Mousavi, and Y. Zhang, "Thermal management improvement of an air-cooled high-power lithium-ion battery by embedding metal foam," *Journal of Power Sources,* vol. 296, pp. 305-313, 2015, doi: 10.1016/j.jpowsour.2015.07.056.

[47] D. O. Ariyo and T. Bello-Ochende, "Constructal design of two-phase stacked microchannel heat exchangers for cooling at high heat flux," *International Communications in Heat and Mass Transfer,* vol. 125, pp. 19-24, 2021, doi: 10.1016/j.icheatmasstransfer.2021.105294.

[48] T. Bello-Ochende, L. Liebenberg, and J. P. Meyer, "Constructal cooling channels for micro-channel heat sinks," *International Journal of Heat and Mass Transfer,* vol. 50, no. 21-22, pp. 4141-4150, 2007, doi: 10.1016/j.ijheatmasstransfer.2007.02.019.

[49] T. Bello-Ochende, J. P. Meyer, and F. U. Ighalo, "Combined numerical optimization and constructal theory for the design of microchannel heat sinks," *Numerical Heat Transfer; Part A: Applications,* vol. 58, no. 11, pp. 882-899, 2010, doi: 10.1080/10407782.2010.529036.

[50] A. M. de Moura, E. D. dos Santos, and J. A. Souza, "Numerical study of three-dimensional microchannel using the Constructal Law," *International Communications in Heat and Mass Transfer,* vol. 146, no. June, pp. 106891-106891, 2023, doi: 10.1016/j.icheatmasstransfer.2023.106891.

[51] T. M. Gulotta, F. Guarino, M. Cellura, and G. Lorenzini, "A Constructal Law optimization of a boiler inspired by Life Cycle thinking," *Thermal Science and Engineering Progress,* vol. 6, no. December 2017, pp. 380-387, 2018, doi: 10.1016/j.tsep.2018.01.008.

[52] O. T. Olakoyejo, A. O. Adelaja, O. O. Adewumi, A. A. Oluwo, S. K. Bello, and S. A. Adio, "Constructal heat transfer and fluid flow enhancement optimization for cylindrical microcooling channels with variable cross-section," *Heat Transfer,* vol. 50, no. 7, pp. 6757-6775, 2021, doi: 10.1002/htj.22202.

[53] Y. S. Duh, J. H. Theng, C. C. Chen, and C. S. Kao, "Comparative study on thermal runaway of commercial 14500, 18650 and 26650 LiFePO4 batteries used in electric vehicles," *Journal of Energy Storage,* vol. 31, no. October 2019, pp. 101580-101580, 2020, doi: 10.1016/j.est.2020.101580.

[54] D. Lisbona and T. Snee, "A review of hazards associated with primary lithium and lithium-ion batteries," *Process safety and environmental protection,* vol. 89, no. 6, pp. 434-442, 2011.

[55] K. Monika, C. Chakraborty, S. Roy, R. Sujith, and S. P. Datta, "A numerical analysis on multi-stage Tesla valve based cold plate for cooling of pouch type Li-ion batteries," *International Journal of Heat and Mass Transfer,* vol. 177, pp. 121560-121560, 2021, doi: 10.1016/j.ijheatmasstransfer.2021.121560.

[56] S. Salimi, M. J. Mozoun, and R. Beigzadeh, "Heat transfer enhancement of serpentine channels with twisted tape insert by computational fluid dynamics and artificial intelligence," *The Canadian Journal of Chemical Engineering,* vol. 102, no. 3, pp. 1322-1340, 2024.

[57] A. I. Alsabery, S. M. Salih, M. A. Ismael, A. K. Hussein, I. Hashim, and J. M. Jalil, "Enhancement of cooling process of hot blocks mounted inside a horizontal channel using flexible baffles—Alternative arrangement," *International Journal of Thermofluids,* vol. 23, p. 100805, 2024.

[58] C. Difiglio, "Oil, economic growth and strategic petroleum stocks," *Energy strategy reviews,* vol. 5, pp. 48-58, 2014.

[59] N. Tamaldin, A. K. M. Yamin, M. F. B. Abdollah, H. Amiruddin, and M. A. Abdullah, "Design optimization of thermal management system for electric vehicleutilizing CFD analysis, DFMEA and CES," *Procedia Engineering,* vol. 68, pp. 305-312, 2013, doi: 10.1016/j.proeng.2013.12.184.

[60] S. Ma *et al.*, "Temperature effect and thermal impact in lithium-ion batteries: A review," *Progress in Natural Science: Materials International,* vol. 28, no. 6, pp. 653-666, 2018, doi: 10.1016/j.pnsc.2018.11.002.

[61] L. t. Science, "How does a lithium-ion battery work," ed, 2019.

[62] S. Basu *et al.*, "Non-isothermal electrochemical model for lithium-ion cells with composite cathodes," *Journal of Power Sources,* vol. 283, pp. 132-150, 2015, doi: 10.1016/j.jpowsour.2015.02.127.

[63] L. Spitthoff, P. Shearing, and O. S. Burheim, "Lithium-Ion Batteries," pp. 1-30, 2021.

[64] A. Lidbeck and K. R. Syed, "Experimental Characterization of Li-ion Battery cells for Thermal Management in Heavy Duty Hybrid Applications," *Chalmers University of Technology Gothenburg,* pp. 1-89, 2017. [Online]. Available: http://publications.lib.chalmers.se/records/fulltext/252994/252994.pdf.

[65] L. Tan, L. Zhang, Q. Sun, M. Shen, Q. Qu, and H. Zheng, "Capacity loss induced by lithium deposition at graphite anode for LiFePO4/graphite cell cycling at different temperatures," *Electrochimica Acta,* vol. 111, pp. 802-808, 2013, doi: 10.1016/j.electacta.2013.08.074.

[66] C. Heubner, M. Schneider, C. Lämmel, and A. Michaelis, "Local heat generation in a single stack lithium ion battery cell," *Electrochimica Acta,* vol. 186, pp. 404-412, 2015, doi: 10.1016/j.electacta.2015.10.182.

[67] P. Ramadass, B. Haran, R. White, and B. N. Popov, "Capacity fade of Sony 18650 cells cycled at elevated temperatures: Part II. Capacity fade analysis," *Journal of Power Sources,* vol. 112, no. 2, pp. 614-620, 2002, doi: 10.1016/S0378-7753(02)00473-1.

[68] Y. Troxler *et al.*, "The effect of thermal gradients on the performance of lithium-ion batteries," *Journal of Power Sources,* vol. 247, pp. 1018-1025, 2014, doi: 10.1016/j.jpowsour.2013.06.084.

[69] M. R. Khan, M. J. Swierczynski, and S. K. Kær, "Towards an ultimate battery thermal management system: A review," *Batteries,* vol. 3, no. 1, 2017, doi: 10.3390/batteries3010009.

[70] C. G. Motloch *et al.*, "High-power battery testing procedures and analytical methodologies for HEV's," *SAE Technical Papers,* vol. 111, 2002, doi: 10.4271/2002-01-1950.

[71] T. M. Bandhauer, S. Garimella, and T. F. Fuller, "A Critical Review of Thermal Issues in Lithium-Ion Batteries," *Journal of The Electrochemical Society,* vol. 158, no. 3, pp. R1-R1, 2011, doi: 10.1149/1.3515880.

[72] T. Waldmann, M. Wilka, M. Kasper, M. Fleischhammer, and M. Wohlfahrt-Mehrens, "Temperature dependent ageing mechanisms in Lithium-ion batteries - A Post-Mortem study," *Journal of Power Sources,* vol. 262, pp. 129-135, 2014, doi: 10.1016/j.jpowsour.2014.03.112.

[73] Q. Zhang *et al.*, "Research on the Reversible and Irreversible Heat Generation of LiNi1−x−yCoxMnyO2-Based Lithium-Ion Batteries," *Fire Technology,* 2022, doi: 10.1007/s10694-022-01220-7.

[74] C. Liang *et al.*, "Precise in-situ and ex-situ study on thermal behavior of LiNi1/3Co1/3Mn1/3O2/graphite coin cell: From part to the whole cell," *Journal of Energy Chemistry,* vol. 54, pp. 332-341, 2021, doi: 10.1016/j.jechem.2020.06.008.

[75] V. V. Viswanathan *et al.*, "Effect of entropy change of lithium intercalation in cathodes and anodes on Li-ion battery thermal management," *Journal of Power Sources,* vol. 195, no. 11, pp. 3720-3729, 2010, doi: 10.1016/j.jpowsour.2009.11.103.

[76] K. Bi, S.-x. Zhao, C. Huang, and C.-w. Nan, "Improving low-temperature performance of spinel LiNi 0 . 5 Mn 1 . 5 O 4 electrode," *Journal of Power Sources,* vol. 389, no. October 2017, pp. 240-248, 2018. [Online]. Available: https://doi.org/10.1016/j.jpowsour.2018.03.071.

[77] J.-s. Hong, H. Maleki, S. A. Hallaj, L. Redey, and J. R. Selman, "Electrochemical - Calorimetric Studies of Lithium - Ion Cells Electrochemical-Calorimetric Studies of Lithium-Ion Cells," 1998.

[78] C. Heubner, M. Schneider, and A. Michaelis, "Reversible heat generation rates of blended insertion electrodes," *Journal of Solid State Electrochemistry,* vol. 21, no. 7, pp. 2109-2115, 2017, doi: 10.1007/s10008-017-3594-3.

[79] A. F. Gunnarshaug, P. J. S. Vie, and S. Kjelstrup, "Review—Reversible Heat Effects in Cells Relevant for Lithium-Ion Batteries," *Journal of The Electrochemical Society,* vol. 168, no. 5, pp. 050522-050522, 2021, doi: 10.1149/1945-7111/abfd73.

[80] T. M. Bandhauer, S. Garimella, and T. F. Fuller, "Temperature-dependent electrochemical heat generation in a commercial lithium-ion battery," *Journal of Power Sources,* vol. 247, pp. 618-628, 2014, doi: 10.1016/j.jpowsour.2013.08.015.

[81] Y. Maeda, "Thermal Behavior on Graphite Due to Electrochemical Intercalation," *Journal of The Electrochemical Society,* vol. 137, no. 10, pp. 3047-3052, 1990, doi: 10.1149/1.2086157.

[82] S. Al Hallaj, R. Venkatachalapathy, J. Prakash, and J. R. Selman, "Entropy Changes Due to Structural Transformation in the Graphite Anode and Phase Change of the LiCoO[sub 2]

Cathode," *Journal of The Electrochemical Society,* vol. 147, no. 7, pp. 2432-2432, 2000, doi: 10.1149/1.1393549.

[83] Y. Lai *et al.*, "Insight into heat generation of lithium ion batteries based on the electrochemical-thermal model at high discharge rates," *International Journal of Hydrogen Energy,* vol. 40, no. 38, pp. 13039-13049, 2015, doi: 10.1016/j.ijhydene.2015.07.079.

[84] C. Xiang, C. W. Wu, W. X. Zhou, G. Xie, and G. Zhang, "Thermal transport in lithium-ion battery: A micro perspective for thermal management," *Frontiers of Physics,* vol. 17, no. 1, 2022, doi: 10.1007/s11467-021-1090-9.

[85] S. J. Drake, D. A. Wetz, J. K. Ostanek, S. P. Miller, J. M. Heinzel, and A. Jain, "Measurement of anisotropic thermophysical properties of cylindrical Li-ion cells," *Journal of Power Sources,* vol. 252, pp. 298-304, 2014, doi: 10.1016/j.jpowsour.2013.11.107.

[86] M. Park, X. Zhang, M. Chung, G. B. Less, and A. Marie, "A review of conduction phenomena in Li-ion batteries," *Journal of Power Sources,* vol. 195, no. 24, pp. 7904-7929, 2010, doi: 10.1016/j.jpowsour.2010.06.060.

[87] D. Oehler, J. Bender, P. Seegert, and T. Wetzel, "Investigation of the Effective Thermal Conductivity of Cell Stacks of Li-Ion Batteries," 2020, doi: 10.1002/ente.202000722.

[88] Y. Yang, X. Huang, Z. Cao, and G. Chen, "Thermally conductive separator with hierarchical nano / microstructures for improving thermal management of batteries," *Nano Energy,* vol. 22, pp. 301-309, 2016, doi: 10.1016/j.nanoen.2016.01.026.

[89] J. Huang, P. Xu, and P. Wang, "Experimental measurement of anisotropic thermal conductivity of 18650 lithium battery," *Journal of Physics: Conference Series,* vol. 1509, no. 1, 2020, doi: 10.1088/1742-6596/1509/1/012013.

[90] A. A. Pesaran and M. Keyser, "Thermal Characteristics of Selected EV and HEV Batteries."

[91] H. Maleki, A. Hallaj, J. R. Selman, R. B. Dinwiddie, and H. Wang, "Thermal Properties of Lithium - Ion Battery and Components Thermal Properties of Lithium-Ion Battery and Components," 1999.

[92] B. Harsh, "Radial Thermal Conductivity Measurements of Lithium-Ion Battery Cells," *Caltech Undergraduate Research Journal,* 2020.

[93] P. Method, "Radial Thermal Conductivity Measurements of Cylindrical Lithium-Ion Batteries — An Uncertainty Study of the Pipe Method," 2022.

[94] B. d. f. c. t. Pack, "Benefits of Aluminium cell housings for cylindrical lithium-ion batteries," ed, 2023.

[95] T. H. Tran, S. Harmand, and B. Sahut, "Experimental investigation on heat pipe cooling for Hybrid Electric Vehicle and Electric Vehicle lithium-ion battery," *Journal of Power Sources,* vol. 265, pp. 262-272, 2014, doi: 10.1016/j.jpowsour.2014.04.130.

[96] H. N. Chaudhry, B. R. Hughes, and S. A. Ghani, "A review of heat pipe systems for heat recovery and renewable energy applications," *Renewable and Sustainable Energy Reviews,* vol. 16, no. 4, pp. 2249-2259, 2012, doi: 10.1016/j.rser.2012.01.038.

[97] R. G. Chi and S. H. Rhi, "Oscillating heat pipe cooling system of electric vehicle's Li-ion batteries with direct contact bottom cooling mode," *Energies,* vol. 12, no. 9, pp. 1-14, 2019, doi: 10.3390/en12091698.

[98] A. Faghri, *Heat Pipe Science and Technology, Taylor & Francis*. 1995.

[99] V. Maziuk, A. Kulakov, M. Rabetsky, L. Vasiliev, and M. Vukovic, "Miniature heat-pipe thermal performance prediction tool - software development," *Applied Thermal Engineering,* vol. 21, no. 5, pp. 559-571, 2001, doi: 10.1016/S1359-4311(00)00066-1.

[100] R. Zhao, J. Gu, and J. Liu, "Optimization of a phase change material based internal cooling system for cylindrical Li-ion battery pack and a hybrid cooling design," *Energy,* vol. 135, pp. 811-822, 2017, doi: 10.1016/j.energy.2017.06.168.

[101] Y. Huo and Z. Rao, "Investigation of phase change material based battery thermal management at cold temperature using lattice Boltzmann method," *Energy Conversion and Management,* vol. 133, pp. 204-215, 2017, doi: 10.1016/j.enconman.2016.12.009.

[102] V. G. Choudhari, A. S. Dhoble, and S. Panchal, "Numerical analysis of different fin structures in phase change material module for battery thermal management system and its optimization," *International Journal of Heat and Mass Transfer,* vol. 163, pp. 120434-120434, 2020, doi: 10.1016/j.ijheatmasstransfer.2020.120434.

[103] C. V. Hémery, F. Pra, J. F. Robin, and P. Marty, "Experimental performances of a battery thermal management system using a phase change material," *Journal of Power Sources,* vol. 270, pp. 349-358, 2014, doi: 10.1016/j.jpowsour.2014.07.147.

[104] F. Bai, M. Chen, W. Song, Z. Feng, Y. Li, and Y. Ding, "Thermal management performances of PCM/water cooling-plate using for lithium-ion battery module based on non-uniform internal heat source," *Applied Thermal Engineering,* vol. 126, pp. 17-27, 2017, doi: 10.1016/j.applthermaleng.2017.07.141.

[105] Y. Lv, G. Liu, G. Zhang, and X. Yang, "A novel thermal management structure using serpentine phase change material coupled with forced air convection for cylindrical battery modules," *Journal of Power Sources,* vol. 468, no. May, pp. 228398-228398, 2020, doi: 10.1016/j.jpowsour.2020.228398.

[106] H. Sun and R. Dixon, "Development of cooling strategy for an air cooled lithium-ion battery pack," *Journal of Power Sources,* vol. 272, pp. 404-414, 2014, doi: 10.1016/j.jpowsour.2014.08.107.

[107] N. Yang, X. Zhang, G. Li, and D. Hua, "Assessment of the forced air-cooling performance for cylindrical lithium-ion battery packs: A comparative analysis between aligned and staggered cell arrangements," *Applied Thermal Engineering,* vol. 80, pp. 55-65, 2015, doi: 10.1016/j.applthermaleng.2015.01.049.

[108] T. Wang, K. J. Tseng, J. Zhao, and Z. Wei, "Thermal investigation of lithium-ion battery module with different cell arrangement structures and forced air-cooling strategies," *Applied Energy,* vol. 134, pp. 229-238, 2014, doi: 10.1016/j.apenergy.2014.08.013.

[109] J. Zhang, X. Wu, K. Chen, D. Zhou, and M. Song, "Experimental and numerical studies on an efficient transient heat transfer model for air-cooled battery thermal management systems," *Journal of Power Sources,* vol. 490, no. January, 2021, doi: 10.1016/j.jpowsour.2021.229539.

[110] S. K. Mohammadian and Y. Zhang, "Thermal management optimization of an air-cooled Li-ion battery module using pin-fin heat sinks for hybrid electric vehicles," *Journal of Power Sources,* vol. 273, pp. 431-439, 2015, doi: 10.1016/j.jpowsour.2014.09.110.

[111] L. Sheng *et al.*, "Numerical investigation on a lithium ion battery thermal management utilizing a serpentine-channel liquid cooling plate exchanger," *International Journal of Heat and Mass Transfer,* vol. 141, pp. 658-668, 2019, doi: 10.1016/j.ijheatmasstransfer.2019.07.033.

[112] J. Neubauer, "Battery Lifetime Analysis and Simulation Tool (BLAST) Documentation Battery Lifetime Analysis and Simulation Tool (BLAST) Documentation," no. December, 2014.

[113] S. K. Mohammadian, Y.-l. He, and Y. Zhang, "Internal cooling of a lithium-ion battery using electrolyte as coolant through microchannels embedded inside the electrodes," *Journal of Power Sources,* vol. 293, pp. 458-466, 2015, doi: 10.1016/j.jpowsour.2015.05.055.

[114] D. Chen, J. Jiang, G. H. Kim, C. Yang, and A. Pesaran, "Comparison of different cooling methods for lithium ion battery cells," *Applied Thermal Engineering,* vol. 94, pp. 846-854, 2016, doi: 10.1016/j.applthermaleng.2015.10.015.

[115] K. Shah *et al.*, "Modeling of steady-state convective cooling of cylindrical Li-ion cells," *Journal of Power Sources,* vol. 258, pp. 374-381, 2014, doi: 10.1016/j.jpowsour.2014.01.115.

[116] S. Wiriyasart, C. Hommalee, S. Sirikasemsuk, R. Prurapark, and P. Naphon, "Thermal management system with nanofluids for electric vehicle battery cooling modules," *Case Studies in Thermal Engineering,* vol. 18, no. January, pp. 1-11, 2020, doi: 10.1016/j.csite.2020.100583.

[117] X. H. Yang, S. C. Tan, and J. Liu, "Thermal management of Li-ion battery with liquid metal," *Energy Conversion and Management,* vol. 117, pp. 577-585, 2016/6// 2016, doi: 10.1016/j.enconman.2016.03.054.

[118] K. Darcovich, D. D. MacNeil, S. Recoskie, Q. Cadic, and F. Ilinca, "Comparison of cooling plate configurations for automotive battery pack thermal management," *Applied Thermal Engineering,* vol. 155, no. March, pp. 185-195, 2019, doi: 10.1016/j.applthermaleng.2019.03.146.

[119] S. Panchal, S. Mathewson, R. Fraser, R. Culham, and M. Fowler, "Thermal Management of Lithium-Ion Pouch Cell with Indirect Liquid Cooling using Dual Cold Plates Approach," *SAE International Journal of Alternative Powertrains,* vol. 4, no. 2, pp. 293-307, 2015, doi: 10.4271/2015-01-1184.

[120] D. Li, "Single phase electrokinetic flow in microchannels," in *Heat Transfer and Fluid Flow in Minichannels and Microchannels*: Elsevier, 2006, pp. 137-174.

[121] C. B. Sobhan and S. V. Garimella, "A comparative analysis of studies on heat transfer and fluid flow in microchannels," *Microscale Thermophysical Engineering,* vol. 5, no. 4, pp. 293-311, 2001, doi: 10.1080/10893950152646759.

[122] X. F. Peng and G. P. Peterson, "Convective heat transfer and flow friction for water flow in microchannel structures," *International Journal of Heat and Mass Transfer,* vol. 39, no. 12, pp. 2599-2608, 1996, doi: 10.1016/0017-9310(95)00327-4.

[123] J. Koo and C. Kleinstreuer, "Viscous dissipation effects in microtubes and microchannels," *International Journal of Heat and Mass Transfer,* vol. 47, no. 14-16, pp. 3159-3169, 2004, doi: 10.1016/j.ijheatmasstransfer.2004.02.017.

[124] R. Chein and Y. Chen, "Performances of thermoelectric cooler integrated with microchannel heat sinks," *International Journal of Refrigeration,* 2005, doi: 10.1016/j.ijrefrig.2005.02.001.

[125] H. H. Bau, "Optimization of conduits ' shape in micro heat exchangers," vol. 41, pp. 2717-2723, 1998.

[126] S. G. Kandlikar, "Fundamental issues related to flow boiling in minichannels and microchannels," *Experimental Thermal and Fluid Science,* vol. 26, no. 2-4, pp. 389-407, 2002, doi: 10.1016/S0894-1777(02)00150-4.

[127] L. W. Jin, P. S. Lee, X. X. Kong, Y. Fan, and S. K. Chou, "Ultra-thin minichannel LCP for EV battery thermal management," *Applied Energy,* vol. 113, pp. 1786-1794, 2014, doi: 10.1016/j.apenergy.2013.07.013.

[128] M. S. Patil, J. H. Seo, S. Panchal, S. W. Jee, and M. Y. Lee, "Investigation on thermal performance of water-cooled Li-ion pouch cell and pack at high discharge rate with U-turn type microchannel cold plate," *International Journal of Heat and Mass Transfer,* vol. 155, pp. 119728-119728, 2020, doi: 10.1016/j.ijheatmasstransfer.2020.119728.

[129] T. Deng, G. Zhang, and Y. Ran, "Study on thermal management of rectangular Li-ion battery with serpentine-channel cold plate," *International Journal of Heat and Mass Transfer,* vol. 125, pp. 143-152, 2018/10// 2018, doi: 10.1016/J.IJHEATMASSTRANSFER.2018.04.065.

[130] Z. Qian, Y. Li, and Z. Rao, "Thermal performance of lithium-ion battery thermal management system by using mini-channel cooling," *Energy Conversion and Management,* vol. 126, pp. 622-631, 2016, doi: 10.1016/j.enconman.2016.08.063.

[131] C. Zhao, W. Cao, T. Dong, and F. Jiang, "Thermal behavior study of discharging/charging cylindrical lithium-ion battery module cooled by channeled liquid flow," *International Journal of Heat and Mass Transfer,* vol. 120, pp. 751-762, 2018, doi: 10.1016/j.ijheatmasstransfer.2017.12.083.

[132] R. Wang, J. Wang, and W. Yuan, "Analysis and optimization of a microchannel heat sink with V-ribs using nanofluids for micro solar cells," *Micromachines,* vol. 10, no. 9, 2019, doi: 10.3390/mi10090620.

[133] A. B. Nohooji, D. Toghraie, F. Pourfattah, O. A. Akbari, and R. Mashayekhi, "Computational modeling of porous medium inside a channel with homogeneous nanofluid: Structural

design of longitudinal arrangement," *Journal of Thermal Analysis and Calorimetry,* vol. 140, no. 2, pp. 843-858, 2020, doi: 10.1007/s10973-019-08863-9.

[134] A. Sarchami *et al.*, "A novel nanofluid cooling system for modular lithium-ion battery thermal management based on wavy/stair channels," *International Journal of Thermal Sciences,* vol. 182, no. June, pp. 107823-107823, 2022, doi: 10.1016/j.ijthermalsci.2022.107823.

[135] X. Xu, T. Xiao, Chen, Shumei, and S. Lin, "Exploring the heat transfer performance of nanofluid as a coolant for power battery pack," *Heat Transfer-Asian Res,* vol. 48, pp. 2974-2974, 2019, doi: 10.1002/htj.21526.

[136] M. Kiani, M. Ansari, A. A. Arshadi, E. Houshfar, and M. Ashjaee, "Hybrid thermal management of lithium-ion batteries using nanofluid, metal foam, and phase change material: an integrated numerical–experimental approach," *Journal of Thermal Analysis and Calorimetry,* vol. 141, no. 5, pp. 1703-1715, 2020, doi: 10.1007/s10973-020-09403-6.

[137] M. Kiani, S. Omiddezyani, A. M. Nejad, M. Ashjaee, and E. Houshfar, "Novel hybrid thermal management for Li-ion batteries with nanofluid cooling in the presence of alternating magnetic field: An experimental study," *Case Studies in Thermal Engineering,* vol. 28, pp. 101539-101539, 2021/12// 2021, doi: 10.1016/J.CSITE.2021.101539.

[138] A. Dewan and P. Srivastava, "A review of heat transfer enhancement through flow disruption in a microchannel," *Journal of Thermal Science,* vol. 24, no. 3, pp. 203-214, 2015, doi: 10.1007/s11630-015-0775-1.

[139] H. Heidary and M. J. Kermani, "Heat transfer enhancement in a channel with block(s) effect and utilizing Nano-fluid," *International Journal of Thermal Sciences,* vol. 57, pp. 163-171, 2012, doi: 10.1016/j.ijthermalsci.2012.02.001.

[140] A. K. Okab, H. M. Hasan, M. Hamzah, K. Egab, A. Al-Manea, and T. Yusaf, "Analysis of heat transfer and fluid flow in a microchannel heat sink with sidewall dimples and fillet profile," *International Journal of Thermofluids,* vol. 15, no. August, pp. 100192-100192, 2022, doi: 10.1016/j.ijft.2022.100192.

[141] T. Wahidi, R. A. Chandavar, and A. K. Yadav, "Stability enhancement of supercritical CO2 based natural circulation loop using a modified Tesla valve," *Journal of Supercritical Fluids,* vol. 166, pp. 105020-105020, 2020, doi: 10.1016/j.supflu.2020.105020.

[142] P. R. Porwal, S. M. Thompson, D. K. Walters, and T. Jamal, "Heat transfer and fluid flow characteristics in multistaged Tesla valves," *Numerical Heat Transfer; Part A: Applications,* vol. 73, no. 6, pp. 347-365, 2018, doi: 10.1080/10407782.2018.1447199.

[143] J. y. Qian, M. r. Chen, X. l. Liu, and Z. j. Jin, "A numerical investigation of the flow of nanofluids through a micro Tesla valve," *Journal of Zhejiang University: Science A,* vol. 20, no. 1, pp. 50-60, 2019, doi: 10.1631/jzus.A1800431.

[144] Z. Guo, Q. Xu, and M. Ni, "A numerical study on the battery thermal management system with mini-channel cold plate considering battery aging effect," *Applied Thermal Engineering,* vol. 219, no. PB, pp. 119564-119564, 2023, doi: 10.1016/j.applthermaleng.2022.119564.

[145] R. Zhao *et al.*, "Performance analysis and optimization of a novel cooling plate with non-uniform pin-fins for lithium battery thermal management," *Applied Thermal Engineering,* vol. 194, no. February, pp. 117022-117022, 2021, doi: 10.1016/j.applthermaleng.2021.117022.

[146] G. Hetsroni, M. Gurevich, and R. Rozenblit, "Sintered porous medium heat sink for cooling of high-power mini-devices," *International Journal of Heat and Fluid Flow,* vol. 27, no. 2, pp. 259-266, 2006, doi: 10.1016/j.ijheatfluidflow.2005.08.005.

[147] T. C. Hung, Y. X. Huang, T. S. Sheu, and W. M. Yan, "Numerical Optimization of the Thermal Performance of a Porous-Microchannel Heat Sink," *Numerical Heat Transfer; Part A: Applications,* vol. 65, no. 5, pp. 419-434, 2014, doi: 10.1080/10407782.2013.836005.

[148] M. Hamdan and M. d. A. Al-Nimr, "The Use of Porous Fins for Heat Transfer Augmentation in Parallel-Plate Channels," *Transport in Porous Media,* vol. 84, no. 2, pp. 409-420, 2010, doi: 10.1007/s11242-009-9510-2.

[149] A. Marafie and K. Vafai, "Analysis of non-Darcian effects on temperature differentials in porous media," *International Journal of Heat and Mass Transfer,* vol. 44, no. 23, pp. 4401-4411, 2001, doi: 10.1016/S0017-9310(01)00099-0.

[150] Z. Wan *et al.*, "Thermal management improvement of air-cooled proton exchange membrane fuel cell by using metal foam flow field," *Applied Energy,* vol. 333, no. August 2022, pp. 120642-120642, 2023, doi: 10.1016/j.apenergy.2023.120642.

[151] S. Tescari, N. Mazet, and P. Neveu, "Constructal method to optimize solar thermochemical reactor design," *Solar Energy,* vol. 84, no. 9, pp. 1555-1566, 2010, doi: 10.1016/j.solener.2010.06.015.

[152] A. Bejan and S. Lorente, "The constructal law of design and evolution in nature," pp. 1335-1347, 2010, doi: 10.1098/rstb.2009.0302.

[153] L. Wang, "Universality of design and its evolution Comment on " The constructal law and the evolution of design in nature "," *Physics of Life Reviews,* vol. 8, no. 3, pp. 257-258, 2011, doi: 10.1016/j.plrev.2011.08.003.

[154] A. Bejan, "The tree of convective heat streams: Its thermal insulation function and the predicted 3/4-power relation between body heat loss and body size," *International Journal of Heat and Mass Transfer,* vol. 44, no. 4, pp. 699-704, 2001, doi: 10.1016/S0017-9310(00)00138-1.

[155] J. P. Meyer, O. T. Olakoyejo, and T. Bello-Ochende, "Constructal optimisation of conjugate triangular cooling channels with internal heat generation," *International Communications in Heat and Mass Transfer,* vol. 39, no. 8, pp. 1093-1100, 2012, doi: 10.1016/j.icheatmasstransfer.2012.07.008.

[156] T. Bello-Ochende, O. T. Olakoyejo, J. P. Meyer, A. Bejan, and S. Lorente, "Constructal flow orientation in conjugate cooling channels with internal heat generation," *International Journal of Heat and Mass Transfer,* vol. 57, no. 1, pp. 241-249, 2013, doi: 10.1016/j.ijheatmasstransfer.2012.10.021.

[157] O. B. T. Y. A. Yilmaz, "Optimum shape and dimensions of ducts for convective heat transfer in laminar flow at constant wall temperature," *Int. J. Heat Mass Transfer,* vol. 43, pp. 767–775-767–775, 2000.

[158] Y. S. Muzychka, "Constructal multi-scale design of compact micro-tube heat sinks and heat exchangers," vol. 46, pp. 245-252, 2007, doi: 10.1016/j.ijthermalsci.2006.05.002.

[159] T. Bello-Ochende, J. P. Meyer, and A. Bejan, "Constructal multi-scale pin-fins," *International Journal of Heat and Mass Transfer,* vol. 53, no. 13-14, pp. 2773-2779, 2010, doi: 10.1016/j.ijheatmasstransfer.2010.02.021.

[160] A. K. da Silva, S. Lorente, and A. Bejan, "Optimal distribution of discrete heat sources on a plate with laminar forced convection," *International Journal of Heat and Mass Transfer,* vol. 47, no. 10-11, pp. 2139-2148, 2004, doi: 10.1016/j.ijheatmasstransfer.2003.12.009.

[161] A. H. Reis, A. F. Miguel, and A. Bejan, "Constructal theory of particle agglomeration and design of air-cleaning devices," *Journal of Physics D: Applied Physics,* vol. 39, no. 10, pp. 2311-2318, 2006, doi: 10.1088/0022-3727/39/10/046.

[162] Y. Li *et al.*, "Citation: Constructal Optimizations of Liquid-Cooled Channels with Triangle or Square Sections in a Cylindrical Heating Body," 2023, doi: 10.3390/math11020357.

[163] D. O. Ariyo and T. Bello-Ochende, "Constructal design of subcooled microchannel heat exchangers," *International Journal of Heat and Mass Transfer,* vol. 146, pp. 118835-118835, 2020, doi: 10.1016/j.ijheatmasstransfer.2019.118835.

[164] T. Jatau and T. Bello-Ochende, "Constructal design of flat plate solar collector," *Proceedings of the Romanian Academy Series A - Mathematics Physics Technical Sciences Information Science,* vol. 19, pp. 160-165, 2018.

[165] T. M. Gulotta, F. Guarino, M. Cellura, and G. Lorenzini, "Constructal law optimization of a boiler," *International Journal of Heat and Technology,* vol. 35, no. Special Issue 1, pp. S261-S269, 2017, doi: 10.18280/ijht.35Sp0136.

[166] A. H. Reis and A. Bejan, "Constructal theory of global circulation and climate," *International Journal of Heat and Mass Transfer,* vol. 49, no. 11-12, pp. 1857-1875, 2006, doi: 10.1016/j.ijheatmasstransfer.2005.10.037.

[167] X. Liu, L. Chen, H. Feng, X. Qin, and F. Sun, "Constructal design of a blast furnace iron-making process based on multi-objective optimization," *Energy,* vol. 109, pp. 137-151, 2016, doi: 10.1016/j.energy.2016.04.101.

[168] V. D. Zimparov, A. K. Silva, and A. Bejan, "Constructal tree-shaped parallel flow heat exchangers," vol. 49, pp. 4558-4566, 2006, doi: 10.1016/j.ijheatmasstransfer.2006.04.035.

[169] S. Chen, A. F. Miguel, and M. Aydin, "Constructal design in the cooling and hydraulic performance of tube heat sinks," *International Communications in Heat and Mass Transfer,* vol. 129, pp. 105668-105668, 2021, doi: 10.1016/j.icheatmasstransfer.2021.105668.

[170] S. Gungor, E. Cetkin, and S. Lorente, "Canopy-to-canopy liquid cooling for the thermal management of lithium-ion batteries, a constructal approach," *International Journal of Heat and Mass Transfer,* vol. 182, 2022, doi: 10.1016/j.ijheatmasstransfer.2021.121918.

[171] Y. Fan, Z. Wang, T. Fu, and H. Wu, "Numerical investigation on lithium-ion battery thermal management utilizing a novel tree-like channel liquid cooling plate exchanger," *International Journal of Heat and Mass Transfer,* vol. 183, pp. 122143-122143, 2022, doi: 10.1016/j.ijheatmasstransfer.2021.122143.

[172] Y. Fan, Z. Wang, and T. Fu, "Multi-objective optimization design of lithium-ion battery liquid cooling plate with double-layered dendritic channels," *Applied Thermal Engineering,* vol. 199, no. August, pp. 117541-117541, 2021, doi: 10.1016/j.applthermaleng.2021.117541.

[173] S. Gungor and E. Cetkin, "Enhanced temperature uniformity with minimized pressure drop in electric vehicle battery packs at elevated C-rates," *Heat Transfer,* vol. 51, no. 8, pp. 7540-7561, 2022, doi: 10.1002/htj.22654.

[174] M. R. H. C and D. Montgomery, "Response surface Methodology: process and product optimisation using designed experiment," A Willey- Interscience publication, 2002.

[175] A. I. Khuri and S. Mukhopadhyay, "Response surface methodology," *Wiley Interdisciplinary Reviews: Computational Statistics,* vol. 2, no. 2, pp. 128-149, 2010, doi: 10.1002/wics.73.

[176] M. Yolmeh and S. Mahdi Jafari, "Applications of Response Surface Methodology in the Food Industry Processes," 1947, doi: 10.1007/s11947-016-1855-2.

[177] H. Öktem, T. Erzurumlu, and H. Kurtaran, "Application of response surface methodology in the optimization of cutting conditions for surface roughness," *Journal of Materials Processing Technology,* vol. 170, no. 1-2, pp. 11-16, 2005, doi: 10.1016/j.jmatprotec.2005.04.096.

[178] L. Quanhong and F. Caili, "Application of response surface methodology for extraction optimization of germinant pumpkin seeds protein," *Food Chemistry,* vol. 92, no. 4, pp. 701-706, 2005, doi: 10.1016/j.foodchem.2004.08.042.

[179] J. Zhou, M. Hatami, D. Song, and D. Jing, "Design of microchannel heat sink with wavy channel and its time-efficient optimization with combined RSM and FVM methods," *International Journal of Heat and Mass Transfer,* vol. 103, pp. 715-724, 2016, doi: 10.1016/j.ijheatmasstransfer.2016.07.100.

[180] A. A. Ahmadi, M. Arabbeiki, H. M. Ali, M. Goodarzi, and M. R. Safaei, "Configuration and Optimization of a Minichannel Using Water-Alumina Nanofluid by Non-Dominated Sorting Genetic Algorithm and Response Surface Method," *Nanomaterials,* vol. 10, pp. 901-901, 2020, doi: 10.3390/nano10050901.

[181] M. Rahimi-Gorji, O. Pourmehran, M. Hatami, and D. D. Ganji, "Statistical optimization of microchannel heat sink (MCHS) geometry cooled by different nanofluids using RSM analysis," *European Physical Journal Plus,* vol. 130, no. 2, pp. 1-21, 2015, doi: 10.1140/epjp/i2015-15022-8.

[182] Y. Peng, U. Khaled, A. A. A. A. Al-Rashed, R. Meer, M. Goodarzi, and M. M. Sarafraz, "Potential application of Response Surface Methodology (RSM) for the prediction and

optimization of thermal conductivity of aqueous CuO (II) nanofluid: A statistical approach and experimental validation," *Physica A: Statistical Mechanics and its Applications,* vol. 554, pp. 124353-124353, 2020, doi: 10.1016/j.physa.2020.124353.

[183] O. O. Adewumi, T. Bello-Ochende, and J. P. Meyer, "Numerical Investigation into the Thermal Performance of Single Microchannels with Varying Axial Length and Different Shapes of Micro Pin-Fin Inserts," 2017, doi: 10.1080/01457632.2016.1239927.

[184] Z. Ling, J. Cao, W. Zhang, Z. Zhang, X. Fang, and X. Gao, "Compact liquid cooling strategy with phase change materials for Li-ion batteries optimized using response surface methodology," *Applied Energy,* vol. 228, no. July, pp. 777-788, 2018, doi: 10.1016/j.apenergy.2018.06.143.

[185] A. Afzal, I. Mokashi, S. A. Khan, N. A. Abdullah, and M. H. B. Azami, "Optimization and analysis of maximum temperature in a battery pack affected by low to high Prandtl number coolants using response surface methodology and particle swarm optimization algorithm," *Numerical Heat Transfer; Part A: Applications,* vol. 79, no. 5, pp. 406-435, 2020, doi: 10.1080/10407782.2020.1845560.

[186] C. M. X. P. A. G. N. B. Xiangping Liao, "Temperature Distribution Optimization of an Air-Cooling Lithium-Ion Battery Pack in Electric Vehicles Based on the Response Surface Method," *Journal of Electrochemical Energy conversion and storage,* vol. 16, no. 4, 2019.

[187] D. Zhao, M. Chen, J. Lv, Z. Lei, and W. Song, "Multi-objective optimization of battery thermal management system combining response surface analysis and NSGA-II algorithm," *Energy Conversion and Management,* vol. 292, no. March, pp. 117374-117374, 2023, doi: 10.1016/j.enconman.2023.117374.

[188] B. Chezeau and C. Vial, "Modeling and Simulation of the Biohydrogen Production Processes," *Biomass, Biofuels, Biochemicals: Biohydrogen, Second Edition,* pp. 445-483, 2019/1// 2019, doi: 10.1016/B978-0-444-64203-5.00019-8.

[189] J. Nanda *et al.*, "Thermophysical properties of LiFePO4 cathodes with carbonized pitch coatings and organic binders: Experiments and first-principles modeling," *Journal of Power Sources,* vol. 251, pp. 8-13, 2014, doi: 10.1016/j.jpowsour.2013.11.022.

[190] S. V. Patankar, *Numerical Heat Transfer and Fluid Flow*. New York, USA:: Hemisphere Publishing Corp, 1980, pp. 205-205.

[191] A. Carranza-Abaid and J. P. Jakobsen, "A Non-Autonomous Relativistic Frame of Reference for Unit Operation Design," *Computer Aided Chemical Engineering,* vol. 48, pp. 151-156, 2020/1// 2020, doi: 10.1016/B978-0-12-823377-1.50026-4.

[192] F. M. White, *Viscous fluid flow*. McGraw-Hill, 1991.

[193] J.-a. Epinette and K. Sutton, "User ' s Guide," no. November, pp. 1-44, 2003.

[194] "ANSYS Fluent Users Guide documents 21R1," 2021.

[195] S. M. Zahraee, J. M. Rohani, and K. Y. Wong, "Application of computer simulation experiment and response surface methodology for productivity improvement in a continuous production line: Case study," *Journal of King Saud University - Engineering Sciences,* vol. 30, no. 3, pp. 207-217, 2018, doi: 10.1016/j.jksues.2018.04.003.

[196] H. Zhang, X. Wu, Q. Wu, and S. Xu, "Experimental investigation of thermal performance of large-sized battery module using hybrid PCM and bottom liquid cooling configuration," *Applied Thermal Engineering,* vol. 159, no. May, pp. 113968-113968, 2019, doi: 10.1016/j.applthermaleng.2019.113968.

[197] A. C. Turkmen, C. Celik, and H. Esen, "The statistical relationship between flow channel geometry and pressure drop in a direct methanol fuel cell with parallel channels," *International Journal of Hydrogen Energy,* vol. 44, no. 34, pp. 18939-18950, 2019, doi: 10.1016/j.ijhydene.2019.04.034.

[198] T. Bello-Ochende, J. P. Meyer, and J. Dirker, "Three-dimensional multi-scale plate assembly for maximum heat transfer rate density," *International Journal of Heat and Mass Transfer,* vol. 53, no. 4, pp. 586-593, 2010, doi: 10.1016/j.ijheatmasstransfer.2009.10.041.

[199] A. Bejan, "Designed porous media: Maximal heat transfer density at decreasing length scales," *International Journal of Heat and Mass Transfer,* vol. 47, no. 14-16, pp. 3073-3083, 2004, doi: 10.1016/j.ijheatmasstransfer.2004.02.025.

[200] M. P. Vasilev, R. S. Abiev, and R. Kumar, "Effect of circular pin-fins geometry and their arrangement on heat transfer performance for laminar flow in microchannel heat sink," *International Journal of Thermal Sciences,* vol. 170, no. June, pp. 107177-107177, 2021, doi: 10.1016/j.ijthermalsci.2021.107177.

[201] O. H. Hassan, G. I. Sultan, M. N. Sabry, and A. A. Hegazi, "Investigation of heat transfer and pressure drop in a porous media with internal heat generation," *Case Studies in Thermal Engineering,* vol. 32, no. January, pp. 101849-101849, 2022, doi: 10.1016/j.csite.2022.101849.